Perspectives of Active Atomic Clock Based on Modelocked Semiconductor Laser with Rubidium Vapor Cell Saturable Absorber

PAR

Xi ZENG

EPFL

ÉCOLE POLYTECHNIQUE
FÉDÉRALE DE LAUSANNE

Suisse
2015

Acknowledgements

The work here would not have been possible without the support of many people. I would like to thank my thesis directors Dr. Dmitri Boïko and Professor Nicolas Grandjean for generously giving me the opportunity to work in this research project. This research would not have gone anywhere without Dr. Boïko's guidance, and my capability as a researcher would not be what it is now without him challenging me to be better.

The majority of the work in this dissertation was performed in Centre Suisse d'Electronique et de Microtechnique SA (CSEM) in Neuchâtel, Switzerland. My fellow colleagues in CSEM have been indispensible for many critical parts in this research. I would like to thank Jacques Haesler, Laurent Balet, and Stefan Kundermann for generously sharing with me their measurement equipment and for insightful research discussions. Furthermore, without Jacques's spectroscopy setup, I would not have been able to produce a significant part of the research here. I am very grateful to Valentin Mitev For allowing me access to his Nd:YAG laser. Jean-François Léchenne has been very helpful for his mechanical and machine shop support in fabricating many components used in this research. Christine Y. Wang played an important role in measuring some of the data presented here. Steve Lecomte has been a great source of intellectual support. I would also like to thank Gilles Buchs, Alex Pollini, Erwin Portuondo, and François Barrot for their company. Finally, I would like to thank my officemate and fellow PhD student Johan Kruis for being a good friend.

My colleagues in EPFL have been indispensible to this research as well. I would like to thank Gatien Cosendey and Jean-François Carlin for providing me with III-nitride VECSEL samples. Raphaël Butté, Jacques Levrat, Georg Rossbach, and Marlene Glauser have been generous in sharing with me their laboratory, without which I would not have been able to produce my first publication in my PhD career. I would also like to thank Luca Sulmoni and Jean-Michel Lamy for their work in III-nitride multi-section diode lasers.

Lastly, I would like to thank my parents for their consistent moral support over the years.

Neuchâtel, November 2014

:: csem   EPFL
ÉCOLE POLYTECHNIQUE
FÉDÉRALE DE LAUSANNE

Abstract

Atomic clocks are a vital technology in the day to day operation of modern society. While passive Rb and Cs microwave atomic clocks find widespread practical applications today, active atomic clocks have the potential to surpass them in frequency stability, compactness, and simplicity. This dissertation is a comprehensive study of the physics of an active atomic clock based on modelocked external cavity semiconductor laser with ^{85}Rb vapor cell saturable absorber. As the starting point for establishing our concept, this study encompasses optical interrogation in the traditional D_1 ($5S_{1/2}$-$5P_{1/2}$, 795 nm wavelength) line in ^{85}Rb atoms, as well as in the less used and less studied $5S_{1/2}$-$6P_{3/2}$ (420 nm) line, which has very different absorption characteristics. The theoretical and experimental work in this dissertation establish a foundational background for the active atomic clock laser, yielding novel results in the field of semiconductor lasers and atomic physics.

We use a state of the art modelocked lasing analysis technique to predict the operating conditions that would yield modelocked oscillations in our proposed active atomic clock. Proper application of this technique requires an accurate and detailed model of the ^{85}Rb absorber, including parameters such as the absorption cross-section, pressure broadening of absorption linewidth, ground state and spin relaxation times as well as the excited state lifetime. To address these aspects, we have developed a six-level atomic model for the absorption characteristics of alkali atoms that accounts for the effects of optical beam size and buffer gas pressure on ground state and spin relaxation times. This model allowed us to establish and experimentally realize a novel pump-probe technique for measuring the excited state lifetime in alkali atoms when under conditions of strong fluorescence quenching by buffer gas.

Our theoretical model for the dependence of relaxation times on the optical beam size, buffer gas pressure, and cell temperature was experimentally validated in detailed absorption spectroscopy measurements in the D_1 line of Rb atoms. Most importantly, we use our novel pump-probe technique to measure the excited $5P_{1/2}$ state lifetime that is quenched by N_2 buffer gas and experimentally confirm its reduction down to about a nanosecond.

For spectroscopy at the $5S_{1/2}$-$6P_{3/2}$ line of Rb atoms, we have built and characterized a blue wavelength external cavity diode laser (ECDL) for use as the optical interrogation source with precisely known linewidth and frequency noise performances. Using this spectroscopic tool for the $5S_{1/2}$-$6P_{3/2}$ line, we measured the linewidth pressure broadening and frequency shift coefficients of N_2 buffer gas. To the best of our knowledge, this is the first time that N_2 pressure broadening and frequency shift coefficients are measured in the blue absorption lines of Rb.

Furthermore, very controversial data were available in the literature about the natural lifetime of the excited states in the blue absorption lines of Rb, and lifetime quenching by molecular buffer gasses was not addressed in the literature at all. We attempted two different approaches to measure the $6P_{3/2}$ excited state lifetime of Rb with pump-probe techniques. In the first approach, both pump and

probe lasers operate at 420 nm wavelength with pumping by short optical pulses. In this approach, we obtained solitary short optical pulse generation with precise wavelength for the $5S_{1/2}$-$6P_{3/2}$ line by using our ECDL, as the master laser, to optically injection lock a passively Q-switched InGaN multi-section laser diode (MSLD). To the best of our knowledge, the optical injection locking of a Q-switched III-nitride MSLD has never been done before. Unfortunately, the pulse energy was insufficient to produce experimentally detectable changes in the transmitted power of the probe ECDL laser beam.

In the second approach to measure the lifetime in the excited state $6P_{3/2}$, we benefitted from the fact that its natural lifetime is expected to be about one order of magnitude longer than the $5P_{1/2}$ state. Therefore, we used a continuous wave (CW) pump laser at the $5S_{1/2}$-$5P_{1/2}$ line and a CW probe laser at the $5S_{1/2}$-$6P_{3/2}$ line to measure the $6P_{3/2}$ state lifetime of ^{85}Rb. Prior to our work, the natural lifetime of the $6P_{3/2}$ state in Rb atoms and its quenching by molecular buffer gas N_2 were not unambiguously known and reported in the literature.

One of the possible realizations of our atomic clock based on modelocked laser with alkali vapor cell absorber, as initially envisioned, incorporate III-nitride based vertical-external-cavity surface-emitting laser (VECSEL) at 420 nm wavelength for operation in the $5S_{1/2}$-$6P_{3/2}$ line of Rb. However, prior to this dissertation work, there were no reports of centimetric length external cavity III-nitride VECSEL suitable for incorporation of intracavity elements. Therefore, we experimentally realized an optically pumped III-nitride VECSEL with injection seeding from a microcavity, and we were able to obtain lasing for a cavity as long as 50 mm, making such VECSEL suitable for incorporation of a saturable absorber cell. This is the longest III-nitride VECSEL cavity that we know of at the time of its realization.

Finally, from the six-level model for alkali atoms and measurements from spectroscopy experiments, we adapted the previously mentioned state of the art modelocked lasing analysis technique, which was originally developed for a laser system with semiconductor electro-absorber, to now incorporate a ^{85}Rb vapor cell saturable absorber. From this, we investigated several laser cavity configurations and the operation conditions that will yield modelocked lasing. Possible realizations of our atomic clock based on modelocked laser with alkali vapor cell absorber include III-V alloy based ECDL and VECSEL as well as III-nitride based ECDL and VECSEL. We conclude that the realization with the most prospects from a practical point of view would be a 795 nm modelocked ECDL with a ^{85}Rb saturable absorber, and we provide its cavity design. This design will serve as the starting point for future experimental realization of such laser system.

Keywords

Atomic clock, modelocking, Rubidium, hyperfine splitting, saturable absorber, spectroscopy, excited state lifetime, beam transit effect, ground state relaxation, spin relaxation, wall collision, gallium nitride, III-nitrides, vertical external cavity surface emitting laser, injection seeding, external cavity diode laser, mode clustering, multi-section laser diode, Q-switching, optical injection locking, pulse-on-demand production

Résumé

Dans notre société moderne, les horloges atomiques sont devenues une technologie indispensable. Alors que les horloges passives basées sur des atomes de Rubidium et de Césium sont largement utilisées dans une large gamme d'applications, les horloges actives possèdent le potentiel de les surpasser en termes de stabilité de fréquence, d'encombrement et de simplicité. La présente thèse constitue une étude complète de la physique d'une horloge atomique active basée sur un laser semi-conducteur à cavité externe à verrouillage de modes avec un absorbeur saturable basé sur une cellule de vapeur de ^{85}Rb. Comme point de départ, cette étude s'intéresse à la traditionnelle raie D_1 ($5S_{1/2}$-$5P_{1/2}$, longueur d'onde 795 nm) de l'atome ^{85}Rb et également à la raie $5S_{1/2}$-$6P_{3/2}$ (420 nm) qui est nettement moins utilisée et étudiée et possède des caractéristiques d'absorption très différentes. Le travail théorique et expérimental présenté dans cette thèse établit une brique fondamentale pour le laser de l'horloge atomique active et fournit de nouveaux résultats dans les domaines des lasers semi-conducteurs et de la physique atomique.

Nous utilisons une technique d'analyse laser pointue dans le but de prédire les conditions opérationnelles conduisant à des oscillations de verrouillage de modes dans notre prototype d'horloge atomique active. Une utilisation appropriée de cette technique requiert un modèle précis et détaillé de l'absorbeur à vapeur de ^{85}Rb, incluant des paramètres tels que la section efficace d'absorption, l'élargissement de la raie d'absorption due à la pression, état fondamental hyperfin et temps de relaxation et également le temps de vie de l'état excité. Pour traiter ces aspects, nous avons développé un modèle atomique à 6 niveaux pour les caractéristiques d'absorption d'atomes alcalins tenant compte des effets liés au diamètre du faisceau optique ainsi que de la pression du gaz tampon sur les temps de relaxation de l'état fondamental hyperfin ainsi que de relaxation de spin. Ce modèle nous a permis d'établir et de réaliser expérimentalement une nouvelle technique de pompe-sonde pour mesurer le temps de vie de l'état excité dans les atomes alcalins dans des conditions de forte extinction (quenching) de la fluorescence due au gaz tampon.

Notre modèle théorique pour la dépendance du temps de relaxation par rapport à la taille du faisceau optique, pression du gaz tampon et température de la cellule a été validé expérimentalement dans le cadre de mesures détaillées de spectroscopie en absorption de la raie D_1 d'atomes de Rubidium. Plus important encore, nous utilisons notre nouvelle technique pompe-sonde pour mesurer la durée de vie de l'état excité $5P_{1/2}$, désactivé par le gaz tampon N_2, et pour confirmer expérimentalement sa diminution jusqu'à la nanoseconde.

Pour la spectroscopie de la raie $5S_{1/2}$-$6P_{3/2}$ de l'atome de Rubidium, nous avons construit et caractérisé une diode laser à cavité externe (ECDL) émettant dans le bleu. Cette dernière est utilisée comme source d'interrogation optique avec une largeur de raie connue précisément et de bonnes performances en termes de bruit. Grace à cet outil, nous avons pu mesurer l'élargissement de la raie d'absorption due à la pression ainsi que le coefficient de décalage de fréquence du gaz tampon N_2. A notre connaissance, il s'agit ici d'une première pour des raies d'absorption du Rubidium dans le bleu.

De plus, les données disponibles dans la littérature concernant le temps de vie naturel des états excités dans les raies d'absorption du Rubidium dans les longueurs d'onde bleues sont controversées. Aussi, le temps d'extinction (quenching) dû au gaz tampon n'est pas du tout traité dans la littérature. Nous avons adopté deux approches différentes pour mesurer le temps de vie de l'état excité $6P_{3/2}$ de l'atome de Rubidium avec notre technique pompe-sonde. Dans la première approche, la pompe et la sonde opèrent à une longueur

d'onde de 420 nm avec un pompage basé sur des impulsions optique courtes. Nous avons verrouillé une diode laser InGaN multi-sections (MSLD) passivement Q-switchée par injection optique en utilisant notre ECDL comme laser principal (laser maître). De cette façon, nous obtenons des impulsions optiques isolées avec une longueur d'onde très précise pour sonder de la raie $5S_{1/2}$-$6P_{3/2}$. A notre connaissance, le verrouillage par injection optique d'une MSLD Q-switchée à la base de III-nitrures n'a jamais été réalisé jusqu'ici. Malheureusement, l'énergie des impulsions n'était pas suffisante pour produire des changements détectables expérimentalement dans la puissance de transmission du faisceau de sonde ECDL.

Dans la seconde approche, nous avons bénéficié du fait que le temps de vie naturel dans l'état excité $6P_{3/2}$ est censé être plus long que dans l'état $5P_{1/2}$ d'un ordre de grandeur. Par conséquent, nous avons utilisé des lasers continus (CW) respectivement pour la pompe de la raie $5S_{1/2}$-$5P_{1/2}$ et pour la sonde de la raie $5S_{1/2}$-$6P_{3/2}$ pour mesurer le temps de vie de l'état $6P_{3/2}$ du ^{85}Rb. Avant nos travaux, le temps de vie naturel de l'état $6P_{3/2}$ de l'atome de Rubidium ainsi son extinction (quenching) par un gaz tampon N_2 n'étaient pas connus sans ambiguïté.

Une des réalisations possibles de notre horloge atomique basée sur un laser à verrouillage de modes avec un absorbeur à cellule de vapeur alcaline, comprend un laser à base de III-nitrures à émission de surface en cavité verticale (VECSEL) fonctionnant à 420 nm pour sonder de la raie $5S_{1/2}$-$6P_{3/2}$ de l'atome de Rubidium. Cependant, avant ce travail de thèse, aucun rapport dans la littérature n'existait concernant des VECSEL à base de III-nitrures à cavité externe de dimension centimétrique appropriée pour une incorporation intra-cavité. C'est pourquoi nous avons construit un VECSEL pompé optiquement avec une injection venant d'une micro-cavité. De cette façon nous avons obtenu un effet laser pour une cavité de 50 mm, rendant un tel VECSEL approprié pour l'incorporation d'une cellule d'absorbeur saturable. Il s'agit de la plus longue cavité de type VECSEL basée sur des III-nitrures reportée à ce jour.

Finalement, grâce au model à six niveaux pour les atomes alcalins et les mesures de spectroscopie, nous avons pu adapter notre technique d'analyse originalement développée pour un système de laser à absorbeur semi-conducteur, avec maintenant l'incorporation d'une cellule d'absorbeur saturable à vapeur de ^{85}Rb. A partir de là, nous avons étudié plusieurs configurations de cavités laser ainsi que les conditions opérationnelles permettant un « lasing » à verrouillage de modes. Les réalisations possibles de nos horloges atomiques basées sur un laser à verrouillage de modes avec une cellule d'absorbeur saturable à vapeur alcaline incluent des ECDLs et VECSELs basées sur des alliages III-V ainsi que des III-nitrures. En conclusion, nous présentons le design d'un ECDL à verrouillage de modes avec un absorbeur saturable basé sur une vapeur ^{85}Rb émettant à 795 nm. Cette configuration nous semble être la plus viable d'un point de vue pratique. Ce design va servir de point de départ pour de futures réalisations expérimentales.

Mots-clés

Horloge atomique, verrouillage de modes, Rubidium, niveaux hyperfins, absorbeur saturable, spectroscopie, temps de vie de l'état excité, relaxation de l'état fondamental, relaxation de spin, wall collision, nitrure de gallium, nitrures de type III, laser à émission de surface en cavité verticale, injection optique, diode laser à cavité externe, mode clustering, diode laser multi-sections, Q-switching, impulsions à la demande

Contents

Nomenclature

List of Acronyms

AR	antireflection
ASE	amplified spontaneous emission
CPT	coherent population trapping
Cs	Cesium
CW	continuous wave
DBR	distributed Bragg reflector
DF	dual frequency
DFB	distributed feedback laser
DR	Double Resonance
EOM	electro-optic modulator
ECDL	external cavity diode laser
FL	focal length of lens
FWHM	full-width at half-maximum
LCP	left circular polarization
HR	high reflectivity
MSLD	multi-section laser diode
QD	quantum dot
QW	quantum well
RCP	right circular polarization
Rb	Rubidium
RF	radio frequency
RIN	relative intensity noise
SESAM	semiconductor saturable absorber mirror
SF	single frequency

SVB   the Smetanin, Vasil'ev, and Boiko approach to modelocked lasing analysis

VCO   voltage controlled oscillator

VCSEL   vertical-cavity surface-emitting laser

VECSEL   vertical-external-cavity surface-emitting laser

Constants

c speed of light in vacuum, 2.99792458×10^8 m/s

e electron charge, $1.60217657 \times 10^{-19}$ C

k_B Boltzmann constant, $1.3806488 \times 10^{-23}$ m$^2 \cdot$kg$\cdot$s$^{-2}\cdot$K^{-1}

$\hbar$ reduced Planck's constant, $1.054571726 \times 10^{-34}$ J$\cdot$s

R gas constant, 8.3144621 J/mol$\cdot$K

r_e classical electron radius, $2.8179403267 \times 10^{-15}$ m

Variables (Units)

A_A cross-sectional area of optical mode on saturable absorber (cm^2)

A_L cross-sectional area of optical mode on optical gain section (cm^2)

d_b effective active region barrier thickness in surface-emitting laser gain chip (μm)

D_{Rb} diffusion coefficient of Rb inside vapor cell (cm^2/s)

d_{sA} diameter of optical mode on saturable absorber (μm)

E_{sA} saturation energy of absorber (J)

E_{sL} saturation energy of optical gain section (J)

F_{sat} saturation fluence of absorber (μJ/cm^2)

f absorption oscillator strength (no units)

I optical intensity (mW/cm^2)

I_{sat} optical saturation energy (mW/cm^2)

J current density (A/cm^2)

l_A length of saturable absorber, (mm)

l_C	length of laser cavity, (mm)
l_L	length of optical gain section (mm)
L_{cell}	length of Rb/alkali vapor cell (mm)
L_{diode}	length of edge-emitting laser diode (μm)
n_{Rb}	population density of Rb/alkali atoms (cm^{-3})
n_{tr}	transparency population density (cm^{-3})
P_{Rb}	spin polarization of Rb/alkali atoms (no units)
s	modelocking stability parameter, $s=E_{sL}/E_{sA}$, (no units)
T	optical intensity transmission through vapor cell (no units)
T_A	recovery time of absorber section (ns)
T_{cell}	alkali vapor cell temperature, (K) or (° C)
T_L	recovery time of optical gain section (ns)
T_{rep}	cavity roundtrip time (s)
T_s	spin relaxation time (μs)
$T_{s,bulk}$	spin relaxation time in the absence of wall collisions (μs)
$T_{s,wall}$	wall collision time constant for spin of Rb/alkali atoms (μs)
V_a	biasing parameter of electro-absorber (V)
W_p	optical pulse energy (pJ)
α_i	intrinsic material loss (cm^{-1})
β_i	branching ratio to ground state $|i>$, i=1 or 2, (no units)
Δv_D	Doppler broadening of absorption linewidth, (MHz) or (GHz)
Δv_L	Pressure broadening of absorption linewidth, (MHz) or (GHz)
Γ	optical mode confinement factor (no units)
λ	wavelength (nm)
v	frequency (Hz)
v_{HF}	ground state hyperfine splitting frequency, (MHz) or (GHz)
v_{RF}	frequency of modulation, (MHz) or (GHz)

ρ	effective spectral overlap parameter (no units)
ρ_M	curvature radius of mirror (mm)
σ	absorption cross-section of Rb/alkali atoms (cm^2)
τ_{beam}	transit time constant of Rb atoms through optical beam (μs)
τ_{ex}	excited state lifetime (ns)
τ_g	ground state relaxation time (μs)
τ_{wall}	wall collision time constant for energy state of Rb/alkali atoms (μs)
ω	angular frequency, $\omega=2\pi v$ (Hz)
ω_L	gain section spectral half-bandwidth (GHz)
$\hbar\omega$	photon energy (eV)
$\partial g/\partial n$	differential material gain (cm^3/s)

Chapter 1   **Introduction**

Highly stable and accurate frequency standards such as atomic clocks are important instruments in modern society. Atomic clocks with timing error of less than 1 ns per day are the key enabling technology in satellite navigation (e.g. GPS), a service that was originally developed for military use but is now utterly vital in everyday civilian lives. Satellite navigation has greatly increased the speed and safety of global commercial shipping, the lifeblood in today's highly interconnected world. Large scale high speed optical communication network equipments routinely synchronize their onboard times to atomic clocks (timing error less than 1 μs per day), without which their network cannot properly function. For these reasons and more, research to improve atomic clock technology is ongoing.

1.1   Conventional Rubidium Atomic Clock

One type of atomic clock typically used for the applications described above is the rubidium (Rb) vapor cell atomic clock. This is a passive atomic clock based on quartz crystal voltage controlled oscillator (VCO) with frequency stabilization feedback loop. A high level schematic of such a clock is given in Fig. 1.1. The quartz crystal VCO is an electronic oscillator whose output oscillation frequency v_0 can be tuned by changing the applied control voltage. The VCO output is fed into a frequency stabilizing feedback loop which converts deviation in v_0 from the targeted value into an adjustment voltage ΔV, which is then applied to the frequency control port. Through this feedback mechanism, the VCO oscillation frequency is kept extremely stable.
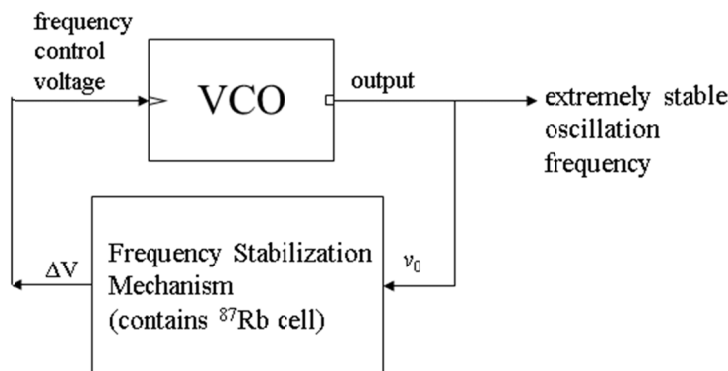
Fig. 1.1. High level schematic of a traditional passive Rb atomic clock. A feedback loop is used to stabilize the oscillation frequency of a VCO. The key component of the frequency stabilization mechanism is the [87]Rb cell, where the stability of its atomic resonance is transferred to the VCO.

The key component in the frequency stabilization mechanism is the [87]Rb vapor cell. The [87]Rb atom ground state is split into two hyperfine levels. With a separation frequency of 6.835 GHz as shown in Fig. 1.2, the ground state hyperfine splitting is very well defined and unaffected by temperature, humidity, and vibration. The frequency stabilization mechanism locks the VCO output frequency v_0 to a value where the [87]Rb ground state hyperfine splitting frequency v_{HF} (6.835 GHz) is a fixed integer multiple of v_0. Therefore, the stability of [87]Rb atomic resonance is transferred into the VCO.
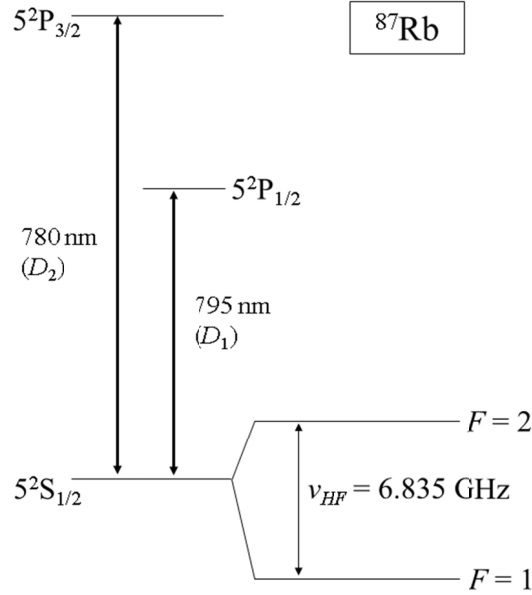
Fig. 1.2. Diagram of [87]Rb energy levels for D_1 and D_2 transitions. Hyperfine structures of excited states are not shown.

Atomic clocks based on Rb vapor cells generally operate using one of two methods of atomic interrogation. The first method, microwave-optical double resonance (DR) interrogation, involves interrogating the [87]Rb atoms at both optical and microwave frequencies as depicted in Fig. 1.3(a). Atoms are optically pumped, by a lamp or a narrowband laser, from one of the ground state hyperfine levels to the excited state, where they decay back to both ground states due to either spontaneous emission or through collisions with buffer gas atoms/molecules. Atoms in the ground state in resonance with the optical interrogation are pumped again to the excited state, while atoms in the other ground state remain there. Repeated cycles of pumping and decay lead to a steady-state condition where the ground state under optical pumping is depleted of population while the unpumped ground state has population far in excess of its equilibrium density. If the atoms are now interrogated with microwave radiation, then atomic absorption of this microwave radiation would transfer some of the excess atoms in the unpumped ground state back to the ground state under pumping. The result is a decrease in the transmission of the optical pump beam through the vapor cell. The transmitted optical intensity is minimized when the microwave radiation is resonant with the ground state hyperfine transition, having frequency equal to the ground state hyperfine splitting frequency v_{HF} as depicted in Fig. 1.3(b).

(a)

P

Optical
Interrogation

S

Microwave
Interrogation

(b)

Transmitted Intensity

Typical linewidth:
~1 kHz

ν_{HF}

Microwave Frequency
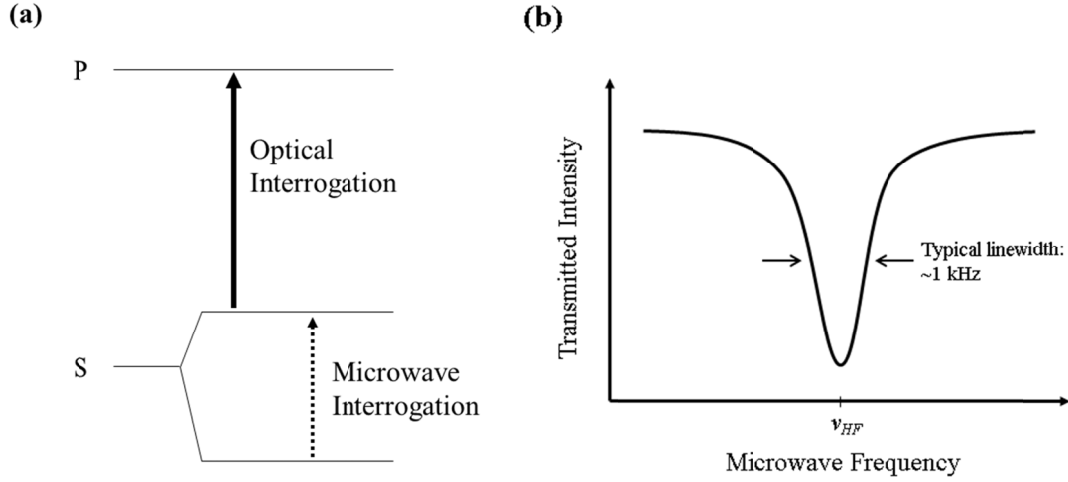
Fig. 1.3. (a) An alkali atom under Double Resonance interrogation. One ground state hyperfine levels is optically pumped, while simultaneously the atom is interrogated by microwave radiation equal to the ground state hyperfine splitting frequency ν_{HF}. (b) Illustration of transmitted light intensity as a function of relative microwave interrogation frequency. Transmission is minimized when the microwave frequency is equal to ν_{HF}.

In an atomic clock, this behavior of atoms under DR interrogation is utilized to lock the oscillation frequency of the VCO. A schematic of such a DR clock is given in Fig. 1.4. The microwave interrogation is seeded by the VCO, where its output frequency is multiplied (by a fixed integer) to where it is equal to the Rb atom ground state hyperfine splitting frequency. Electronic feedback is utilized to continuously adjust the VCO control voltage so as to minimize the optical transmission through the Rb vapor cell, resulting in extremely stable VCO oscillations. A more detailed description of the physics and the electronics involved can be found in [1], [2].
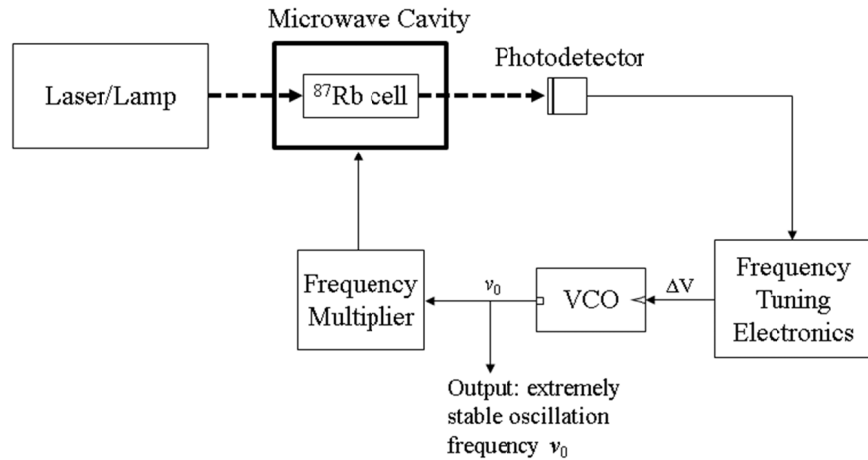
Fig. 1.4. Schematic of a Rb vapor cell atomic clock utilizing the DR interrogation method.

As an alternative to DR interrogation, Rb vapor cell atomic clocks can be realized by taking advantage of Coherent Population Trapping (CPT) effect. Here, the alkali atom is optically interrogated by two optical bands in Λ-pumping configuration, as depicted in Fig. 1.5, where both ground states are simultaneously pumped. When the optical radiation is simultaneously on resonance with both absorption lines, i.e. Raman detuning is zero with $\Delta\nu=0$, the atoms will end up (in steady-state)

in a coherent superposition of the ground states [3], [4] that does not absorb the optical radiation. This is referred as to the atoms being trapped in a "dark state." In practical Rb cells interrogated by real optical sources, absorption is nonzero when Λ-pumping is on resonance, but it is lower than the absorption when the Λ-pumping is off resonance. We have an example of CPT resonance in cell transmission spectrum as a function of Δv in Fig. 1.11 (top panel).
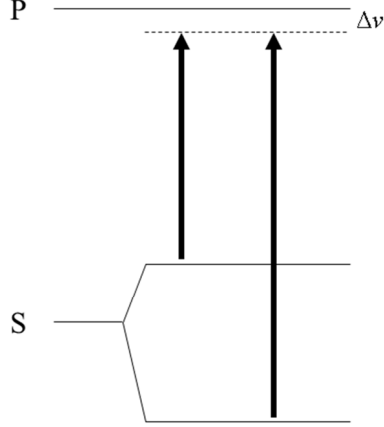
Fig. 1.5. An alkali atom under Λ-pumping. The two ground state hyperfine levels are simultaneously pumped by two optical bands.

CPT under Λ-pumping of atoms serves as the chief mechanism for realizing an atomic clock. For clockwork applications, the typical methods to obtain these two optical bands with the correct frequency separation is to use a single wavelength semiconductor laser and either (i) modulate the optical output with an electro-optic modulator (EOM), or (ii) directly modulate the drive current of this laser. By modulating at frequency v_{RF}, modulation sidebands are generated, with the two 1st order modulation sidebands being separated from the main carrier band by $\pm v_{RF}$. CPT effect is obtained when either $v_{RF}=v_{HF}$ or $v_{RF}=0.5v_{HF}$, resulting in simultaneous interrogation of the atomic transitions with either the main carrier band and one 1st order modulation sideband, or with both 1st order modulation sideband, respectively. We illustrate the optical spectrum of a laser under modulation in Fig. 1.6. Note that while direct modulation of the laser current, as in option (ii), requires fewer components and can be much more compact, it is suitable only if one uses a laser with adequately high bandwidth, e.g. vertical-cavity surface-emitting laser (VCSEL).

The microwave source used to modulate either the EOM or the laser drive current is seeded by the VCO, where its output frequency is multiplied (by a fixed integer). Electronic feedback is utilized to continuously tune the VCO control voltage so as to maximize the optical transmission through the Rb vapor cell by using the CPT effect. The result of the feedback loop and continuous adjustments to the VCO is that the oscillation frequency is extremely stable. We present a schematic of such a CPT atomic clock utilizing direct current modulation in Fig. 1.7.

The two types of aforementioned Rb vapor cell atomic clocks require complex and well calibrated feedback electronics to generate the adjustment voltage ΔV applied to the VCO. Therefore, there is an interest in Rb vapor cell clocks that can bypass the need for such complex electronic feedback equipment.
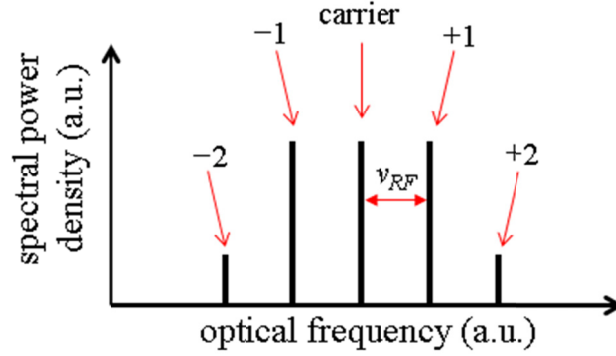
Fig. 1.6. Illustration of optical spectrum of laser under modulation at frequency v_{RF}, resulting in generation of optical sidebands. The sidebands are labeled by their modulation order number.
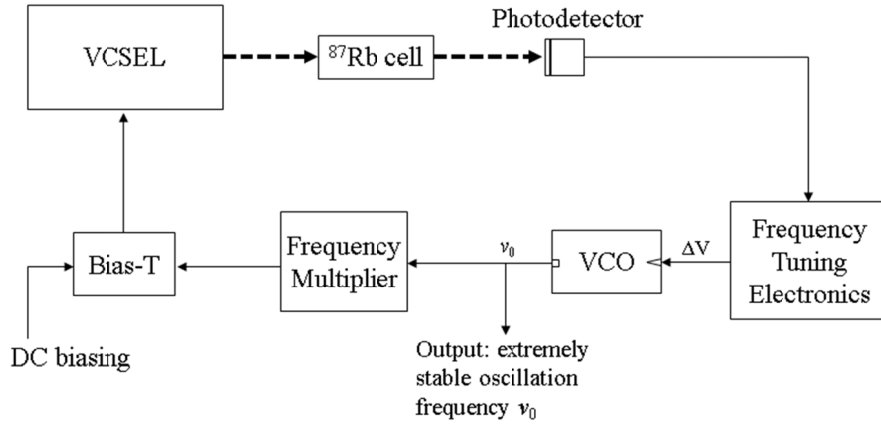
Fig. 1.7. Schematic of a Rb vapor cell atomic clock utilizing the effects of coherent population trapping (CPT).

1.2 Frequency Stability

One of the main performance metrics of atomic clocks is the stability of their oscillation frequency. More specifically, this stability metrics is the Allan deviation σ_y of the fractional frequency y, with $y=[v(t)-v_0]/v_0$, where v_0 is the targeted atomic clock oscillation frequency and $v(t)$ is the instantaneous oscillation frequency. An in-depth description and explanation of atomic clock frequency stability metrics is found in [1].

In Fig. 1.8, the frequency stability characteristics of several state of the art *microwave* atomic clocks are given along with that of a simple quartz oscillator. This includes the Rb vapor atomic clock which was described in Section 1.1 as well as the Cesium (Cs) atomic clock, the technology that is used to define the standard unit of *second*. Similar to the Rb clock, in a Cs clock the quartz oscillator locks onto the Cs ground state hyperfine frequency splitting of 9.193 GHz. Both of these atomic clocks are classified as *passive* clocks, where the atoms are part of a feedback mechanism for a quartz oscillator VCO that corrects for its frequency deviations.

Of note here is the *active* Hydrogen Maser atomic clock which has the best short term frequency stability. Unlike a *passive* clock, in an *active* clock the oscillation is directly generated by the cavity that holds the atoms. This direct generation of the oscillatory signal is one of the reasons why active clocks tend to have better frequency stability than passive clocks, and it is one of the motivations for research in active atomic clocks in general.
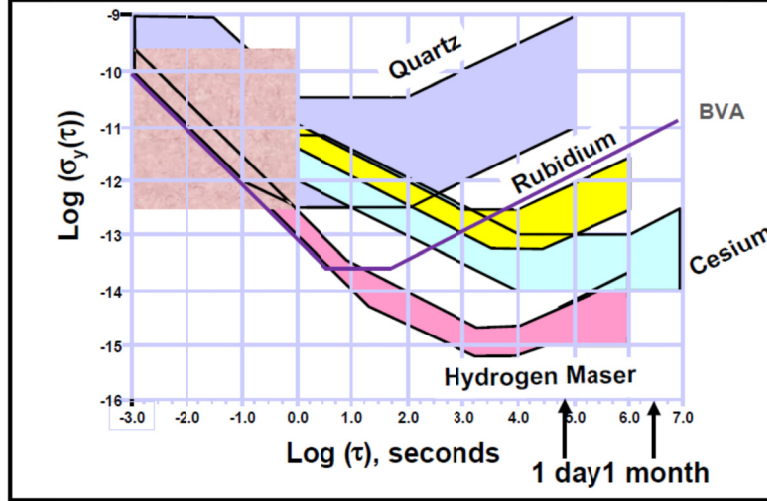
Fig. 1.8. Frequency stability characteristics of several types of atomic clocks as well as that of a simple quartz oscillator. *Disclaimer*: This figure is taken from [5].

In addition to *microwave* atomic clocks, there are *optical* atomic clocks which have demonstrated even more impressive frequency stability. For example, optical clocks have been able to achieve frequency stability on the order of 6×10^{-18} [6]. Unfortunately, optical clocks tend to be much more complex than microwave clocks, and currently they remain as laboratory prototypes and are not yet commercially available.

1.3   Active Atomic Clock Based on External Cavity Semiconductor Laser and Intracavity Alkali Vapor Cell

A novel and unique active atomic clock laser was reported in 2007 by Y.-Y. Jau and W. Happer of Princeton University [7]. It is based on a semiconductor laser in external cavity configuration. An alkali vapor cell is placed inside the laser cavity. This laser cavity behaves similarly to a modelocked laser in that it produces optical pulses with repetition period equal to the cavity round-trip time. However, the optical pulsation mechanism is not modelocking as we discuss in Section 3.2. The laser cavity length is chosen such that the optical pulse repetition frequency corresponds to the ground state hyperfine splitting of the alkali atom. When there is a train of optical pulses in this laser cavity, two of the optical modes in the pulse train are locked onto the ground state hyperfine resonance of the alkali atom, and the repetition frequency of this laser is stabilized (discussion below).

Figure 1.9 is the schematic of the pulsating external cavity laser reported by Jau and Happer in [7]. The alkali atom is ^{39}K, and the atomic line utilized is the D_1 line at 770 nm wavelength. The ground state hyperfine splitting frequency of ^{39}K is 462 MHz, thus the cavity length is about 32.5 cm (half wavelength of 462 MHz). An edge-emitting laser diode with antireflection (AR) coated facet is used as the optical gain chip, and it is forward biased with constant current. An optical grating is used to provide external feedback, simultaneously forming the cavity with the laser diode and tuning the lasing frequency to 770 nm. The ^{39}K vapor cell is placed inside the cavity, where it is held inside an oven and Helmholtz coils that provide temperature and magnetic field control, respectively. In this laser cavity, circularly polarized light is used to interrogate the ^{39}K atoms, and this is obtained by placing quarter-waveplates on both sides of the cell to convert the linearly polarized light output from the laser diode. A high speed photodetector (not shown) converts the oscillating optical intensity at the laser cavity output into an oscillating electrical signal.
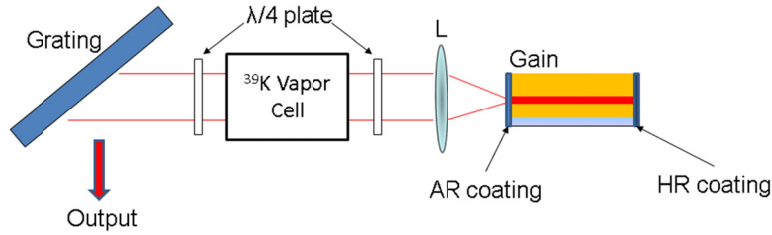
Fig. 1.9. Schematic of the laser cavity realized by Jau and Happer. It consists of an edge-emitting laser diode in external cavity configuration. An optical grating provides the external optical feedback. A ^{39}K vapor cell is placed inside the cavity. Abbreviation: AR – antireflection; HR – high reflectivity; L – lens.

The physics behind this frequency stabilization is push-pull optical pumping [7]–[9], a mechanism that has also recently been utilized for realizing atomic magnetometer [10]. Push-pull optical pumping is the Λ-pumping of both ground state hyperfine levels in the alkali atoms with pulses of alternating circular polarization. The pump light is propagating through the atomic cell in the same axis as the magnetic field, and it has pulse repetition frequency of $2v_{HF}$, where v_{HF} is the atomic ground state hyperfine splitting frequency. The pulses in the optical pulse train have alternating circular polarization, i.e. a pulse with left circular polarization (LCP) is followed by a pulse with right circular polarization (RCP), and vice versa. The pulses are assumed to have duration much shorter than $1/(2v_{HF})$. We conceptually depict the optical pulses in the time domain and their polarization in Fig. 1.10. Note that in the cavity in Fig. 1.9, a single optical pulse traveling inside the cavity subjects the alkali vapor cell to push-pull optical pumping: the pulse interacts with the absorber twice per cavity roundtrip, and the pulse polarization is circular and changes in rotational orientation at each interaction due to the quarter-waveplates.
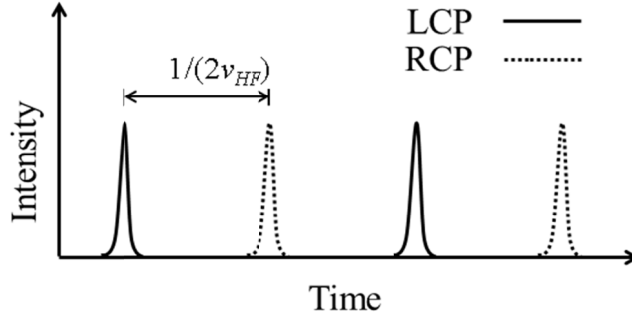
Fig. 1.10. Push-pull optical pumping of alkali atoms with ground state hyperfine splitting frequency v_{HF} is performed with a train of optical pulses of alternating circular polarization. The pulse repetition frequency is $2v_{HF}$.

The optical pulses in Fig. 1.10 is essentially the superposition, with $1/(2v_{HF})$ time shift, of two separate pulse trains of different polarizations, and each pulse train has repetition frequency v_{HF}. Because the spectrum of each individual pulse train consists of optical modes separated by v_{HF}, optical pulses are in CPT resonance with the alkali atoms. It has been found that the CPT resonance effect obtained from push-pull optical pumping is one to two orders of magnitude greater than conventional optical pumping as shown in Fig. 1.11 [8]. Even larger CPT resonance contrasts have been reported [11], with the largest at 78% [12].
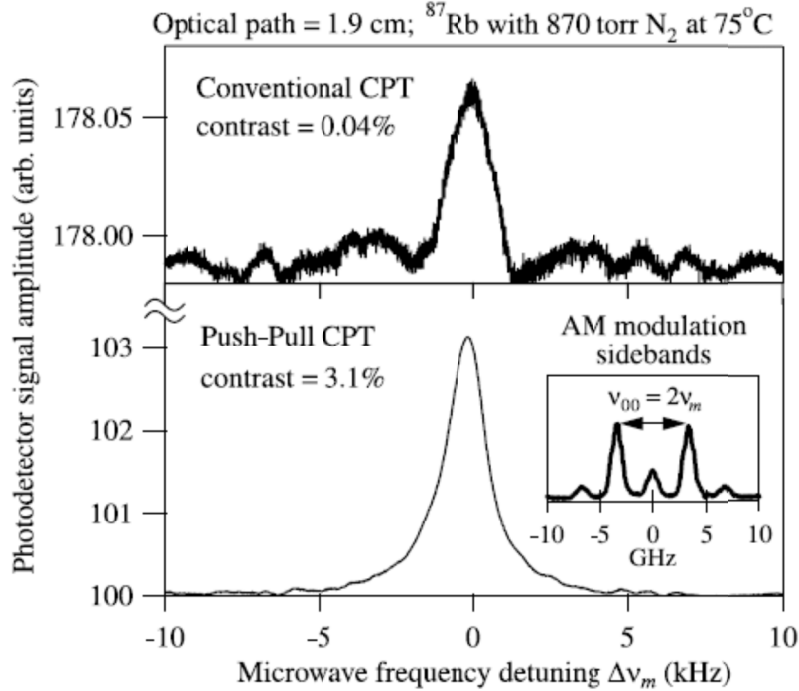
Fig. 1.11. Transmitted optical intensity as a function of Raman detuning frequency for conventional CPT (top panel) and push-pull CPT (bottom). Note that Δv_m in this figure is the same as Δv used in Fig. 1.5. *Disclaimer*: This figure is taken from [8].

When alkali atoms are under resonant Λ-pumping (zero Raman detuning), the atoms are in a coherent superposition of the ground states. Therefore, the expectation value of the electron spin projection on optical axis is time-varying and periodic with frequency v_{HF}, reaching positive and negative

maxima with a half period time of $1/(2\nu_{HF})$. Respectively, with a half period of $1/(2\nu_{HF})$, the atoms are not absorbing (in the dark state) either for one or the other circular polarization of the optical pulse, behaving as an optical filter. In the laser cavity in Fig. 1.9, intracavity loss is minimized when the pulse repetition frequency is equal to ν_{HF}.

If the repetition frequency of the optical pulse train deviates from ν_{HF}, intracavity loss would increase, which is then counteracted by the alkali atoms pulling the optical modes in the pulse train onto resonant Λ-pumping. Thus, the result of placing the alkali vapor cell inside the cavity is that the optical pulse train repetition frequency is locked onto the atom's hyperfine splitting frequency ν_{HF}.

For this first and unique demonstration of push-pull laser atomic oscillator, the frequency stability is moderate. As seen in Fig. 1.12, the measured Allan deviation of the clock oscillation frequency is lower than 10^{-8} after 1 s of integration time [7]. The poor relative frequency stability in this active ^{39}K atomic clock in comparison with the passive Rb and Cs clock in Fig. 1.8 can be attributed to several factors. (i) The hyperfine frequency of 462 MHz in ^{39}K atoms is quite low compared to the hyperfine frequency of 6.835 GHz in ^{87}Rb and 9.193 GHz in Cs clocks, while in general, higher hyperfine splitting frequency results in better relative frequency stability. (ii) The laser cavity is quite long at 32.5 cm, and it is difficult to mechanically and thermally stabilize long cavities. (iii) The last reason, which we believe is important, is that the push-pull laser atomic oscillator does not operate in modelocking regime.
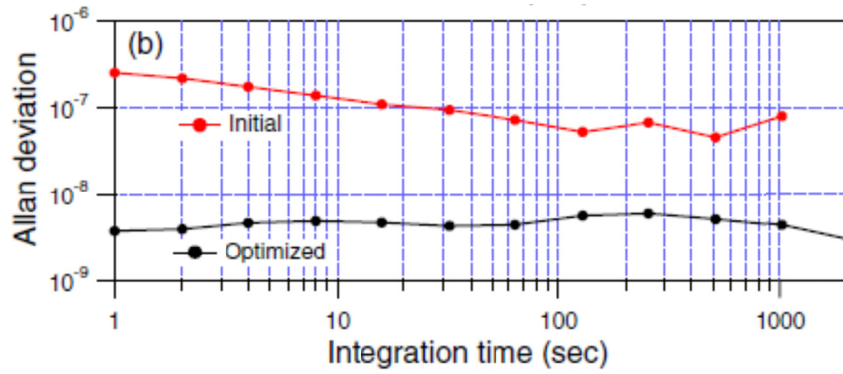
Fig. 1.12. Measured frequency stability characteristics of the active atomic clock by Jau and Happer. Allan deviation is lower than 10^{-8} after 1 s of integration time. *Disclaimer*: This figure is take from [7].

1.4 Motivation and Goal for This Research

The new class of active atomic clock realized by Jau and Happer [7] opens up a new venue of active atomic clocks that are simpler in architecture, especially in regards to electronics used for frequency stabilization, than both existing optical and microwave clocks. The goal of this research is to pursue an atomic clock based on semiconductor laser in external cavity with intracavity alkali vapor cell. Unlike the clock realized by Jau and Happer, we intend to pursue optical oscillations based on modelocked operation instead of the push-pull phenomenon. Thus, the intracavity alkali vapor cell will serve as the saturable absorber.

To improve upon the frequency stability of such an atomic clock based on laser cavity, one should investigate the use of atomic species with higher ground state hyperfine splitting frequency. This would result in a clock with better frequency stability because Allan deviation σ_y scales with $1/v_{HF}$, assuming everything else is equal. In addition, since the laser cavity length is inversely proportional to the hyperfine splitting frequency, this can lead to a much more compact and stable laser cavity than the 32.5 cm long cavity of Jau and Happer [7].

For this research, the atomic species chosen for the saturable absorber is ^{85}Rb. It has ground state hyperfine frequency v_{HF} of 3.036 GHz. For modelocked laser operation, the laser cavity must have optical path length of ~49.3 mm. From a practical point of view, there are a couple reasons why ^{85}Rb is favorable. First of all, it has a moderately high v_{HF} that corresponds to a reasonable laser cavity length. While atomic species with higher v_{HF} exist, such as ^{87}Rb with 6.835 GHz, the laser cavities employing these atoms are shorter by necessity. It can be challenging to fit in an alkali vapor cell in shorter cavities because the cell must be held in a holder with integrated heater (explained in Section 2.3.3), and small-size cell holders with precision temperature control are not easy to build.

Secondly, ^{85}Rb has several atomic transitions that are favorable for saturable absorber behavior. A diagram of ^{85}Rb energy transition lines is given in Fig. 1.13. It contains the commonly used D_1 and D_2 lines in the near infrared, at wavelengths of 795 nm and 780 nm, respectively. Furthermore, there are the less commonly used lines of $5S_{1/2}$-$6P_{1/2}$ and $5S_{1/2}$-$6P_{3/2}$ at 420 nm and 422 nm wavelength, respectively. It is of interest to investigate the blue spectral lines in addition to the traditional D-lines because they have very different absorption cross-sections and excited state relaxation times. Absorption cross-section and excited state lifetime are two vital parameters in a saturable absorber when it relates to obtaining modelocked lasing operation. Furthermore, the two blue lines of ^{85}Rb are situated very close to each other. There is the possibility to simultaneously interrogate both excited states, resulting in effectively greater absorption cross-section and perhaps leading to interesting physics phenomenon. With recent advances in III-nitride semiconductor epitaxy and device fabrication, it is now possible to build external cavity lasers to target these blue transitions.
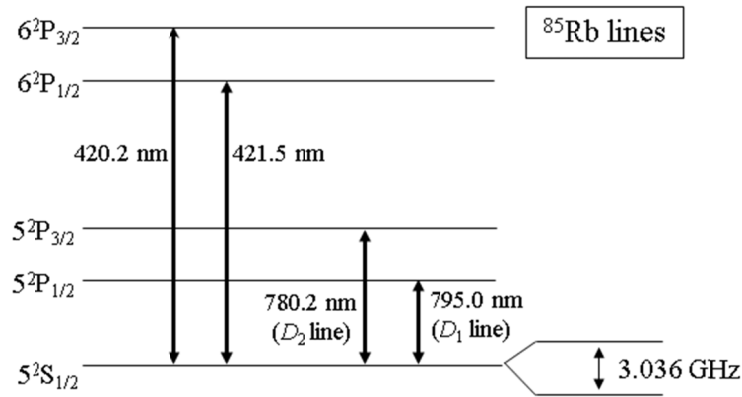
Fig. 1.13. The energy transition lines of ^{85}Rb are given. Excited state hyperfine structures are not depicted.

10

In this research, we theoretically and experimentally investigate the viability of using ^{85}Rb vapor cell as a saturable absorber to modelock an external cavity semiconductor laser. We limit ourselves to two energy transitions in ^{85}Rb: the D_1 line at 795 nm wavelength, and the $5S_{1/2}$-$6P_{3/2}$ line at 420 nm. The ultimate goal is to build an active atomic clock based on modelocked semiconductor laser with ^{85}Rb saturable absorber.

1.5   Outline of This PhD Dissertation

This PhD dissertation contains the theoretical and experimental research performed as well as related background materials. It is organized in the following way.

In Chapter 2, we first briefly describe modelocked laser operation and the typically realized modelocked semiconductor lasers. Then, we will present the proposed laser cavity configurations for modelocked semiconductor lasers utilizing ^{85}Rb vapor cell saturable absorber, and give some details on the optical gain chips and vapor cells we have on hand that may be used to build such a laser cavity. Then, we present the modelocked laser analysis model that was developed for semiconductor modelocked laser with slow saturable absorber of semiconductor material. This particular modelocked laser model cannot be directly used for our research and needs to be modified in order to account for alkali vapor cell saturable absorbers. Before such modification can be done, theoretical and experimental work needs to be performed to properly characterize ^{85}Rb absorption, and they are detailed in Chapters 3, 4, and 5. Chapter 2 presents the motivation for a large portion of the experimental research performed in this dissertation.

In Chapter 3, we develop a six-level model of optical absorption in alkali atom vapor cell with buffer gas. In contrast to the traditional model, the model developed here is applicable for a more general case where the alkali atom is interrogated by narrowband optical pumping, and the ground state hyperfine structure can be resolved (especially in cells with low and intermediate buffer gas pressures). Furthermore, our model accounts for the effects of the optical beam size interrogating atoms in the cell. Finally, using our new model for optical absorption, we develop a new technique to measure the excited state lifetime of an alkali atom using time-resolved pump-probe spectroscopy.

In Chapter 4, we present the spectroscopy results performed on ^{85}Rb and ^{87}Rb in the D_1 line in 795 nm wavelength. We experimentally verify the model for optical beam size effect first described in Chapter 3. We also experimentally measure the effects of buffer gas pressure and temperature on saturation intensity and spin relaxation times, and discuss the agreements and discrepancies with theory. Finally, we experimentally use the time-resolved pump-probe spectroscopy technique that was theoretically developed in Chapter 3 to measure the excited state lifetime of ^{85}Rb quenched by N_2 molecular buffer gas.

In Chapter 5, we detail the experimental work performed on the blue wavelength $5S_{1/2}$-$6P_{3/2}$ line (420 nm wavelength) in ^{85}Rb. As lasers for blue wavelength spectroscopy are not widely available, we therefore built a blue wavelength external cavity diode laser (ECDL) for spectroscopic applications. We first measured the linewidth of our ECDL. We then detail the ^{85}Rb absorption characteristics obtained by using the ECDL as the optical interrogation source. This includes the first meas-

urement of pressure broadening and frequency shift coefficients by N_2 buffer gas in this transition, two things that are not found in literature. We then detail the work that was done to obtain short optical pulse generation with precise wavelength in the blue spectra from a multi-section laser diode using optical injection locking. While we were not able to utilize such a laser in pump-probe experiment to measure the excited state lifetime in this research, we nonetheless believe that it has spectroscopy potentials for other applications. Finally, we use a variant of the time-resolved pump-probe spectroscopy technique where we pump and probe the ^{85}Rb atoms at two different atomic lines, at D_1 and 5S$_{1/2}$-6P$_{3/2}$ respectively. Our goal is to measure the ^{85}Rb excited state lifetime at the 5S$_{1/2}$-6P$_{3/2}$ line, where the value in literature is not definitive.

In Chapter 6, we theoretically and experimentally investigate the behavior and performance of an optically pumped III-nitride vertical-external-cavity surface-emitting laser (VECSEL) for interrogation of 420 nm wavelength transition in Rb atoms. We do this because III-nitride VECSEL technology is not matured, and long external cavities have not been previously realized. We thoroughly characterize many effects, including the effects of cavity length on lasing threshold, lasing spectra, and beam profile, and the impact of pump pulse duration on lasing threshold (pulsed pump sources are usually used for III-nitride VECSELs). Theoretically, we developed models for the experimentally observed VECSEL behavior.

In Chapter 7, we return to the modelocked laser analysis model first presented in Chapter 2. Armed with the theoretical model and experimentally measured ^{85}Rb optical absorption, we modify the analysis model to be fully compatible with the ^{85}Rb saturable absorber in both the D_1 and 5S$_{1/2}$-6P$_{3/2}$ absorption lines at 795 and 420 nm wavelength, respectively. Then, we use the modelocked laser analysis model to investigate the viability of obtaining modelocked operation from the laser cavity configurations proposed in Chapter 2. Of the two laser cavities that are predicted to work, we then use ray transfer matrix with Gaussian beam analysis to design the laser cavities and the placement/position of the optical elements. These designs will serve as the starting point for experimental realization of active atomic clocks based on modelocked semiconductor laser with ^{85}Rb vapor cell saturable absorber.

Chapter 2 **Passively Modelocked Semiconductor Laser Configurations and Analysis Techniques**

In this chapter, we make a brief overview of the typically realized passively modelocked semiconductor lasers, and then we present our proposed cavity configurations for the target of this research: passively modelocked semiconductor laser with alkali vapor cell saturable absorber. We present the analysis methods that we will use to theoretically investigate the proposed laser cavity configurations, determining their viability in obtaining modelocked operation and predicting the operating parameters. Before these modelocked laser models can be used, however, they require adaptation to our laser cavities, especially for the description of the alkali vapor cell saturable absorber. The theoretical and experimental work to adapt the modelocked laser models is reported later in Chapters 3, 4, and 5.

2.1   Brief Introduction to Passively Modelocked Lasers

Modelocking is a technique to obtain pulsed optical emission from lasers. Contrasting from other methods for optical pulse generation, such as gain-switching or Q-switching, modelocking occurs when different optical modes existing in a laser cavity are forced to have the same phase. Mathematically, this is described by the following. Suppose the electric field inside a laser cavity is given by $E(t) = \sum_{i=1}^{N} A_i \cos[(\omega_0 + \Delta\omega \cdot i)t + \phi_i]$, where N is the total number of cavity optical mode. When the mutual phases of the modes $\phi_i - \phi_j$ are constant, the system is modelocked. In this situation, interference between the optical modes results in a train of pulses in the temporal domain with frequency $\Delta\omega/2\pi$, which is the reciprocal of the laser cavity roundtrip time.

There are several methods to obtain modelocking. The method relevant to this research is to passively modelock the laser system with a saturable absorber placed in the cavity. When the absorber is hit by an optical pulse, it saturates and the intracavity losses are reduced. For optical pulses of adequately high intensity, the intracavity loss can be reduced such that the intracavity optical gain sufficiently compensates it. Weaker optical pulses, on the other hand, still experience intracavity loss greater than gain. Thus, pulsed lasing operation with high peak optical intensity is preferred over continuous wave operation because the effective intracavity loss is lower for pulsed lasing operation. Intuitively, modelocking can occur only if the absorber recovers fast enough such that there

is net negative cavity gain after optical intensity builds, resulting in the termination of optical intensity and hence a pulsed waveform. These and other requirements for modelocking are explored in detail in Section 2.4.

2.2   State of the Art in Passively Modelocked Semiconductor Lasers

This section gives a brief description of typical laser cavity configurations that are used in practice. These laser cavities consist of a semiconductor optical gain chip and semiconductor saturable absorber. We will limit ourselves to *passively* modelocked laser cavities, where the gain and absorber sections are biased or excited with constant current/optical pump power and voltage, respectively.

The first configuration is the monolithic multi-section laser diode (MSLD), and it is depicted in Fig. 2.1(a). It is a laser diode with monolithically integrated optical gain and saturable absorber sections. The two sections are electrically isolated, and each section has its own electrical contact. Typically, the longer section is the optical gain section, and it is forward biased with current. The shorter section is the saturable absorber, and it is reversed biased with voltage. Careful selection of operating parameter results in modelocked lasing.
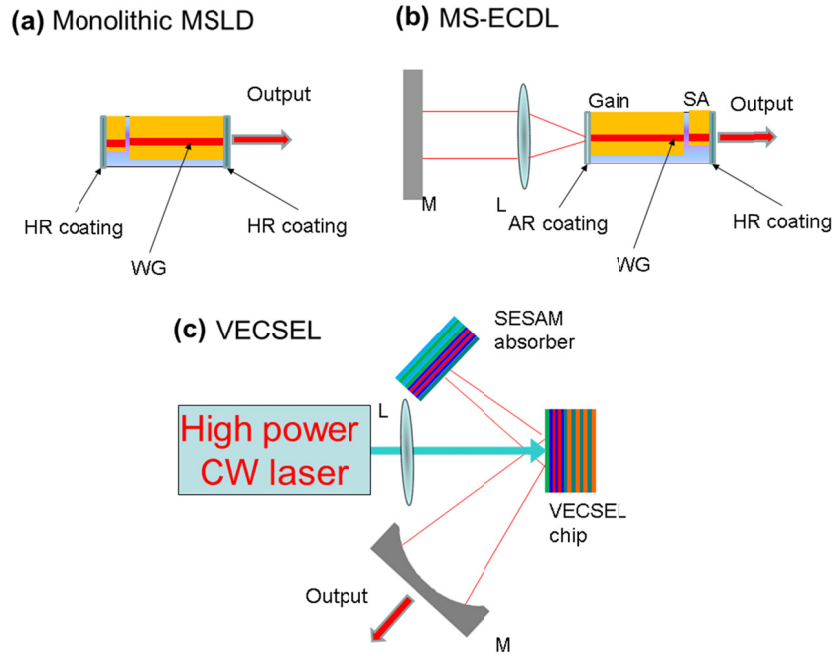
Fig. 2.1. Different cavity configurations for modelocked semiconductor diode laser systems: (a) monolithic multi-section laser diode (MSLD); (b) multi-section external cavity diode laser (MS-ECDL); (c) optically pumped VECSEL with SESAM saturable absorber. Abbreviations: SA – saturable absorber, GAIN – gain section, M – mirror, L – lens, WG – waveguide AR – antireflection coating, HR – high reflectivity coating. *Disclaimer*: This figure is adapted from figures in [13].

As monolithic laser diodes can be made to be as short as 300 μm, high modelocked repetition frequency can be achieved in monolithic MSLD. For example, a modelocked monolithic MSLD at 1.58 μm wavelength was reported with 40 GHz pulse repetition frequency, 1.3 ps long optical puls-

es, and 0.02 pJ pulse energy [14]. Three-section variants of the MSLD exist, for example in colliding pulse modelocked (CPM) designs where even higher modelocked repetition frequency is possible. Modelocked frequency as high as 350 GHz with 640 fs pulse durations has been reported for a 1.5 μm wavelength CPM laser diode [15]. Variants of MSLD utilizing tapered ridge waveguide gain section can achieve much higher peak and average power, capable of demonstrating average power as high as 209 mW with peak power around 3.6 W, 3.2 ps pulse duration, and 14.65 GHz repetition frequency (wavelength of 1.25 μm) [16].

The second configuration is that of a multi-section external cavity diode laser (MS-ECDL), and it is depicted in Fig. 2.1(b). It consists of a MSLD in external cavity configuration. The laser cavity is formed by a high-reflectivity (HR) coated facet of the laser diode on one side, and an external cavity mirror on the other. One significant advantage of MS-ECDL over monolithic MSLD for modelocked laser operation is that the modelocked repetition frequency can be tuned by changing the cavity length. MS-ECDLs tend to be more practical than monolithic MSLDs for achieving modelocked repetition frequency below 10 GHz because the monolithic device would need to be long (>4 mm). Another advantage of external cavity design is that optical elements (e.g., filter) can be inserted inside the cavity. This includes optical amplification elements such as semiconductor optical amplifier (SOA), enabling high power output as demonstrated in [17], with peak power as high as 30.3 W for a MS-ECDL operating in 1.26 μm wavelength, with average power of 208.2 mW, pulse energy of 321 pJ, and pulse repetition frequency of 648 MHz.

The third configuration of modelocked semiconductor laser cavity that is typically used is depicted in Fig. 2.1(c), which is an optically pumped vertical-external-cavity surface-emitting laser (VECSEL) utilizing a semiconductor saturable absorber mirror (SESAM) [18], [19]. The optical gain chip is pumped by a continuous wave (CW) high power laser. The laser cavity is formed by three reflectors: an external mirror that also serves as the output coupler, the bottom side distributed Bragg reflector (DBR) stacks in the gain chip, and the SESAM bottom side DBR stack. The VECSEL gain chip provides optical gain with either quantum wells (QWs) or quantum dots (QDs) [20] when it is optically pumped. In an optimally designed VECSEL chip, the bottom side DBR stack is highly reflective in both the lasing wavelength and the pump laser wavelength. Additionally, such a VECSEL chip has an epitaxial and/or deposited dielectric layers on top of its gain region that simultaneously behave as antireflection (AR) layer for both the lasing wavelength and the pump laser wavelength, with proper account for the incidence angle of the pump laser beam. A properly designed AR layers on the VECSEL chip can significantly increase pump efficiency and reduce the lasing threshold.

The SESAM provides absorption using its own QWs or QDs. Bottom side DBR stack on the SESAM performs as a high reflectivity mirror that is part of the laser cavity. The top layer of the SESAM is an important engineering design that determines the light intensity entering the absorption region that is below it, and hence the effective saturation energy and absorption cross-section of the entire absorber [19]. (We will elaborate on the absorber saturation energy in Section 2.4.) For example, if the top layer is a high reflectivity (>95%) DBR stack [18], then the intensity reaching the absorption layer would be quite small, resulting in a SESAM with an effectively large saturation

energy. The opposite example of SESAM top layer would be an AR layer that maximizes the light reaching the absorption layer.

In a modelocked VECSEL, the gain and absorber saturation energies can also be tuned by changing the cavity optical mode size on either element, which is done by using output couplers of different curvature as well as changing the total cavity length. This ability to tune the various parameters using optics, as well as the ability to tune both the gain and absorber section characteristics through semiconductor epitaxial design, is an important advantage that VECSEL laser cavities have over edge-emitting laser cavities.

In terms of performance, the output beam quality of optically pumped surface emitters can be quite good (near M^2=1) while simultaneously achieving high output peak and average power. Research on developing *electrically pumped* VECSEL gain chips suitable for this type of modelocked laser cavity is ongoing [21]. Meanwhile, the performance metrics already achievable by modelocked VECSELs are already quite impressive. For example, a 960 nm wavelength modelocked VECSEL can operate with 50 GHz repetition frequency, 100 mW average power, and pulse duration of 3.3 ps [22]. More advanced VECSEL designs where the gain section and absorption section are integrated into one chip have achieved modelock frequency as high as 101 GHz [23].

2.3 Beyond State of the Art: Modelocked Semiconductor Laser Utilizing Alkali Vapor Cell Saturable Absorber

2.3.1 Proposed Laser Cavities

This section details the passively modelocked laser cavity configurations consisting of semiconductor laser gain chip and alkali vapor cell saturable absorber that we investigate in this dissertation. Similar to typical modelocked semiconductor laser cavity configurations presented in Section 2.2, the configurations analyzed here fit into two categories: external cavity edge-emitting or surface-emitting laser cavities. In contrast to the typically used configurations shown in Fig. 2.1, where the saturable absorber is made of semiconductor material, here the absorber is an alkali vapor cell. Specific to our research, the alkali atom species is ^{85}Rb.

The possible laser cavity configurations are depicted in Fig. 2.2. An alkali vapor cell is inserted in the middle of the cavity. Figure 2.2(a) consists of an edge-emitting gain chip and a mirror as the external feedback element. In contrast to spectrally narrowband optical feedback from a grating utilized by Jau and Happer in push-pull clock laser cavity [7] (see Section 1.3), we use a broadband output coupling mirror. An optional etalon filter may be introduced to tailor the cavity modes and fine tune the bandwidth. We have determined that our laser cavity configurations will not use λ/4 waveplates, and that the intracavity light polarization must be linear in order for modelocking to occur. The reason is that we intend to pursue modelocking operation, which requires an absorber with fast recovery time. Fast recovery time in an alkali vapor cell absorber is not possible if it is interrogated with circularly polarized light, a point that which we will discuss in Section 3.2.

Figures 2.2(b) and (c) depict configurations with surface-emitting gain chip. We consider both traditional optically pumped device as in panel (b) and an electrically pumped VECSEL as in (c). Electrically pumped VECSELs chip were once commercially available from the company Novalux, sold under the product line Novalux Extended Cavity Surface Emitting Laser (NECSEL) [24]. However, this company and its products no longer exist. On the other hand, near infrared vertical-cavity surface-emitting laser (VCSEL) are commercially available. Despite the presence of top DBR stack, external cavity feedback still has an effect [25], and it might be possible to etch away the top DBR stack to obtain a VECSEL, thus allowing for the chance of modelocked operation through interaction with the saturable absorber in external cavity.
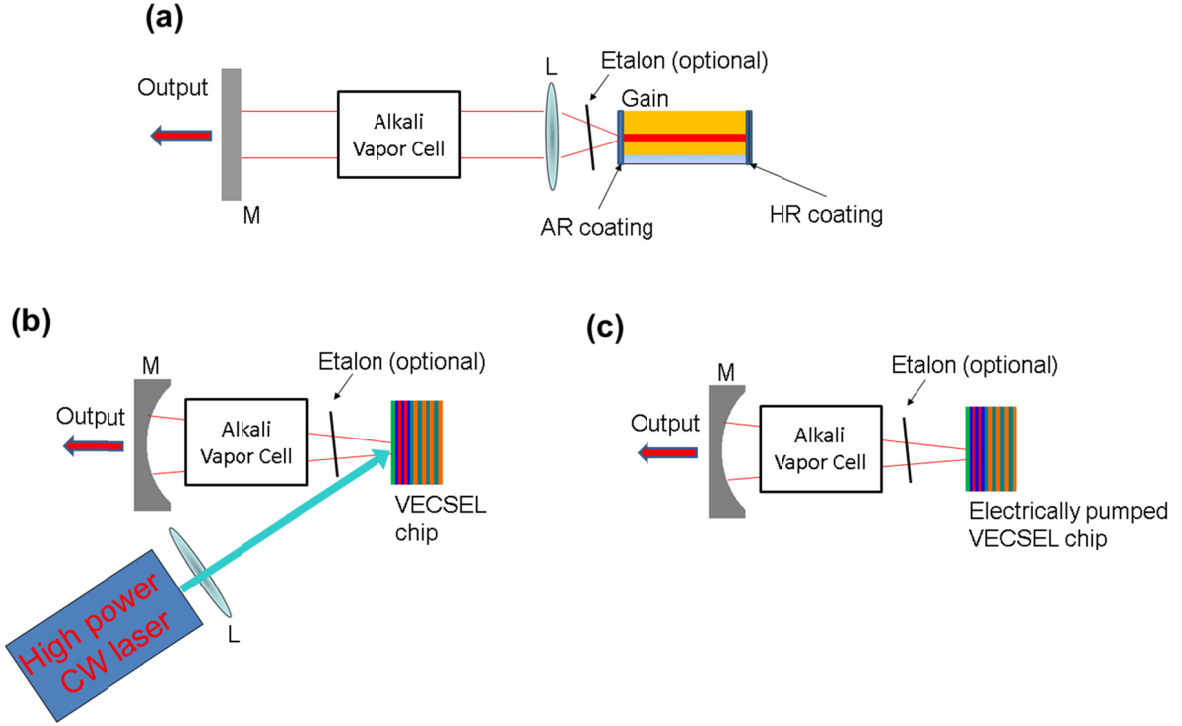
Fig. 2.2. Different laser cavity configurations for modelocking a semiconductor gain chip with alkali vapor cell saturable absorber analyzed in this dissertation. (a) An edge-emitting gain chip with an external mirror as the feedback element. An optional etalon can be inserted for narrowband optical filtering. (b) Cavity configuration utilizing optically pumped surface-emitting VECSEL gain chip. (d) Another surface-emitter, but the gain chip is an electrically pumped VECSEL.

2.3.2 Optical Gain Chips

For this research, in addition to the choice of laser cavity configuration as discussed in Section 2.3.1, there is a choice of laser wavelength. As discussed in Section 1.4, we will pursue two very different atomic lines in ^{85}Rb: the D_1 line at 795 nm wavelength, and the $5S_{1/2}$-$6P_{3/2}$ at 420 nm.

In theory, each of these two atomic lines can be investigated in both edge-emitting and surface-emitting gain chip cavity configurations, allowing for four possible cavity configurations. In practice, it was possible to procure only the following optical gain chips: 795 nm wavelength edge-

emitting laser diode of the III-V material system (AlGaAs) with AR and HR coated facets, 795 nm VCSEL (also AlGaAs), 420 nm wavelength edge-emitting laser diode of the III-nitride material system (InGaN) that has no coating on facets, and a 420 nm wavelength InGaN VECSEL chip designed and grown at the EPFL-LASPE laboratory for optical pumping. The optical gain chip wavelengths, emission profiles, and how they can be pumped are summarized in Table 2.1. Characterization of the optically pumped 420 nm InGaN VECSEL chip is detailed in Chapter 6. The measured L-I curves and optical spectra of the other three gain chips are given in Fig. 2.3. These optical gain chips have been mounted in dedicated physics packages suitable for integration in external laser cavity assembly as shown in Fig. 2.4, and these packages incorporate thermistors and thermoelectric coolers for precision temperature control and fine tuning of the lasing wavelength.

We therefore have *four* different configurations to pursue and investigate: two edge-emitting configurations as in Fig. 2.2(a) using (i) 420 nm and (ii) 795 nm edge-emitting laser diodes; (iii) optically pumped surface-emitting configuration as in Fig. 2.2(b) with the 420 nm VECSEL chip; (iv) electrically pumped surface-emitting configuration as in Fig. 2.2(d) with the electrically pumped 795 nm VECSEL, obtained by modifying a VCSEL or procured separately. The full characteristics of these gain chips are given in Table 7.1 in Section 7.1.3.

	Wavelength (nm)	Emission Profile	Pump Method	Manufacturer
Chip #1	420	Edge-emitting	Electrical	Toptica
Chip #2	795	Edge-emitting	Electrical	Sacher Laser
Chip #3	420	Surface-emitting	Optical	EPFL-LASPE
Chip #4	795	Surface-emitting	Electrical	Oclaro

Table 2.1. Summary of optical gain chips available for this research.
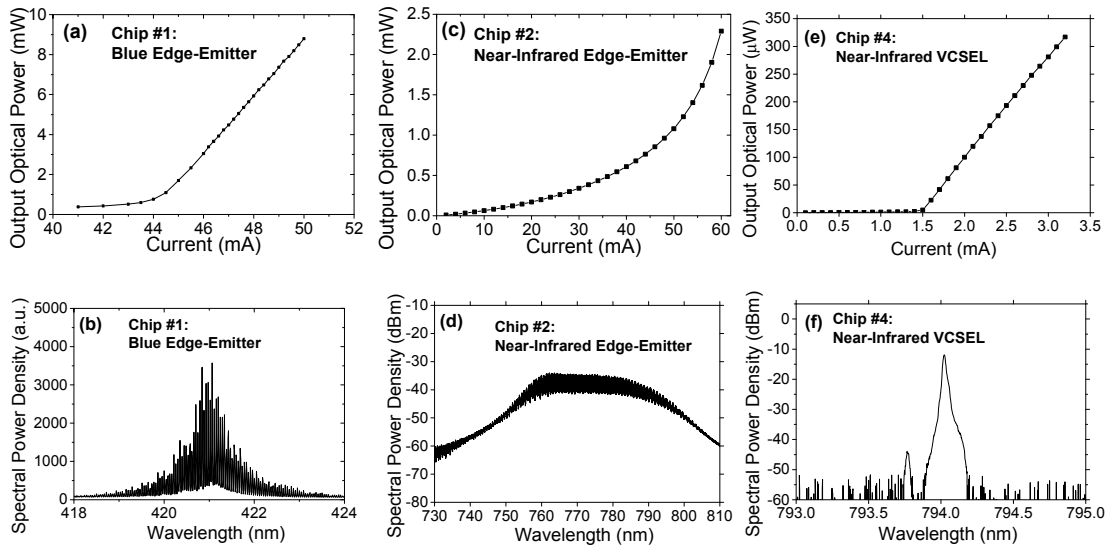
Fig. 2.3. Chip #1, blue wavelength edge-emitting gain chip by Toptica: (a) L-I curve, (b) amplified spontaneous emission (ASE) spectrum, at 44 mA and temperature of 22° C. Chip #2, near-infrared edge-emitting gain chip by Sacher Laser, with AR coated facet: (c) L-I curve, (d) ASE spectrum at 50 mA and temperature of 32° C. Chip #4, near-infrared VCSEL gain chip by Oclaro: (e) L-I curve, (f) lasing spectrum at 3.2 mA and temperature of 32° C.
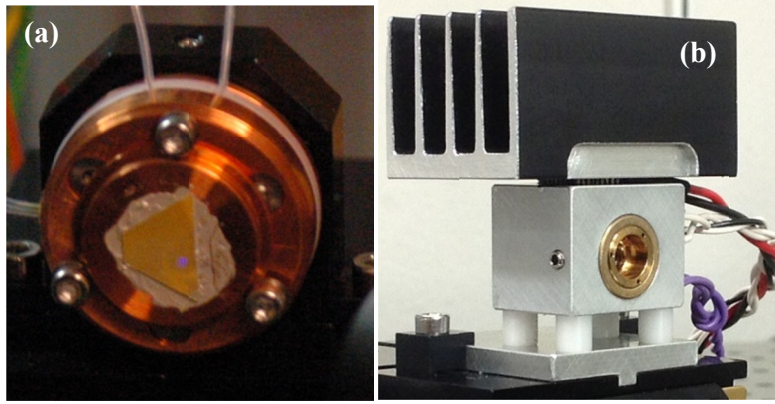
Fig. 2.4. (a) Photograph of the mounted III-nitride 420 nm wavelength VECSEL chip. The faint violet spot on the chip is due to luminescence from optical pumping by a high power ultraviolet laser. (b) Photograph of an electrically pumped III-nitride 420 nm wavelength edge-emitting gain chip. A removable aspheric lens is also mounted for colli-mating the optical output. Identical mounting packages are used for mounting electrically pumped III-V 795 nm wave-length edge-emitting and surface-emitting gain chips.

2.3.3 Alkali Vapor Cells

For this study, we have procured several [85]Rb cells with different buffer gas pressure and chemical composition. These cells are made out of quartz and are cylindrical in shape. The circular windows are optically flat, and they are antireflection (AR) coated for either 420 nm or 795 nm wavelengths. The inner diameter of the circular windows is 4 mm. The cell inner cylinder length is 5 mm for the 420 nm AR coated cells and 7 mm for the 795 nm AR coated cells. AR coating is important because reflections off of cell walls can result in a parasitic Fabry-Perot cavity. Not only would such a para-sitic cavity be quite deleterious for modelocked lasing operation, it would greatly impede spectros-copy measurements as well. Thus, the cells are procured with the appropriate AR coating for the two atomic transitions of interest in [85]Rb.

In addition to the [85]Rb cells, we also have several [87]Rb cells. These cells have the same form-factor as the [85]Rb cells and with inner cylinder length of 5 mm. While these cells are not suitable for the atomic clockwork in this research, they are instrumental in developing the theory and model for understanding the impact of optical beam size and buffer gas pressure on alkali atom optical absorp-tion, an effect that is identical for both [85]Rb and [87]Rb. This is explored theoretically in Section 3.3 and experimentally in Sections 4.2 and 4.3. A summary of the Rb vapor cells, their contents, and their dimensions are given in Table 2.2. A photograph of an example Rb vapor cell is given in Fig. 2.7(a).

It should be noted that two [85]Rb cells in Table 2.2, the ones AR coated for 420 nm with He buffer gas of 40 and 90 torr, were originally supplied with 200 torr of He. However, the actual buffer gas pressures at the time of measurement were less than 200 torr because He leakage via permeation through the quartz cell wall is a significant effect. We therefore estimate the buffer gas pressure using a gas permeation model with rate of 1×10^{-10} cm$^3 \cdot$mm/(cm$^2 \cdot$s$\cdot$torr) for He through quartz [26]. We plot the estimated He buffer gas pressure as a function time in Fig. 2.5. For one He cell, with about 3 months between manufacturing and measurement, we estimate the remaining He pressure

was 90 torr at the moment of measurement. For the other cell, the time between manufacturing and measurement was 6 months, and we estimate the He pressure to be 40 torr.

Atomic Species	AR Coating Wavelength (nm)	Buffer Gas Species	Buffer Gas Pressure (torr)	Cell Length (mm)
^{85}Rb	420	He	0	5
^{85}Rb	420	He	40	5
^{85}Rb	420	He	90	5
^{85}Rb	420	N_2	6	5
^{85}Rb	420	N_2	200	5
^{85}Rb	795	N_2	6	7
^{85}Rb	795	N_2	50	7
^{85}Rb	795	N_2	100	7
^{85}Rb	795	N_2	200	7
^{87}Rb	Not Coated	58% Ar, 42% N_2	10	5
^{87}Rb	Not Coated	58% Ar, 42% N_2	22.5	5
^{87}Rb	Not Coated	58% Ar, 42% N_2	75	5

Table 2.2. Summary of alkali vapor cells used in this research. According to the manufacturer, all buffer gas pressures are rated for 24° C, the temperature at which the cells were sealed.
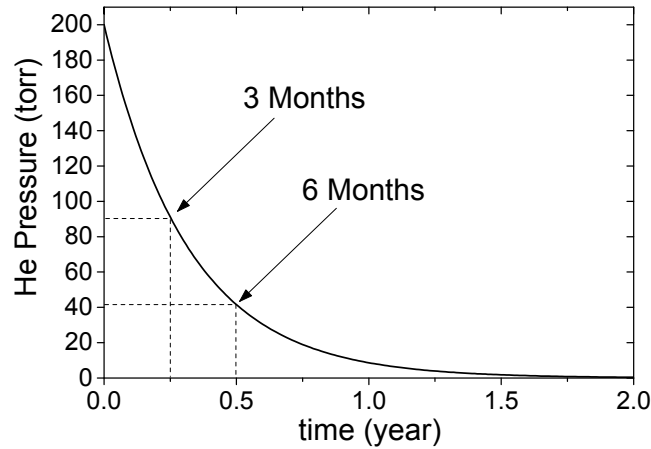
Fig. 2.5. For a quartz cell initially containing 200 torr of He (at 24° C), the estimated He pressure is plotted as a function of the time. He pressure decreases due to permeation through the cell wall.

N_2 and He buffer gases have different effects on the excited state lifetime of ^{85}Rb. For modelocking operation, the saturable absorber needs to have short recovery time compared to that of the optical gain section. Molecular buffer gases such as N_2 quench the excited state lifetime of the alkali atoms. On the other hand, atomic buffer gases such as He have effectively no quenching effect. Their lifetime quenching cross-sections are smaller than that of N_2 by three to four orders of magnitude [1], [27]. Therefore, a saturable absorber based on ^{85}Rb (or any alkali atom) vapor cell should contain N_2 buffer gas. The exact pressure of N_2 that adequately quenches the excited state lifetime in ^{85}Rb cell saturable absorber is something that needs to be theoretically and experimentally determined. The ^{85}Rb cells with He buffer gas are not suitable for saturable absorber operation, but they are useful as references in excited state lifetime measurements.

The absorption linewidth of ^{85}Rb increases with buffer gas pressure, reducing the absorption cross-section. Thus, while higher buffer gas pressure results in a faster absorber, it also results in a smaller absorption cross-section and higher saturation energy. Different buffer gas pressures will allow us

to select the optimum cell pressure for saturable absorber work. Cells with buffer gas pressures ranging from a few torrs to 200 torrs allow us to explore this trade-off and select the optimum cell pressure for saturable absorber work.

At room temperature, Rb is in solid form, and the partial Rb vapor pressure is on the order of 10^{-7} torr, which is very low. At such a low vapor pressure, and hence low population density, Rb vapor cells of a few mm long have nearly negligible absorption. For Rb cells to be used as absorbers, the Rb population in the cell must be increased by a few order of magnitudes. This is achieved by heating the cell above the melting point at about 312 K (39° C). The Rb population density n_{Rb} at cell temperature T_{cell} is given by $n_{Rb} = P/k_B T_{cell}$ [28], where Rb vapor pressure P_{Rb} is

$$\log_{10}(P) = 7.193 + 4040/T_{cell} \text{ for } T_{cell} > 312 \text{ K.} \tag{2.1}$$

Here, P is the Rb vapor pressure in torr, k_B is the Boltzmann constant, and cell temperature T_{cell} must be in units of K. We plot n_{Rb} as a function of cell temperature in Fig. 2.6, and one can see the exponential growth in the Rb population density with heating. Thus, by controling the vapor cell temperature, one can efficiently tailor the absorption coefficient in the cell over several orders of magnitudes.
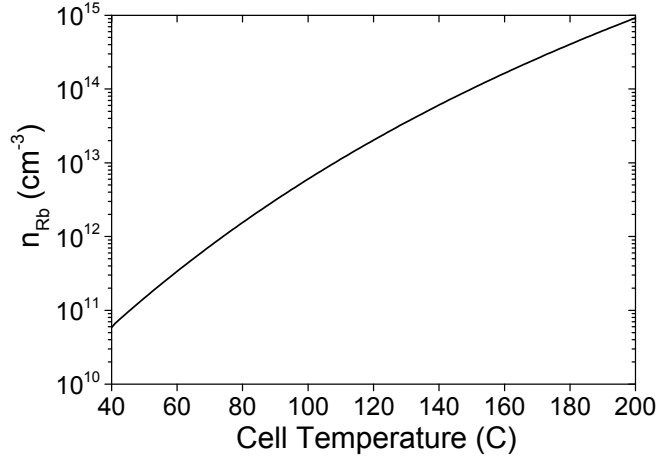
Fig. 2.6. Rb population density n_{Rb} is plotted as a function of cell temperature.

For precise control of the cell temperature and magnetic field applied to Rb atoms, a dedicated alkali vapor cell holder was built. The core of the cell holder is made of high magnetic permeability metal which provides magnetic shielding from the outside environment. Wire coils are looped inside the shielded core, enabling one to apply magnetic field of well-defined strength onto the vapor cell and tailoring the Zeeman sub-level splitting in Rb atoms. With 239 wire coils looped over a 17 mm long cell holder, and a typical operation current of 10 mA, the estimated magnetic field inside the cavity is 0.177 mT. Four MOSFET transistors attached to the cell holder act as heating elements. Four thermistors are placed within the cell holder, acting as temperature sensors. Two 3 mm diameter apertures allow for optical interrogation and transmission measurements of the Rb atoms. Photographs of the cell holder are given in Fig. 2.7(b) and (c).
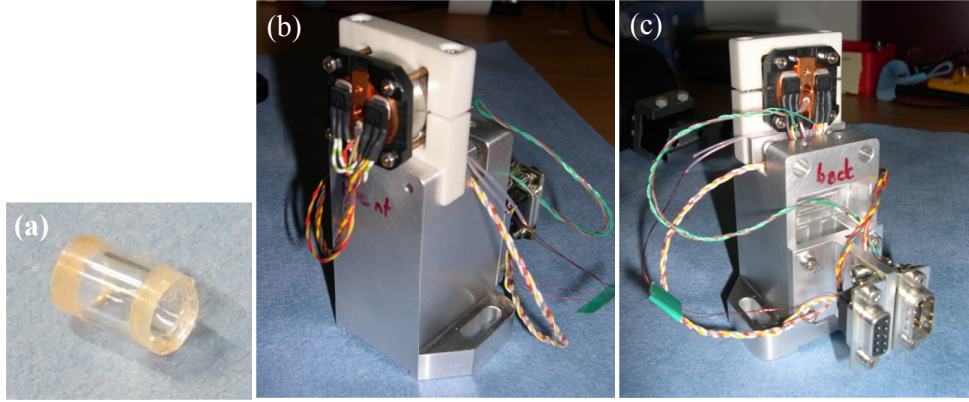
Fig. 2.7. (a) Photograph of an example Rb vapor cell used in this research. Cells like this are loaded into the homebuilt alkali vapor cell holder, with photographs given in (b) and (c) as shown from front and back, respectively.

A dedicated temperature control unit for the alkali vapor cell holder was built to drive the cell holder's MOSFETs. It contains a commercial feedback controller (PTC2.5K-CH from Wavelength Electronics) and MOSFET biasing circuitry. Operating on a 7 volt, 2 ampere DC power supply, the alkali vapor cell temperature can be controlled in the range 40 to 105° C with temperature stability of <0.05° C (determined by monitoring the thermistors, limited by measurement equipment sensitivity).

Measured characteristics of these Rb vapor cells such as absorption spectrum, cross-section, ground state and spin relaxation times as well as our measured excited state lifetimes are reported in Chapters 4 and 5.

2.4   State of the Art Theoretical Model for Modelocked Semiconductor Laser with Slow Saturable Absorber

One of the commonly used theoretical approaches to analyze the passive modelocking phenomenon in lasers has been elaborated by Haus and New [29], [30]. This model is applicable for a laser system with gain and a saturable absorber recovery times longer than the pulse width (*slow* gain and absorber). In this dissertation, the theoretical analysis of modelocked laser systems is done using an extension of the Haus-New model that was proposed by Smetanin, Vasil'ev, and Boiko (SVB) [31] and developed in the framework of the European FP7 Project FemtoBlue [32]. Previous analytical solutions [33] of the Haus-New master equation were limited to the small signal regime, where the optical pulse energy is much smaller than the saturation energy of the absorber. The SVB approach provides an analytical solution to the Haus-New master equation for a passively modelocked laser, and this solution is valid for both the small signal regime as well as the large signal regime, where the pulse energy may be comparable to or higher than the saturation energy of the absorber. In this section, an overview of the SVB approach to the Haus-New model is provided.

2.4.1 Ring Cavity Configuration

The Haus-New model was originally developed for a passively modelocked laser system with optical gain element and saturable absorber element placed in a ring cavity configuration as depicted in Fig. 2.8. (Adaptation to Fabry-Perot cavity configuration will be detailed in Section 2.4.2.) The steady-state time-domain master equation in Haus-New theory, accounting for the phase-amplitude coupling effects in a passively modelocked semiconductor laser diode [34], [35], is

$$\{1+(1-i\alpha_A)q_i\exp(-E(t)/E_{sA})-(1-i\alpha_L)g_i\exp(-E(t)/E_{sL})+\xi^2+i(\psi+\xi)$$
$$+(1+\delta-2i\xi)\frac{1}{\omega_L}\frac{d}{dt}-(1+iD)\frac{1}{\omega_L^2}\frac{d^2}{dt^2}\}A(t)=0. \tag{2.2}$$

In the master equation, $A(t)$ is the electric field of the laser pulse with chirped hyperbolic secant shape $A(t)=[A_0\mathrm{sech}(t/\tau_p)]^{1+i\beta}$, where β is the chirp parameter. The electric field amplitude A is normalized on photon number density, such that $|A|^2$ is the photon density of the mode area in the gain section. The SVB approach was explicitly developed for the case where both absorber and gain are separate sections of a ridge waveguide edge-emitting laser diode structure (the multi-section laser diode as described in Section 2.2), with the following terms defined: Γ is the optical mode confinement factor, w is the ridge waveguide width, d is the total thickness of all quantum wells (QWs). The term $E(t)=(wd/\Gamma)\int_{-\infty}^{t}\hbar\omega v_g|A(t')|^2 dt'$ is the instantaneous cumulative pulse energy, where e is the electron charge and c is the speed of light in vacuum. The total pulse energy is $W_p=(wd/\Gamma)\int_{-\infty}^{\infty}\hbar\omega v_g|A(t')|^2 dt'=2\hbar\omega v_g A_o^2\tau_p(wd/\Gamma)$.
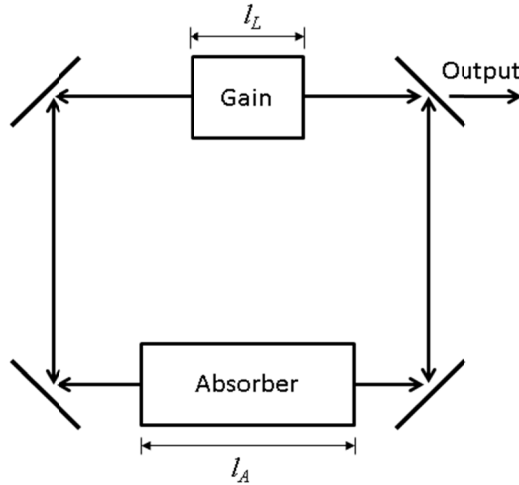
Fig. 2.8. Modelocked laser consisting of optical gain and saturable absorber sections in ring cavity configuration.

The master equation accounts for the optical gain section saturation energy E_{sL}, absorber saturation energy E_{sA}, the lengths of the gain and absorber sections l_L and l_A, the half-width spectral bandwidth of the gain section ω_L, frequency detuning of the carrier optical frequency from the center of the gain line $\xi=\Delta\omega/\omega_L$, and intracavity dispersion D. Saturation energy of the optical gain section is given by $E_{sL}=\hbar\omega\cdot A_L\cdot v_g/(\partial g/\partial n)\Gamma$, where $\hbar\omega$ is the photon energy, A_L is the cross-sectional area of the optical mode in the gain section, v_g is the group velocity in the gain medium, and $\partial g/\partial n$ is the dif-

ferential material gain. With a semiconductor saturable absorber monolithically integrated with the gain section, the absorber saturation energy is conveniently $E_{sA}=E_{sL}/s$, where s is the modelocking stability parameter, defined as the ratio of gain to absorber section saturation energies. Note that the condition $s>1$ must be true for modelocked operation to be possible.

The master equation is normalized to the cold cavity loss $\alpha_C l_C$, where α_C is the loss coefficient and l_C is the cavity roundtrip length. The expression for $\alpha_C l_C$ is dependent on the geometry or configuration of the laser system. For example, in the case of a multi-section external cavity diode laser as in Fig. 2.1(b), the cold cavity loss is $\alpha_C l_C=\alpha_i(l_L+l_A)+(1/2)\ln(1/R_1R_2)$, where α_i is the intrinsic material loss, and R_1 and R_2 are the cavity mirror reflectivities.

The SVB approach to the Haus-New model was developed for laser systems with two important characteristics: (i) the polarization relaxation time of the gain and absorber media, commonly referred to as dephasing time T_2, is much shorter than the optical pulse duration, and (ii) the carrier relaxation times T_L and T_A in the gain and absorber sections are longer than the optical pulse duration. The first characteristic allows for the approximation that the polarization follows the optical field adiabatically. Thus, denoting P_L and P_A as the macroscopic polarization of the gain and absorber media, respectively, we can take $\partial P_L/\partial t, \partial P_L/\partial z = 0$ and $\partial P_A/\partial t, \partial P_A/\partial z = 0$.

The second characteristic allows for the approximation that absorber and gain relaxation effects are neglected *during* the pulse. The implication is that the evolution of large-signal absorption and gain (second and third term in left-hand-side of Eq. (2.2)) during the optical pulse buildup is described by simple exponential expressions. The terms q_i and g_i are taken as the saturated absorption and gain in the cavity at the beginning of the optical pulse, and $q_i\exp(-W_p/E_{sA})$ and $g_i\exp(-W_p/E_{sL})$ are the same parameters at the end of the pulse [34], [35]. Solving the laser rate equations over the cavity roundtrip time T_{rep} (also the modelocked optical pulse repetition period), these two parameters should relax and recover back to the initial q_i and g_i, and this yields the relationship between steady-state saturated and unsaturated values for absorption and gain in the cavity to be [34], [35]

$$q_i = q_0 \frac{1-\exp(-T_{rep}/T_A)}{1-\exp(-W_p/E_{sA}-T_{rep}/T_A)}, \quad g_i = g_0 \frac{1-\exp(-T_{rep}/T_L)}{1-\exp(-W_p/E_{sL}-T_{rep}/T_L)}, \quad (2.3)$$

where q_0 and g_0 are the unsaturated absorption and gain in a cold cavity. These two terms are given as [31]

$$q_0 = \frac{l_A \Gamma s}{v_g \alpha_C l_C}\left(\frac{\partial g}{\partial n}\right)n_{tr}\cdot(1-V_a), \quad g_0 = \frac{l_L \Gamma}{v_g \alpha_C l_C}\left(\frac{\partial g}{\partial n}\right)\left(\frac{J\cdot T_L}{ed}-n_{tr}\right), \quad (2.4)$$

where V_a is the external bias parameter of the absorber, and J is the pump current density in the gain section. Transparency carrier density of the optical gain section is n_{tr}. Once again, we note that Eq. (2.4) is valid for gain and absorber sections defined in a ridge waveguide edge-emitting laser diode.

The last four terms on the left hand side of Eq. (2.2) accounts for dispersion coefficient $D^*=[(l_L+l_A)/l_C]\omega_L^2\partial^2k/\partial\omega^2$, the round trip phase shift ψ_0 and time delay ΔT of the optical pulse. These three terms are written in Eq. (2.2) as $D=2D^*/\alpha_C$, $\psi=2\psi_0/\alpha_C l_C$, and $\delta=2\omega_L\Delta T/\alpha_C l_C$.

The modelocking master equation Eq. (2.2) is then solved analytically. The solving method used by Haus in [29] assumes optical pulse energies much smaller than the saturation energy of the absorber, $E(t), W_p \ll E_{sA}$. This assumption allows for linear expansion of the exponential terms, which makes an analytic solution possible in the time domain. This solve method is not applicable for all semiconductor laser systems because the pulse energy and absorber saturation energy can be comparable. The SVB approach bypasses this limitation by solving the master equation in the energy domain. The full detail of the solving method is given in [31]. The solution of the master equation yields important information such as pulse energy and duration, and the expressions are given below.

We define the normalized pulse energy as $\mu = W_p/E_{sA}$. The expressions for μ and optical pulse duration τ_p are [31]

$$\mu_\pm = \frac{T_2}{T_1} \pm \sqrt{\frac{T_2^2}{T_1^2} + \frac{T_3}{T_1}} \; , \; \tau_{p,\pm} = \frac{4}{\omega_L} \frac{Y^{1/2}}{\mu_\pm \Delta_1^{1/2}} \; . \tag{2.5}$$

Note that there are two branches of solutions. The constituent terms in Eq. (2.5) are given as follows. First, we start with an approximation that makes the solution much easier to solve and is generally valid for semiconductor lasers:

$$\gamma = \left[\frac{\alpha_L^{\,s}}{\alpha_A} \right]^{1/(s-1)} \approx 3 \; . \tag{2.6}$$

The terms α_L and α_A are the linewidth enhancement factors [36] of the optical gain and absorber sections, respectively. In this research, the typical value of s is ~10 (see Table 7.2 in Section 7.3.5). We therefore make the approximation that $\alpha_A^{1/(s-1)} \approx 1$, which is a good approximation even when α_A is as large as 10 (an unrealistically large value). Also, we use the approximation that $s/(s-1) \approx 1$, which results in $\gamma \approx \alpha_L$, and typical values of α_L ranges from 2 to 5 for semiconductor laser diodes [37]. Thus, the approximation that $\gamma \approx 3$ should be valid for this research.

The rest of the expressions:

$$Y = \frac{3}{2} \frac{(1+D^2)}{(\gamma+D)} \left\{ \sqrt{2 + \frac{9}{4} \frac{(1-\gamma D)^2}{(\gamma+D)^2} - \frac{3}{2} \frac{(1-\gamma D)}{(\gamma+D)}} \right\}, \; \beta = -\frac{2}{3} \frac{(\gamma+D)}{(1+D^2)} Y^2,$$

$$\Delta_1 = \frac{s-1}{s} \left[\frac{(g_i/s)^s}{q_i} \right]^{1/(s-1)}, \; b_1 = \frac{s}{s-1} \ln \left(\frac{s q_i}{g_i} \right),$$

$$T_1 = Y^{-1} + 4Y \left(\frac{\beta+\gamma}{1+\beta^2} \right)^2 + \frac{2}{3} \frac{4(\gamma+D) - 3(\gamma D - 1)}{1+D^2}, \; T_2 = 4b_1 + 8Y \left(\frac{\beta+\gamma}{1+\beta^2} \right)^2 b_1,$$

$$T_3 = 16 \left(s - \frac{1}{\Delta_1} \right) - 8b_1^{\,2} - 16Y \left(\frac{b_1(\beta+\gamma)}{1+\beta^2} \right)^2 . \tag{2.7}$$

Once again, these expressions are taken from [31], but with corrections for errors and with approximations that are valid for this research.

The existence of a real and positive solution for pulse energy solved using Eq. (2.5) is not sufficient for obtaining stable self-sustaining modelocking. This operation regime requires (i) positive saturated net cavity gain at the peak of the lasing pulse and (ii) negative net gain before and after the modelocked pulse, which can be achieved if the recovery time of absorber is comparable or shorter than the recovery time of the gain section. Furthermore, it is highly desirable if the modelocking behavior is self-starting.

Condition (i) is fulfilled if the following conditions are true [31]:

$$0 \leq x_{max} \leq 1 \text{ where } x_{max} = s\ln(sq_i/g_i)/\mu(s-1), \text{ and}$$

$$f(x_{max}) > 0 \text{ where } f(x) = -1 - q_i\exp(-\mu x) + g_i\exp(-\mu x/s). \tag{2.8}$$

Condition (ii) is fulfilled when the following conditions are true:

$$1 + g_i < q_i, \text{ and } 1 + g_i \exp(-W_p / E_{sL}) < q_i \exp(-W_p / E_{sA}). \tag{2.9}$$

Finally, self-starting modelocking occurs when the unsaturated cavity gain is positive:

$$1 + g_0 > q_0. \tag{2.10}$$

2.4.2 Adaptation to Fabry-Perot Cavity Configuration and Incorporating Gain Compression

The Haus-New modelocking model was originally developed for a laser system in ring cavity configuration. The SVB approach to the Haus-New model in the large-signal regime (Section 2.4.1) has followed this framework. In a ring cavity, the optical pulse traveling in the cavity interacts with each intracavity element (gain or absorber element or section) once per cavity roundtrip. However, our intended laser cavity configurations with alkali vapor cell saturable absorber (described in Section 2.3.1 and Fig. 2.2) are Fabry-Perot cavities, and the modelocking model must be adjusted.

All of our Fabry-Perot laser cavity systems (Fig. 2.2) are formed by an external mirror on one end and a facet/surface of the semiconductor gain chip on the other, and the saturable absorber is located in the center of the cavity. The simplified model system for this arrangement is depicted in Fig. 2.9. First of all, we clarify that we assume a lasing operation regime where the output pulse repetition period is equal to the cavity roundtrip time, as opposed to the regime of colliding pulse modelocking where the output pulse repetition period is equal to half of the cavity roundtrip time. In a Fabry-Perot cavity, the optical pulse interacts with each element placed in the middle of the cavity twice per cavity roundtrip, and this applies to the absorber in Fig. 2.9. As such, the roundtrip time is replaced by $T_{rep}/2$ in the Eq. (2.3) for the saturated absorption term. For elements located near the edges of the cavity, like the gain chip in our system, the optical pulse incident on and reflected back from the cavity mirror overlaps with each other in a very small interval of time, a time

scale that is typically much shorter than the absorber recovery time. This effect is taken into account by assuming one interaction per cavity roundtrip at double the energy of the pulse depleting the initial gain g_0, leading to the saturated gain after the pulse to be $g_i \exp(-2W_p/E_{sL})$. We account for these differences from the ring cavity configuration by modifying Eq. (2.3) and (2.8), where the constituent terms T_{rep} and W_p in relations to the saturated cavity gain and absorption terms are changed depending where the gain and absorber section are situated. For this research, the laser cavity is formed by an external mirror on one end and a facet of the semiconductor gain chip on the other, and the saturable absorber is located at the center of the cavity as shown in Fig. 2.9. The modified expression for saturated initial gain and absorption (from Eq. (2.3)) as well as the conditions for stable modelocking (from Eq. (2.9)) that describe our system are

$$q_i = q_0 \frac{1 - \exp(-T_{rep}/2T_A)}{1 - \exp(-W_p/E_{sA} - T_{rep}/2T_A)} , \quad g_i = g_0 \frac{1 - \exp(-T_{rep}/T_L)}{1 - \exp(-2W_p/E_{sL} - T_{rep}/T_L)} ,$$

$$1 + g_i < q_i , \quad 1 + g_i \exp(-2W_p/E_{sL}) < q_i \exp(-W_p/E_{sA}) . \tag{2.11}$$
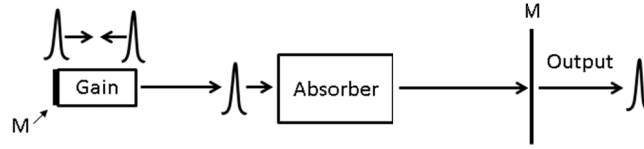
Fig. 2.9. The laser cavity utilizing semiconductor optical gain chip and alkali vapor cell saturable absorber is a Fabry-Perot cavity formed by an external mirror and the back facet/bottom side DBR stack of the semiconductor chip. Depictions of the optical pulse is drawn in to conceptually show that the overlap between the wave incident on and reflected from the semiconductor mirror results in effective doubling of pulse energy experienced by the gain chip. Abbreviation: M – Mirror.

In addition to changes induced by different cavity geometry, we modify the modelocking model to account for the effect of gain compression. Gain compression effect might be important for the optically pumped VECSEL case that was shown in Fig. 2.2(b), where peak output power of the pulse might be very high. The source for optical gain compression can be traced to the carrier rates equation in the optical gain section:

$$\frac{\partial n}{\partial t} = -\frac{n}{T_L} - \frac{(\partial g/\partial n)(n - n_{tr})}{\left(1 + \varepsilon(A_+^2 + A_-^2)\right)\left(1 + \frac{(\omega - \omega_p)^2}{\omega_L^2}\right)}(A_+^2 + A_-^2) + \frac{J}{ed} . \tag{2.12}$$

Here, the terms A_+ and A_- are the electric field amplitudes of forward and backward traveling waves. Gain compression arises from the term ε, which is due to finite intersubband relaxation time.

Accounting for gain compression requires a slight modification to the SVB solutions. Beginning with the definitions of inverse pulse width $B = 1/4\omega_L\tau_p$ and $\theta = 2\varepsilon\omega_L/(\partial g/\partial n)$, where ε is a the gain compression factor (1.5×10^{-17} cm^3 for GaAs). Defining the new variable Θ, given by

$$\Theta = \theta B\mu/s, \tag{2.13}$$

one can incorporate gain compression effects as detailed in [38]. For the Fabry-Perot laser cavity with gain section near the cavity end and absorber section in the middle of the cavity, the following substitutions must be made into Equations (2.5), (2.7), (2,8), and (2.9):

$$(s/2)(1+4\Theta/3) \to s,$$

$$g_i/(1+2\Theta) \to g_i. \tag{2.14}$$

When accounting for gain compression effects, Eq. (2.5) (with the modifications from Eq. (2.14)) can no longer be used to calculate pulse energy μ and pulse duration τ_p because the parameters T_2 and T_3 are now dependent on Θ, which in turn is dependent on μ and τ_p. Instead, we solve for Θ first by using the expression

$$\Theta = \theta B \mu / s = \theta \frac{1}{16} \frac{\Delta_1^{1/2}}{Y^{1/2}} \frac{\mu^2}{s}, \tag{2.15}$$

which yields the equation

$$\Theta = \theta \frac{[\Delta_1(\Theta)]^{1/2}}{16Y^{1/2}s} \left[\frac{T_2(\Theta)}{T_1} \pm \sqrt{\frac{T_2(\Theta)^2}{T_1^2} + \frac{T_3(\Theta)}{T_1}} \right]^2 \tag{2.16}$$

Given that Δ_1, T_2, and T_3 are functions of Θ, one can numerically solve for Θ for a given g_i and q_i. From that, one can calculate all other important parameters μ, τ_p, g_0, q_0, and from those, one can find the physical operating current density J and effective biasing parameter of the absorber V_a.

2.5   Summary

A brief overview of modelocked lasers has been given. We presented the typically used cavity configurations for passively modelocked semiconductor lasers. For this research, we proposed several laser configurations that utilize alkali vapor cell saturable absorber.

We gave an overview of the SVB approach for the analysis of modelocked laser operation. This analysis method is an extension of the Haus-New model with the significant improvement in that it is also applicable for passively modelocked laser systems where the pulse energy is comparable or higher than the absorber saturation energy. Thus, it is useable in laser systems based on semiconductors, and the validity of its solutions will not be limited due to high pulse energies.

There are additional adaptation of the SVB model that still need to be performed, and they are related to the actual operating parameters of J and V_a. The expressions in Eq. (2.4) are directly suitable only for gain and absorber sections defined in the ridge waveguide of a semiconductor edge-emitting laser diode. Different expressions relating J and g_0 are needed for surface-emitting laser gain chips. For the alkali vapor cell saturable absorber, the effective biasing parameter is not voltage but rather the cell temperature T_{cell}. Adapting the alkali vapor cell saturable absorber to the SVB model is not straight forward. We must first investigate the behavior of the alkali vapor cells absorption characteristics theoretically and experimentally. These topics will be covered in Chapters

3, 4, and 5, and the adaptation of the model to fit the theoretical and experimentally measured behavior will be covered in Chapter 7.

Chapter 3   Theory and Model for Optical Absorption in Alkali Atoms

In this chapter, we discuss the theory and modeling of optical absorption in alkali atoms. We begin by briefly presenting the traditional four-level model for optical absorption under broadband optical interrogation. Then, we present the six-level model we developed for optical absorption under narrowband optical interrogation, where the ground state hyperfine splitting levels are resolved. We describe the methods to analyze absorption spectra and techniques to extract relaxation time constants from them, developed from the six-level model. Finally, we propose a new method to measure the excited state lifetime.

3.1   Four-Level Model

The four-level model of alkali atoms was introduced for analyzing spin-polarized pumping of noble gases via collisions with spin-polarized alkali [27], [39]. In noble gas atoms, because the outermost electronic shell is entirely filled, the electronic spins cannot be polarized via optical absorption (followed by spontaneous decay) of circularly polarized light. This leaves a place only for nuclear polarization of noble gas atoms via spin-exchange collisions with alkali atoms. To make this possible, the alkali atoms firstly have to be spin polarized via optical pumping (circularly polarized light with atoms in magnetic field). The typical arrangement assumes high pressure of noble gas atoms in the cell and the use of broadband circularly polarized optical pumping of alkali atoms.

The four-level model is therefore applicable when the alkali atoms hyperfine states are unresolvable. This occurs when the interrogating optical source is spectrally broadband compared to the hyperfine splitting frequencies, or when pressure broadening of the absorption lines is far greater than ground state hyperfine splitting frequency. In this situation, the model treats the alkali atom as a two-energy level system: one ground state and one excited state. Each energy level is two-fold degenerated by spin, which may take spin states spin-up ↑ or spin-down ↓. Therefore, there are four levels total in this model, as shown in Fig. 3.1.
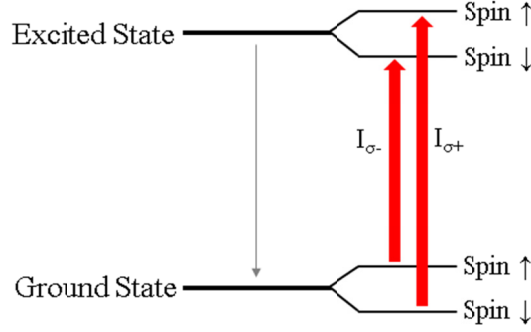
Fig. 3.1. Four-level model treatment of alkali atom under spin polarized optical pumping. $I_{\sigma+}$ and $I_{\sigma-}$ denote the optical intensity of $\sigma+$ and $\sigma-$ pumping.

For the cases where the buffer gas pressure is low or moderate, as in the case we considered here, an alkali atoms ground state hyperfine structure can be easily resolved by a laser with linewidth less than 100 MHz, e.g., vertical-cavity surface-emitting lasers (VCSELs) or distributed feedback lasers (DFBs). In this situation, the four-level model is no longer valid. The two hyperfine splitted ground state levels need to be treated as separate energy levels. This is where the six-level model becomes necessary, which we develop in this research.

3.2   Six-Level Model

The six-level model is applicable when the alkali atoms excited state hyperfine structure cannot be resolved, but the ground state hyperfine structure can be. This occurs when (i) the buffer gas pressure is low to moderate (the exact boundary is set by the atom's absorption linewidth pressure broadening coefficient for a specific buffer gas), and (ii) the interrogating optical source is a single wavelength laser with narrow linewidth (much smaller than the absorption line width and ground state hyperfine frequency splitting).

The six-level model is generally applicable in this research given the alkali vapor cells on hand. For example, in the D_1 transition in ^{87}Rb atoms, the two excited state hyperfine splitting levels are separated by 815 MHz [40]. In contrast, the buffer gas pressure broadening with 75 torr of Ar and/or N_2 (pressure rated for 24° C) is over 1 GHz at cell temperature of 65° C. Thus, there is very good amount of intermixing between the two excited state levels that they can be approximated as one energy level. As another example, the ^{85}Rb $5S_{1/2}$-$6P_{3/2}$ transition (420 nm) has four excited state hyperfine splitting levels separated by 40, 20, and 10 MHz [41], while the Doppler broadening of the linewidth is 1 GHz at temperatures 80 to 100° C (See Chapter 3.4.1 and Eq. (3.26)). In this case, the excited state levels can be approximated as one energy level even without the presence of buffer gas, which is another motivation to investigate the atomic transition at 420 nm.

We model an alkali atom under narrowband optical pumping as a three-energy level model system: |1> and |2> are ground energy states (arising from two hyperfine ground states), |3> is the excited state. Note that electrons in each energy state of alkali atom can be magnetically (spin) polarized. Due to degeneracy of atomic magnetic sub-levels and the symmetry of the sum of Glebsch-Gordan

coefficients [28], [40], the main features of the atomic ensemble can be entirely reproduced by a simple model. Distinguishing only two possible magnetic sub-levels in each energy states, one may reproduce features such as the overall electronic spin polarization degree and the overall transition rates between energy levels. Like the four-level model in [39], we denote these two possible states as "spin states" for sake of brevity. Thus in our six-level model, each energy level is two-fold de-generated by spin, which may take two spin states: spin-up ↑ and spin-down ↓. In this manner, for narrowband optical pumping, we have a system with six levels as depicted in Fig. 3.2.
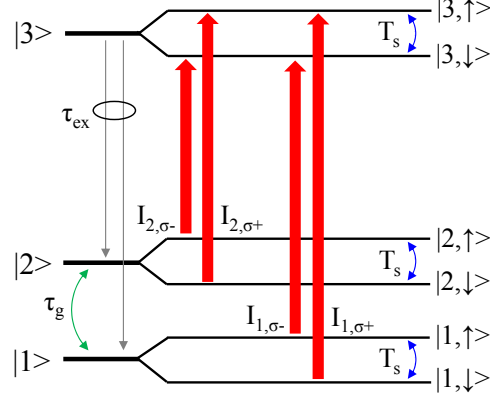
Fig. 3.2. Six-level model for the alkali atom under narrowband spin-polarized optical pumping.

This model accounts for the absorption cross-section σ, excited state lifetime τ_{ex}, branching ratios β_1 and $\beta_2 = 1 - \beta_1$ with which excited states |3> decay into ground states |1> and |2> respectively, the ground state relaxation time τ_g between hyperfine levels and the spin relaxation time T_s. The six-level model ignores the excited state hyperfine structure and treats it as one energy level.

The branching ratios β_1 and β_2 can be calculated from the reduced matrix element of the dipole op-erator by summing over transitions from magnetic sub-levels of the ground states to the magnetic sub-levels of the excited hyperfine states [28], [40]. The final expressions are fortunately quite sim-ple. Let F_i denote the quantum number of total atomic angular momentum of ground state |i>. The branching ratios are $\beta_1 = (2F_1+1)/(2F_1+1+2F_2+1)$ and $\beta_2 = (2F_2+1)/(2F_1+1+2F_2+1)$. The quantum numbers F for [85]Rb and [87]Rb are shown in Fig. 3.3, where we reproduce the full hyperfine struc-tures of both ground and excited states in the D_1 and $5S_{1/2}$-$6P_{3/2}$ energy lines.
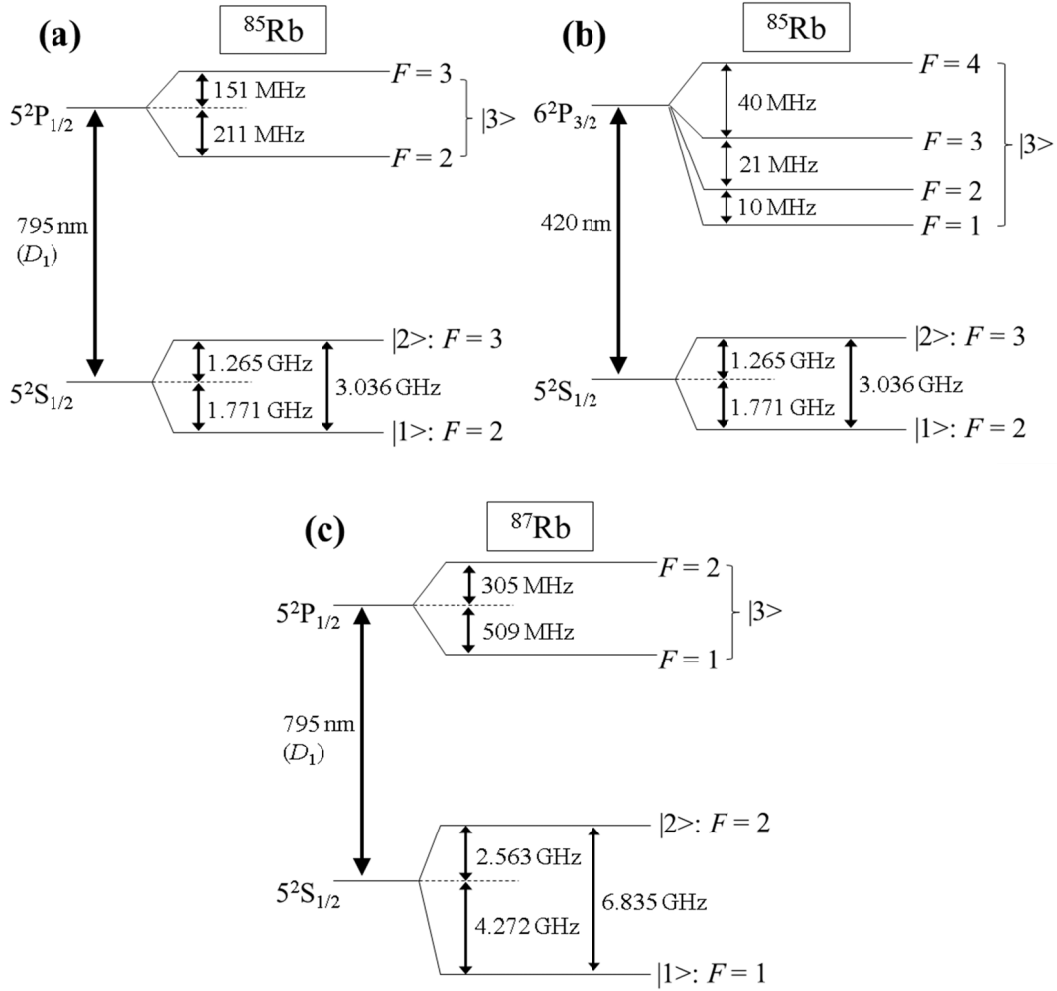
Fig. 3.3. Hyperfine structures of (a) ^{85}Rb D_1 transition at 795 nm wavelength, (b) ^{85}Rb $5S_{1/2}$-$6P_{3/2}$ transition at 420 nm, and (c) ^{87}Rb D_1 transition at 795 nm. The quantum number F is given for each state. Adapted from [28], [40], [41].

Rate equations of the model account for several combinations of σ+ and σ− circularly polarized optical pumping components from |1> to |3> and/or |2> to |3> with intensities $I_{1,σ+}$, $I_{1,σ-}$, $I_{2,σ+}$, and $I_{2,σ-}$, respectively. Note that superposition of two circularly polarized components σ+ and σ− at the same frequency is needed to model the effect of linearly polarized pumping. For *single frequency* (SF) pumping, atoms are pumped either from energy level |1> to |3> or from |2> to |3>. For *dual frequency* (DF) pumping (Λ-pumping configuration), atoms are simultaneously pumped from |1> and |2> to |3>. We define the spin polarization degree P_{Rb} as $(n_{1,↑} + n_{2,↑} − n_{1,↓} − n_{2,↓})/n_{Rb}$, where n_{Rb} is total density of the alkali atom vapor, and $n_{i,↑}$ and $n_{i,↓}$ denotes the population density of a ground state |i> with spin up or down, respectively. The most general form of the rate equations for the six-level model is as follow:

$$\frac{\partial}{\partial t} n_{i,\uparrow/\downarrow} = \frac{1}{2}\beta_i \frac{n_{3,\uparrow}+n_{3,\downarrow}}{\tau_{ex}} \mp \frac{1}{2}\frac{n_{i,\uparrow}-n_{i,\downarrow}}{T_s} - \frac{2\sigma(n_{i,\uparrow/\downarrow}-n_{3,\downarrow/\uparrow})}{\hbar\omega}I_{i,\sigma-/+} - \frac{1}{2}\frac{n_{i,\uparrow}+n_{i,\downarrow}-n_{i,eq}}{\tau_g},$$

$$\frac{\partial}{\partial t}n_{3,\uparrow/\downarrow} = -\frac{n_{3,\uparrow/\downarrow}}{\tau_{ex}} \mp \frac{1}{2}\frac{n_{3,\uparrow}-n_{3,\downarrow}}{T_s} + \frac{2\sigma(n_{1,\downarrow/\uparrow}-n_{3,\uparrow/\downarrow})}{\hbar\omega}I_{1,\sigma+/-} + \frac{2\sigma(n_{2,\downarrow/\uparrow}-n_{3,\uparrow/\downarrow})}{\hbar\omega}I_{2,\sigma+/-} - \frac{1}{2}\frac{n_{3,\uparrow}+n_{3,\downarrow}-n_{3,eq}}{\tau_g}, \quad (3.1)$$

where i denotes the ground state $|i\rangle$, τ_{ex} is the excited state lifetime, T_s is the spin relaxation time, and τ_g is the ground state relaxation time between hyperfine levels (see Fig. 3.2). The first term on the right-hand-side of the rate equations accounts for relaxation from the excited states to the ground states. Coefficients β_1 and β_2 account for the branching ratio between hyperfine ground states, while the coefficient $1/2$ accounts for the branching ratio between spin-up and spin-down sub-levels in the presence of collisional mixing in the excited states due to buffer gas. The second term corresponds to spin relaxation between the spin-up and spin-down states of the same energy. The terms containing intensity I accounts for optical pumping (see Fig. 3.2). The last term accounts for ground state relaxation towards thermal equilibrium densities

$$n_{1,eq}=\beta_1 n_{Rb}, \quad n_{2,eq}=\beta_2 n_{Rb}, \text{ and } n_{3,eq}=0, \quad (3.2)$$

where each state is two-fold degenerated in our six-level atom system, and the equilibrium densities for spin-up ($\uparrow$) and spin-down ($\downarrow$) magnetic sub-levels are at a half of corresponding values. Note that this is a closed system where $\partial(n_{1,\uparrow}+n_{1,\downarrow}+n_{2,\uparrow}+n_{2,\downarrow}+n_{3,\uparrow}+n_{3,\downarrow})/\partial t = 0$, for which the relationship $n_{1,\uparrow}+n_{1,\downarrow}+n_{2,\uparrow}+n_{2,\downarrow}+n_{3,\uparrow}+n_{3,\downarrow} = n_{1,eq}+n_{2,eq}+n_{3,eq} = n_{Rb}$ applies.

The expression for absorption coefficient $\tilde{\alpha}$ follows directly from the commonly recognized differential equation $\partial I/\partial z = -\tilde{\alpha}I$, where z is the direction of the beam propagation. The pump intensity is $I = I_{1,\sigma-}+I_{1,\sigma+}+I_{2,\sigma-}+I_{2,\sigma+}$. The overall equation for absorption becomes

$$\frac{\partial I}{\partial z} = -2\sigma[(n_{1,\uparrow}-n_{3,\downarrow})I_{1,\sigma-}+(n_{1,\downarrow}-n_{3,\uparrow})I_{1,\sigma+}+(n_{2,\uparrow}-n_{3,\downarrow})I_{2,\sigma-}+(n_{2,\downarrow}-n_{3,\uparrow})I_{2,\sigma+}]. \quad (3.3)$$

Table 3.1 summarizes the steady-state solutions for saturated absorption coefficient $\tilde{\alpha}$ in our six-level rate equation model for the four main optical pumping configurations, which include the single-frequency linearly polarized (SF π), single frequency circularly polarized (SF $\sigma+$ or $\sigma-$), dual frequency linearly polarized (DF π) and dual frequency circularly polarized (DF $\sigma+$ or $\sigma-$). Out of these configurations, only SF or DF circularly polarized pumping provide spin polarization to alkali atoms. In the table, the saturated absorption coefficient $\tilde{\alpha}$, saturation intensity I_{sat}, and spin polarization of rubidium atoms P_{Rb} are calculated under steady-state continuous wave (CW) pumping conditions. In the case of SF pumping, index i=1,2 denote hyperfine ground states. These expressions are valid in almost all practical cases, when τ_g and $T_s \gg \tau_{ex}$. Note that the expression for saturation intensity I_{sat} and its dependence on time constant(s) is a function of optical pumping configuration, thus allowing one to measure each relaxation time constant τ_{ex}, τ_g, or T_s independently (see Sections 3.4 and 3.5).

Pumping Configuration	Pump Intensity I	Absorption Coefficient $\tilde{\alpha}$	Saturation Intensity I_{sat}	Spin Polarization P_{Rb}
SF π	$I_{i,\sigma+} = I_{i,\sigma-} = I/2$	$\dfrac{\beta_i \sigma n_{Rb}}{1 + I/I_{sat}}$	$\dfrac{\hbar\omega}{\sigma\tau_g(1-\beta_i)}$	0
SF $\sigma\pm$	$I_{i,\sigma\pm} = I$	$\dfrac{\beta_i \sigma n_{Rb}}{1 + I/I_{sat}}$	$\dfrac{\hbar\omega}{\sigma[T_s + \tau_g(1-\beta_i)]}$	$\pm\dfrac{\beta_i \sigma T_s}{\hbar\omega}\cdot\dfrac{I}{1 + I/I_{sat}}$
DF π	$I_{1,\sigma+} = I_{1,\sigma-} = I_{2,\sigma+} = I_{2,\sigma-} = I/4$	$\dfrac{\sigma n_{Rb}/2}{1 + I/I_{sat}}$	$\dfrac{2\hbar\omega}{3\sigma\tau_{ex}}$	0
DF $\sigma\pm$	$I_{1,\sigma\pm} = I_{2,\sigma\pm} = I/2$	$\dfrac{\sigma n_{Rb}/2}{1 + I/I_{sat}}$	$\dfrac{2\hbar\omega}{\sigma T_s}$	$\pm\dfrac{I/I_{sat}}{1 + I/I_{sat}}$

Table 3.1. Absorption parameters α, saturation intensity I_{sat}, and spin polarization P_{Rb} under different optical pumping configurations at steady-state. For SF pumping, the index i denotes the ground state $|i\rangle$ being pumped, where i = 1 or 2.

Following from Table 3.1, the expressions describing absorption under the different pumping configurations, whether for π or $\sigma\pm$, are

$$\text{SF } |1\rangle \text{ to } |3\rangle: \quad \frac{\partial I}{\partial z} = \frac{-\beta_1 \sigma n_{Rb}}{1 + I/I_{sat,1}} I ,$$

$$\text{SF } |2\rangle \text{ to } |3\rangle: \quad \frac{\partial I}{\partial z} = \frac{-\beta_2 \sigma n_{Rb}}{1 + I/I_{sat,2}} I = \frac{-(1-\beta_1)\sigma n_{Rb}}{1 + I/I_{sat,2}} I ,$$

$$\text{DF } |1\&2\rangle \text{ to } |3\rangle: \quad \frac{\partial I}{\partial z} = \frac{-\sigma n_{Rb}/2}{1 + I/I_{sat}} I, \tag{3.4}$$

where saturated absorption coefficients for π or $\sigma\pm$ polarizations in a particular spectral composition of a narrowband optical beam differ only in saturation intensities. In particular, from Table 3.1, one can see that the saturation intensity for DF π pumping $I_{sat,DF\pi} = 2\hbar\omega/3\sigma\tau_{ex}$ is much higher than that for DF $\sigma\pm$ polarized pumping $I_{sat,DF\sigma\pm} = 2\hbar\omega/\sigma T_s$ due to the fact that the former is governed by the short excited state relaxation time τ_{ex}, while the latter is governed by the slow spin relaxation time T_s (relative magnitudes of τ_{ex} and T_s will be made clear from measurements in Chapter 4). This is the basis for our interest to operate modelocked laser at linear polarization, where the alkali vapor cell may perform as a saturable absorber with fast recovery time τ_{ex}. This is in contrast with the circularly polarized laser interaction with the alkali vapor cell used by Jau and Happer in a push-pull laser oscillator [7], where the slow recovery time of T_s renders the alkali vapor cell unsuitable for saturable absorber work in a modelocked laser.

Transmission of the optical interrogation beam through the vapor cell is defined as $T = I_{out}/I$, where I_{out} is the transmitted intensity. For an alkali vapor cell of length L_{cell}, if the interrogating optical intensity I is well below saturation at $I \ll I_{sat}$, the expressions for transmission can be derived from Eq. (3.4), and they are

$$\text{SF } |1\rangle \text{ to } |3\rangle: \ T = \exp(-\beta_1 \sigma n_{Rb} L_{cell}),$$

$$\text{SF } |2\rangle \text{ to } |3\rangle: \ T = \exp(-\beta_2 \sigma n_{Rb} L_{cell}),$$

$$\text{DF } |1\&2\rangle \text{ to } |3\rangle: \ T = \exp(-\sigma n_{Rb} L_{cell} / 2). \tag{3.5}$$

3.3 Optical Beam Transit and Wall Collision Effects

We now adapt the six-level model given by Eq. (3.1) for the typical situation encountered in this research, where the optical pump beam is smaller than the cell diameter as shown in Fig. 3.4. For this, we apply the model for atomic populations inside and outside the optical pump beam, and we account for the transit time of atoms through the optical beam and collisions effects with other atoms in the cell and with the wall of the cell.
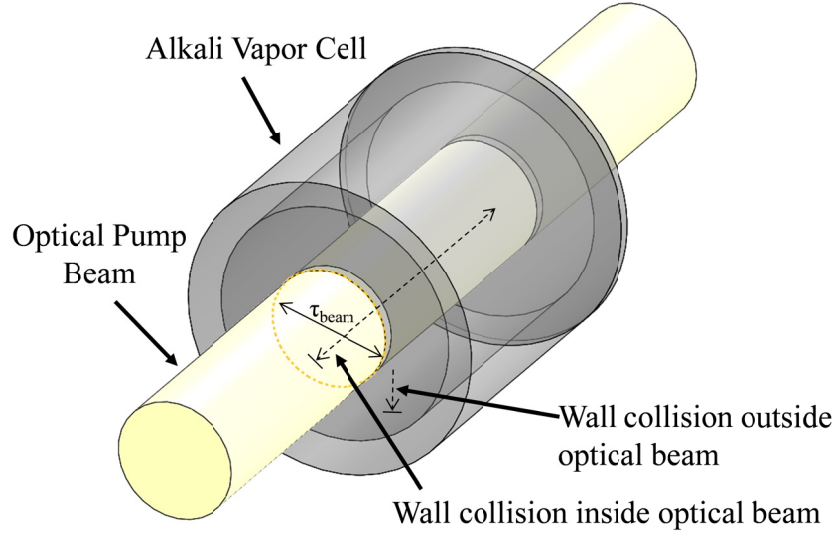
Fig. 3.4. Schematics of the model system for the alkali vapor cell and optical pump beam configuration.

3.3.1 Transit Time Through Optical Beam

It takes finite time for an alkali atom to transit through the optical beam, where it then exchanges with the population of atoms outside the optical beam. Due to the presence of buffer gas, the transit mechanism is diffusion rather than ballistic propagation. The transit time τ_{beam} is given by the following expression

$$\tau_{beam} = r_{beam}{}^2 / 4D_{Rb}. \tag{3.6}$$

Here, $2r_{beam}$ is the full-width at half-maximum (FWHM) of the optical beam intensity, and D_{Rb} is the diffusion coefficient of the alkali atom. This expression is adapted from [42]. Note that D_{Rb} is dependent on buffer gas species, their partial pressures, and cell temperature.

3.3.2 Wall Collision

We derive the wall collision time constants starting from the diffusion equation with a (bulk) relaxation process

$$\frac{\partial n^*}{\partial t} = -\frac{n^*}{\tau} - \nabla \cdot \vec{J} \ . \tag{3.7}$$

In order to recast this equation into a more convenient rate equation form,

$$\frac{dn}{dt} = -\frac{n}{\tau} - \frac{n}{\tau_{wall}} = -\frac{n}{\tau^*} \ , \tag{3.8}$$

the spatial diffusion towards the walls and wall collisions will be accounted for in the effective time constant

$$\frac{1}{\tau^*} = \frac{1}{\tau} + \frac{1}{\tau_{wall}} \ , \tag{3.9}$$

where τ_{wall} is the wall relaxation time constant.

We base the solution to Eq. (3.7) on the expression from [43], which takes the spin-polarized alkali atom population to be near constant far away from the cell walls, and to vanish at the walls. In the one-dimensional case, the solution is:

$$n^*(t,z) = n(t)\left(1 - \frac{\cosh(z/\Lambda)}{\cosh(L_{cell}/2\Lambda)}\right). \tag{3.10}$$

where the cell walls at located at $z=\pm L_{cell}/2$, D_{Rb} is the diffusion constant and the diffusion length Λ is defined by the bulk relaxation time [43]

$$\Lambda = \sqrt{D_{Rb} \cdot \tau} \ . \tag{3.11}$$

It follows that near the cell wall, the flux density of atoms is $J_z = -D_{Rb} \frac{\partial}{\partial z} n^*(t,z) = n(t) \frac{D_{Rb}}{\Lambda} \frac{\sinh(z/\Lambda)}{\sinh(L_{cell}/2\Lambda)}$

and the normal component of the flux density is $J_n = n(t)\frac{D_{Rb}}{\Lambda}$ directed outward. Assuming the same normal component of the flux density at all walls in the cell, which is valid as Λ is much smaller than cell dimensions, integrating Eq. (3.7) over the cell volume and using the divergence theorem of $\int_V (\nabla \cdot \vec{J})dV = \oint_A J_n dA$, we find that

$$\frac{1}{\tau_{wall}} = \frac{A}{V}\frac{D_{Rb}}{\Lambda} \ . \tag{3.12}$$

The parameters A and V are the surface area and the volume of the vapor cell. Equations (3.11) and (3.12) result in the following expression for wall relaxation time:

$$\tau_{wall}^{-1} = \frac{A}{V}\sqrt{\frac{D_{Rb}}{\tau}} \ . \tag{3.13}$$

When this analysis is applied to the case depicted in Fig. 3.4, where the optical beam size is smaller than the cell diameter, the parameters A and V are then tailored separately for the atomic populations inside and outside of the optical pump beam, yielding separate time constants $\tau_{wall,in}$ and $\tau_{wall,out}$.

Our expression in Eq. (3.13) for the wall relaxation time is very different from what is typically used in literature. In literature sources such as [42], the given thermal rate of collision with the walls does not account for the reduced density of spin polarized atoms in the vicinity of the wall, leading to the expression

$$\tau_{wall}^{-1} = \frac{A}{V}\frac{v_T}{4} \ , \tag{3.14}$$

where v_T is the thermal velocity. As a result, Eq. (3.14) overestimates the wall relaxation rate by several orders of magnitude.

The analysis in [27] originates from the series expansion of the spatial profile of population density over the complete set of the normal diffusion modes of the system. The normal modes account for particular cell geometry (e.g. by using a product of the cosine and Bessel functions for cylindrical cell). But at the next step of analysis, an assumption is made that the fundamental diffusion mode with very smooth spatial distribution $n \propto J_0(\mu_n \frac{2r}{d})\cos(\pi\frac{z}{l})$ entirely suffices, yielding the analytic expression

$$\tau_{wall}^{-1} = \left(\frac{\pi^2}{L_{cell}^2} + \frac{2.405^2}{r_{cell}^2}\right)D_{Rb} \ , \tag{3.15}$$

where r_{cell} and L_{cell} are the radius and the length of a cylindrical cell. Note that the fundamental diffusion mode profile, which is the basis for Eq. (3.15), is a very crude approximation of the actual plateau-shape spatial profile of atomic population in Eq. (3.10).

The wall relaxation times calculated from literature expressions as in Eq. (3.14) and (3.15) do not match experimentally measured values, while our model does (see Fig. 4.6 in Section 4.2.2).

3.3.3 Incorporation into Six-Level Model

The optical beam size and wall collision effects described in Sections 3.3.1 and 3.3.2 have to be incorporated into the six-level model. We define the portion of the alkali vapor cell inside the optical beam as the *inner* region of the cell, and the portion outside the optical beam as the *outer* region.

The rate equations for the different sub-levels as well as for populations in the inner and outer (index "out") region of the vapor cell are

$$
\begin{aligned}
\frac{\partial}{\partial t} n_{i,\uparrow/\downarrow} &= \frac{1}{2}\beta_i \frac{n_{3,\uparrow}+n_{3,\downarrow}}{\tau_{ex}} \mp \frac{1}{2}\frac{n_{i,\uparrow}-n_{i,\downarrow}}{T_{s,bulk}} \mp \frac{1}{2}\frac{n_{i,\uparrow}-n_{i,\downarrow}}{T_{s,wall,in}} - \frac{2\sigma(n_{i,\uparrow/\downarrow}-n_{3,\downarrow/\uparrow})}{\hbar\omega}I_{i,\sigma-/+} \\
&\quad -\frac{n_{i,\uparrow/\downarrow}-n_{i,\uparrow/\downarrow,out}}{\tau_{beam}} - \frac{1}{2}\frac{n_{i,\uparrow}+n_{i,\downarrow}-n_{i,eq}}{\tau_{wall,in}}
\end{aligned}
$$
,

$$
\begin{aligned}
\frac{\partial}{\partial t} n_{3,\uparrow/\downarrow} &= -\frac{n_{3,\uparrow/\downarrow}}{\tau_{ex}} \mp \frac{1}{2}\frac{n_{3,\uparrow}-n_{3,\downarrow}}{T_{s,bulk}} \mp \frac{1}{2}\frac{n_{3,\uparrow}-n_{3,\downarrow}}{T_{s,wall,in}} + \frac{2\sigma(n_{1,\downarrow/\uparrow}-n_{3,\uparrow/\downarrow})}{\hbar\omega}I_{1,\sigma+/-} + \frac{2\sigma(n_{2,\downarrow/\uparrow}-n_{3,\uparrow/\downarrow})}{\hbar\omega}I_{2,\sigma+/-} \\
&\quad -\frac{n_{3,\uparrow/\downarrow}-n_{3,\uparrow/\downarrow,out}}{\tau_{beam}} - \frac{1}{2}\frac{n_{3,\uparrow}+n_{3,\downarrow}-n_{3,eq}}{\tau_{wall,in}}
\end{aligned}
$$
,

$$
\frac{\partial}{\partial t} n_{i,\uparrow/\downarrow,out} = \mp\frac{1}{2}\frac{n_{i,\uparrow,out}-n_{i,\downarrow,out}}{T_{s,bulk}} \mp \frac{1}{2}\frac{n_{i,\uparrow,out}-n_{i,\downarrow,out}}{T_{s,wall,out}} + \frac{n_{i,\uparrow/\downarrow}-n_{i,\uparrow/\downarrow,out}}{\tau_{beam}} - \frac{1}{2}\frac{n_{i,\uparrow,out}+n_{i,\downarrow,out}-n_{i,eq}}{\tau_{wall,out}}
$$
,

$$
\frac{\partial}{\partial t} n_{3,\uparrow,out} = \frac{\partial}{\partial t} n_{3,\downarrow,out} = 0 \ . \tag{3.16}
$$

The two first equations in (3.16) are for the atomic densities of the two hyperfine ground states $n_{i,\uparrow/\downarrow}$ ($i=1,2$) and excited states $n_{3,\uparrow/\downarrow}$ in the inner region of the cell. The two last equations are for the atomic densities $n_{i,\uparrow/\downarrow,out}$ and $n_{3,\uparrow/\downarrow,out}$ in the outer region of the cell. Because without optical pumping, the excited states $n_{3,\uparrow/\downarrow,out}$ quickly relax to one of the ground states (τ_{ex} is a few orders of magnitude smaller than the other relaxation time constants), we use the approximation $n_{3,\uparrow,out}=n_{3,\downarrow,out}=0$ in the outer part of the cell. Note that Eq. (3.16) satisfies the condition of a closed system, such that in each region, the population densities of atoms in each state sum up to that of total Rb population density n_{Rb}.

In the first two differential equations of Eq. (3.16), the first term on the right-hand-side which contains τ_{ex} accounts for relaxation from the excited states to the ground states. The second term is the spin relaxation between the spin-up and spin-down states of the same energy level. $T_{s,bulk}$ is the spin relaxation time due to collision with buffer gas and in the absence of wall collision effects.

The third term on the right-hand-side of the first two differential equations and the second term in the third differential equation in Eq. (3.16) contain $T_{s,wall,in}$ or $T_{s,wall,out}$, which are the spin relaxation time constant due to collisions with the cell walls in the inner or outer cell region (with and without optical pumping, respectively). This term accounts for the effects of wall collision on the spin polarization of the system.

The term containing optical intensities I accounts for optical pumping. The term containing τ_{beam} accounts for the exchange of atoms between the inner and outer cell region through transiting the optical beam, and the τ_{beam} here is the same as in Eq. (3.6).

Finally, the last term in the first three differential equations contains either $\tau_{wall,in}$ or $\tau_{wall,out}$, and they are analogous to $T_{s,wall,in}$ and $T_{s,wall,out}$ except that they apply to relaxation between hyperfine ground states. As can be seen in our model, wall collisions are responsible for the relaxation of the ground

states toward equilibrium (compare to the last terms in the model system Eq. (3.1)). Natural relaxation time constant between ground state hyperfine levels [1] is much longer than either $\tau_{wall,in}$ or $\tau_{wall,out}$, and is ignored in this model.

We now clarify how the wall collision model of Section 3.3.2 applies, and we start on the spin relaxation times $T_{s,wall,in}$ and $T_{s,wall,out}$ due to wall collisions. For this, we recast the spin relaxation terms of Eq. (3.16) into the form of Eq. (3.8). The spin relaxation terms in Eq. (3.16) for the inner and outer parts of the cell can be made evident by taking a difference between two corresponding spin sub-levels:

$$\frac{\partial}{\partial t}(n_{i,\uparrow} - n_{i,\downarrow}) = -\frac{n_{i,\uparrow} - n_{i,\downarrow}}{T_{s,bulk}} - \frac{n_{i,\uparrow} - n_{i,\downarrow}}{T_{s,wall,in}} - \frac{n_{i,\uparrow} - n_{i,\downarrow}}{\tau_{beam}} + \left[\frac{n_{i,\uparrow,out} - n_{i,\downarrow,out}}{\tau_{beam}} \right],$$

$$\frac{\partial}{\partial t}(n_{i,\uparrow,out} - n_{i,\downarrow,out}) = -\frac{n_{i,\uparrow,out} - n_{i,\downarrow,out}}{T_{s,bulk}} - \frac{n_{i,\uparrow,out} - n_{i,\downarrow,out}}{T_{s,wall,out}} - \frac{n_{i,\uparrow,out} - n_{i,\downarrow,out}}{\tau_{beam}} + \left[\frac{n_{i,\uparrow} - n_{i,\downarrow}}{\tau_{beam}} \right]. \quad (3.17)$$

Here, the terms accounting for exchange between the inner and the outer regions of the cell are shown in square brackets. In these equations, the spin relaxation time constant $T_{s,bulk}$ in the absence of wall collisions and beam transit effects is the reciprocal of the sum of spin-exchange and spin-relaxation rates between Rb and the buffer gas, and their values are taken from literature [39]. The spin exchange and relaxation cross-sections as well as the $T_{s,bulk}$ values used in this research can be found in Section 4.2.1.

The third terms on the right-hand-side of Eq. (3.17), which contain τ_{beam}, accounts for the relaxation of spin-polarized atoms due to beam transit effect. Formal comparison of relaxation rates in Eq. (3.17) and Eq. (3.8) indicates that this should be accounted by the model as a contribution to the effective "bulk" relaxation rate (the term $\sim 1/\tau$ in Eq. (3.8)). The expressions for the wall collision time constants $T_{s,wall,in}$ and $T_{s,wall,out}$ then follow from Eq. (3.13), in which the parameters A and V would be the cell surface area and volume corresponding to the part of the cell either inside or outside the optical interrogation beam:

$$T_{s,wall,in}^{-1} = \frac{A_{in}}{V_{in}} \sqrt{D_{Rb} \cdot (T_{s,bulk}^{-1} + \tau_{beam}^{-1})} \,,$$

$$T_{s,wall,out}^{-1} = \frac{A_{out}}{V_{out}} \sqrt{D_{Rb} \cdot (T_{s,bulk}^{-1} + \tau_{beam}^{-1})} \,. \quad (3.18)$$

Note that these expressions assume that each collision with the cell wall results in spin relaxation.

Having defined all spin relaxation times in Eq. (3.17), we may now exclude the atomic spin population densities in the outer region of the cell. Considering a steady-state solution for $(n_{i,\uparrow,\text{out}} - n_{i,\downarrow,\text{out}})$ in the outer region of the cell, substituting it into the spin generation term due to exchange between the inner and the outer region of the cell, we find the following effective relaxation rate for the spin sub-levels:

$$\frac{1}{T_s} = \frac{1}{T_{s,bulk}} + \frac{1}{T_{s,wall,in}} + \cfrac{1}{\tau_{beam} + \cfrac{1}{\cfrac{1}{T_{s,bulk}} + \cfrac{1}{T_{s,wall,out}}}} \ . \tag{3.19}$$

It allows us to recover the dynamics of spin sub-level in the original six-level rate equation model in Eq. (3.1).

Proceeding along the same lines for the total atomic populations at each hyperfine ground state ($n_{i,\uparrow}$ + $n_{i,\downarrow}$), we find that expressions Eq. (3.13) for the wall collision time constants $\tau_{wall,in}$ and $\tau_{wall,out}$ are entirely defined by the beam transit effect. Indeed, the natural relaxation rate between hyperfine ground states in Rb atoms is very low, with lifetime on the order of a several tenths of ms [1], and can be neglected in comparison to beam transit rate, which has lifetime (inverse of rate) in the range of a few tens to few hundred µs for the typical optical beam size, cell size, buffer gas compositions and pressures used in this study. The expressions for $\tau_{wall,in}$ and $\tau_{wall,out}$ are:

$$\tau_{wall,in}^{-1} = \eta \frac{A_{in}}{V_{in}} \sqrt{D_{Rb} \cdot \tau_{beam}^{-1}} \ ,$$

$$\tau_{wall,out}^{-1} = \eta \frac{A_{out}}{V_{out}} \sqrt{D_{Rb} \cdot \tau_{beam}^{-1}} \ . \tag{3.20}$$

Note that we introduce a *slow down* factor η *(0<η<1)*. This term accounts for the fact that a wall collision event is less likely to change the atomic energy level than it is to produce a spin flip between two spin sub-levels of the same hyperfine state. In our model, we assume an uncoated cell, and the wall collision almost always results in spin relaxation. This "dephasing" process does not produce a change in the energy of an atom colliding with the wall. At the same time, the relaxation of an atom between two ground hyperfine states may not occur at each wall collision as it requires an energy exchange between the alkali atom and atoms of the wall.

Following along the lines of the steady-state approach used in Eq. (3.19), we exclude the hyperfine state population densities in the outer region of the cell. As a result we find the following effective relaxation rate between hyperfine ground states:

$$\frac{1}{\tau_g} = \frac{1}{\tau_{wall,in}} + \frac{1}{\tau_{beam} + \tau_{wall,out}} \ . \tag{3.21}$$

This allows us to recover the dynamics of the hyperfine levels in the original six-level rate equation model in Eq. (3.1), just as it was done for T_s above.

The effective relaxation rates defined just above in Eq. (3.19) and (3.21) allows us to apply the six-level rate equation model in Eq. (3.1) for studying the dynamics of alkali vapor cell absorber. In our model, the slow down factor for the wall relaxation of hyperfine ground states η is a number between 0 and 1. It is effectively a fitting parameter to match the model described here with measured τ_g (see Fig. 4.6 in Section 4.2.2). Note that spin relaxation time constants T_s has no need of this or other fitting parameter.

3.4　Single Frequency Absorption Spectra Analysis

Now we clarify how the effective parameters of our six-level model for the alkali vapor cell absorber are related to experimental measurements, which include steady-state absorption spectroscopy and time-domain pump-probe measurements.

The most commonly performed absorption spectroscopy is done with single frequency (SF) optical interrogation, and the analysis of the acquired SF absorption spectra is as follows. We measure the absorption spectra of alkali atoms (see Chapters 4 and 5 for results) by tuning our interrogation laser to the exact wavelength of the atomic transition and perform mode hop free frequency tuning over wide enough frequency range such that it covers all hyperfine lines of the atomic transition.

The absorption spectrum is acquired by measuring the optical intensity transmission as a function of lasing frequency, $T(v)=I_{out}(v)/I(v)$. $T(v)$ can be transformed to either the effective absorption coefficient $\tilde{\alpha}(v)$ or the effective absorption cross-section $\tilde{\sigma}(v)$, with the expression

$$\tilde{\alpha}(v) = \tilde{\sigma}(v)n_{Rb} \approx -\ln[T(v)]/L_{cell} , \tag{3.22}$$

where L_{cell} is the alkali vapor cell length. The reason why this expression is an approximation is discussed below, in relation to Eq. (3.34). In the following sections, we distinguish unsaturated (small signal) absorption coefficient $\alpha(v)$ and cross-section $\sigma(v)$ from the ones at arbitrary intensity levels, which are subjected to intensity saturation effect and are indicated with a tilde over the symbol. The absorption spectrum, in either $\tilde{\alpha}(v)$ or $\tilde{\sigma}(v)$, can be analyzed using the following techniques and methods.

3.4.1　Absorption Spectroscopy at Well Below Saturation Intensity

At well below optical saturation $I<<I_{sat}$, the spectrum $\alpha(v)$ under SF optical pumping (either π or $\sigma\pm$) is described by the expression [28], [40], [44], [45]

$$\alpha(v) = n_{Rb}\sigma(v) = n_{Rb}\pi r_e cf \left[\beta_1 \sum_{F'} s_{F_1F'} \cdot V(v - v_{0,F_1F'}) + \beta_2 \sum_{F'} s_{F_2F'} \cdot V(v - v_{0,F_2F'}) \right]. \tag{3.23}$$

This expression accounts for all allowed transitions originating from the two ground hyperfine states, as given by the two terms in square brackets, to all excited hyperfine states of the line, as accounted for in the summations. For each transition, the ground states |1> and |2> have atomic angular momentum quantum number F_1 or F_2, respectively, and the excited hyperfine state has quantum number F' as shown in Fig. 3.3. The lineshape of each individual transition is described by the Voigt profile function $V(v)$ that is integration normalized with $\int_{-\infty}^{\infty} V(v)dv = 1$. The frequency separations between the frequency center of each transition, $v_{0,FF'}$, are defined by both the ground and excited state hyperfine splitting frequencies (see [28], [40], [41] and Fig. 3.3 for the atoms and transitions covered in this dissertation).

The amplitude of each hyperfine transition in Eq. (3.23) is defined by the relative hyperfine strength transition factors $s_{F_1F'}$ and $s_{F_2F'}$ [28], [40], which are derived from the summing of all matrix elements from a single ground state magnetic sub-level in F_1 or F_2 state to all magnetic sub-levels in F' state. The terms $s_{F_1F'}$ and $s_{F_2F'}$ are the sums of squares of the corresponding Clebsch-Gordan coefficients with appropriate scaling for degeneracy of the upper states magnetic sub-levels. Note that the symmetry of the relative hyperfine strength transition factors $s_{F_1F'}$ and $s_{F_2F'}$ results in $\sum_{F'} s_{F_1F'} = 1$, and $\sum_{F'} s_{F_2F'} = 1$ for the sum over all excited hyperfine states of the line.

The amplitudes of hyperfine transitions in Eq. (3.23) also accounts for summation over magnetic sub-levels in the ground states F_1 or F_2. Therefore, the transition amplitudes are also scaled by branching ratio β_i to account for magnetic sub-level degeneracy of the ground hyperfine states, that is $\beta_1 = (2F_1+1)/(2F_1+1+2F_2+1)$ and $\beta_2 = (2F_2+1)/(2F_1+1+2F_2+1)$. Note that $\beta_1 + \beta_2 = 1$, and therefore the broadband absorption cross-section that follows from Eq. (3.23) recovers the definition of the absorption oscillator strength f:

$$\int \sigma(v)dv = \pi r_e cf\left[\beta_1 \sum_{F'} s_{F_1F'} \cdot \int V(v - v_{0,F_1F'})dv + \beta_2 \sum_{F'} s_{F_2F'} \cdot \int V(v - v_{0,F_2F'})dv\right] = \pi r_e cf , \qquad (3.24)$$

where r_e is the classical electron radius (2.818×10^{-15} m) and c is the speed of light in vacuum (2.997×10^8 m/s).

The absorber oscillator strength f is 0.342 for the Rb D_1 line [28], [40] and 9.4×10^{-3} for the Rb $5S_{1/2}$-$6P_{3/2}$ line [46]. A summary of energy transition parameters used in this research is given in Table 3.2.

The Voigt profile function $V(v)$ of each hyperfine transition accounts for homogeneous and inhomogeneous broadening of the lineshape. It is the result of convolution of Gaussian and Lorentzian profiles, as given by

$$V(v) = \int_{-\infty}^{\infty} G(x)L(v-x)dx , \text{ where}$$

$$G(v) \equiv \frac{2}{\Delta v_D}\sqrt{\frac{\ln 2}{\pi}} \exp(\frac{-v^2 \cdot 4\ln 2}{\Delta v_D^2}) ,$$

$$L(v) \equiv \frac{\Delta v_L / 2}{\pi[v^2 + (\Delta v_L / 2)^2]} . \qquad (3.25)$$

Transition line	^{85}Rb D_1 (λ=795 nm)	^{87}Rb D_1 (λ=795 nm)	^{85}Rb 5S$_{1/2}$-6P$_{3/2}$ (λ=420 nm)
f Absorber oscillator strength	0.342 [28]	0.342 [40]	9.4×10^{-3} [46]
quantum number F_1 of $|1\rangle$	$F_1 = 2$	$F_1 = 1$	$F_1 = 2$
quantum number F_2 of $|2\rangle$	$F_2 = 3$	$F_2 = 2$	$F_2 = 3$
quantum numbers $\{F'\}$ of $|3\rangle$	$F' = \{2, 3\}$	$F' = \{1, 2\}$	$F' = \{1, 2, 3, 4\}$
β_1 Branching ratio for $|1\rangle$	β_1=5/12	β_1=3/8	β_1=5/12
β_2 Branching ratio for $|2\rangle$	β_2=7/12	β_2=5/8	β_2=7/12
$s_{F_1F'}$ Relative Hyperfine Strength Transition Factors from $|1\rangle$	s_{22}=2/9 s_{23}=7/9	s_{11}=1/6 s_{12}=5/6	s_{21}=3/10 s_{22}=7/18 s_{23}=14/45
$s_{F_2F'}$ Relative Hyperfine Strength Transition Factors from $|2\rangle$	s_{32}=5/9 s_{33}=4/9	s_{21}=1/2 s_{22}=1/2	s_{32}=5/63 s_{33}=5/18 s_{34}=9/14

Table 3.2. Summary of parameters for atomic transitions used in this research. Note that for each transition line: $\beta_1 + \beta_2 = 1$, $\sum_{F'} s_{F_1F'} = 1$, and $\sum_{F'} s_{F_2F'} = 1$.

The Gaussian profile function $G(v)$ has full-width at half-maximum value (FWHM) of Δv_D. The Lorentzian profile $L(v)$ has FWHM of Δv_L.

The Gaussian component of the Voigt functions arises from Doppler broadening. The broadening has FWHM of

$$\Delta v_D = \frac{2}{\lambda}\sqrt{\frac{2RT_{cell}}{M}\ln(2)}, \tag{3.26}$$

where R is the gas constant (8.314 J/mol·K), T_{cell} is the cell temperature, and M is the molar mass of the alkali atom. (For the Rb D_1 transition at temperatures of 60° to 80° C, Δv_D is about 540 MHz. For the 5S$_{1/2}$-6P$_{3/2}$ transition at 80° to 100° C, Δv_D is about 1 GHz.)

The Voigt profile Lorentzian characteristics Δv_L accounts for both the natural line broadening due to finite lifetime of the excited state and the buffer gas pressure broadening due to collisions with the buffer gas atoms (or molecules). For vapor cells with buffer gas, natural broadening can ignored because it is usually very small (<10 MHz for Rb transitions) compared to pressure broadening (>100 MHz at a few torrs of N$_2$ or He; see Chapter 4).

With the theory established in this section so far, we can now relate the effective absorption cross-section σ of the six-level model (as defined in Section 3.2) to the absorption spectrum measured at well below saturation $I \ll I_{sat}$. Equation (3.23) is used to fit the spectrum, and the pressure broadened linewidth Δv_L is the only parameter that is allowed to vary in this fitting process. Once Δv_L is extracted, we can now calculate σ.

The six-level model ignores the excited state hyperfine structure while Eq. (3.23) does not. To make Eq. (3.23) compatible with the model, we make the approximation that all transitions originating from the same ground state overlap each other perfectly, i.e. for the same F, all $v_{0,FF'}$ are the same

regardless of F'. This approximation is valid when excited state hyperfine structure cannot be resolved due to sufficient pressure broadening, which is very good approximation in most of the cases considered here. Combining this approximation with the expressions for SF on-resonance absorption at well below optical saturation in Eq. (3.5), and noting that $\beta_1 + \beta_2 = 1$, $\sum_{F'} s_{F_1F'} = 1$, and $\sum_{F'} s_{F_2F'} = 1$, we obtain

$$\alpha = n_{Rb}\sigma = n_{Rb}\pi r_e cf \cdot V(0), \text{ or}$$

$$\sigma = \pi r_e cf \cdot V(0), \tag{3.27}$$

with the Voigt lineshape profile $V(v)$ utilizing the actual pressure broadening Δv_L and Doppler broadening Δv_D in the particular cell, which is defined from fitting the absorption spectrum.

3.4.2 Saturation Effects in Absorption Spectra

At optical interrogation intensities no longer well below the saturation intensity I_{sat}, the measured absorption spectra is no longer described by Eq. (3.23). Due to saturation effects, the amplitude of each atomic transition is scaled down with the coefficient $1/(1+I/I_{sat})$, with I_{sat} depending on the interrogation scheme and polarization (SF π or SF $\sigma\pm$) of interrogating optical beam. As indicated in Table 3.1 and Eq. (3.4), for single frequency interrogation, the saturation intensity for transition originating from hyperfine ground state |1> is different from transition originating from hyperfine ground state |2>. Assuming we have an absorption coefficient spectra measured, $\tilde{\alpha}(v)$, the expressions, with the approximation that the excited state has no hyperfine splitting, are

$$\tilde{\alpha}(v) = n_{Rb}\pi r_e cf\left[\frac{\beta_1}{1+I/I_{sat,1}} \cdot V(v - v_{0,F_1}) + \frac{\beta_2}{1+I/I_{sat,2}} \cdot V(v - v_{0,F_2})\right] \tag{3.28}$$

where $I_{sat,1}$ and $I_{sat,2}$ are the saturation intensities, with indices denoting transition from ground state |1> and |2>, respectively. It is easy to see that in the case of optical interrogation at well below saturation of $I \ll I_{sat,1}$ and $I \ll I_{sat,2}$, Eq. (3.28) simply becomes Eq. (3.23).

The *saturated* absorption coefficients, for on-resonance from |1> to |3> and |2> to |3>, is

$$\tilde{\alpha}_1 = n_{Rb}\pi r_e cf \frac{\beta_1}{1+I/I_{sat,1}} V(0) = \frac{\alpha_1}{1+I/I_{sat,1}},$$

$$\tilde{\alpha}_2 = n_{Rb}\pi r_e cf \frac{\beta_2}{1+I/I_{sat,2}} V(0) = \frac{\alpha_2}{1+I/I_{sat,2}}. \tag{3.29}$$

Equation (3.29), in conjunction with the expressions for saturation optical intensities $I_{sat,1}$ and $I_{sat,2}$ in Table 3.1, allows for the extraction of the time constants τ_g and T_s from experimentally measured absorption spectra under SF π or $\sigma\pm$ polarized optical interrogation. This is detailed in Section 3.4.3.

3.4.3 Measuring Relaxation Times for Hyperfine Ground States and Spin Sub-levels

In this section, we will detail how one can measure the ground state hyperfine levels relaxation times τ_g and spin relaxation time T_s using single frequency absorption spectroscopy. First, we account for the saturation effects that impact the overall transmitted intensity. We start with saturated differential absorption expressions that are in the general form of

$$\frac{\partial I}{\partial z} = -\frac{\alpha_i I}{1 + I/I_{sat,i}} , \tag{3.30}$$

where $\alpha_i = \beta_i \sigma n_{Rb}$ for SF interrogation of hyperfine ground state $|i\rangle$ (see Table 3.1). Solving this differential equation for the cell length L_{cell}, we obtain

$$\ln(I_{out,i}) + \frac{I_{out,i}}{I_{sat,i}} = -\alpha_i L_{cell} + \ln(I) + \frac{I}{I_{sat,i}} , \tag{3.31}$$

where I is the optical intensity incident on the cell, $I_{out,i}$ is the optical intensity transmitted through the cell when it is on absorption resonance corresponding to ground state $|i\rangle$. This equation can be rewritten into a more useable form

$$I = \frac{I_{sat,i}[\ln(T_{SF,i}) + \alpha_i L_{cell}]}{1 - T_{SF,i}} , \tag{3.32}$$

where $T_{SF,i} = I_{out,i}/I$ is the intensity transmission of the cell. We emphasize that saturation intensity $I_{sat,i}$ is a function of the branching ratio β_i, the unsaturated absorption cross-section σ, and mostly importantly, relaxation times τ_g and/or T_s, depending on whether the optical interrogation is SF π or SF $\sigma\pm$ as shown in Table 3.1.

The relationship between optical interrogation intensity I and transmission $T_{SF,i}$ presented in Eq. (3.32) give rise to a method with which to measure relaxation times τ_g and T_s. First, we measure a series of absorption spectra with SF π interrogation at different intensities I. Then, using Eq. (3.23) and Eq. (3.27), we extract the unsaturated absorption cross-section σ from the spectrum measured at well below saturation ($I \ll I_{sat,1}$ and $I \ll I_{sat,2}$). Note that while saturation intensities are not known beforehand, one can confirm that a particular optical intensity is well below saturation if its corresponding absorption spectrum fulfills Eq. (3.24). It is important to calculate σ because it is embedded inside Eq. (3.32) in both $I_{sat,i}$ and α_i.

The next step is to measure $T_{SF,i}$ for the two hyperfine lines from the measured absorption spectra. In the ideal case where the excited state hyperfine levels can be approximated as overlapping each other perfectly and the ground state hyperfine structure is perfectly resolved (i.e., the situation for which the six-level model was developed), these are simply the minimums/peaks of the transmission/absorption spectra. With a given series of $T_{SF,1}$ and $T_{SF,2}$ for different interrogation intensity I, we then fit these series of data with Eq. (3.32). Note that for SF π interrogation, the saturation intensities $I_{sat,1}$ and $I_{sat,2}$ are functions of τ_g, and this is the only unknown parameter in Eq. (3.32). Thus, analysis of transmission with Eq. (3.32) allows us to calculate τ_g, the relaxation time between the ground state hyperfine levels.

Finally, we repeat the measurement of absorption spectra with SF σ± interrogation at different optical intensities. Applying the same analysis with Eq. (3.32) allows us to calculate spin relaxation time T_s. Thus, by measuring the absorption spectra for a series of different optical intensities under both single frequency π and σ± interrogation, we can obtain the relaxation lifetimes τ_g and T_s.

We now analyze the error in the right-hand-side of Eq. (3.22), which is the assumption that the saturated absorption coefficient $\tilde{\alpha}(\nu)$ can be approximated as $-\ln[T(\nu)]/L_{cell}$. Using Eq. (3.32) and the relationship between saturated and unsaturated absorption coefficient $\alpha_i = \tilde{\alpha}_i(1 + I/I_{sat,i})$ (see Eq. (3.29)), we modify Eq. (3.32) into the following expression

$$I = \frac{I_{sat,i}[\ln(T_{SF,i}) + \tilde{\alpha}_i(1 + I/I_{sat,i})L_{cell}]}{1 - T_{SF,i}},$$

(3.33)

from which we then solve for $\tilde{\alpha}_i$, leading to the expression

$$\tilde{\alpha}_i = -\frac{1}{L_{cell}}\ln(T_{SF,i}) + \frac{1}{L_{cell}}[1 - T_{SF,i} + \ln(T_{SF,i})]\frac{I/I_{sat,i}}{1 + I/I_{sat,i}}.$$

(3.34)

From Eq. (3.34), we can see that it becomes Eq. (3.22) in the situation when $I \ll I_{sat,i}$ or $T \rightarrow 1$. The error obtained from using Eq. (3.22) is in the second term in the right-hand-side of Eq. (3.34). For a 5 mm long cell (applicable for most of our cells), in the situation where the interrogation intensity is nearly the same as the saturation intensity $I \approx I_{sat,i}$, we find that the relative error obtained in using Eq. (3.22) is above 10% when the transmission on absorption resonance is $T < 0.69$.

3.5   Dual Frequency Absorption Spectra Analysis

As can be seen from Table 3.1, dual frequency (DF) optical interrogation at π and σ± polarization allows one to extract, respectively, the excited state lifetime τ_{ex} and the spin relaxation time T_s from measured saturation intensity and absorption coefficient. The method to extract τ_g and T_s from single frequency (SF) optical interrogation, described in Section 3.4.3 and using Eq. (3.32), can be similarly applied to the case of DF optical interrogation. By measuring the on-resonance transmission T_{DF} as a function of I under DF interrogation, we can extract τ_{ex} and T_s. The main difference here is that the measured spectra under DF interrogation are significantly different from those of SF interrogation.

To simultaneously pump both ground state hyperfine splitting levels, we need two optical bands. Dual frequency pumping is achieved when these two optical bands are directly on absorption resonances corresponding to from |1> to |3> and from |2> to |3>. Thus, the frequency separation between the two optical bands must be equal to the ground state hyperfine splitting frequency ν_{HF}. For this discussion, we will denote one optical band as the *main carrier band*, and the second band as the *sideband*. (For now, we will assume there are only two optical bands.) We will also assume that the sideband frequency is lower than that of the main carrier band by ν_{HF}. For clarity, when discussing absorption spectra in this section, we will use the frequency of the optical main carrier band as the reference.

The absorption spectrum obtained from DF optical pumping is more complicated than SF pumping. Assuming that the absorption spectrum is obtained by sweeping the frequencies of both optical bands simultaneously, and that the frequency separation between the two bands is always fixed, there can be occasions where only one optical band is on absorption resonance. Thus, the measured absorption spectrum would contain features from both SF and DF pumping.

Assuming that the two optical bands interrogating the alkali atoms are of equal intensity, their individual intensity I_{band} in relation to the total optical intensity I is therefore $I_{band}=I/2$. When we sweep the frequency (from low to high) of the lasing optical main band, the measured absorption spectrum contains three different cases of on-resonance optical pumping: (i) SF pumping of $|2>$ by the main carrier band; (ii) DF pumping by main carrier band and the sideband; (iii) SF pumping of $|1>$ by the sideband. We will account for all three features by a modified form of Eq. (3.28):

$$\tilde{\alpha}(\nu) = \frac{n_{Rb}\pi r_e cf\beta_2}{1+I/2I_{sat,2}}V(\nu-\nu_{0,F_2}) + \frac{n_{Rb}\pi r_e cf/2}{1+I/I_{sat,DF}}[V(\nu-\nu_{0,F_1})] + \frac{n_{Rb}\pi r_e cf\beta_1}{1+I/2I_{sat,1}}V(\nu-\nu_{0,F_1}-\nu_{HF}) . \quad (3.35)$$

The first and third terms in the right-hand-side of Eq. (3.35) account for the SF pumping spectral features. The third term has absorption resonance frequency at $\nu_{0,F_1}+\nu_{HF}$ because it is pumped by the optical sideband. Note that the optical saturation effects for the SF pumping spectral features are accounted for by an effective optical intensity of $I/2$ and the corresponding SF saturation intensities $I_{sat,1}$ and $I_{sat,2}$.

The second term in the right-hand-side of Eq. (3.35) accounts for the DF pumping spectral features, which occurs when the two absorption resonances are simultaneously pumped by the optical main carrier band and the optical sideband. The optical pump intensity for DF pumping is I, and this is accounted for in the denominator for saturation effects, where $I_{sat,DF}$ is the saturation intensity for DF pumping (see Table 3.1). Note that the factor of 1/2 in the numerator here comes from the absorption coefficient, and it is analogous to the factor of β_i for SF pumping (see Table 3.1 and Eq. (3.28)).

From Eq. (3.35), the saturated DF absorption coefficient is therefore

$$\tilde{\alpha}_{DF}(\nu) = \frac{n_{Rb}\pi r_e cf/2}{1+I/I_{sat,DF}}V(0) . \quad (3.36)$$

In addition to the treatment of absorption spectra, we need to make minor adjustments to Eq. (3.32) to adapt to the case of DF interrogation here. We need to use the transmission T_{DF} corresponding to DF absorption resonance. We also need to replace the unsaturated SF absorption coefficient α_i with α_{DF} (where $\alpha_{DF} = n_{Rb}\sigma/2$ as per Table 3.1). The saturation intensity must also be replaced with the appropriate one for DF interrogation (either π or $\sigma\pm$ polarized). The expression becomes

$$I = \frac{I_{sat,DF}[\ln(T_{DF})+\alpha_{DF}L_{cell}]}{1-T_{DF}} . \quad (3.37)$$

As stated previously, the capability to measure the excited state lifetime τ_{ex} and the spin relaxation time T_s comes from the dependence of saturation intensity $I_{sat,DF}$ to these relaxation times in π and

σ± polarized pumping. The procedure to measure these two relaxation lifetimes is similar to what is described in Section 3.4.3, except Eq. (3.37) is used here.

3.6　Measuring Excited State Lifetime with Pump-Probe Time-Resolved Optical Transmission

To properly understand the behavior of an alkali vapor cell saturable absorber, we need to know its excited state lifetime τ_{ex}. In cells with high pressure molecular buffer gases (N_2), the excited state lifetime may be quenched down to the order of 1 ns. (Such a short lifetime is necessary if it is to be used as a saturable absorber for modelocked laser.) With a large pressure broadening of the absorption line and hence small absorption cross-section (see Eq. (3.25)), in combination with short cell lengths (5 to 7 mm), measuring the τ_{ex} of such a cell with the standard technique of time-resolved fluorescence spectroscopy can be impractical because the photodetector must be both extremely sensitive and has sub-nanosecond temporal resolution.

We have developed an alternative technique to measure the excited state lifetime τ_{ex} of an alkali vapor cell. In this section, we will explain what this technique entails, and analyze it using the six-level model developed earlier in this chapter.

The new measurement method for τ_{ex} is a form of pump-probe technique. Initially, the alkali vapor cell is optically interrogated by two lasers. The first laser is the Pump Laser, and it operates in dual frequency (DF) π interrogation. Its total optical intensity is I_{pump}, and this is evenly divided into its two optical bands. The second laser is the Probe Laser, and it operates in single frequency (SF) π interrogation on one of the ground state hyperfine absorption lines, originating either from ground state |1> or |2>. The Probe Laser intensity is I_{probe}. The cell is optically interrogated by both lasers until the alkali atoms reach steady-state. When the system is at steady-state, it is perturbed by removing optical interrogation from the Pump Laser. The optical transmission of the Probe Laser is measured and analyzed in the time domain. The excited state lifetime τ_{ex} is extracted from the transmitted Probe Laser signal.

We now analyze this system using the six-level model. Specifically, we will solve the rate equations in Eq. (3.1) in both the steady-state case and nonsteady-state case. Furthermore, we will establish how the excited state lifetime τ_{ex} is extracted from the transmitted Probe Laser signal, and the necessary requirements for parameters such as Probe Laser intensity.

First, we solve the initial situation in the system, where the system is optically pumped by both Pump and Probe lasers until the alkali atoms are considered to be in steady-state. Given the steady condition $\partial \vec{n}(t)/\partial t = 0$, we therefore solve Eq. (3.1) for the populations $\vec{n}$. The steady-state solution, denoted as $\vec{n}_{init}$, will serve as the initial condition for the next step. The main purpose of this initial optical pumping step is to place a non-negligible portion of Rb atoms into the excited state.

Next, the system is perturbed by removing the Pump Laser. Because we intend to experimentally observe the system in the time domain, we therefore solve Eq. (3.1) in the nonsteady-state case

where $\partial \vec{n}(t)/\partial t \neq 0$. We note that as there is only optical π pumping in this system, the six rate equations in Eq. (3.1) can be collapsed into a system of three rate equations for the atomic populations of three energy levels, without distinguishing spin sub-levels. This is done by summing together the spin up and spin down levels of the same energy, and making the substitution $n_j = n_{j,\uparrow} + n_{j,\downarrow}$ for j=1,2,3.

The rate equations constitute a system of three differential equations of the form $\partial \vec{n}(t)/\partial t = \vec{A}\vec{n}(t) + \vec{B}$, where $\vec{A}$ is the 3×3 characteristics matrix, and $\vec{B}$ is the 3×1 nonhomogeneous component (note that it is not a function of time t). The solution has the form

$$\vec{n}(t) = \vec{K}_A \exp(-t/T_A) + \vec{K}_B \exp(-t/T_B) + \vec{K}_C \exp(-t/T_C) + \vec{K}_D, \tag{3.38}$$

where $\vec{K}_A$, $\vec{K}_B$, and $\vec{K}_C$ are the eigenvectors to matrix $\vec{A}$, and T_A, T_B, and T_C are the characteristic time constants. $\vec{K}_D$ is the solution to the nonhomogeneous system, and it is not a function of time t. Defining t=0 as the time when the pump laser is removed, we obtain the initial condition of $\vec{n}(0) = \vec{n}_{init}$.

The most important terms in Eq. (3.38) are the time constants. Their analytical expressions are

$$T_A = \tau_g,$$

$$T_B \approx \left(\tau_g^{-1} + (\hbar\omega/I_{probe}\sigma\beta_i)^{-1} \right)^{-1},$$

$$T_C \approx \left(\tau_{ex}^{-1} + \tau_g^{-1} + [\hbar\omega/I_{probe}\sigma(2-\beta_i)]^{-1} \right)^{-1}. \tag{3.39}$$

Here, I_{probe} is the Probe Laser intensity. The branching ratio β_i corresponds to the ground state $|i>$ (i=1 or 2) that the Probe Laser is interrogating ($|i>$ to $|3>$). The term $\hbar\omega$ is the photon energy, σ is the unsaturated absorption cross-section, and τ_g is the relaxation time between hyperfine ground state levels. The excited state lifetime τ_{ex} is the key term of interest.

From Eq. (3.39), we note that time constant T_C is a function of τ_{ex}. Note that when

$$\tau_g \gg \tau_{ex}, \text{ and } \hbar\omega/I_{probe}\sigma(2-\beta_i) \gg \tau_{ex}, \tag{3.40}$$

we obtain $T_C \approx \tau_{ex}$. This is the key to measuring the excited lifetime τ_{ex}: by properly tailoring τ_g and I_{probe} to fulfill the condition in Eq. (3.40), the transmitted signal of the Probe Laser through the alkali vapor cell after removal of the Pump Laser contains an exponential decay term with characteristic time constant of τ_{ex}.

We rewrite the second condition in Eq. (3.40) to obtain the optical intensity requirement for I_{probe}:

$$I_{probe} \ll \hbar\omega/\tau_{ex}\sigma(2-\beta_i). \tag{3.41}$$

The model presented here provides insights relevant to experiments beyond that of Eq. (3.40) and (3.41). Our model predicts when excited state lifetime τ_{ex} becomes shorter, the $\vec{K}_C$ term in Eq.

(3.39) also becomes smaller. The implication for measurements is that for alkali vapor cells with short τ_{ex}, the relative change in the transmitted optical signal of the Probe Laser will be small. This can be a problem because the *absolute* change in the transmitted optical signal intensity decreases with the *relative* change. On the other hand, when τ_{ex} becomes shorter, it is possible to fulfill the condition in Eq. (3.41) with a larger I_{probe}, which will increase the absolute change of the transmitted signal and offset the previously described penalty of smaller relative change.

From this particular insight in our model, we conclude that for some experimental measurements, we have to use high optical intensities for both pump and probe beams when measuring alkali vapor cells expected to have short τ_{ex}, such as the D_1 transition of a ^{85}Rb cell with 200 torr N_2 buffer gas where the expected τ_{ex} is on the order of 1 ns.

We experimentally apply this technique in Section 4.4 where its validity is verified. We also use it to measure a cell with high pressure of molecular (N_2) buffer gas, where τ_{ex} is reduced due to quenching effects.

3.7   Summary

In this chapter, we have developed the six-level rate equation model to describe the optical pumping and absorption behavior of alkali vapor atoms. We find that under different pumping configurations—single frequency or dual frequency, π or $\sigma\pm$—the saturation intensity I_{sat} of absorption is dependent on different relaxation time constants: relaxation time between ground states τ_g, spin relaxation T_s, excited state lifetime τ_{ex}. These effective time constants account for the effects of finite optical beam size interrogating an alkali vapor cell and wall collision effects.

We have presented the methods to analyze absorption spectra obtained using either single frequency or dual frequency optical interrogation. With help of the six-level model, we developed a method to find all three relaxation time constants from measured absorption spectra.

Finally, we propose a new technique to measure excited state lifetime τ_{ex}. This is a form of pump-probe time-resolved optical transmission measurement, which we developed by solving the rate equations in the six-level model. This method would allow us to measure the excited state lifetime in small cells with high pressure of molecular buffer gases.

The theoretical work that has been developed in this chapter serves as the basis for the experimental work detailed in chapters 4 and 5.

Chapter 4 Measurements of ^{85}Rb and ^{87}Rb Absorber at D_1 Line

In this chapter, we measure the important characteristics of the D_1 line (795 nm wavelength) in ^{85}Rb and ^{87}Rb that are relevant to the six-level rate equations model of alkali vapor cell absorber. We performed two types of measurements in this Chapter. In the first series of measurements, we studied the dependence of ground state relaxation time τ_g and spin relaxation time T_s on the buffer gas pressure, cell temperature and interrogation beam diameter. These measurements were made on a series of ^{87}Rb cells offering convenient set of Ar and N$_2$ buffer gas pressure values in the range 10 to 75 torr (see Table 2.2). In the second series of measurements, we examined the dependence of ^{85}Rb excited state lifetime τ_{ex} on the pressure of the molecular buffer gas using pump-probe technique proposed in Section 3.6. We experimentally confirmed the quenching effect of τ_{ex} in a cell with 200 torr of N$_2$ buffer gas, where natural lifetime was reduced from 28 ns down to 1 ns.

4.1 Experimental Methods

4.1.1 Single Frequency Optical Interrogation

The absorption cross-section, ground state relaxation time τ_g and spin relaxation time T_s parameters of the six-level rate equations model for Rb atoms are extracted from absorption spectrum. The optical interrogation source is a vertical cavity surface emitting laser (VCSEL) operating at 795 nm wavelength. For single frequency (SF) optical interrogation, each absorption spectrum is acquired by sweeping the lasing frequency of the VCSEL across the hyperfine structure in the D_1 absorption line. Lasing frequency sweep is obtained by sweeping the VCSEL drive current. The lasing frequency sweeping range is >20 GHz, and the sweeping rate is 17 Hz, low enough to be considered as steady-state interrogation.

Spin polarized (either σ+ or σ−) optical interrogation is obtained by using circularly polarized light, and turning on the magnetic field of 0.177 mT inside the cell holder (see Section 2.3.3 for details on the cell holder). Interrogation with π polarization is obtained by turning off the magnetic field without changing the polarization of the laser. By removing the magnetic field, the preferable orientation direction for the spin is no longer defined. After initial spin relaxation on the time scale set by T_s (<1ms), even though the interrogating light is circularly polarized, its interaction with the unpolarized alkali atoms is no different than how a linearly polarized light would interact with the atoms.

When performing spectroscopy on alkali vapor cells, the standard method to also perform spectroscopy on a reference cell. This reference cell should contain the same alkali atom as the cells being tested, and it should contain no buffer gas. Preferably, the reference cell and the cell of interest are simultaneously interrogated by splitting the optical source with a beamsplitter. The usefulness of a reference cell, beyond serving as a calibration guide for the optical source, is that one can measure the frequency shift in absorption resonances due to the buffer gas, an effect that can be significant under large buffer gas pressure. We do not use a reference cell in the spectroscopy measurements performed in this chapter as we do not care about the frequency shift effects here. (However, we do use a reference cell for measurements performed in Chapter 5 on the ^{85}Rb 5S$_{1/2}$-6P$_{3/2}$ line.)

An example of absorption spectrum measurement and treatment is illustrated in Fig. 4.1, where a ^{87}Rb cell undergoes SF π interrogation at intensity well below the saturation level. In Fig. 4.1(a), as a function of the relative change in the drive current of the VCSEL, we plot the measured cell transmission $T=I_{out}/I$, where I is the incident optical intensity on the cell and I_{out} is the transmitted intensity. In Fig. 4.1(b), we obtain the unsaturated absorption coefficient $\alpha=-\ln(T)/L_{cell}$, where L_{cell} is the vapor cell length (5 mm). Introducing in Eq. (3.23) the current tuning coefficient of the lasing frequency K, we obtain the following fitting function for the measured absorption spectrum

$$\alpha(J) = n_{Rb}\pi r_e cf\left[\beta_1\sum_{F'}s_{F_1F'}\cdot V(J\cdot K-v_{0,F_1F'}) + \beta_2\sum_{F'}s_{F_2F'}\cdot V(J\cdot K-v_{0,F_2F'})\right]. \tag{4.1}$$

where J the relative change in the laser drive current. For convenience, we use relative frequency, usually taking one of the absorption resonances as the reference $v=0$. Using the model Eq. (4.1), we fit the absorption spectrum in Fig. 4.1(b) to simultaneously obtain K and the pressure broadening linewidth Δv_L (note that $K<0$ for semiconductor lasers). From this, we can finally plot the absorption spectrum as a function of relative lasing frequency as seen in Fig. 4.1(c).
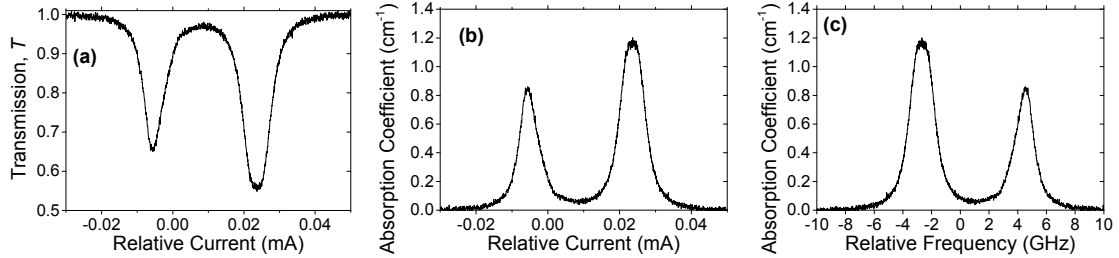
Fig. 4.1. Measurement and treatment of an example absorption spectrum obtained from ^{87}Rb cell with 75 torr of buffer gas (58% Ar, 42% N$_2$) at 66° C. Optical interrogation is SF π, and the intensity is 0.00412 mW/cm^2. (a) Cell transmission as a function of the VCSEL drive current. (b) Absorption coefficient vs current. Numerical fit with Eq. (4.1) yields the current tuning coefficient of the lasing frequency $K=-247$ GHz/mA and pressure broadening of the absorption linewidth $\Delta v_L=1.06$ GHz. (Fitting curve is not shown.) (c) The absorption spectrum is plotted as a function of the relative lasing frequency of the VCSEL.

4.1.2 Dual Frequency Optical Interrogation

For dual frequency (DF) optical interrogation, the optical spectrum of the interrogating optical beam must contain two optical bands with frequency separation equal to the ground state hyperfine split-

ting frequency ν_{HF}. This is achieved by modulating the VCSEL drive current from a radio frequency synthesizer (Agilent E8276D) through a bias-T. At modulation frequency ν_{HF}, two 1st order optical sidebands are generated (Fig. 4.2). The relative intensity of the sidebands with respect to the main carrier band can be adjusted by changing the power of radio frequency (RF) modulation.

We obtain DF interrogation when the main carrier band is on one hyperfine transition, and either the +1 or −1 order sideband is on the other resonance. However, because the interrogating laser has three optical bands, the absorption spectrum model in Eq. (3.35) and large signal absorption in Eq. (3.37) from Section 3.5 must be modified.

Firstly, we must recognize that the measured transmission of the cell, $T_{DF,meas}=I_{out}/I$, has contributions from all modulation sidebands. In the case where two optical bands simultaneously interrogate two hyperfine absorption lines, the third optical band is out of any atomic absorption resonance. It is not affected by the alkali vapor cell and we need to remove its contribution from the measured transmission $T_{DF,meas}$ in order to recover the DF resonant absorption of the cell.

Let us denote the total incident intensity on the cell as I, and the total intensity of the two optical bands interrogating two hyperfine absorption lines as ζI, where $0<\zeta<1$. In the ideal case, each optical band has intensity $I/3$, therefore $\zeta=2/3$. (Deviation from the value of 2/3 occurs when I is not evenly distributed across the three optical bands or if there exists higher order optical sidebands.) We now distinguish between the measured transmission of the cell $T_{DF,meas}$ and the transmission $T_{DF,atom}$ that would have been measured if there are only two resonant optical bands of overall intensity ζI :

$$T_{DF,meas} = \zeta \cdot T_{DF,atom} + (1 - \zeta). \tag{4.2}$$

Following from Eq. (4.2), we modify Eq. (3.37) and obtain

$$\zeta I = \frac{I_{sat,DF}[\ln(T_{DF,atom}) + \alpha_{DF} L_{cell}]}{1 - T_{DF,atom}} = \frac{I_{sat,DF}[\ln(\frac{T_{DF,meas}}{\zeta} - 1 + \zeta) + \alpha_{DF} L_{cell}]}{1 - (\frac{T_{DF,meas}}{\zeta} - 1 + \zeta)} . \tag{4.3}$$

where α_{DF} is the small signal absorption coefficient under DF interrogation ($\alpha_{DF} = n_{Rb}\sigma/2$). Numerical fit of experimentally measured dependence for $T_{DF,meas}$ at different incident intensity I with Eq. (4.3) allows one to extract the saturation intensity $I_{sat,DF}$ and, hence, the relaxation time constants.

The second issue to recognize from using an optical source with three optical bands instead of two bands is that the measured absorption spectrum is also modified and Eq. (3.35) no longer applies. When we sweep the optical frequency (from low to high) of the main carrier band, the measured absorption spectrum contains four different cases of on-resonance optical interrogation: (i) SF interrogation of |2> by the +1 sideband; (ii) DF interrogation by main carrier band and +1 sideband; (iii) DF interrogation by main carrier band and −1 sideband; (iv) SF interrogation of |1> by the −1 sideband:

$$\tilde{\alpha}(v) = n_{Rb}\tilde{\sigma}(v) = \frac{n_{Rb}\pi r_e c f \beta_2}{1+(1-\zeta)I/I_{sat,2}}V(v - v_{0,F_2} + v_{HF})$$

$$+ \frac{n_{Rb}\pi r_e c f /2}{1+\zeta I/I_{sat,DF}}[V(v - v_{0,F_2}) + V(v - v_{0,F_1})]$$

$$+ \frac{n_{Rb}\pi r_e c f \beta_1}{1+(1-\zeta)I/I_{sat,1}}V(v - v_{0,F_1} - v_{HF})$$

$$\text{(4.4)}$$

We generate optical sidebands by modulating the VCSEL drive current with a RF synthesizer at RF frequency v_{RF} equal to the ground state hyperfine frequency v_{HF}, which is 6.835 GHz for [87]Rb. We analyze the VCSEL optical spectrum with a scanning Fabry-Perot interferometer (Toptica FPI 100-750-3V0). The injected RF power is adjusted such that the main carrier band and the 1st order modulation sidebands are at nearly equal intensity as seen in Fig. 4.2. Note that this interferometer has free spectra range (FSR) of 1 GHz, which is smaller than the modulation frequency v_{RF} of 6.835 GHz. This means the observed spectrum contains aliasing effects. Despite this, we can still clearly resolve the relative strengths of the main carrier band and the 1st order sidebands as seen in Fig. 4.2. We obtain nearly equal intensity between main carrier band and each 1st order sideband at RF power of −10.7 dBm.
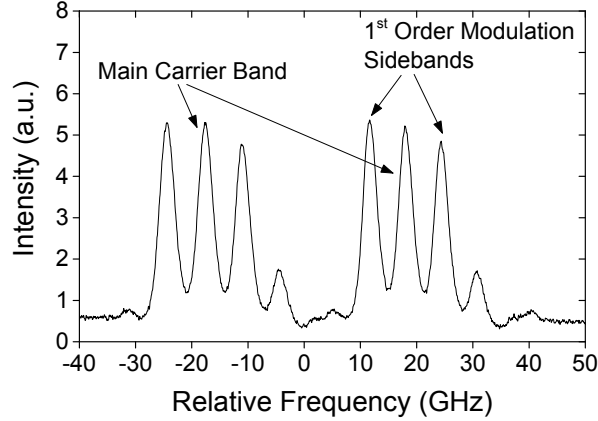
Fig. 4.2. VCSEL optical spectrum under current modulation at 6.835 GHz and −10.7 dBm injected RF power as measured by a scanning Fabry-Perot interferometer with FSR of 1 GHz. The RF power used to modulate the VCSEL was adjusted to obtain nearly equal amplitude of main carrier band and 1st order modulation sidebands. Note that 2nd order modulation sidebands can be seen in the optical spectrum because of high RF power.

To measure the absorption spectra, we modulate the VCSEL drive current in both RF and near DC frequencies. Current modulation at near DC frequency sweeps the frequency of the main carrier band and modulation sidebands across the absorption features of the alkali atom absorption line. We use the same low frequency current modulation here as we do for SF measurements, which is 17 Hz.

We give an example absorption spectra acquired with RF modulated VCSEL in Fig. 4.3, where we plot the measured transmission as a function of relative frequency. These two spectra were acquired under π and spin polarized interrogation. One can see the absorption features due to two optical bands on absorption resonance (DF) as well as the features due to SF absorption resonance from 1st order sidebands. The two central absorption lines at approximately 0 GHz and −6.8 GHz and la-

beled as "|1&2> to |3>" in the absorption spectra are acquired under conditions of DF optical inter-
rogation. The absorption lines at +6.8 GHz and −13.6 GHz are due to SF optical interrogation by
the −1 and +1 order sidebands, respectively. The absorption features at +13.6 and −20.4 GHz are
due to SF interrogation by 2nd order optical sidebands.
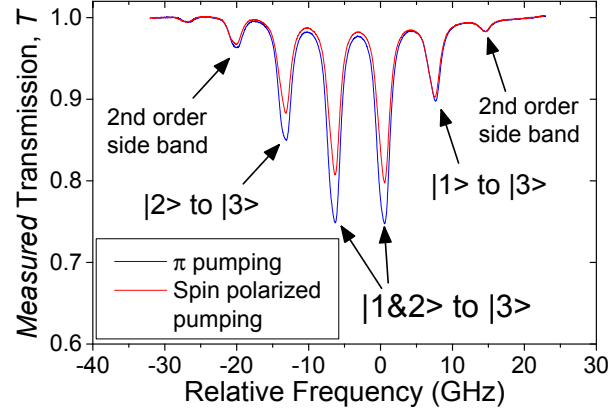
Fig. 4.3. Absorption spectra, in measured transmission vs. relative frequency, of ^{87}Rb cell with 75 torr buffer gas (58%
Ar, 42% N$_2$) under DF optical interrogation for π and spin polarized pumping at 0.507 mW/cm^2 intensity. The cell tem-
perature is 65.6° C. The VCSEL drive current is RF modulated at 6.835 GHz at −10.7 dBm power.

4.2 Beam Size Effect on Relaxation Time Constants τ_g and T$_s$ in ^{87}Rb Vapor Cell

In Section 3.3, we presented our model for the optical beam size effect on the relaxation time be-
tween hyperfine splitting ground states τ_g and spin relaxation time T_s. Here, we experimentally con-
firm our model on the ^{87}Rb cell with 75 torr of Ar and N$_2$ buffer gases (see Section 2.3.3 and Table
2.2) in the D_1 transition.

4.2.1 Model Parameters

There are two parameters in the model presented in Section 3.3 that must be calculated. These are
the bulk spin relaxation time $T_{s,bulk}$ and the diffusion coefficient D_{Rb}.

For $T_{s,bulk}$, we begin with the expression

$$T_{s,bulk}^{-1} = \gamma_{ex} + \gamma_{sd} ,$$

(4.5)

where γ_{ex} and γ_{sd} are the spin exchange and spin destruction rates, respectively. Spin exchange is the
effect where the electron spin polarization of alkali atoms (^{87}Rb, in our case) is transferred to the
nuclear spin of noble gas atoms (Ar) via collision. We treat the spin polarization of the alkali atom
as being lost in the process. The expression for γ_{ex} is

$$\gamma_{ex} = \sigma_{ex} n_{Ar} \sqrt{\frac{8RT_{cell}}{\pi} \left(\frac{1}{M_{Rb}} + \frac{1}{M_{Ar}} \right)} \; , \tag{4.6}$$

where σ_{ex} is the spin exchange cross-section between Rb and Ar, n_{Ar} is the Ar population density, R is the gas constant value (8.314 J/mol·K), T_{cell} is the Rb cell temperature, M_{Rb} is the molar mass of ^{87}Rb (86.9 g/mol), and M_{Ar} is the molar mass of Ar (39.9 g/mol). This exchange term applies only to noble gas isotopes with uneven nuclear spin, which in the case of Ar are all unstable isotopes. Nevertheless, as can be seen from spin exchange and spin destruction cross- sections in Table 4.1, this term is at least two orders of magnitude smaller than spin destruction rate in Rb-Ar collisions.

Spin destruction is simply the loss of spin polarization of the alkali atoms via collision with other atoms, including buffer gas atoms/molecules as well as collision with other alkali atoms. The expression for spin destruction rate γ_{sd} is

$$\gamma_{sd} = \sigma_{sd,1} n_{Rb} \sqrt{\frac{8RT_{cell}}{\pi} \frac{2}{M_{Rb}}} + \sigma_{sd,2} n_{N2} \sqrt{\frac{8RT_{cell}}{\pi} \left(\frac{1}{M_{Rb}} + \frac{1}{M_{N2}} \right)} + \sigma_{sd,3} n_{Ar} \sqrt{\frac{8RT_{cell}}{\pi} \left(\frac{1}{M_{Rb}} + \frac{1}{M_{Ar}} \right)} \; , \tag{4.7}$$

where $\sigma_{sd,1}$ is the spin destruction cross-section between Rb and Rb, $\sigma_{sd,2}$ is the spin destruction cross-section between Rb and N_2, $\sigma_{sd,3}$ is the spin destruction cross-section between Rb and Ar, and M_{N2} is the molar mass of N_2 (28 g/mol). The terms n_{Rb}, n_{N2}, and n_{Ar} are the population densities of Rb, N_2, and Ar, respectively.

We summarize the literature values of spin exchange and spin destruction cross-sections in Table 4.1. We note that at typical operating temperatures of this research, we have $\gamma_{sd} \gg \gamma_{ex}$.

σ_{ex} Spin Exchange, Rb-Ar	2×10^{-23} cm^2 [39]
$\sigma_{sd,1}$ Spin Destruction, Rb-Rb	9×10^{-18} cm^2 [47]
$\sigma_{sd,2}$ Spin Destruction, Rb-N_2	1.2×10^{-22} cm^2 [47]
$\sigma_{sd,3}$ Spin Destruction, Rb-Ar	1×10^{-21} cm^2 [39]

Table 4.1. Summary of cross-sections for spin exchange and spin destruction used in our model.

For diffusion coefficient D_{Rb}, the overall expression is [48], [49]

$$D_{Rb}^{-1} = D_1^{-1} + D_2^{-1} + D_3^{-1} , \tag{4.8}$$

where D_1 is the diffusion coefficient of Rb through Rb, D_2 is the diffusion coefficient of Rb through N_2, and D_3 is the diffusion coefficient of Rb through Ar. The individual diffusion coefficients take the form [50]

$$D_1 = \frac{3\pi}{8 n_{Rb} \sigma_{scatter,1}} \sqrt{\frac{8 R T_{cell}}{\pi} \left(\frac{2}{M_{Rb}} \right)} \ ,$$

$$D_2 = \frac{3\pi}{8 n_{Rb} \sigma_{scatter,2}} \sqrt{\frac{8 R T_{cell}}{\pi} \left(\frac{1}{M_{Rb}} + \frac{1}{M_{N2}} \right)} \ ,$$

$$D_3 = \frac{3\pi}{8 n_{Rb} \sigma_{scatter,3}} \sqrt{\frac{8 R T_{cell}}{\pi} \left(\frac{1}{M_{Rb}} + \frac{1}{M_{Ar}} \right)} \ . \tag{4.9}$$

Here, $\sigma_{scatter,k}$ are the scattering cross-sections of Rb through Rb, N_2, and Ar for k=1,2,3, respectively. The coefficient values for $D_2 = 0.33$ cm^2/s and $D_3 = 0.4$ cm^2/s at 273 K can be found in [27], and this allows us to calculate the scattering cross-sections for Eq. (4.9). We summarize this in Table 4.2. (We note that the contribution from Rb-Rb scattering is small compared to the other two terms.)

$\sigma_{scatter,1}$ **Scattering Cross-Section, Rb-Rb**	1.15×10^{-14} cm^2
$\sigma_{scatter,2}$ **Scattering Cross-Section, Rb-N$_2$**	6.93×10^{-15} cm^2
$\sigma_{scatter,3}$ **Scattering Cross-Section, Rb-Ar**	5.05×10^{-15} cm^2

Table 4.2. Summary of scattering cross-section values we use to calculate diffusion coefficient D_{Rb} for our model.

With the parameter values given in Tables 4.1 and 4.2, we can now use the model presented in Section 3.3 to calculate the relaxation lifetimes τ_g and T_s.

4.2.2 Measured and Modeled Relaxation Time Constants

In experiment, we obtain optical interrogation beams of different sizes by placing pinhole apertures of different diameters in front of the cell. The size of the optical beam incident on the Rb vapor cell is measured using a beam profiler (Thorlabs BP209-IR). We interrogated the ^{87}Rb cell with optical beams at four different diameters: 2.0 mm, 1.32 mm, 0.50 mm, and 0.41 mm.

For each optical beam size, we perform π and σ polarized *single frequency* (SF) interrogation at different optical pump intensities I and measure the absorption spectra. One series of measured absorption spectra is presented in Fig. 4.4. We labeled each transition as $F_g=j$, where j is the quantum number F of that particular ground state hyperfine level.
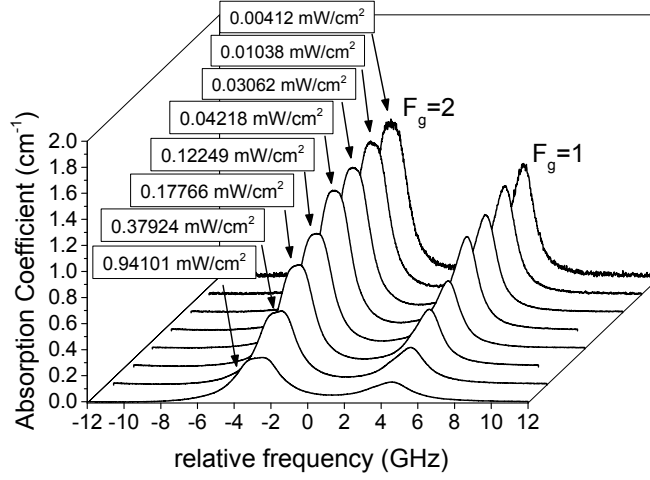
Fig. 4.4. Measured absorption spectra, calculated from measured transmission $T(v)$ using expression $-\ln[T(v)]/L_{cell}$, at different intensities of ^{87}Rb cell with 75 torr of buffer gas (58% Ar, 42% N_2) at cell temperature of 65.6° C. Cell length L_{cell} is 5 mm. Optical interrogation is SF π. The optical beam diameter is 2.0 mm.

From each series of absorption spectra, we measure the on-resonance absorption coefficients (saturated and unsaturated). Figure 4.5 plots, for beam diameter of 2.0 mm, the measured absorption coefficients as a function of interrogating optical intensity I for both π and spin polarized pumping on both hyperfine lines F_g=1 and 2.
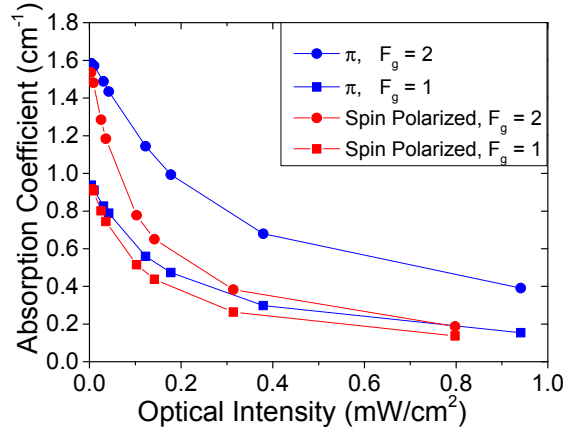
Fig. 4.5. Measured absorption coefficient vs. optical intensity for SF π and spin polarized optical interrogation. The optical beam diameter is 2.0 mm. The cell temperature is 65.6° C. (58% Ar, 42% N_2) Note that the data series for π interrogation comes from Fig. 4.4.

For data series such as those in Fig. 4.5, we then use the method detailed in Section 3.4 to extract the ground state relaxation time τ_g and spin relaxation time T_s. We repeat these measurements for several different beam diameters in order to observe the effect of the optical beam size on these relaxation times.

Figure 4.6 plots the measured relaxation times τ_g and T_s as a function of the optical beam diameter (points). We obtain good agreement between the measured T_s and the values calculated from our model (dashed line). Recall that our model calculates T_s using literature parameters (see Section

4.2.1), and that there are no terms that have been varied in order to obtain agreement with measurement. Therefore, we view this as an important validation for our model.
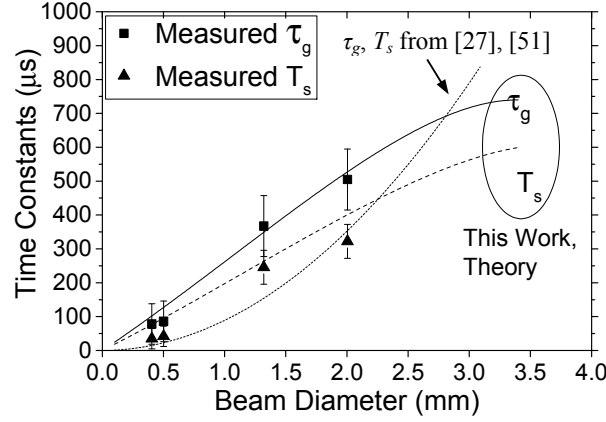
Fig. 4.6. Experimentally measured (points) time constants τ_g and T_s for ^{87}Rb cell with 75 torr buffer gas (58% Ar, 42% N$_2$). We obtain good agreement between the measured values and our model (solid and dashed lines). The wall collisional time constants calculated using traditional expressions found in literature [27], [51] (dotted line) have poor agreement with our measurement.

We next use our model to calculate τ_g. As noted in Section 3.3.3, our model calculates τ_g by using a slow down factor η $(0<\eta<1)$, and that η is effectively a fitting parameter. We obtain good agreement between measured τ_g for this cell and our model when $\eta=0.75$.

Finally, we calculate and plot the dependence of wall relaxation time on optical beam diameter using a model from existing literature (dotted curve), whose expression is given in Eq. (3.15) and found in [27], [51]. One can see that there is significant discrepancy with the measured data in both absolute value and in its trend as a function of beam diameter.

4.2.3 Spin Polarization in ^{87}Rb Cells

In the course of research performed in this dissertation, we have arrived to the conclusion that we do not need to use the push-pull interrogation approach in order to realize our targeted atomic clock, which will be based on modelocked laser operation. Therefore, we do not need to use spin polarized interrogation of the alkali atoms. Nonetheless, the six-level model we have established in Chapter 3 can be used to analyze spin polarization, and this can be a useful tool for use in other area of research.

Having measured relaxation times τ_g and T_s in ^{87}Rb cells, we estimate the spin polarization of alkali atoms, P_{Rb}, under steady-state spin polarized optical pumping by using the six-level model presented in Section 3.2. The expressions for spin polarization under SF and DF spin polarized pumping are shown in Table 3.1, which we use to estimate the spin polarization of alkali atoms P_{Rb} at a specific optical intensity or to obtain the asymptotic value for the maximum possible P_{Rb} under pumping at optical intensities that are much higher than saturation intensity I_{sat}.

In Fig. 4.7(a), we plot the spin polarization $|P_{Rb}|$ as a function of intensity for the ^{87}Rb cell with 75 torr buffer gas under SF spin polarized pumping. Spin polarization was calculated using τ_g and T_s that were measured and at intensities that were used in experiments. Note that since achieving high spin polarization was not the goal during measurements (the goal was to measure relaxation times), higher optical intensities were not used. In Fig. 4.7(b), we plot the same thing for DF spin polarized pumping of ^{87}Rb cells with 75, 22.5, and 10 torr buffer gas.

Using theoretically calculated τ_g and T_s, we plot the maximum possible $|P_{Rb}|$ for our ^{87}Rb cell when pumped from ground state $F_g=2$ as a function of beam diameter in Fig. 4.8(a). One can see that for SF spin polarized pumping, the maximum spin polarization achievable at high optical power increases with the pump beam diameter. This is due to decreasing ratio τ_g/T_s. Our model predicts that for ^{87}Rb, the maximum possible $|P_{Rb}|$ under SF spin polarized pumping is 47% for hyperfine ground state $F_g=2$, or 24% for $F_g=1$. The hyperfine ground state relaxation is the dominant mechanism for limiting the maximum achievable spin polarization under narrowband SF spin polarized pumping.

Under dual frequency spin polarized pumping, the calculated maximum possible $|P_{Rb}|$ is 100% (the same as that calculated for broadband spin polarized pumping using traditional models). In Fig. 4.8(b), we plot $|P_{Rb}|$ as a function of beam diameter under *fixed optical pump intensity* of 50 mW/cm^2. We find that for dual frequency spin-polarized pumping, it is favorable to use pump beam with larger diameter, too.

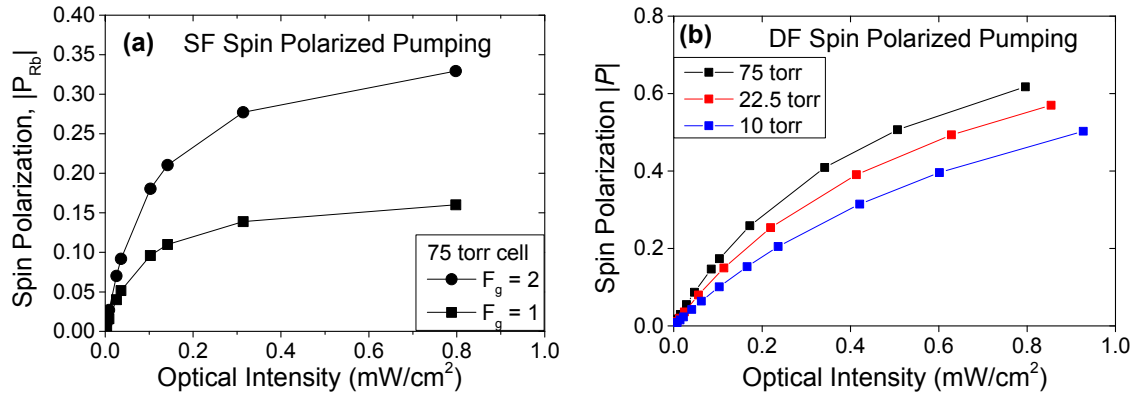Fig. 4.7. Spin polarization $|P_{Rb}|$ is plotted as a function of optical intensity for (a) ^{87}Rb cell with 75 torr buffer gas (58% Ar, 42% N$_2$) under SF spin polarized pumping, and (b) ^{87}Rb cell with 75, 22.5, and 10 torr buffer gas under DF spin polarized pumping. Measurement temperature is 65.6° C. The values of $|P_{Rb}|$ are calculated using experimentally measured τ_g and T_s.
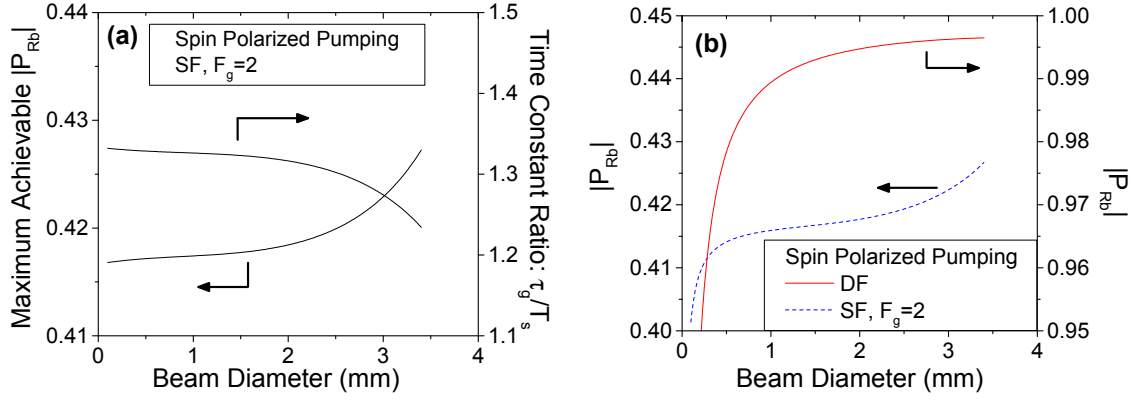
Fig. 4.8. ^{87}Rb cell with 75 torr buffer gas (58% Ar, 42% N$_2$), at temperature 65.6° C. (a) Maximum possible $|P_{Rb}|$ vs. optical beam diameter under SF spin polarized pumping from F_g=2. We also plotted the ratio of τ_g to T_s. (b) Spin polarization $|P_{Rb}|$, under fixed optical pump intensity of 50 mW/cm^2, as a function of optical beam diameter for SF and DF spin polarized pumping. Note: $|P_{Rb}|$ was calculated using theoretically predicted τ_g to T_s.

The advantages of using DF spin polarized pumping over SF pumping schemes in obtaining high degrees of alkali atom spin polarization are very clear from Fig. 4.7 and 4.8. Note that DF optical pumping of alkali atoms has been used as early as the 1970s using dye lasers [52]. With modern day semiconductor lasers that have high modulation bandwidths (e.g. VCSELs), there is no reason not to use DF optical pumping if obtaining high polarization degree of alkali atoms is the goal.

4.3   Buffer Gas Pressure Effect on τ_g and T_s in ^{87}Rb Vapor Cell

Dual frequency (DF) optical pumping provides another method to measure the spin relaxation time T_s. In this section, we compare the T_s measured using single frequency (SF) pumping and DF pumping at different buffer gas pressure in the cell.

Example ^{87}Rb absorption spectra acquired under interrogation by VCSEL with RF modulation were shown in Fig. 4.3 in Section 4.1.2. Here, we measure these absorption spectra at a series of different intensities I under DF spin polarized pumping. All measurements were made with fixed optical beam diameter of 2.0 mm. We interrogated three ^{87}Rb cells, with buffer gas pressures of 75, 22.5, and 10 torr (58% Ar, 42% N$_2$). From each spectrum, we obtain the *measured* transmission under DF pumping $T_{DF,meas}$. In Fig. 4.9, we plot the DF absorption coefficient, calculated from measured $T_{DF,meas}$ using expression $-\ln(T_{DF,meas})/L_{cell}$, as a function of interrogation intensity I for each cell.

We then repeat absorption spectra measurements with SF interrogation in both π and σ polarized pumping for each cell. This way, we can extract spin relaxation time T_s from both SF and DF interrogation data and compare them. For SF pumping, the method used is detailed in Section 3.4.3, with Eq. (3.33) as the key expression for extracting T_s (and hyperfine ground state relaxation τ_g). For the DF pumping, method used is detailed in Section 3.5 and Section 4.1.2, with Eq. (4.3) as the key expression for extracting T_s. We summarized the measured τ_g and T_s in Table 4.3 alongside with the theoretically calculated values.
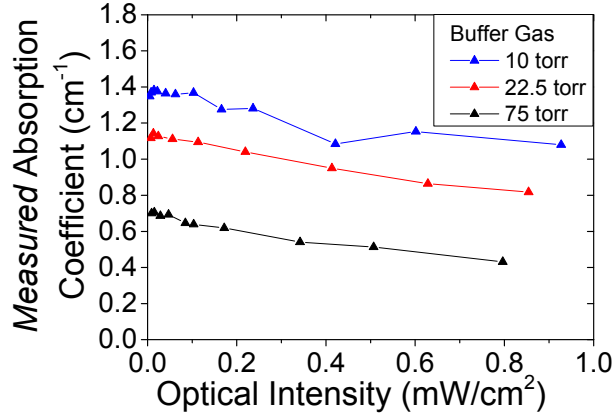
Fig. 4.9. Measured DF absorption coefficient as a function of optical intensity, under spin polarized pumping, for ^{87}Rb cells at buffer gas pressures of 10, 22.5, and 75 torr (58% Ar, 42% N$_2$). Cell length L_{cell} is 5 mm. Cell temperature is 65.6° C. The optical beam diameter is 2.0 mm.

Buffer gas pressure (torr)	τ_g (μs) Measured, SF	T_s (μs) Measured, SF	T_s (μs) Measured, DF	τ_g (μs) Theoretical	T_s (μs) Theoretical
75	505	332	376	526	400
22.5	179	47	128	158	126
10	91	35	71	70	56

Table 4.3. Summary of spin relaxation time T_s from measurements in either SF or DF optical interrogation and from theoretical calculations. For all measurements, optical beam diameter is 2.0 mm, and cell temperatures are 65.6° C. For theoretical calculations of τ_g, we use slow down factor η=0.75, same as what was used in Section 4.2.2.

For the ^{87}Rb cell with 75 torr total buffer gas pressure, our measured T_s from DF interrogation is in reasonable agreement with the value measured from SF interrogation. However, the discrepancy between experimentally measured T_s under SF and DF interrogation is significantly larger for cells with smaller buffer gas pressure. Interestingly, the T_s values measured from DF interrogation for all three cells are very close to the theoretically predicted ones. We observe a similar trend for ground state relaxation time τ_g, where the measured value for the 75 torr cell from SF interrogation is in good agreement with the theoretically predicted value, but the discrepancies between the measurement and theory become larger for cells with smaller buffer gas pressures.

We attribute the large discrepancy between spin relaxation time T_s measured with SF approach and the theoretically calculated value in the low-pressure cells to two factors. Firstly, larger errors are accumulated in the SF interrogation method since, for T_s, it involves making and analyzing two sets of measurements, one in π and another in spin polarized configuration. Secondly, our method of extracting absorption cross-section σ from absorption spectra is far more accurate for the high buffer gas pressure cell where there is significantly more intermixing between the excited state hyperfine splitting levels, and hence it behaves more similarly to our six-level model where the hyperfine splitting effect in the excited state is ignored. Note that for DF interrogation, the partial intermixing of the upper states is less crucial for the model validity.

4.4 Excited State Lifetime Quenching by Molecular Buffer Gas N_2 in the D_1 Line of ^{85}Rb

The natural lifetime of the excited state $5P_{1/2}$ in ^{85}Rb atoms is 27.6 ns [53], [54]. For operation as a saturable absorber in our modelocked laser, this lifetime must be made comparable to the carrier lifetime in the gain section QWs, which ranges from 1 to 2 ns for semiconductor lasers structures considered here. Quenching of the upper state lifetime is possible by using molecular buffer gas such as N_2 due to their vibrational energy structure yielding relatively large cross-sections for energy transfer from excited states in alkali atoms [1], [27]. Here we report on measurements of the upper state lifetime quenching in ^{85}Rb vapor cells.

According to Table 3.1, we find that under dual frequency (DF) π pumping, the saturation intensity $I_{sat,DF}$ is dependent on excited state lifetime τ_{ex}. In theory, one can measure τ_{ex} using the method detailed in Sections 3.5 and 4.1.2. However, because τ_{ex} (27.6 ns or shorter) is shorter than the other relaxation lifetimes τ_g and T_s (a few tens to a few hundreds of μs) by a few orders of magnitude, the saturation intensity under DF π pumping would be a few orders of magnitude larger than the saturation intensity under other optical pumping schemes. Semiconductor laser diodes with linewidth and noise characteristics suitable for spectroscopy do not necessarily retain these characteristics at high output powers (>100 mW), if they can reach it at all. We therefore use a different method to measure τ_{ex}.

We have experimentally measured the excited state lifetimes of ^{85}Rb cells with different buffer gas content using the model and technique proposed in Section 3.6. This measurement technique is a form of pump-probe time-resolved optical transmission experiment. A schematic of our measurement setup is given in Fig. 4.10.

We have used two lasers, a distributed feedback laser (DFB) and VCSEL, for interrogating an alkali vapor cell at 795 nm wavelength (D_1 transition in Rb atoms). All optical interrogations are done with π polarized beams. Here, the VCSEL is the SF Probe Laser and it is tuned to one of the hyperfine absorption lines of the alkali atoms. For all results presented, the resonance line is F_g=2. The VCSEL is always on, and its operating conditions are kept fixed throughout the experiment. We measure its time varying transmitted optical power through the alkali vapor cell with a high speed photodetector (EOT ET-2030A, 30 kHz to 1.2 GHz bandwidth) followed by a RF amplifier (RF Bay Inc. LNA-1450, 10 kHz to 1.45 GHz bandwidth). The DFB is the Pump Laser, and it operates at much higher optical intensities than the VCSEL. Before making data acquisition of the transmitted VCSEL power, the initial non-equilibrium atomic state has to be prepared. For this, the DFB laser drive current is modulated at 1.518 GHz, which is half of the ground state hyperfine splitting frequency of the ^{85}Rb atoms (3.036 GHz). This current modulation generates two 1st order optical modulation sidebands that are used for DF optical interrogation of both hyperfine ground states.
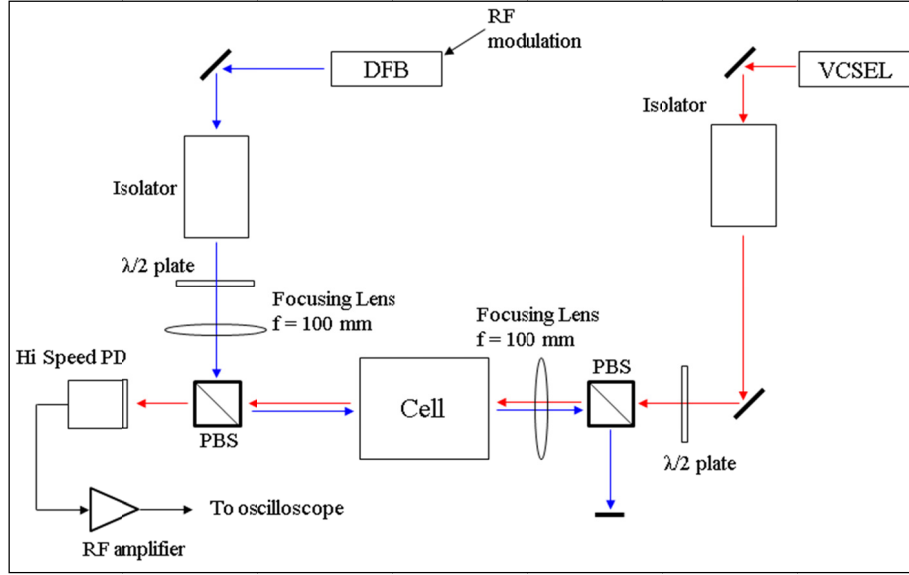
Fig. 4.10. Schematics of the experimental setup for measuring upper state lifetime τ_{ex}. Polarizing beam splitters (PBS) are used to spatially combine the two laser beams in the alkali vapor cell. Focusing lenses are used when measuring high buffer gas pressure cells with small τ_{ex} and are removed when measuring low buffer gas pressure cells. A high speed photodetector (PD) acquires the transmitted signal of the probe laser (VCSEL) for analysis.

Initially, the DFB laser injected with RF power at 6 to 7 dBm, where we maximize the intensity of each individual 1st order modulation sideband with respect to the main carrier band and the 2nd order modulation sidebands (with $v_{RF}=0.5v_{HF}$, DF pumping is done by the two 1st order modulation sideband). The DFB laser, along with the VCSEL, initially pumps the atoms into steady-state, where the DFB is performing DF pumping, and the VCSEL is performing SF interrogation.

The next step, as required by the method detailed in Section 3.6, is to perturb the system by instantaneously remove DF optical pumping by the DFB. This is performed by turning off the RF modulation of the drive current using a high speed RF switch (Mini-Circuits ZFSWA-2-45). Note that beside the generation of optical modulation sidebands, the injected RF power also produces an optical frequency shift of the DFB laser. At low current modulation frequency, the optical frequency shift would be a pure thermal effect. But at RF modulation, the optical frequency shift has a large contribution from the carrier density change. The removal of current modulation instantaneously shifts the DFB's lasing frequency by a few GHz, due to the carrier density change. As such, the DFB laser is no longer on absorption resonance, neither in DF nor in SF configuration. Effectively, at this moment, the DFB laser does not produce any optical pumping of the atoms into the excited state. The ensuing change in the transmitted signal of the probe beam from the VCSEL contains useful information about the decay of the excited state and allows us to measure the excited state lifetime τ_{ex}. By making sure our VCSEL intensity fulfills the requirement detailed in Eq. (3.41), the transmitted signal should decay with time constant τ_{ex} right after the removal of DF interrogation. On a long time scale, the cell transmission for the probe beam will approach the steady-state transmission for SF interrogation. This latter one is higher than that for the DF interrogation because a significant part of Rb atom is re-pumped into a second hyperfine ground state and thus excluded from interaction with SF probe beam.

As mentioned in Section 3.6, we need to use higher optical intensities when attempting to measure alkali vapor cells that are expected to have short τ_{ex}, such as the D_1 transition of a ^{85}Rb cell with 200 torr N_2 buffer gas where the expected τ_{ex} is on the order of 1 ns. Here, we obtain the high optical intensities by using focusing lenses as shown in Fig. 4.10. These focusing lenses are not used when measuring cells expected to have much longer τ_{ex}.

The measured time-resolved transmitted power through the ^{85}Rb cell with buffer gas of 200 torr N_2 is plotted in Fig. 4.11(a). In Fig. 4.11(b), we plot the simulated time varying transmission obtained by analytically solving the rates equations in our six-level model for this transit process with the same parameters as that of the experiment (e.g., pump and probe laser intensities, τ_{ex}).
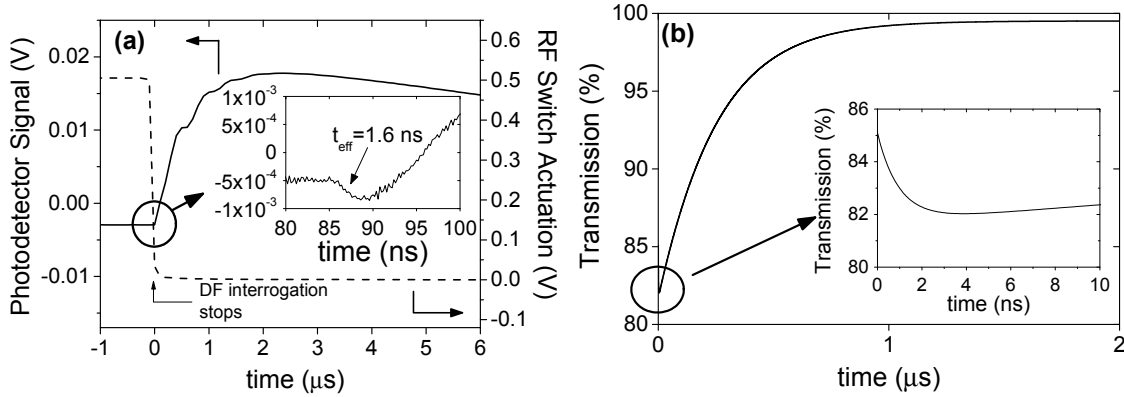

Fig. 4.11. (a) Measured time varying transmitted signal of the probe laser through the ^{85}Rb cell with 200 torr of N_2 buffer gas (solid curve). The cell temperature is 65° C. The dashed curve plots the voltage actuating the RF switch which turns on or off the VCSEL drive current modulation. The falling front, occurring at time t=86 ns, corresponds to the RF modulation (and hence DF interrogation) being turned off. The inset is the magnification of the circled region. (b) Simulated optical transmission through the cell.

In both experimental measurement and model simulation, right after switching off of the DF pump beam, the transmitted optical signal of the SF probe laser beam exhibits an onset of the rapid decay of the excited state with the time constant τ_{ex}, and then it begins to slowly increase. Note that experimental data are acquired using amplifier with low frequency cutoff of 30 kHz, and thus incapable of transmitting the DC component of the signal. As a consequence, the measured probe laser (VCSEL) intensity starts to decrease at time t=1.8 μs, while no such decrease is predicted by the model, where the transmission eventually reaches the steady-state value for SF π polarized optical interrogation with the probe beam.

From exponential decay fitting of the signal immediately after the removal of DF interrogation, the characteristic time constant t_{eff} is 1.60 ns. However, the actual lifetime of τ_{ex} should be shorter because the measured time constant contains non-negligible rise time components from our equipment. The oscilloscope (Agilent DSO7104B) used to acquire the waveform has a bandwidth BW of 1 GHz. Using the expression $t_r \approx 0.34/BW$, the oscilloscope is estimated to have rise time t_r of 350 ps, which is certainly significant compared to the measurement time scales involved.

To recover the actual lifetime of τ_{ex}, we need to remove the effects of finite rise time in our measurement instruments. We use the following treatment. Consider a waveform with the rise time of t_1.

When it passes through a system with the finite rise time t_2, the effective rise time t_{eff} of the waveform at the output of the system is [55]

$$t_{eff} = \frac{\sqrt{t_1 t_2}}{\left[\sqrt{\frac{(t_1^2 + t_2^2)^2}{4t_1^2 t_2^2} + 1} - \frac{t_1^2 + t_2^2}{2t_1 t_2} \right]^{1/2}} \, . \qquad (4.10)$$

In our case, we have measured t_{eff} (1.60 ns), and we know t_2 (350 ps). Therefore, we need to solve Eq. (4.10) for t_1:

$$t_1 = \frac{2t_2 t_{eff} (2t_2 t_{eff}^4 - 2t_2^3 t_{eff}^2)(t_2 - t_{eff})(t_2^2 + t_{eff}^2)(t_2 + t_{eff}) \sqrt{-\frac{1}{t_2^4 - t_{eff}^4}}}{4t_2^2 t_{eff}^6 - 4t_2^6 t_{eff}^2} \, . \qquad (4.11)$$

Using Eq. (4.11), we obtain t_1=1.53 ns. However, we note that there are additional instruments with finite rise times in our system, namely, the photodetector (BW=1.2 GHz) and RF amplifier (BW=1.45 GHz). Removing contributions from those two instruments, we obtain excited state lifetime τ_{ex} of 1.43 ns for the ^{85}Rb cell with 200 torr of N_2 buffer gas in the D_1 transition.

We also measured excited state lifetime of a ^{85}Rb cell with 6 torr of N_2 buffer gas and a cell without buffer gas. The measured lifetimes τ_{ex} are 17.6 ns and 29.5 ns, respectively. The last value is reasonably close to the literature value, which is 27.6 ns [53], [54]. One difficulty we encountered in measuring the cell without buffer gas is that the excited state hyperfine splitting levels are not well intermixed. When performing DF interrogation, the DFB laser must stay on relatively narrow absorption resonance lines. The discrepancy between measured and literature values can be attributed to the effects of DFB frequency drift over the course of the measurement.

We compare our measured τ_{ex} to a model that uses literature value for D_1 line quenching cross-section due collisions with N_2 molecules, given by the expression

$$\tau_{ex}^{-1} = \tau_{ex,0}^{-1} + \sigma_Q n_{N2} v_T \, . \qquad (4.12)$$

Here, $\tau_{ex,0}$ is the natural excited state lifetime (27.6 ns). n_{N2} is the population density of N_2 in the cell, and it is calculated from the buffer gas pressure using ideal gas law. v_T is the thermal velocity of ^{85}Rb, given by $v_T = (8RT_{cell}/\pi M_{Rb})^{1/2}$. The most important term is σ_Q, which is the quenching cross-section of N_2 with respect to Rb atomic lines. The value of σ_Q for N_2 on the Rb D_1 line is 50±12 Å^2 [56].

In Fig. 4.12, we plot the theoretical estimate of τ_{ex} as a function of cell buffer gas pressure (line) along with our measured values (points). While the theory slightly underestimates τ_{ex} with respect to measurement, the discrepancies are not so large as to render our calculations unusable.
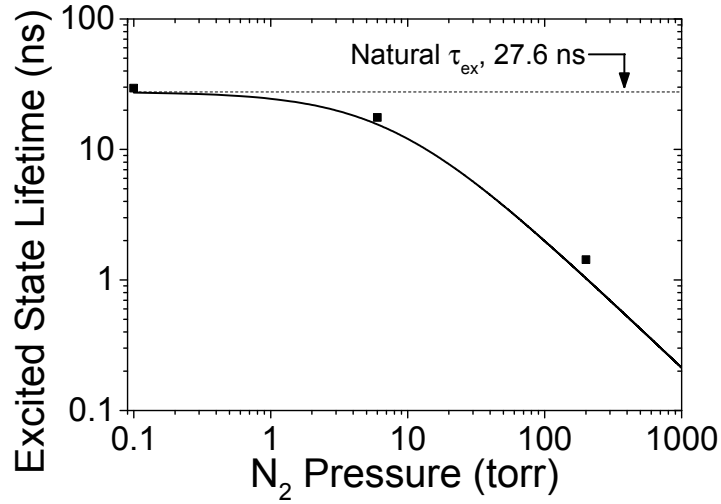
Fig. 4.12. Theoretical (solid line) and measured (points) excited state lifetime τ_{ex} as a function of N_2 buffer gas pressure at cell temperature of 65° C. For purpose of plotting, the measured τ_{ex} at 0 torr pressure is placed at 0.1 torr. Note that the value of N_2 pressure is rated for 24° C (manufacturer specification).

The good agreement between our τ_{ex} measurements and estimates based on literature values for excited state lifetime quenching attests to the validity of our measurement technique. To further confirm the validity of our technique, we measure the τ_{ex} of a [85]Rb cell with ~90 torr of He. Because He is an atomic buffer gas, there is no quenching effect on the excited state [1], [27], thus the τ_{ex} here should be the same as the unquenched value of 27.6 ns. We experimentally measure 28.3 ns, which is in agreement with our expectations.

The measured τ_{ex} of 1.43 ns for the 200 torr N_2 cell is an important parameter as we expect to use this [85]Rb cell as the saturable absorber in our modelocked laser system. Knowing this parameter is necessary for accurate modeling of modelocked laser behavior detailed in Chapter 7.

4.5   Summary

We have performed measurements of relaxation time constant between ground state hyperfine splitting levels τ_g and spin relaxation time T_s for different sizes of the optical beam interrogating a [87]Rb cell with high buffer gas pressure (75 torr) under *single frequency* π and spin polarized interrogation. There is a good agreement between the measured time constants and our theoretical predictions based on our model described in Section 3.3. In addition, we have performed *dual frequency* π and spin polarized interrogation on three different [87]Rb cells with varying buffer gas pressure, and the measured T_s here also matches well with our theoretical predictions.

The most important work presented in this Chapter is our measurement of the D_1 transition excited state lifetime τ_{ex} for a [85]Rb cell with 200 torr N_2 buffer gas. The measured τ_{ex} is 1.43 ns at 65° C. Our measurement technique is a form of pump-probe time-resolved optical transmission experiment that was first theoretically developed from the six-level model for alkali atom optical absorption in Section 3.6. We have confirmed the validity of this technique by comparing the measured τ_{ex} of

^{85}Rb cells at 200 torr N$_2$ buffer gas pressure, 6 torr N$_2$, and with no buffer gas. The obtained values are in good agreement with literature and theory.

From the work performed here, we have the information needed to accurately model a ^{85}Rb vapor cell as a saturable absorber in a modelocked laser system operating in the D_1 line.

Chapter 5   Characteristics of ^{85}Rb Absorber at 5S$_{1/2}$-6P$_{3/2}$ Line

Disclaimer: The material presented in Section 5.1 has been published in Optics Letters.[1]

Understanding the behaviors of ^{85}Rb absorption lines is necessary before we can use them as saturable absorbers in a modelocked laser system. While the D_1 (795 nm) and D_2 (780 nm) transitions have been deeply studied and characterized in various applications, little information is available about the 5S$_{1/2}$-6P$_{3/2}$ line at 420.18 nm wavelength.

5.1   Blue Wavelength External Cavity Diode Laser

In order to measure the characteristics of the ^{85}Rb 5S$_{1/2}$-6P$_{3/2}$ transition, we need a narrowband optical source with a continuous frequency tuning range several times larger than the ground state hyperfine splitting of 3.036 GHz. Such sources with precisely quoted noise performances are not readily available. In this dissertation, we have to first address the linewidth and noise aspects of such a source in order to achieve reliable results in spectroscopic studies of the ^{85}Rb 5S$_{1/2}$-6P$_{3/2}$ transition.

Currently, GaN-based DFBs [57], [58] and electrically pumped VCSELs [59], [60] are not yet adequately mature for atomic spectroscopy due to the challenges of group III-nitride epitaxy and processing. GaN-based external cavity diode lasers (ECDLs) are the most mature and common [61]–[66], and a few commercial models are available. Most of these ECDLs achieve free running lasing linewidth on the order of several MHz, though with external optical feedback from a high finesse resonator, the lasing linewidth can be as low as 7 kHz [66]. The typical mode hop free frequency tuning range is 20 to 30 GHz, though tuning range up to 110 GHz has been reported [65]. However, so far all available blue-violet tunable semiconductor lasers lack vital information on the white and flicker noise contributions in *frequency noise* and *relative intensity noise (RIN) spectra*. For majority of semiconductor lasers, the integral noise features such as the linewidth and RIN are defined by flicker ($1/f$) noise due to generation-recombination processes through recombination centers in defects (e.g. dislocations) [67]. (In this section, we use f instead of v to denote frequency due to engineering naming conventions for $1/f$ noise.) The dislocation density in as-grown GaN laser epitaxy is relatively high ($>1 \times 10^5$ cm^{-2} [68]) compared to the well matured conventional III-V materials ($<$1

---

[1] X. Zeng and D. L. Boïko, *Opt. Lett.*, vol. 39, no. 6, pp. 1685–1688, Mar. 2014.

$\times 10^4$ cm^{-2} [69]). Therefore, one would expect higher RIN and larger linewidth in group III-nitrides lasers compared to their conventional III-V counterparts.

Here, we report on $1/f$ frequency noise and RIN spectra measurements in our realization of an InGaN ECDL with lasing wavelength around 420 nm. We discuss challenges in atomic spectroscopy applications caused by defects and mode clustering effect in GaN lasers that we had to overcome in order to interrogate the $5S_{1/2}$-$6P_{3/2}$ transition in ^{85}Rb atoms.

The semiconductor gain chip used for the ECDL reported here is a commercial InGaN/GaN Fabry-Perot (FP) laser. No specific provision for antireflection coating of the cleaved facet was made. The laser diode is collimated by an aspheric lens with focal length 4.5 mm, and the beam diameters are 3.4 mm and 1.6 mm along the fast and slow axes, respectively. External cavity feedback is provided by a diffraction grating with 1800 grooves/mm installed in Littrow configuration. The grating is held on a kinematic mount with two piezoelectric actuators for alignment and wavelength tuning. All components are held in a physics package with thermoelectric temperature control. A photograph of the ECDL is given in Fig. 5.1.
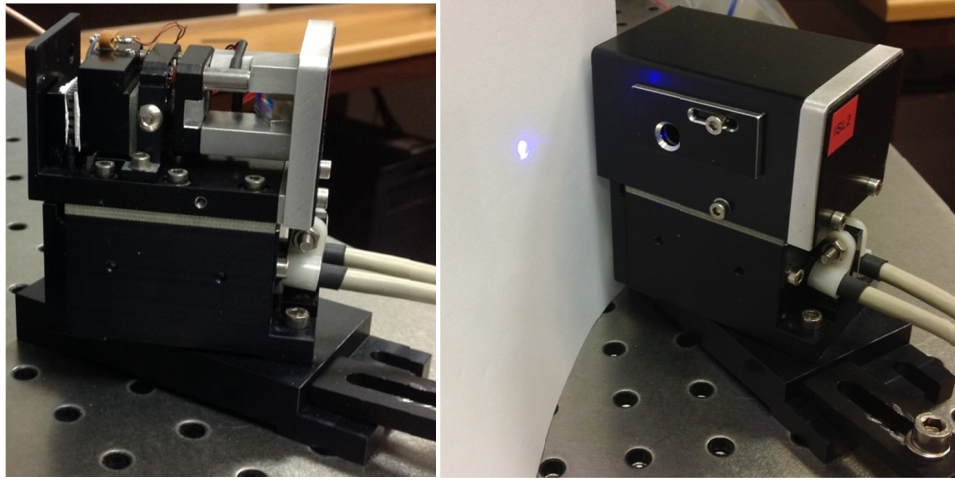
Fig. 5.1. (Left) Photograph of the ECDL laser with the packaging cover removed. The rainbow colored component is the optical grating used to tune the lasing wavelength. (Right) The ECDL with the packaging cover on. The circular hole is the output aperture for the lasing beam. Note the blue beam spot on the paper.

The fast axis of the laser diode is set perpendicular to the grating grooves, an orientation that yields the narrowest grating full-width at half-maximum (FWHM) bandwidth of 110 GHz (estimated). In this configuration, beam polarization is parallel to the optical grating's grooves, reaching first-order diffraction efficiency of ~40%. From subthreshold optical spectra in Fig. 5.2, FP modes of the free running (no external feedback) laser diode gain chip are separated by 56 GHz. Thus, the grating enables good selectivity of the lasing mode with respect to its adjacent side modes at ±56 GHz.

Group III-nitride ECDLs face severe challenges in obtaining lasing operation at the desired wavelength. Due to the mode clustering effect typically found in GaN-based laser diodes [70]–[73], uniform wavelength tuning is not always possible. The exact origin of the mode clustering is not well understood and is the subject of ongoing debates. To get an insight into its cause, we studied the evolution of the amplified spontaneous emission (ASE) with laser diode aging.

Fig. 5.2. Amplified spontaneous emission spectrum of free running GaN-based FP laser at 40 mA drive current (a) before and (b) after device aging.
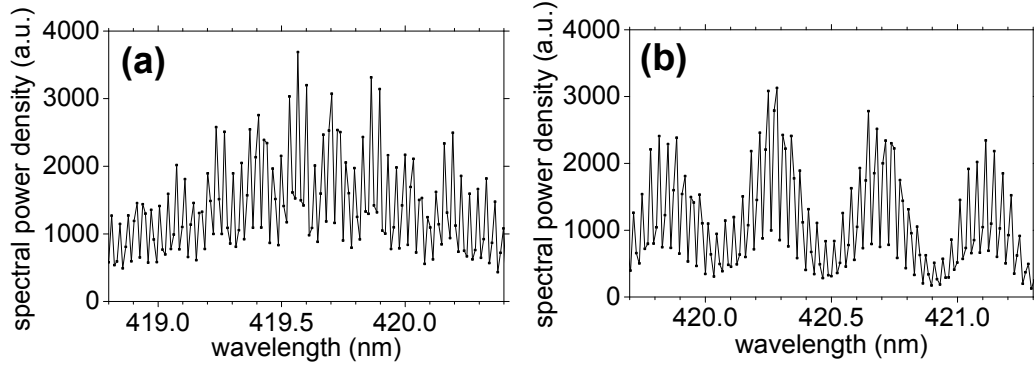
Figure 5.2 shows the ASE spectrum of the free running laser diode (a) before and (b) after several months of operation (59 mA, 32 °C). It exhibits periodic (0.2 to 0.4 nm) ripples in the spectral envelope of the cavity modes. Similar Fabry-Perot etalon features were observed in the photoluminescence spectrum of bulk GaN layers and attributed to backscattering from microcracks [73]. Here, we report that with aging of the laser chip, the ripple contrast in the ASE spectrum becomes more pronounced, and the ripple period increases.

The cleavage of diode laser optical facets may create microcracks near and parallel to the facet with spacing of several tens of microns [73]. The evolution of the ASE spectrum in Fig. 5.2 indicates the growth of microcracks in an aging device.

Indeed, in GaN laser epitaxy, initial dislocation density is high [68], causing performance degradation [74]. Dislocations may create seeds for microcracks [75], which grow with aging. Microcrack nucleation and propagation enables intrinsic stress release in the epitaxial film [76] and release of the stress and plastic deformations induced in the sample during dicing and facet cleavage. Ulterior stress release in the vicinity of facet of an aging device may lead to formation and propagation of new microcracks, leading to intracavity backscattering and retroreflections.

Intracavity FP etalon features in Fig. 5.2 were analyzed using the Hakki-Paoli model (also used in [73]) assuming a solitary backscattering defect near the laser output coupling facet. The model reveals that with device aging, the intensity of backscattered light coupled into the laser cavity mode increases from 0.014% to 0.021%. In Fig. 5.2(a), the effective FP etalon has thickness of ~140 μm; for the aged device in Fig. 5.2(b), the effective thickness is reduced to ~70 μm. This indeed can be interpreted as the propagation of a second microcrack defect, due to aging, in a location at half the distance away from the laser facet compare to the original defect location.

In free running operation above lasing threshold, FP etalon filtering prevents lasing of certain modes, leading to formation of large (0.2 nm width) inaccessible spectral gaps when laser current and/or temperature are continuously varied (Fig. 5.3). These gaps remain inaccessible even when an external grating feedback is introduced because it cannot compensate for the built-in intracavity mode filtering. Therefore, defects and mode clustering in GaN lasers can render atomic spectroscopy at the desired atomic lines impossible.

We overcome this challenge by careful choice of the free running laser diode operating current and temperature so that one of the mode clusters overlaps with the desired atomic transition (420.18 nm line of ^{85}Rb atoms in our case). After that, introduction of optical feedback from the grating matching the target wavelength provides efficient side mode filtering by the ECDL cavity. (All further results reported in this section are obtained with the aged laser.)
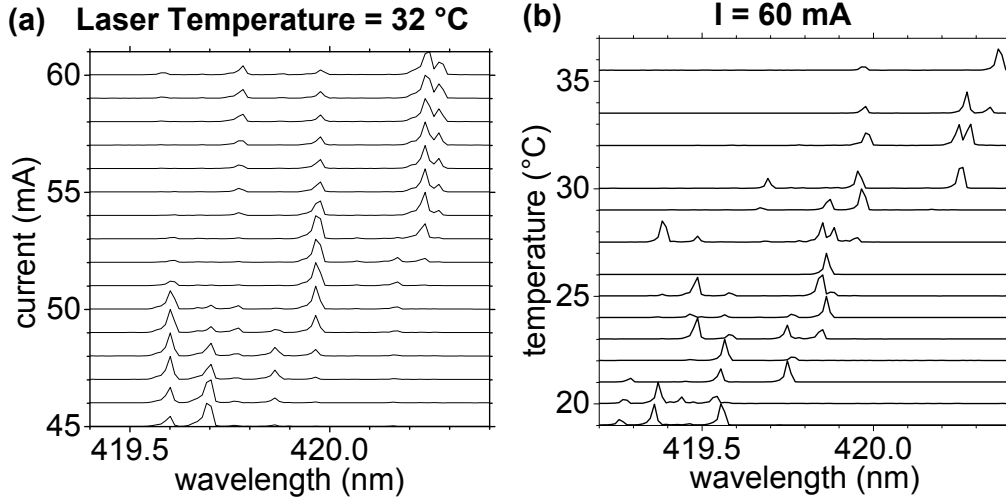
Figure 5.3. Normalized lasing spectra of the free running GaN laser: (a) fixed laser diode temperature, varying current; (b) fixed current, varying temperature. The spectra shown are shifted vertically by the value of the parameter indicated in the left axis. The calibration error of spectrometer is 0.07 nm.

Figure 5.4(a) shows the light-current (L-I) curves of the laser diode without external feedback (lasing threshold I_{th}=41 mA) and in ECDL configuration (I_{th}=33 mA). The ripples in the ECDL's L-I curve are caused by mode hopping effects. The ECDL can achieve output power of 13 mW at injection current of 60 mA (slope efficiency is 0.5 W/A). Figure 5.4(b) shows a superposition of several (but not exhaustive) single-mode ECDL lasing spectra. It demonstrates total wavelength tuning range of almost 7 nm achieved by changing the grating tilt angle while maintaining constant current and temperature. The wavelength tuning is discontinuous, with mode hops both within and across mode clusters.
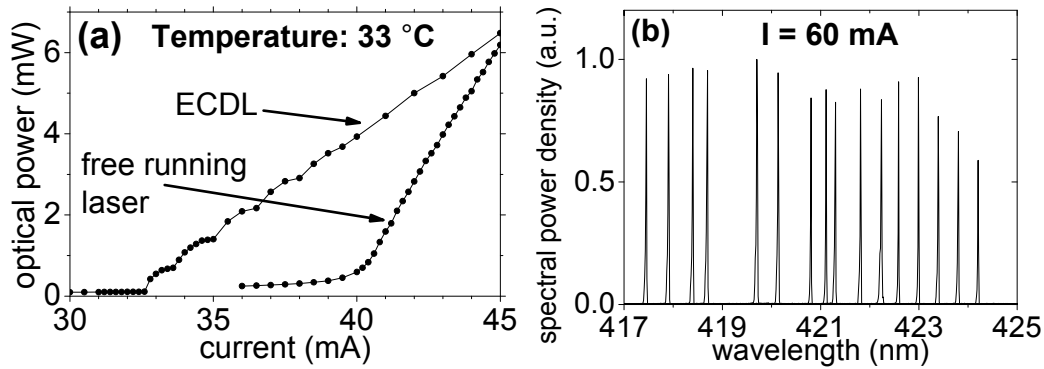
Figure 5.4. (a) L-I curves of the laser diode without external feedback and in ECDL configuration at 33 °C. (b) Wavelength tuning range is represented by a superposition of several single-mode lasing spectra. ECDL driving current is 60 mA.

To interrogate the hyperfine structure of alkali atoms, the ECDL lasing frequency must be continuously tunable over ~10 GHz range, which is achieved here through simultaneously changing the ECDL injection current to shift the lasing mode frequency of the free running laser and adjusting the external cavity length and grating tilt angle [65]. For this, a triangular wave modulation was applied to both the diode current and piezoelectric actuator voltage. After optimization of the modulation amplitudes, the mode hop free tuning range is measured by monitoring the laser power through a FP etalon with free spectral range (FSR) of 4.16 GHz and counting the number of regular light transmission resonances. The mode hops are identified by monitoring jumps in ECDL output power. Figure 5.5(a) shows a mode hop free tuning range of 29 GHz.

To measure the frequency noise spectrum, we first perform absorption spectroscopy measurements in a ^{85}Rb vapor cell of length L_{cell}=5 mm with 6 torr N_2 buffer gas. To detect the $5S_{1/2}$-$6P_{3/2}$ transition lines, the cell is heated to 100 °C temperature. The ECDL is driven near 60 mA while simultaneous triangular wave modulation of the current of 6 mA amplitude and of the piezoelectric actuator voltage allows for mode hop free frequency tuning over the hyperfine splitting of the ground state (3.036 GHz). Figure 5.5(b) plots the normalized transmission $T(\nu)$ as a function of the relative ECDL frequency. The absorption coefficient $\alpha n_{Rb} = -\ln[T(\nu)]/L_{cell}$ has FWHM linewidth of 1.18 GHz for each component. The absorption oscillator strength of f_{ij}=9.4×10^{-3} at the $5S_{1/2}$-$6P_{3/2}$ transition [46] is weaker by an order of magnitude compare to the D_1 (f_{ij} =0.34) or D_2 (f_{ij} =0.70) 5S-5P lines [28], hence the saturation intensity at 420 nm line is one order of magnitude higher. The absorption oscillator strength 9.9×10^{-3} calculated from the data in Fig. 5.5(b) is very close to the literature value, attesting that the measurements are done well below the saturation intensity level. More details on the absorption spectroscopy of this atomic transition can be found in Section 5.2.
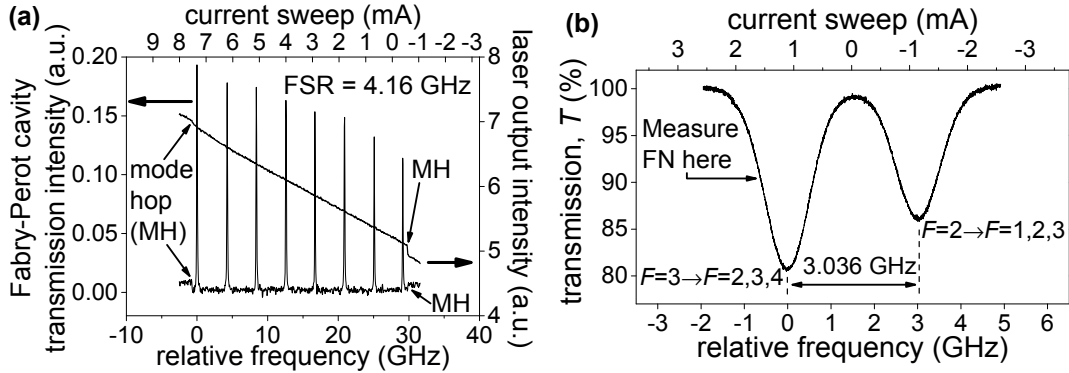
Figure 5.5. ECDL transmission spectrum, as a function of the drive current modulation (top axis) and relative frequency change (bottom axis), through (a) a FP etalon (left axis), plotted with output power (right axis), and (b) a ^{85}Rb cell with 6 torr N_2 buffer gas of 5 mm length in the $5S_{1/2}$-$6P_{3/2}$ transition (420.18 nm wavelength) at 100 °C cell temperature.

Frequency noise (FN) is measured by tuning the *free running* ECDL frequency (no frequency stabilization) to the slope of the ^{85}Rb absorption line, where FN is converted into intensity noise and is superimposed onto the normal laser intensity noise. Performing Fast Fourier Transform (FFT) on the intensity of the laser beam transmitted through the cell yields the sum of the frequency and intensity noise spectra. Note that the FFT data acquisition time is 5 s, so the eventual ECDL frequency drifts are negligible (~300 MHz for 1.5 hour). A second FFT measurement with the cell heating off (no atomic absorption and hence no frequency-amplitude conversion) yields the laser RIN.

Proper FN spectrum is finally obtained by subtracting contribution of the RIN FFT spectrum from the first measurement and dividing by the slope of frequency-amplitude transmission curve. The two measurements are separated by half an hour (the cooling time of the Rb vapor cell assembly) while the long-term stability of our current source and laser chip temperature controller is better than 10 μA and 5 mK, respectively. Such variations have no impact on measured RIN spectrum. As there is no frequency-amplitude conversion involved in the second measurement, the eventual frequency drifts are not significant.

The measured FN spectrum is plotted in Fig. 5.6(a) along with, for comparison, that of a *free running* commercial DFB laser used in atomic spectroscopy at 852 nm wavelength (D_2 line of ^{133}Cs atoms) and a 780 nm ECDL [77] *actively stabilized* at D_2 line in ^{85}Rb atoms. Discontinuities in our measured spectra are caused by technical limitations of the FFT spectrum analyzer (Stanford Research Systems SR770) requiring us to superimpose three separate noise spectra measured in the ranges 0.244-97.4 Hz, 50.8-1609 Hz, and 0.25-100 kHz. A few data points at the low frequency edge of each band (set by the resolution bandwidth) incorporate DC contribution and were discarded. The FN spikes from 0.2 to 2 kHz in our ECDL data are due to acoustic noise.

The FN power spectral density (PSD) in our 420 nm ECDL exhibit $1/f$ behavior until intersection with the line $8\ln(2)f/\pi^2$ [78], indicating that the linewidth (see below) is mainly defined by excessive frequency flicker noise [67]. White frequency noise due to amplified spontaneous emission ($\propto \Delta\nu_{res}^2/\lambda P_{out}$ [79]) is not significant. Despite the high dislocation density and mode clustering effects in GaN lasers, the FN PSD in our 420 nm ECDL is smaller by a factor of 30 than in commercial NIR DFB spectroscopic lasers. This can be attributed to longer cavity and hence narrower resonator bandwidth $\Delta\nu_{res}$ of an ECDL. This is also attested by noise in actively stabilized 780 nm ECDL from [77]. At Fourier frequency below 2 kHz, the frequency noise in this GaAlAs ECDL is reduced by the frequency locking servo loop of that laser. However, for Fourier frequency above 100 Hz and disregarding the acoustic noise spikes, our InGaN ECDL has lower flicker noise PSD than that of the GaAlAs ECDL. This behavior is opposite to expectations when considering the larger density of microcracks in III-nitride epitaxy. We attribute the noise reduction in the shorter wavelength laser to the correlations between $1/f$ frequency noise and intensity noise [67], which exhibits PSD $\propto \lambda^6$ (see below).

Lasing linewidth is estimated from the measured FN spectrum utilizing the method in [78]. (Delayed self-heterodyne measurement is not possible due to high attenuation in silica fiber of ~30 dB/km at 420 nm, and the accuracy of heterodyne beat note measurements using two lasers is penalized by eventual frequency drifts [63].) The lasing linewidth FWHM is calculated from the frequency noise density $\Delta\nu_f$, given by the expression

$$\text{Linewidth} = \sqrt{8\ln(2)}\sqrt{\int_{f_1}^{f_2} \Delta\nu_f(f)df} \ . \tag{5.1}$$

The lower limit of integration f_1 is set by the DC cut-off of the measurement equipment, which is 0.488 Hz. This is also sets the effective integration time of the linewidth measurement as 2 s. The

upper limit of integration f_2 is set by the intercept of the frequency noise curve $\Delta\nu_f$ and the line $8\ln(2)f/\pi^2$.

Using this method, the ECDL linewidth is estimated to be 870 kHz. This is close to the linewidth previously reported for free running GaN-based ECDLs, obtained from heterodyne beat signal with a second ECDL and 50 ms integration time [63]. (For integration time of 20 s, the heterodyne linewidth of that ECDL was one order of magnitude larger.) To validate our results, we estimate the linewidth of the 852 nm DFB laser from its frequency noise spectrum as well, yielding 3.5 MHz. This is very close to the 3.3 MHz value estimated from the measured beat signal obtained through heterodyning with a second identical DFB laser.
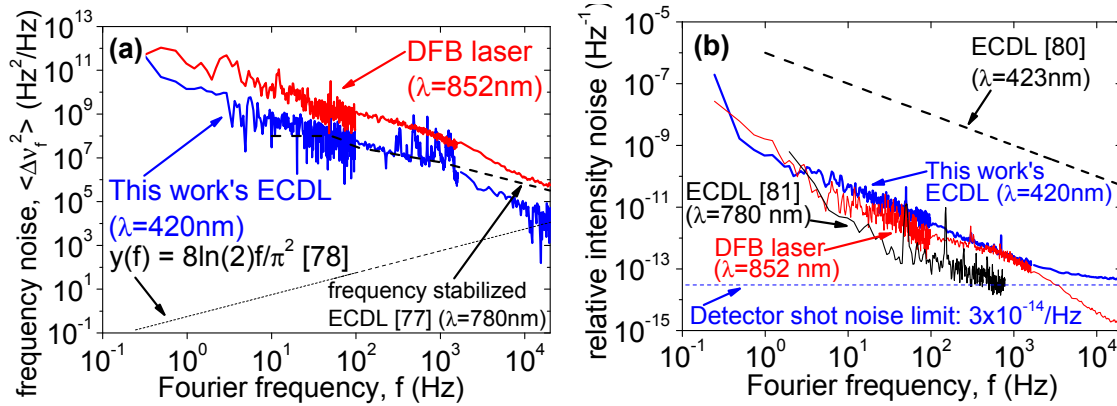
Figure 5.6. (a) Frequency noise and (b) RIN spectra of the 420 nm ECDL in comparison with a DFB laser for ^{113}Cs atom spectroscopy and data from [77], [80], [81].

The measured low frequency RIN spectrum of our ECDL at 12 mW output power is plotted in Fig. 5.6(b) along with that of the commercial 852 nm DFB laser, an uniquely reported 423 nm ECDL [80], and a 780 nm ECDL [81]. At high Fourier frequency (1 MHz), the RIN is white noise (due to spontaneous emission) with the spectral noise density being higher by a factor of 10 in shorter wavelength GaN lasers than in GaAs lasers [82]. (White spectrum RIN is not affected by the resonator bandwidth and varies as $\propto I^2/\lambda^3 P_{out}^3$ [79]). However, in low frequency range, which provides important contribution to the integral RIN characteristic of a semiconductor laser, the main constituent is flicker (1/f) noise with PSD $\propto \lambda^6 P_{out}^{4k}/L_{cav}^{3+m}\Delta\nu_{res}^m$ and indexes $0 \le k \ll 1$ and $m=1$ ($m=0$) for facet reflectivity product $R_1 R_2 < 0.14$ ($R_1 R_2 > 0.14$)[83]. Strong wavelength and cavity length dependences may explain why low frequency RIN PSD in our 420 nm ECDL is comparable to that of 852 nm DFB laser despite higher defect density in GaN and hence higher amplitude of 1/f noise sources. The lower RIN PSD in the 780 nm ECDL is attributed to the much lower defect density in technologically matured III-V epitaxy. The origin of excessive RIN PSD in the 423 nm ECDL from [80] is not known.

With the realization of the blue wavelength ECDL, we now have a single frequency narrowband optical source at 420 nm wavelength. Our characterization of lasing linewidth and noise characteristics confirms its suitability for performing absorption spectroscopy on the $5S_{1/2}$-$6P_{3/2}$ transition of ^{85}Rb.

5.2   Absorption Spectroscopy at $5S_{1/2}$-$6P_{3/2}$ Line

5.2.1   Pressure Broadening and Line Shift Due to N_2 Buffer Gas

While characterization on the pressure broadening of the $5S_{1/2}$-$6P_{3/2}$ transition linewidth due to collisions with atomic buffer gases such as He and Ar exists in literature [45], this data for molecular buffer gases such as N_2 is not available. This is a significant deficiency because though both atomic and molecular buffer gases broaden absorption linewidths, only molecular buffer gases can quench the excited state lifetime of an atomic transition [1], [27].

We measure the absorption spectra of ^{85}Rb cells with 6 and 200 torr of N_2. The interrogating laser is the ECDL detailed in Section 5.1. During the acquisition of the spectral profile of the absorption line, the sweep rate of the lasing frequency needs to be low enough such that the optical interrogation of the absorption line can be considered as steady-state interrogation. In these measurements, the lasing frequency tuning range is >10 GHz, and the sweep rate of this tuning is 10 Hz.

Figure 5.7 gives an example of measured absorption spectra at 420 nm for cell with 6 and 200 torr of N_2 buffer gas at cell temperature of 100 °C. One can resolve the absorption features arising from ground state hyperfine splitting in the 6 torr cell. We labeled each transition as F_g=j, where j is the quantum number F of that particular ground state hyperfine level. It is not possible to resolve the hyperfine ground state features for the 200 torr cell due the pressure broadening of the absorption linewidth. Furthermore, high buffer gas pressure significantly shifts the absolute frequency of absorption resonance with respect to the low pressure cell.
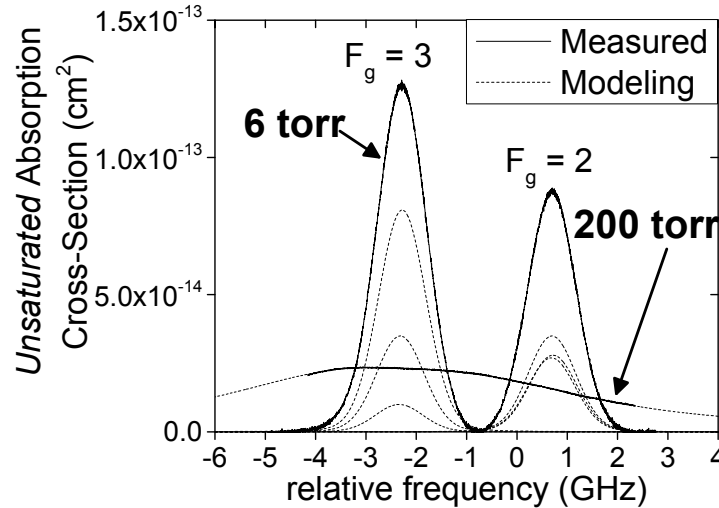
Fig. 5.7. Measured (solid) absorption spectra of ^{85}Rb at 420 nm with 6 and 200 torr of N_2 buffer gas at 100 °C under optical intensity of 0.89 mW/cm^2. Modeled absorption curves (dotted) for each six component energy transition is plotted for the 6 torr cell, while the modeled curve for the 200 torr cell is the superposition of all six components.

By using the estimated Doppler line broadening from the cell temperature with Eq. (3.26) and fitting the measured spectra with the absorption line profile model of Eq. (4.1), we extract the Lorentzian profiled pressure broadening linewidth from absorption spectra. From that, we calculate the

pressure broadening coefficient in units of MHz/torr as given in [45]. However, buffer gas pressure varies with temperature, and the cell buffer gas pressures of 6 or 200 torr are rated for 24° C, the cell sealing temperature. The buffer gas pressures at 100° C are calculated using Ideal Gas Law. Thus, 6 and 200 torr at 24° C become 7.5 and 251 torr at 100° C, respectively. Figure 5.8 plots the extracted pressure broadening as a function of N_2 pressure at 100° C. We obtain a pressure broadening coefficient of 22.8 MHz/torr at temperature of 100° C. Our measured N_2 broadening coefficient, after adjustment to temperature of 368 K, is smaller than the pressure broadening coefficient of He in the same atomic transition [45] (368 K is the measurement temperature in [45]). However, it does fit the trend of N_2 having smaller pressure broadening coefficient than He in the D_1 and D_2 transitions [44].
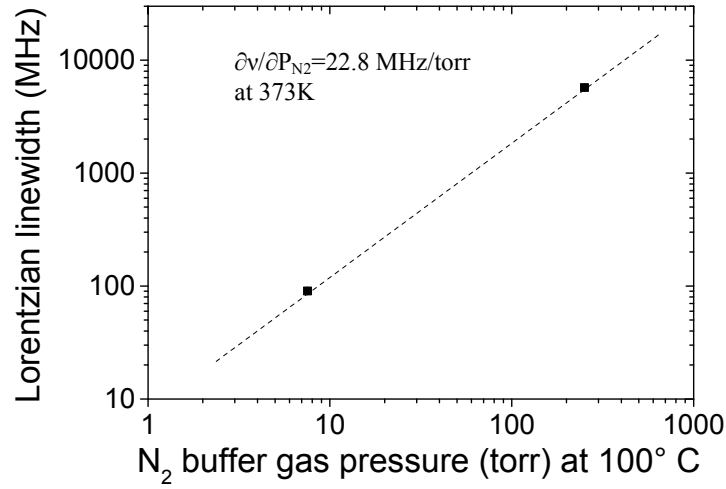
Fig. 5.8. Linewidth broadening due to collision with N_2 buffer gas as a function of buffer gas pressure measured at 100 °C (373 K). The pressure broadening coefficient is 22.8 MHz/torr.

Finally, we measure the shift in absorption resonance in the cell due to N_2 buffer gas. Under the same ECDL settings and within half hour of each other, absorption spectroscopy was performed on two cells at 100° C, one with no buffer gas and one with 200 torr of N_2. It was determined that the absorption resonance frequency shift with 200 torr of N_2 is −1.2 GHz. This corresponds to a coefficient of −4.8 MHz/torr at 100° C. One can see this frequency shift effect in Fig. 5.7, where the spectrum of the 200 torr buffer gas cell is considerably shifted with respect to the spectrum of the 6 torr cell.

We summarize the pressure broadening coefficients of He and N_2 for the D_1, D_2, and 420 nm transitions of ^{85}Rb in Table 5.1.

^{85}Rb	N$_2$		He	
Transition	**Broadening**	**Frequency Shift**	**Broadening**	**Frequency Shift**
5S$_{1/2}$-6P$_{3/2}$ (420 nm)	22.8 MHz/torr, 373 K [This Work]	−4.8 MHz/torr, 373 K [This Work]	47.1 MHz/torr, 368 K [45]	−4.85 MHz/torr, 368 K [45]
D_1 (795 nm)	16.3 MHz/torr, 394 K [44]	−7.4 MHz/torr, 394 K [44]	18.9 MHz/torr, 394 K [44]	+4.71 MHz/torr, 394 K [44]
D_2 (780 nm)	18.3 MHz/torr, 394 K [44]	−5.79 MHz/torr, 394 K [44]	20.0 MHz/torr, 394 K [44]	+0.37 MHz/torr, 394 K [44]

Table 5.1. Summary of pressure broadening and frequency shift coefficients, measured in this research and taken from literature, of N$_2$ and He buffer gas on ^{85}Rb lines at D_1, D_2, and 5S$_{1/2}$-6P$_{3/2}$. We also list the temperature at which these coefficients were measured. Note that the values for He at 5S$_{1/2}$-6P$_{3/2}$ from [45] were provided separately for each hyperfine ground state, which we average for presentation here.

5.2.2 Saturation Effects in Optical Absorption

We experimentally measure the hyperfine ground state relaxation time τ_g and the saturation intensity I_{sat} for the ^{85}Rb cell with no buffer gas. This is achieved by measuring the absorption spectra of the cell over a wide range of optical intensities at SF π-interrogation and analyzing them with the method detailed in Sections 3.4. Figure 5.9 plots the measured resonant absorption coefficients as a function of optical intensity for ground states F_g=2 and F_g=3. The resonant absorption cross-section σ is obtained from the absorption spectra acquired at the lowest intensities far below I_{sat}. Our analysis yields relaxation time between ground states τ_g=31.5 µs, and saturation intensities of 102 and 170 mW/cm^2 for hyperfine ground states F_g=2 and F_g=3.
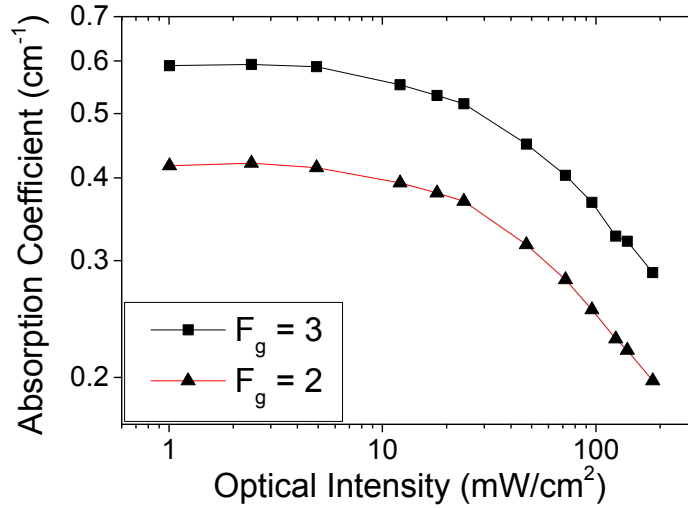
Fig. 5.9. Resonant absorption coefficients of ^{85}Rb, without buffer gas and at 100 °C cell temperature, plotted as a function of optical intensity.

Unfortunately our experimental measurement of I_{sat} (and evaluation of τ_g) for high buffer gas pressure cell (200 torr of N$_2$) using the methods described above was not conclusive. High buffer gas pressure cell has weak absorption coefficient even at optical intensities well below the saturation level (see Fig. 5.7). At high intensities (much higher than saturation intensity), the absorption coef-

ficient α becomes small, and our measurement equipment is not sensitive enough to detect a small change in transmitted spectral power density. Therefore, we use the model for optical beam transit and wall collision effects detailed in Section 3.3 to estimate τ_g and I_{sat} in the high buffer gas pressure cell. Results of our measurements and estimates are summarized in Table 5.2. In the zero buffer gas pressure cell, the propagation of Rb atoms inside the cell is ballistic, and this prevents the use our model because its key component is the transit time of Rb atoms through the optical beam due to diffusion as shown in Eq. (3.6).

N_2 Pressure (torr)	σ (cm^2) Measured	τ_g	I_{sat} at F_g=2 (mW/cm^2)	I_{sat} at F_g=3 (mW/cm^2)
0	2.3×10^{-13}	31.5 µs	102	170
6	2.16×10^{-13}	50.5 µs*	74*	104*
200	2.88×10^{-14}	1.68 ms*	17*	23*

Table 5.2. Measured and calculated absorption parameters for cells with N_2 buffer gas. The (unsaturated) absorption cross-section σ is measured from absorption spectra. The * denotes values calculated using model detailed in Section 3.3.

5.3   Generation of Optical Pulse with Precise Wavelength Using Optical Injection Locking

Measuring the excited state lifetime of the $5S_{1/2}$-$6P_{3/2}$ line and its quenching in the presence of buffer gas is an important part of this research, as the recovery time of alkali vapor cell absorber is mainly defined by the excited state lifetime. Toward this goal, we have developed a method to generate short optical pulses at the precise atomic transition wavelength. The original idea was to measure excited state lifetime by simultaneously interrogating Rb atoms with two spatially overlapping laser beams, both lasing on atomic absorption resonance and operating in the pump-probe configuration. The probe beam is operating in continuous wave (CW) and at optical intensity lower than that of the Rb saturation intensity. The pump beam is pulsed and has intensities significantly higher than that of Rb saturation. By monitoring the change in transmission of the CW beam, we expected to extract the upper state lifetime. We detail those experimental attempts in Section 5.4.

In group III-nitride lasers, short optical pulses with high peak powers have been obtained from multi-section laser diodes (MSLD) operating in either Q-switching or mode locking regime [72], [84]–[86]. To obtain the desired wavelength from the pulsed MSLD, one solution is to perform optical injection locking [87], [88], where the output from a master laser is injected into a slave laser, forcing the latter to lase at the same optical frequency. While injection locking of CW group III-nitride lasers [89], [90] have been performed, to the best of our knowledge there have been no report on injection locking of self-pulsating or passively Q-switched blue-violet diode lasers.

In this section, we investigate the behavior of a Q-switched InGaN MSLD under external optical injection from an ECDL operating in CW. Unlike typical injection locking experiments, here the power and optical frequency of the master ECDL laser is held constant. Instead, the drive current pulse amplitude and duty cycle of the slave MSLD laser are varied to enable fine-tuning to the lock-

ing region. We report that when the Q-switched InGaN MSLD is operated well above threshold, CW optical injection reduces the peak power of optical pulses, in agreement with dynamic behavior reported for conventional III-V lasers [91]. However when our InGaN MSLD is operated near free running lasing threshold, external optical injection increases the peak output power, and we demonstrate solitary optical pulse generation.

Our slave laser is a MSLD designed and fabricated within the framework of European FP7 Project FemtoBlue [92], [93]. Its epitaxial structure, which incorporates three $In_{0.10}Ga_{0.90}N$ quantum wells (QWs), is designed for lasing at around 420 nm wavelength. Ridge waveguide structure of 3 μm width provides lateral optical guiding. The device is divided into three sections. A short center section of 80 μm length is reversed biased and operates as a saturable electro-absorber. The two end sections are forward biased to provide optical gain. The device used here was mounted on an AlN submount, installed on a temperature controlled heat sink, and was wirebonded to dedicated contact pads for the gain and absorber sections.

A schematic of the measurement setup is given in Fig. 5.10. The free running MSLD is operated in the self-Q-switching regime, which is achieved by reverse biasing the saturable absorber with a precision DC voltage supply at −9.4 V and electrically driving the gain sections with a current pulse generator. The current pulses have durations of 8.4 ns full width at half maximum (FWHM) and about 2 μs periods (see below). The master laser used is the CW blue wavelength ECDL described in Section 5.1. For these measurements, the ECDL wavelength is tuned to 420 nm ($5S_{1/2}$-$6P_{3/2}$ line of Rb atoms).
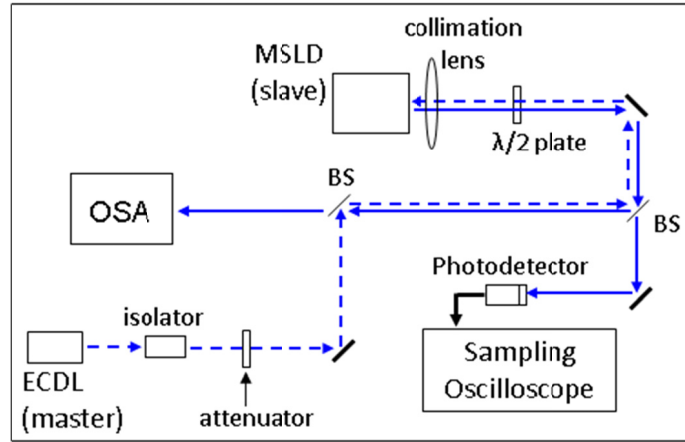
Fig. 5.10. Schematic of the setup used for injection locking experiments. The ECDL output beam (dashed) is injected into the MSLD. MSLD output (solid) spectrum and optical waveform are simultaneously analyzed.

The MSLD integrated optical spectrum and time-resolved optical waveform are simultaneously analyzed using an optical spectrum analyzer (OSA) with resolution of 0.025 nm and a sampling oscilloscope with high speed photodetector (response time 35 ps). The oscilloscope is triggered on the current pulse driving the MSLD. To perform optical injection, the collimated ECDL output beam is re-focused at the output facet of the MSLD. A half-waveplate is used to rotate the ECDL linear polarization to match that of the free running MSLD so as to avoid possible polarization in-

stabilities [94]. The ECDL optical power incident on the MSLD collimation lens is held constant at 280 μW.

As noted previously, the optical frequency of the master ECDL laser is held constant. Thus, to ensure injection locking can occur, the free running MSLD spectra must overlap with that of the ECDL wavelength. Coarse tuning of the MSLD wavelength was done using a thermoelectric cooler (the nominal temperature used in these experiments is 22° C). Fine temperature tuning was done by changing the pulse repetition period of the MSLD gain section drive current.

Peak output power per facet was calculated by measuring the MSLD average power in free running configuration and analyzing the waveforms acquired on the sampling oscilloscope. The measured peak powers matches what was reported elsewhere for lasers from the same fabrication batch [85]. Figure 5.11 plots the peak output power (first optical pulse in a waveform is used) as a function of the drive current for the free-running MSLD and when it is subjected to optical injection. It reveals three different operation regimes. At currents far below lasing threshold, optical injection has very little effect on the slave laser. At near free running lasing threshold, the peak output power significantly increases under optical injection (pulse enhancement regime). At well above free running lasing threshold, optical injection reduces peak output power (pulse suppression regime). We denote these three regions as "no effect", pulse enhancement regime, and pulse suppression regime, respectively.
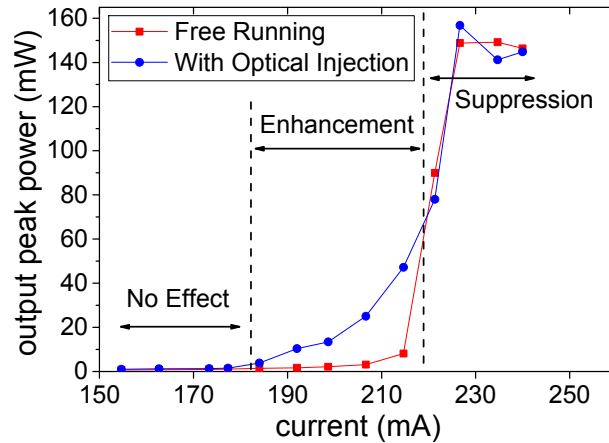
Fig. 5.11. Peak output power per facet of MSLD waveforms as a function of drive current in free running (red) and under optical injection (blue) configuration.

In the pulse enhancement regime, external optical injection causes the MSLD to lase even when it is not lasing or at the threshold of lasing in free running configuration. This can be seen in Fig. 5.12, where the MSLD (a) time-resolved waveforms and (b) integrated spectra are plotted at drive current of 215 mA. When free running, the laser is at the threshold of lasing with optical spectrum FWHM of ~1.5 nm, which is narrower than the spectral FWHM of ~3 nm when the MSLD is at well below threshold. Thus, the spectrum here contains contributions from both amplified spontaneous emission (ASE) as well as spectral narrowing effects arising from the onset of lasing.
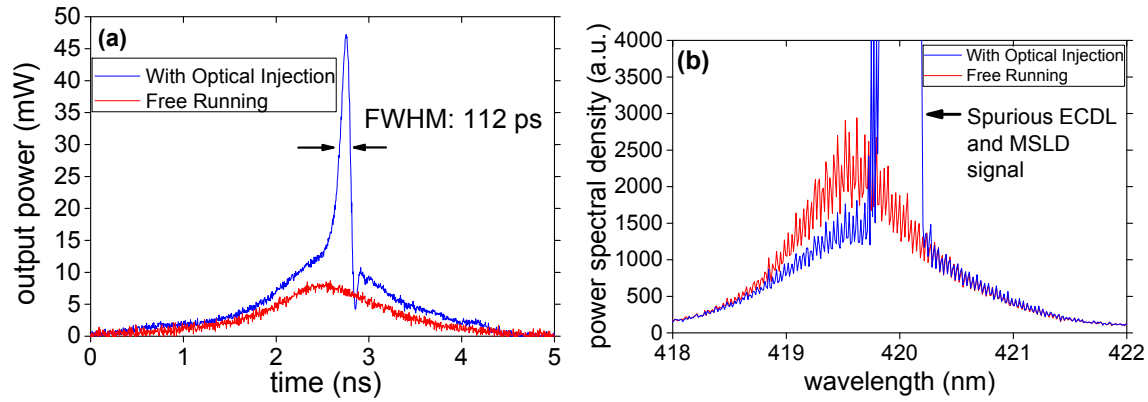
Fig. 5.12. (a) Waveforms and (b) spectra of MSLD, driven at 215 mA. The laser is not lasing when free running (red), and lases with single optical pulse with optical injection (blue).

With optical injection, peak power is significantly enhanced from less than 10 mW in free running to nearly 50 mW. The optical waveform acquired from the sampling oscilloscope contains a sharp pulse with 112 ps FWHM, much shorter than the current pulse of 8.4 ns driving the laser. The actual pulse width should be shorter (and the peak power higher) than the measured value due to (i) rise time of the photodetector (35 ps) and (ii) jitter in the delay time between the applied current pulse and emitted lasing pulse (>10 ps) [95]. This jitter directly affects the result of our measurements on the sampling oscilloscope because the current pulses driving the MSLD are used as the acquisition trigger for each sampling sequence. Under external optical injection, the pulse energy of the slave MSLD is increased from 13 to 25 pJ, estimated by integrating the measured waveform power vs. time. (The average power also increased.)

In Fig. 5.12(a), on the downward slope from the pulse peak, the waveform overshoots before recovering back to the level that corresponds to ASE. Since the sampling oscilloscope constructs each waveform by sampling multiple realizations of optical pulses (in successive acquisition sequences), this particular overshoot is not an artifact of the measurements. The source of this feature is likely the onset of a second optical pulse, which does not develop because the duration of the current pulse is too short and does not allow the second optical pulse to build up. This opens interesting possibility to produce on-demand solitary optical pulses at the desirable wavelength (see below).

In Fig. 5.12(b), the optical spectra for MSLD while free running and subjected to optical injection are both acquired with equal integration times. Unfortunately, spurious light from the ECDL operating in CW is reflected off of the MSLD output facet and coupled back into the OSA. Since the slave MSLD operates at low duty cycle (0.4%), the spurious light from the master ECDL masks the most interesting portion in the integrated optical spectra. However, it can still be seen that under optical injection, ASE spectral components with wavelengths shorter than that of the injected master ECDL (420 nm) are reduced in intensity with respect to the free running MSLD spectrum. The longer wavelength components of ASE are unaffected. From this behavior, in combination with the large enhancement in the optical pulse energy, we conclude that there should be a strong component in the MSLD spectrum hidden by the spurious ECDL signal. Therefore, the injected radiation from the master ECDL is almost certainly causing the slave MSLD to lase at the same wavelength.

We note that from the measured time domain pulse width of 112 ps, the spectral width of the MSLD output is 8.9 GHz, which is sufficient broad for dual frequency (DF) pumping of both hyperfine ground states to the excited state in Rb atoms.

Under condition of optical injection locking, the power spectral density reduction in the high-energy part of ASE might be attributed to spectral hole burning in the gain curve at 420 nm when the MSLD starts lasing. Fast intraband relaxation of hot carriers into the energy states depleted by the spectral hole burning leads to a reduction of carrier densities at higher energies. As a consequence, the intensity of the short-wavelength part of ASE is reduced.

Different behavior is observed in the pulse suppression regime, corresponding to the MSLD drive current being significantly above the free running threshold. Here, the free running MSLD operates in Q-switching regime. Figure 5.13 shows the impact of the optical injection on the time-resolved optical waveforms and integrated spectra of the MSLD driven at 235 mA.

From the time-resolved optical waveforms in Fig. 5.13(a), the delay time to the first lasing pulse for MSLD under external optical injection is slightly shorter than that of the free running configuration. Optical injection decreases the peak power and reduces the period of the optical pulses. The amplitude decrease is less pronounced for the first optical pulse, but is clearly seen and quite significant for all subsequent optical pulses. Interestingly, the total pulse train energy (hence also the average power) increases under optical injection, from 92 to 94 pJ.
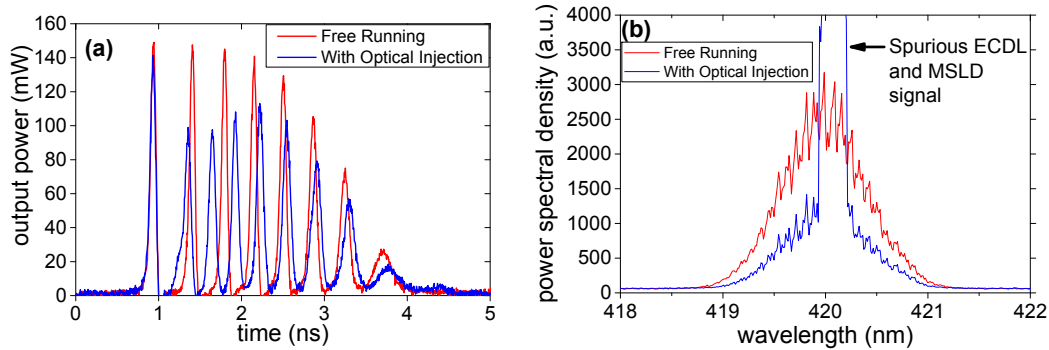
Fig. 5.13. (a) Waveforms and (b) spectra of MSLD, driven at 235 mA, when free running (red) and with optical injection (blue). The laser is Q-switched under these operating conditions.

The spectrum of free running MSLD at 235 mA pump current pulses is relatively broad, of ~1 nm FWHM as shown in Fig. 5.13(b). This spectral broadness is due to multimode lasing emission. Similar to Fig. 5.12(b), spurious CW ECDL signal partially masks the MSLD spectrum when operating with optical injection. Nevertheless, one can see that optical injection reduces the amplitude of lasing modes that do not match the wavelength of ECDL. Moreover, since the estimated optical pulse train energy (and average power) is higher than that in free running MSLD, we conclude that under optical injection, the MSLD should exhibit a strong spectral component at the injected ECDL lasing frequency. In Fig. 5.13(b), it is hidden by the spurious ECDL signal. The side mode suppression accompanied by an increase of the pulse train energy (and average power) attests for the optical injection locking of MSLD at the frequency of injected ECDL radiation.

The reduction of the peak power of Q-switched pulses with optical injection can, at first glance, be considered unusual. However, the pulse suppression regime at well above threshold as well as the pulse enhancement regime near threshold is reproduced by modeling. Our numerical simulations are based on the standard semiconductor laser rate equation model [96], which was modified to separately account for carrier dynamics in both gain and absorber sections as well as for external optical injection into the cavity and contribution from ASE [97], [98]. The model uses the adiabatic approximation for the medium polarization and thus excludes any coherence ordering effects in the medium [99].

Simulated optical waveforms from our model are given in Fig. 5.14. In the model, the short absorber section is moderately reversed biased. The lasing threshold is 215 mA at our model's simulated absorber bias. At time t = 0, a current pulse is injected into the gain section. In Fig. 5.14(a), the simulated drive current amplitude is 190 mA, and the optical output in free running configuration (red curve) is purely due to ASE. With external optical injection of 1 mW in the cavity, the output power is significantly enhanced, yielding emission of a narrow width solitary pulse, like the one observed experimentally in Fig. 5.12(a).

In Fig. 5.14(b), the simulated drive current of 240 mA is well above threshold, and the free-running laser operates in self Q-switching regime. With external injection of 1 mW power in the cavity, peak optical power reduces and pulse period decreases. The simulated behavior with injection locking is similar to what was observed experimentally in Fig. 5.13(a).
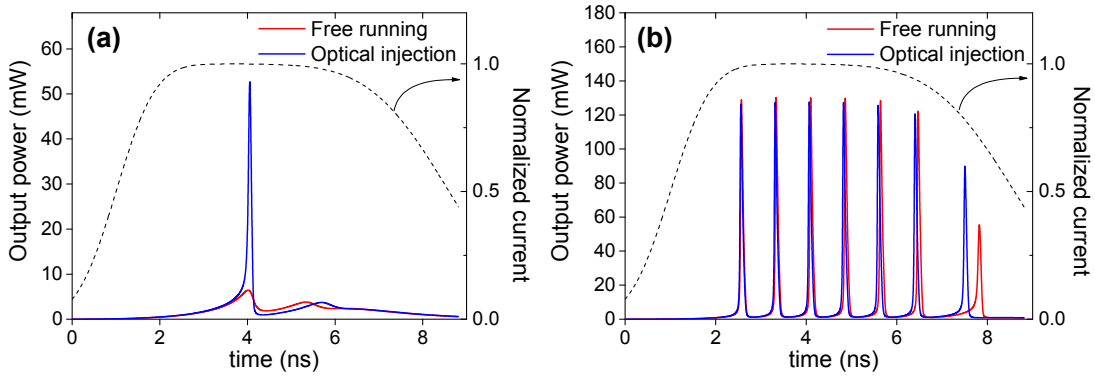
Fig. 5.14. Simulated waveforms for multi-section laser in free running (red) and with optical injection (blue) when (a) driven at 190 mA and (b) 240 mA. The dashed curve (right axis) shows current waveform used in simulations. External optical injection leads to enhancement or suppression of peak output powers, respectively, matching well with experimental observations.

Interestingly, the main mechanism responsible for the pulse enhancement or suppression induced by optical injection is revealed to be the partial bleaching of the saturable absorber by the externally injected photons. Figure 5.11 indicates a switching-on kink typical for bi-stable lasing operation [100]. At near threshold (Fig. 5.14(a)), the reduction in overall intracavity loss due to the bleached absorber turns on the Q-switched lasing regime with low pulse repetition rate, enabling the buildup of the first lasing pulse. Quenching of subsequent Q-switched lasing pulses is conditioned by duration of the pump current pulse and low repetition rate of these pulses.

The partial bleaching of absorber has different implications for operation well above the lasing threshold in the Q-switching regime. In between the optical pulses in a self Q-switched MSLD, the carriers in the gain sections are depleted and the absorber prevents the MSLD from lasing. Non-bleached absorber allows accumulation of electrically injected carriers in the gain section, leading to buildup of the optical gain and ASE. The ASE eventually grows large enough to bleach the saturable absorber, resulting in buildup of the lasing Q-switched pulse. Carriers are then rapidly depleted, lasing stops, the absorber recovers, and the cycle starts again. With partial bleaching of the saturable absorber due to externally injected photons (Fig. 5.14(b)), full bleaching of absorber occurs at lower carrier densities in the gain sections. Thus, the optical pulse period decreases, and the peak output power is smaller compared to that of free running configuration.

To summarize, the implication of our experimental observations, supported by simulations, is that while a MSLD can be injection locked, thereby obtaining the desired wavelength operation, there can be accompanying tradeoffs. If the MSLD operating in Q-switching regime is driven at well above free running threshold, injection locking reduces the output pulse peak power compared to free running. Note that further increase of the injected optical power totally quenches the Q-switching operation [101]. On the other hand, if the MSLD is driven very near threshold, injection locking allows one to obtain lasing operation with a single, short duration optical pulse. However, the peak power of such solitary pulse is comparable or below the peak power in Q-switched regime. The operation regimes described here have potential applications such as time-resolved spectroscopy of atoms.

5.4   Excited State Lifetime Measurements of $5S_{1/2}$-$6P_{3/2}$ Line

The excited state lifetime τ_{ex} of the $5S_{1/2}$-$6P_{3/2}$ line in ^{85}Rb is not well established. Whereas one can find the τ_{ex} of the traditional D_1 and D_2 lines in literature, measured using a wide variety of techniques under a wide number of conditions (e.g., temperature and buffer gas content), this is not the case for the $5S_{1/2}$-$6P_{3/2}$ line. For example, two publications cite τ_{ex} of 112 ns [102], [103] for Rb in a cell with no buffer gas, but there is no detail on how this value was obtained. However, it is reasonable to expect the $5S_{1/2}$-$6P_{3/2}$ line to have have larger natural τ_{ex} than the D_1 line given that it has a weaker transition strength, with the former having 1.77×10^6 s^{-1} and the latter having 3.61×10^7 s^{-1} [104]. In this section, we attempt to measure τ_{ex} using the equipment and techniques that we have developed.

5.4.1   Short Pulse Pump and Single Frequency Continuous Wave Probe Experiment

For the pump-probe experiment described in this section, the Rb cell is placed in the setup with the injection-locked MSLD as shown in Fig. 5.15. The pump laser is the injection-locked MSLD, which is performing broadband pumping of the Rb system with solitary pulses of 122 ps FWHM duration. The ECDL is used as the single frequency (SF) interrogation source, placed on one of the ground state absorption resonance lines. Therefore, the ECDL is both the master laser that injection-locks the MSLD and the probe laser in the spectroscopy measurement. The goal is to measure ex-

cited state lifetime τ_{ex} by observing the change in the transmitted probe laser intensity through the Rb cell.

Unfortunately, we were not able to measure any appreciable change in the ECDL optical signal transmitted through the Rb cell. Analysis with the six-level model revealed that the MSLD pulse energy in solitary pulse production regime was insufficient to produce noticeable excited state pumping. In order to measure τ_{ex} of ~100 ns, we estimate that the pulse energy must be larger by a factor of 100. Thus for a pump pulse of the same duration (112 ps), a peak power of at least 5 W is needed to obtain an observable signal. Unfortunately this was not attainable in our setup. An alternative approach would be to increase the pulse width. When it becomes much longer than τ_{ex}, the atomic level populations will approach to that one of a steady-state under CW pumping. This approach is suitable even at lower pump power.
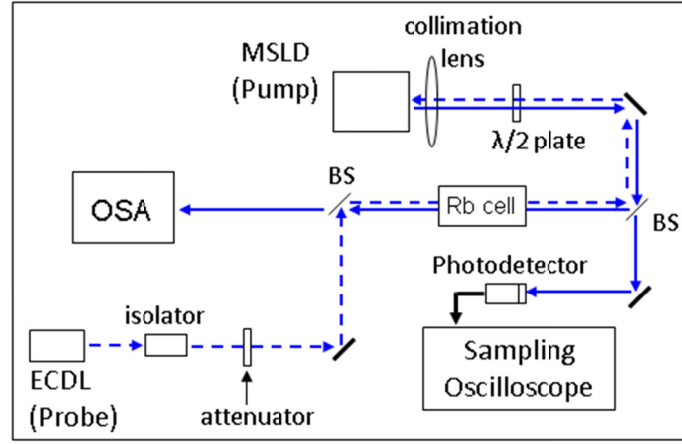
Fig. 5.15. Schematic of pump-probe experiment with MSLD as the pump laser, and the ECDL as the probe laser. The Rb cell is placed such that it is in the beam path of both lasers, where it can be simultaneously interrogated.

5.4.2 Dual Frequency Continuous Wave Pump at 795 nm and Single Frequency Probe at 420 nm

In this section, we detail the experiments made with a CW pump laser and a CW probe laser interrogating ^{85}Rb atoms at two different transitions. The experimental setup is similar to that depicted in Fig. 4.10 in Section 4.4, except that the 795 nm wavelength VCSEL is replaced with the 420 nm wavelength ECDL. Thus, while we pump the ^{85}Rb atoms at the D_1 line with a 795 nm DFB laser (DF pumping), we probe them at $5S_{1/2}$-$6P_{3/2}$ line with 420 nm ECDL (SF interrogation). We illustrate the pumping and probing transitions in ^{85}Rb atom in Fig. 5.16. The procedure to operate this setup is the same as that in Section 4.4.
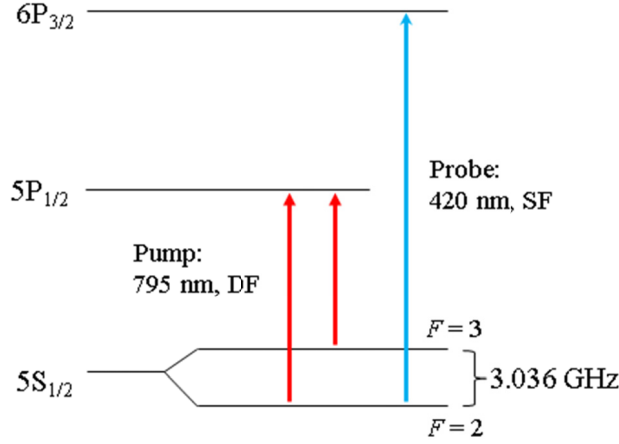
Fig. 5.16. A simplified energy level diagram of ^{85}Rb detailing how the atoms are optically pumped and probed. The pump laser is a 795 nm DFB operating in DF pumping. The probe laser is the 420 nm ECDL operating in SF interrogation.

The 795 nm DFB, in DF pumping, places a certain number of atoms in the excited state at $5P_{1/2}$. With the sudden removal of optical pumping by the DFB (through removal of RF current modulation), carriers decay from the $5P_{1/2}$ state to the two ground states with time constant equal to the excited state lifetime of the D_1, which we denote in this section as $\tau_{ex,D1}$. This distribution of populations in the ground states, however, is different from the steady-state population where only the probe laser is interrogating the Rb atoms in $5S_{1/2}$-$6P_{3/2}$ transition. In particular, the steady-state population of ground state hyperfine level F=3 under SF interrogation significantly exceed the population of F=2. Because $\tau_{ex,D1}$ is significantly shorter than the excited state lifetime at $6P_{3/2}$, which we will denote simply as τ_{ex}, we may consider that the initial decay from $5P_{1/2}$ level occurs almost instantaneously. Rb atoms will undergo a transient process toward the steady-state population distribution for SF pumping. Because ground state relaxation time τ_g is much longer than τ_{ex}, the main mechanisms for ground state relaxation at the initial stage is through the optical absorption followed by spontaneous decay from $6P_{3/2}$ state to both hyperfine grounds states. Therefore, we intend to measure the lifetime τ_{ex} of $6P_{3/2}$ state by observing the initial stage of the transient process in the transmitted probe laser (ECDL) intensity through the cell, like it was used in Section 4.4.

We performed pump-probe measurements on ^{85}Rb cells without buffer gas and with 6 torr of N_2 buffer. For these measurements, in order to increase the ground state relaxation time τ_g, we do not use the focusing lenses (see Fig. 4.6), unlike the setup shown in Fig. 4.10. The measured time varying probe laser intensity through the ^{85}Rb cell with no buffer gas is presented in Fig. 5.17(a). The measured lifetime τ_{ex} is 124 ns, which is in reasonable agreement with the literature value of 112 ns [102], [103]. We also perform the same measurement on the ^{85}Rb cell with 6 torr of N_2 buffer gas, shown in Fig. 5.17(b), and the measured τ_{ex} is 84 ns. Unfortunately, we were not able to measure the $6P_{3/2}$ state lifetime in the ^{85}Rb cell with 200 torr of N_2 buffer gas. Fast relaxation process in such a cell (~1 ns) demanding large operation bandwidth of our acquisition equipment as well as the small absorption cross-section of pressure broadened line have rendered the signal to noise ratio to be lower than what our setup can detect.
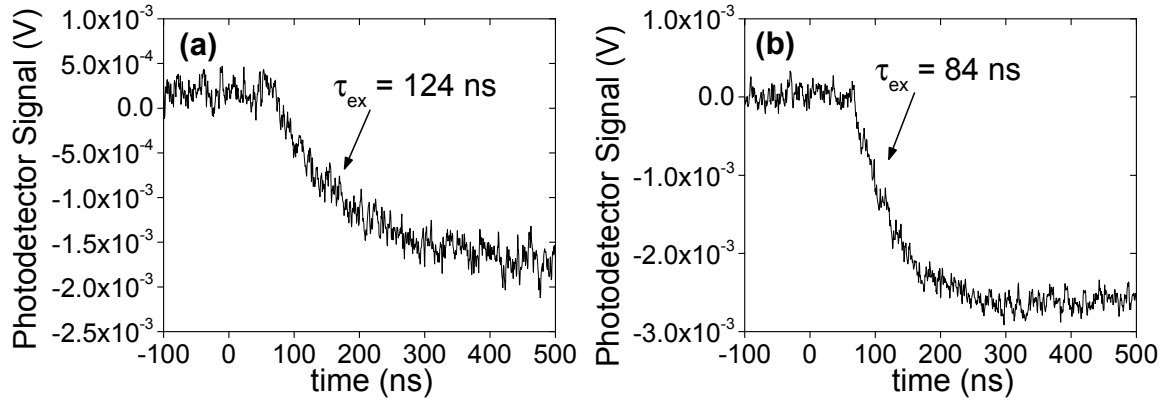
Fig. 5.17. (a) Measured time varying 420 nm probe laser signal transmitted through a [85]Rb cell with no buffer gas. The extracted decay time constant of 124 ns is in reasonable agreement with the excited state lifetime cited in [102], [103]. (b) Same measurement for a [85]Rb cell with 6 torr N_2 buffer gas.

Equation (4.12) is suitable for the theoretical estimation of the quenched excited lifetime as a function of buffer gas pressure. However, some parameter values are not definitive for this atomic line. For the natural lifetime $\tau_{ex,0}$ of excited state $6P_{3/2}$, one can use value of 112 ns as cited in [102], [103]. However, these references do not provide any support on the validity of this value. Alternatively, one can use $\tau_{ex,0}$=565 ns, calculated from the reciprocal of the transition strength 1.77×10^6 s^{-1} [104]. This method of calculating $\tau_{ex,0}$ can be justified by noting that the reciprocal of the D_1 line transition strength (3.61×10^7 s^{-1} [104]) is 27.7 ns, which is the same as the excited state lifetime values found in literature for the D_1 line [53], [54].

There is also no literature reported value for the N_2 quenching cross-section σ_Q in the Rb $5S_{1/2}$-$6P_{3/2}$ line. The only available quenching cross-section in literature is the value for the D_1 and D_2 lines in Rb, with both being the same at 50 ± 12 Å^2 [56], as cited previously, or 25 Å^2 [105] for Rb atoms in flame. We therefore make the decision to calculate the theoretical values of τ_{ex} using four different combinations of $\tau_{ex,0}$ and σ_Q: $\tau_{ex,0}$ at 112 ns or 565 ns, σ_Q at 50 Å^2 or 25 Å^2.

In Fig. 5.18, we plot the theoretical estimate of τ_{ex} as a function of cell buffer gas pressure (line) along with our measured values (points). The measured data points show better agreement with the curve at $\tau_{ex,0} = 112$ ns and σ_Q=25 Å^2, although the number of points do not allow us to make a definitive conclusion. Nevertheless, we note that in all these theoretical estimations, we calculate τ_{ex} to range from 1 to 2 ns at N_2 pressure of 200 torr, making the cell suitable for saturable absorber operation in a modelocked laser.
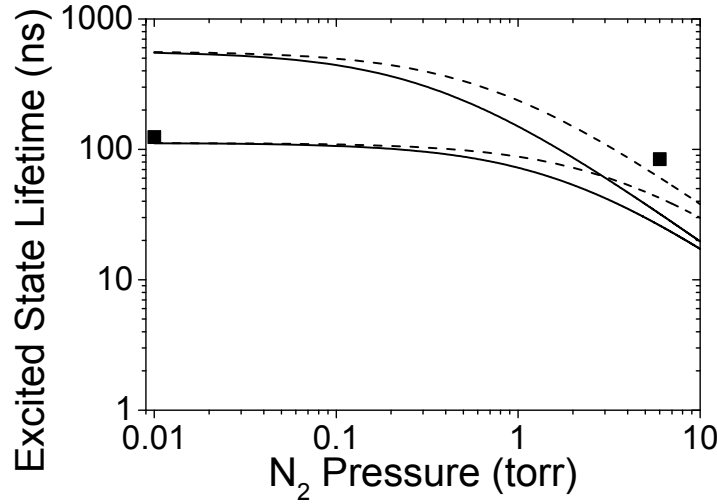
Fig. 5.18. Theoretical (lines) and measured (points) excited state lifetime τ_{ex} as a function of N_2 buffer gas pressure at cell temperature of 100° C. For purpose of plotting, the measured τ_{ex} at 0 torr pressure is placed at 0.01 torr. The theoretical curves were calculated assuming either the natural lifetime is 112 ns or 565 ns, and having buffer gas quenching cross-section of either 50 $Å^2$ (solid) or 25 $Å^2$ (dashed). Note that the value of N_2 pressure is rated for 24° C (manufacturer specification).

5.5   Summary

A narrow linewidth, single wavelength, tunable ECDL operating at around 420 nm has been developed. This ECDL has been extensively characterized, with emphasis on the analysis of frequency noise, relative intensity noise, and the impact of mode clustering effect found in the III-nitride material system—something that has not been previously reported for blue wavelength ECDLs.

Using our ECDL, we have performed absorption spectroscopy on the ^{85}Rb $5S_{1/2}$-$6P_{3/2}$ transition. From the measured absorption spectra of ^{85}Rb cells with no buffer gas and with 6 torr N_2 buffer gas over a range of temperatures, we have extracted absorber oscillator strength that matches very well with that in literature. We have measured the saturation intensities and relaxation time between the ground state hyperfine splitting levels in the presence of N_2 buffer gas. In addition, we have measured the buffer gas pressure induced linewidth broadening and absorption resonance shift coefficients, which are not found in literature.

We have also developed a method to generate short optical pulses at very precise wavelengths by injection locking III-nitride multi-section diode lasers. While this method was ultimately not useful for us, we believe there are potential uses in other applications, especially in time resolved photofluorescence of atoms and molecules.

Finally, we have used a pump-probe technique to measure the excited state lifetime at the $5S_{1/2}$-$6P_{3/2}$ line of ^{85}Rb, both natural and with quenching by N_2 buffer gas. This is similar to the work performed in Section 4.4, except that we pump at wavelength of 795 nm (D_1) and probe at 420 nm ($5S_{1/2}$-$6P_{3/2}$). There is agreement between our measured lifetime and literature for in the case of no

buffer gas. The discrepancy between our measured lifetime and theoretical value at 6 torr buffer gas pressure is not so unreasonably large.

Chapter 6   III-Nitride   Vertical-External-Cavity Surface-Emitting Laser for Atomic Clock Applications

Disclaimer: The material presented in Chapter 6 has been published in Applied Physics Letters[2] and Journal of Applied Physics.[3]

For our goal of achieving an atomic clock based on modelocked semiconductor laser with ^{85}Rb vapor cell as saturable absorber, one possible configuration is that of using optically pumped vertical-external-cavity surface-emitting laser (VECSEL) of the group III-nitride material system for interrogation of Rb atoms at 420 nm wavelength. In this chapter, we investigate its feasibility for atomic clockwork by experimentally realizing an optically pumped group III-nitride VECSEL and characterizing its performance. We also measure important modelocked laser model parameters for Chapter 7.

6.1   Brief Introduction to VECSELs

VECSELs incorporate many attractive features of both semiconductor and solid state lasers. Like other semiconductor lasers, they can lase in the visible or near infrared spectral range as a function of the alloy composition of the semiconductor heterostructure. Unlike edge-emitting diode lasers (monolithic or external cavity laser), VECSELs can achieve high output power simultaneously with high quality circular-shaped output beam [106], [107]. Their spectrally broad optical gain and external cavity configuration allow for insertion of intracavity saturable absorber for modelocking operation. Optically pumped modelocked VECSELs based on conventional III-V alloys emitting in the infrared spectral range already show impressive performance in peak power and pulse width [20], [22]. Today, research with this material system is focused on electrically-pumped VECSELs [21].

---

[2] X. Zeng *et al.*, *Applied Physics Letters*, vol. 101, no. 14, pp. 141120-1 – 141120-4, 2012.

[3] X. Zeng *et al.*, *Journal of Applied Physics*, vol. 113, no. 4, pp. 043108-1 – 043108-8, 2013.

To cover the blue to ultraviolet (UV) spectrum, VECSELs based on group III-nitrides are needed. Existing literature on nitride-based VECSELs is sparse, highlighting the difficulties of this material system for VECSEL applications. Reported VECSELs exhibit cavity lengths on the order of 2 mm or less [108]–[110]. The thresholds range from 100 to 700 kW/cm^2 for optical pump pulse durations of 1.7 to 5 ns. These extremely short external cavity lengths and the fact that some of these external cavities are made of the semiconductor sample wafer substrate mean that the placement of additional intracavity elements is not possible.

Here, we report optically pumped InGaN/GaN quantum well (QW) VECSELs with latticed-matched AlInN/GaN bottom distributed Bragg reflector (DBR), partially transmitting top DBR, and external mirror at cavity lengths of up to 50 mm. Lasing is achieved at 420 nm wavelength. The lasing features are measured and analyzed by examining variations of the lasing threshold, optical spectrum, far field, and near field patterns as a function of the cavity length. Their behavior give strong evidence of external cavity mode lasing. Furthermore, we perform in-depth analysis on these and other parameters such as spontaneous emission and the delay time to lasing.

6.2   VECSEL Samples

Our group III-nitride semiconductor samples are designed and grown at the LASPE laboratory of EPFL via metalorganic chemical vapor deposition in an AIXTRON 200/4 RF-S reactor. Grown on free-standing GaN substrates from Lumilog, the VECSEL epitaxial layers contain a 42-period GaN/Al$_{0.8}$In$_{0.2}$N bottom side DBR stack [111] and an optical gain region consisting of 24 In$_{0.12}$Ga$_{0.88}$N multiple QWs of 2 nm thickness separated by 4.5 nm thick GaN barrier layers. The total active region thickness l is 370 nm. The optical gain region and the bottom DBR design are optimized for the 420 nm wavelength. The bottom DBR stack has a measured reflectivity $R_1 = 99.6\%$.

The optical gain in InGaN/GaN heterostructure QWs is generally reduced due to the internal built-in field inherent to III-nitride heterostructures grown along c-axis. The use of a VESCEL heterostructure with large number of equally spaced QWs as reported here reduces inhomogeneous broadening of the gain line [112] and increases the cavity fill factor for the gain medium, yielding better absorption of the pump beam and larger optical gain. Thus in a heterostructure with small number of QWs placed at field antinode positions, the side wells do not experience the same built-in field, leading to an inhomogeneous broadening of the QW emission. In contrast, in a heterostructure with large number of equally spaced QWs, the side QWs have a lower contribution compared to the inner wells. Indeed, the photoluminescence measurements have revealed that inhomogeneous broadening does not increase significantly in these 24 QW samples compared to 2 QW samples, attesting to the absence of relaxation in the InGaN QWs due to low In content as well as to the quality of our epitaxial growths.

Furthermore, contrasting from vertical-cavity surface-emitting laser (VCSEL), which operates on a single longitudinal mode, the long cavity VESCEL is expected to exhibit multimode lasing. For a particular mode, the resonant periodic gain structure geometry in VECSEL cavity configuration [108], [109] is very sensitive to displacement of the output coupling mirror as a small shift in the

antinode positions of the VECSEL cavity mode with respect to the QWs results in significant decrease of gain enhancement for this particular mode. The resonant gain structure will thus play the role of an additional intracavity filter favoring lasing of clusters of external cavity modes and leading to a complicated interplay of modes due to inevitable variations of the output coupling mirror position (e.g. caused by temperature fluctuations). Therefore a choice has been made in favor of the optically pumped structure with large number of equally spaced QWs that have already shown lasing action in VCSEL configuration [113].

A top DBR stack consisting of 4 periods of SiO_2/ZrO_2 layers is deposited via electron-beam evaporation, yielding a measured reflectivity $R_2 = 86.6\%$ at 420 nm wavelength. As a reference, a second sample with 7 periods of top SiO_2/ZrO_2 DBR is used here ($R_2 = 98.1\%$). When these samples are excited at 355 nm wavelength (above the GaN barrier layers band edge and within the transmission band of top DBR), photoluminescence spectra show emission intensity maximum near 420 nm wavelength. A schematic of the VECSEL sample epitaxial and dielectric layers is given in Fig. 6.1.
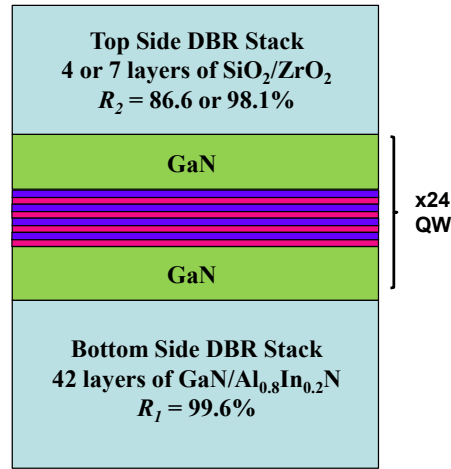
Fig. 6.1. Schematic of the epitaxial and dielectric layers of the VECSEL samples.

In optical pumping experiments (see Section 6.3), the measured reflection coefficient of the pump beam off of the VECSEL sample surface ranges from 20 to 30%. Due to imperfections in the epitaxial growth, there might be significant optical scattering near the gain region. The measured surface roughness σ_{sr} from atomic force microscopy over a 10 µm × 10 µm area is less than 3 nm (rms) before deposition of the partial top DBR stack, yielding estimates of scattering loss $T_s = 1-\exp\{-(\pi\sigma_{sr}/\lambda)^2\}$ as low as 0.05% at the 420 nm lasing wavelength [114]. (This also attests to the good quality of epitaxial growth, showing that the surface morphology is not degraded by the growth of large number of QWs.) On the other hand, assuming a Lambertian profile of scattering pattern, the integrated scattering loss T_s across the sample is measured to be from 1.5 to 7.2% at 420 nm wavelength.

6.3 Experimental Setup

Figure 6.2 shows a schematic of the experiment setup. A VECSEL sample is mounted on a precision translation stage, enabling adjustments of the excitation spot across the sample. The external cavity is closed by a concave mirror with reflectivity R=99.5% and curvature radius ρ_M=50 mm. The flat side of the output mirror is AR coated. The output coupling mirror is mounted on a translation stage, allowing for cavity alignment and length adjustment. A continuously variable neutral density filter wheel is used to adjust the pump power (not shown in the figure). An aspheric lens with focal length of 50 mm focuses the pump beam onto the semiconductor sample at 45° incident angle. For the pump lasers used (see below), the achieved pump beam spot size is slightly elliptical, with measured diameters of ~60 and ~50 μm. Beam profile measurements indicate that the Rayleigh range z_R of the focused pump beam is ~1 mm, indicating acceptable tolerance for the focusing lens position.
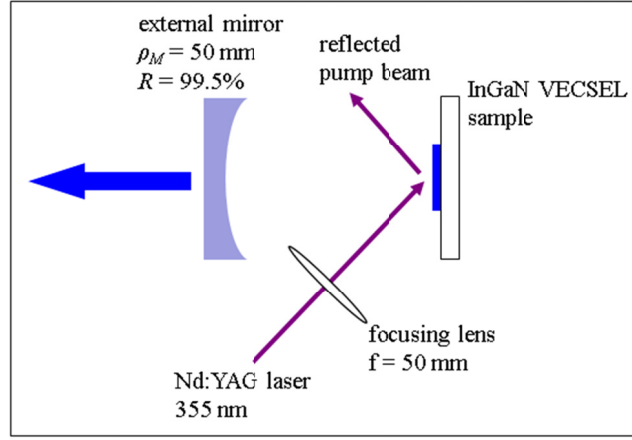
Fig. 6.2. Schematic of the VECSEL cavity arrangement.

The preliminary estimates of threshold pump power for cavity mode size of ~30 μm diameter (at the sample) exceeds 10 W. Therefore, we use high peak power pulsed UV lasers as the optical pump for our VECSELs. (Unlike high power continuous wave UV lasers, Q-switched lasers delivering pulses with peak power >10 W can be procured at a reasonable budget.) In the experiments reported here, we use two different Q-switched frequency-tripled Nd:YAG lasers (λ_p = 355 nm). The first laser (Teem Photonics, SNV-02E) has a pulse width τ_p of 400 ps and repetition rate f_{rep} of 6 kHz. The second laser (Quanta System, Handy H700) produces pulses of 7 ns width and repetition rate f_{rep} = 10 Hz, and its output pulses are stretched to τ_p = 10 ns using a 12 meter long multimode fiber (Thorlabs, custom order). A multimode fiber is used due to modal dispersion and its significantly higher coupling efficiency compared to single mode fiber. Obtaining the same output power from a single mode fiber will require higher pump laser power incident at the fiber end, which might damage the epoxy fixing the fiber in the ferrule.

For a VECSEL cavity of 50 mm length, the cavity roundtrip time is 330 ps, which is only slightly shorter than the pulse duration of the first pump laser. Without the partial top DBR, the time T_b required for lasing modes to build up in a 50 mm long cavity is ~680 ns when pumped at twice the threshold according to the expression $T_b=25T_{rep}/(r-1)G_{th}$ [115], where T_{rep} is the cavity round trip

time, $r = I_{pump}/I_{th}$ is the normalized pump rate, and G_{th} is the cavity round trip gain at threshold. Thus, lasing under pumping with either 400 ps or 10 ns pulses in such standalone long cavity VECSEL would not be possible because the pump pulses do not last long enough [108]. In contrast, the buildup time of lasing emission in the VCSEL cavity itself (l=370 nm) is much shorter at 10 ps or less. Therefore, we overcome the difficulties of achieving lasing in VECSELs of long cavity lengths by forming an auxiliary microcavity to provide injection seeding for the external cavity mode at early stages of the lasing build up. This is done by depositing a partially transmitting top DBR stack as indicated in Fig. 6.1. (No such auxiliary microcavity is needed under continuous wave pumping.)

The onset of lasing in the microcavity provides injection seeding into the lasing mode of external VECSEL cavity. In the rest of this chapter, we examine various lasing characteristics of such VECSELs. We show that they are drastically different from the lasing features of a solitary micro-cavity, i.e. a VCSEL.

6.4   Lasing Threshold Measurement and Analysis

6.4.1 Light-Light Measurement Method with 400 ps Pump Laser

The majority of measurements presented in this chapter are made using the pump laser with 400 ps pulse duration. This includes the important results on lasing threshold presented in Section 6.4.4. Here, we detail the procedure and method used to produce light-light (L-L) curves for these measurements, because they are not straightforward with respect to the usual methods.

In experiments made with the pump laser with 400 ps pulse duration, lasing emission from the external cavity output coupling mirror was injected into a fiber-coupled spectrometer (Jobin Yvon, TRIAX 550). Similar fiber-coupling was done for measurements in VCSEL configuration, i.e. with no external cavity mirror. Optical pump powers incident on and reflected from sample were measured with a Newport 1918-C optical power meter with a 918D-UV-OD3 detector head. As mentioned previously, the reflected power range from 20-30% of the incident power. The absorbed pump power is then calculated from the difference of incident and reflected powers.

The (average) output power from our VECSEL was below the sensitivity of the power meter available. Therefore, to construct the L-L curves, we first measure the spectra of the VECSEL emission at a series of different optical pump powers. We then normalize (with respect to the integration time) and integrate the spectral power density to obtain the relative output intensity. An example of this is given in Fig. 6.3, where we characterize a 35 mm long VECSEL constructed using the semiconductor sample with 4-period top DBR. In Fig. 6.3(a), we plot the series of spectra of the VECSEL output, normalized to the integration time of each spectra measurement. From these spectra, we construct the L-L curve, which is given in Fig. 6.3(b). The smooth transition to lasing is a feature we partially attribute to amplified spontaneous emission (see Section 6.7).

The chief weakness of this method is that while we can construct L-L curves and obtain the lasing thresholds, we cannot measure the absolute output power from our VECSEL. We overcame this problem in the set of measurements made with the 10 ns pump laser.
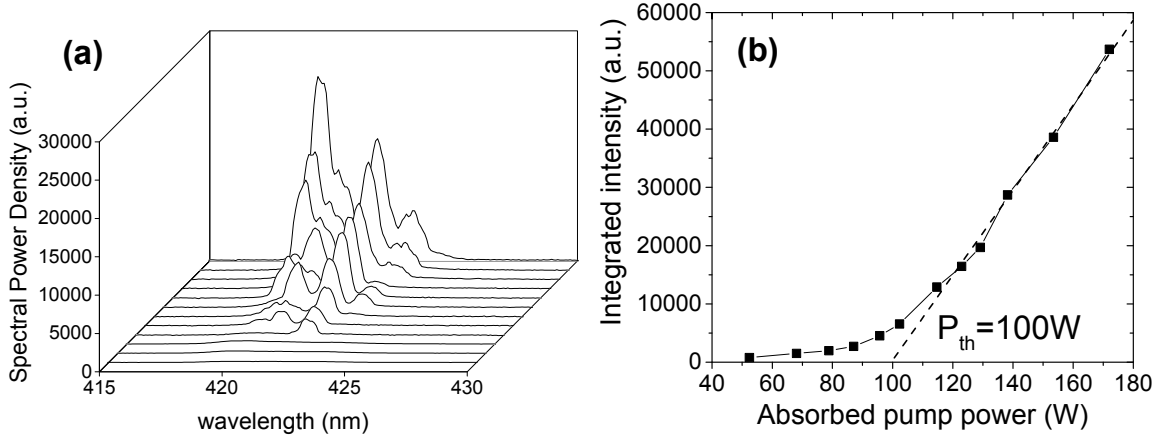

Fig. 6.3. We characterize a 35 mm long VECSEL cavity with 4-period top DBR. The pump laser pulse duration is 400 ps. (a) Measured spectra at different pump powers. (b) L-L curve, constructed from measured spectra. Peak threshold pump power of 100 W correspond to power density of ~4200 kW/cm^2. Pump pulse duration is 400 ps.

6.4.2   Light-Light Measurement Method and Results with 10 ns Pump Laser

In experiments made with the pump laser with 10 ns pulse width, the pump powers were measured with an Ophir Nova optical power meter with a PD300 detector head. In these measurements, we procured a reverse biased calibrated photodiode (Thorlabs, FDS010) with rise/fall time less than 1 ns, which we use to observe the VECSEL output on an oscilloscope. Therefore, we are able measure the instantaneous VECSEL output power in the time domain. With a fast calibrated photodiode, we bypass the challenge of measuring low average output power with a (slow) optical power meter, which was the obstacle that prevented us from making absolute power measurements in experiments using the 400 ps pulse pump laser. Here, L-L curves are constructed using the peak power measured in oscilloscope waveforms.

Under 10 ns pumping, we performed in total four L-L measures. These are (i) the 7-period top DBR sample operating as a VCSEL (no external cavity mirror); (ii) the 7-period top DBR sample operating as a VECSEL in semiconfocal configuration (nearly 50 mm long cavity); (iii) the 4-period top DBR sample operating as a VCSEL; and (iv) the same sample operating in semiconfocal configuration.

The L-L curves of the 7-period top DBR sample in VCSEL configuration as well as in semiconfocal cavity configuration are given in Fig. 6.4. The 7-period top DBR sample, operating as a VCSEL, has peak threshold pump power of 1.41 W and slope efficiency of 7.36×10^{-4} W/W, with measured peak output power up to 3.2 mW. The same sample operated as a VECSEL in semiconfocal configuration has a slightly lower lasing threshold of 1.26 W and slope efficiency of 2.38×10^{-4} W/W. We measured peak output powers of up to 1.4 mW, lower than what was possible in VCSEL configuration. We attribute this to the high reflectivity of the combined mirror formed by the output coupler

and top DBR as well as due to losses caused by a lateral mismatch between the external cavity mode and spatial gain distribution. For the 4-period top DBR sample under 10 ns pumping, we made the same type of L-L measurements, and we measured peak threshold pump powers of 3.38 W and 2.57 W and slope efficiencies of 2.23×10^{-4} W/W and 1.14×10^{-5} W/W for VCSEL and semi-confocal VECSEL configurations, respectively.
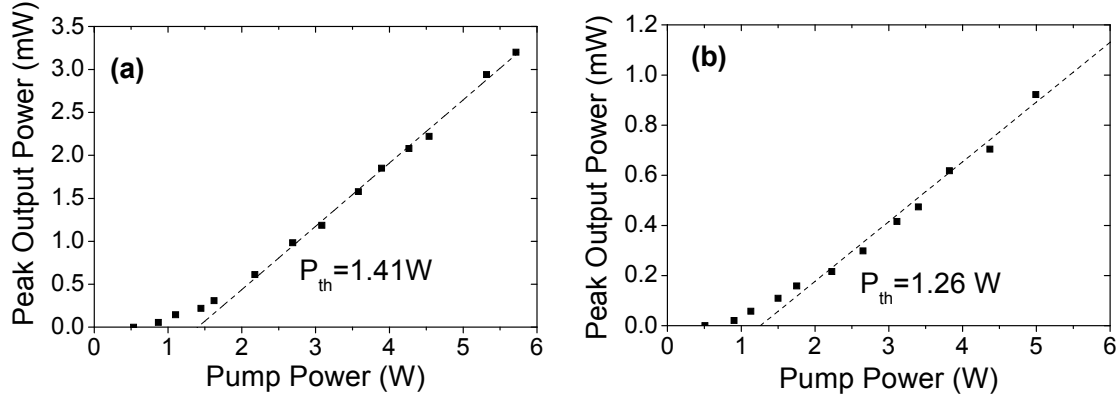
Fig. 6.4. Under optical pumping by 10 ns pulses, the L-L curve of 7-period top DBR sample in (a) VCSEL configuration (no external cavity mirror). Threshold pump power is 1.41 W, and the slope efficiency is 7.36×10^{-4} W/W. (b) The same sample in semiconfocal cavity configuration (nearly 50 mm long cavity). Threshold pump power is reduced to 1.26 W, and the slope efficiency is 2.38×10^{-4} W/W.

6.4.3 Impact of the Pump Pulse Duration on Lasing Threshold

There are significant differences in VECSEL threshold powers when using pump lasers of different pulse duration. The measured threshold powers in the 10 ns pump laser setup are lower than those measured in the 400 ps pump laser setup by a factor of 17. This is shown in Fig. 6.5 where the normalized L-L curves of the 7-period top DBR sample in semiconfocal VECSEL configuration from both measurement setups are plotted together (in logarithmic scale).

To understand the mechanism behind this large difference in lasing threshold, we analyzed the rate equation for carriers below threshold,

$$\frac{d}{dt}n(t) = P(t) - \frac{1}{\tau_e}n(t) \, ,$$

(6.1)

where $n(t)$ is the carrier concentration, $P(t)$ is the carrier pump rate (rate of optically generated carriers captured by the QWs), and τ_e is the carrier lifetime. Note that this is a very simplistic treatment where the full dynamics of the carriers, which include spontaneous radiative recombination and Auger recombination processes, are ignored. These effects are ignored on the grounds that their effects on lasing threshold are small compared to the effects of optical pulse duration in the cases considered here, but this is not necessarily true in general. Nonetheless, this simple treatment allows for analytical solutions where valuable insights can be gained.

Fig. 6.5. L-L measurement data for 7-top DBR sample in semiconfocal VECSEL configuration, pumped by frequency-tripled Nd:YAG lasers with pulse lengths 10 ns (triangles) and 400 ps (squares). Peak threshold powers are 1.26 W and 22.2 W, respectively.

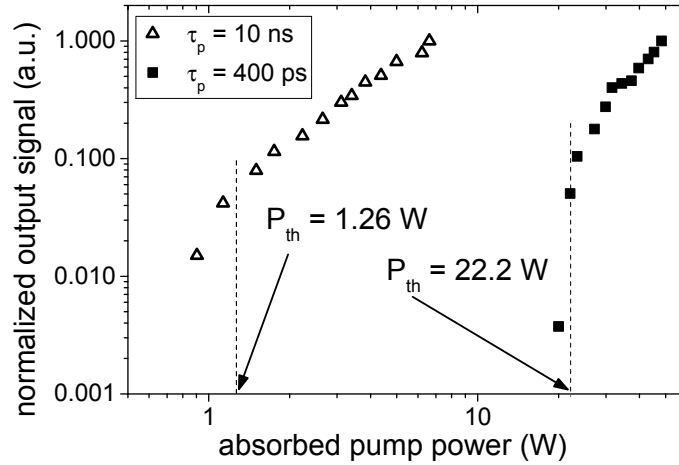Under continuous wave (CW) pumping, $P(t) = P_0$ is constant, and the steady-state carrier concentration is $n_{CW} = P_0\tau_e$. When the optical pump pulses are 10 ns long, the extracted carrier lifetime in the QWs is 2.5 ns (see Section 6.8), which is shorter than the pump pulse. We thus approximate the case of 10 ns pumping as that of quasi-CW pumping, where the carrier density reaches that of steady-state n_{CW}.

To understand the effect of short pulse pumping of same peak power, we assume the pump waveform to be Gaussian, $P(t)=P_0\exp(-t^2/(\tau_p/2)^2)$ with τ_p being the pulse width at e^{-1} intensity level. Solving Eq. (6.1) for carrier density, we obtain

$$\frac{n_{pulsed}(t)}{n_{CW}} = \exp\left(\frac{\tau_p^2}{16\tau_e^2}\right)\frac{\tau_p\sqrt{\pi}}{4\tau_e}\exp\left(-\frac{t}{\tau_e}\right)\left[1 + erf\left(\frac{2t - \tau_p^2/4\tau_e}{\tau_p}\right)\right].\qquad(6.2)$$

The implication of Eq. (6.2) is that when $\tau_p < \tau_e$, $n_{pulsed}(t)$ peaks at a value significantly smaller than n_{CW}. This means under equal peak pump power, short pulse optical pumping provides smaller carrier density when compared to quasi-CW pumping. Hence, peak threshold power is higher under short pulse pumping. In Fig. 6.6, we plot the ratio in Eq. (6.2) taking $\tau_e = 2.5$ ns, $\tau_p = 400$ ps, and approximating pumping with 10 ns pulses as quasi-CW pumping. The carrier density under short-pulse pumping is smaller by a factor of 8.1. Respectively, in the considered case of Gaussian pump pulse of 400 ps width, the threshold should be higher by the same factor of 8.1 as compared to quasi-CW pumping.

Larger difference of thresholds, as we observed in experiment, can be attributed to the non-Gaussian shape of the Q-switched pulse of the pump laser with steeper rising front and smoother trailing edge, to the slightly larger spot size of the focused pumping beam in the setup utilizing 400 ps width pulses, as well as to difference in calibration of the two detectors.
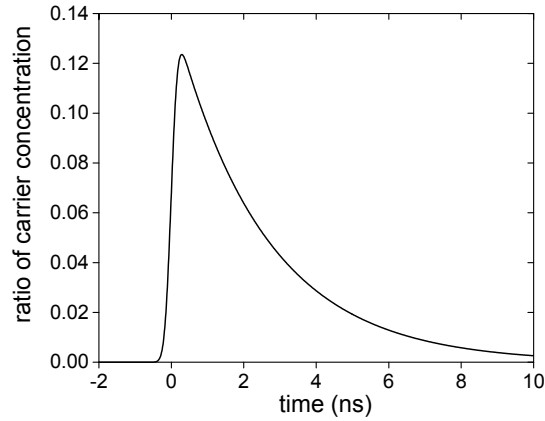
Fig. 6.6. Ratio of carriers under 400 ps pump pulses to 10 ns pump pulses assuming $\tau_e = 2.5$ ns and $\tau_p = 400$ ps. The ratio peaks at 0.1236.

6.4.4 Threshold vs. Cavity Length Relationship

In experiments with the 400 ps pump laser, we made extensive measurements of lasing threshold at different external cavity lengths. In Fig. 6.7, the threshold pump power is shown as a function of the external cavity length L, which is varied from 25 mm (where cavity mode is at its largest) to 50 mm (semiconfocal configuration, where cavity mode is at its smallest). In agreement with the mode size considerations, there is a general trend of increasing threshold pump power when the cavity length is decreased from 50 mm down to 25 mm. The threshold pump powers for the sample with 4-period top DBR is consistently greater than those of the 7-period top DBR sample.
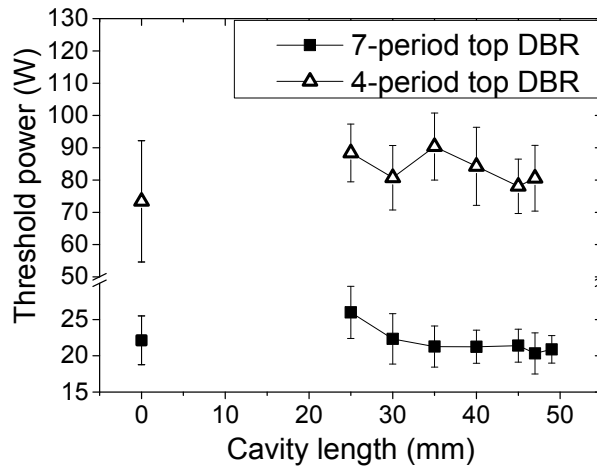
Fig. 6.7. Peak threshold absorbed pump powers for the VECSELs with 4 (open triangles) and 7 (squares) top DBR periods at different cavity lengths. Lasing thresholds without external cavity mirror (i.e. VCSEL configuration) are indicated at L=0 mm. The pump laser duration is 400 ps.

Interestingly, contrary to the expected behavior for a semiconductor laser operating with external cavity, the VECSEL thresholds are not always smaller than the VCSEL thresholds. The lasing thresholds of 25 mm cavity length VECSELs are larger than their thresholds when operated as VCSELs. To understand this unusual behavior, we use a conventional model for a VCSEL with

101

feedback from an external mirror [25] but with several important modifications. From analysis, the ratio of the threshold pump power of a VCSEL with external mirror feedback to that of a VCSEL without is

$$\frac{P_{th}}{P_{th0}} = \left[\frac{2\alpha l + T_{sc} - \ln(R_1 R_{eff})}{2\alpha l + T_{sc} - \ln(R_1 R_2)} \right] \left[\frac{1}{2} \left(1 + \frac{w^2}{w_p^2} \right) \right],$$ (6.3)

where α is the intrinsic loss of the semiconductor gain region (35 cm^{-1}), l is the VCSEL microcavity length, R_1 and R_2 are the bottom and top DBR stack reflectivities, respectively, R_{eff} is the effective reflectivity of the combined mirror formed by top DBR and external output coupling mirror, and T_{sc} is the scattering loss coefficient. The last term on the right hand side accounts for the mismatch between the external cavity mode and the pump laser spot [116]. Here, $2w$ is the external cavity mode diameter on the semiconductor sample, and $2w_p \approx 50$ μm is the pump laser spot size. When operating as a VCSEL, $2w_p$ defines the size of the lasing mode. However, under external cavity configuration, w_p defines the spatial gain distribution, accounted for by the model as an aperture with Gaussian profile. Respectively, the threshold rises if the VECSEL cavity mode does not match the gain distribution.

The spatial gain distribution is accounted for by the model as an intracavity aperture with Gaussian profile. The VECSEL cavity mode size $2w$ is calculated with a Gaussian aperture of size $2w_p$ embedded in the active region and represented by the ray transfer ABCD matrix

$$\begin{bmatrix} 1 & 0 \\ -\frac{i\lambda}{\pi w_p^2} & 1 \end{bmatrix},$$ (6.4)

where $\lambda = 420$ nm is the lasing wavelength (not the pump beam wavelength). The resulting ABCD matrix of the VECSEL cavity roundtrip, starting at the bottom DBR of semiconductor sample, is

$$\begin{bmatrix} 1 & 0 \\ -\frac{i\lambda}{\pi w_p^2} & 1 \end{bmatrix} \begin{bmatrix} 1 & L \\ 0 & 1 \end{bmatrix} \begin{bmatrix} 1 & 0 \\ -\frac{2}{\rho_M} & 1 \end{bmatrix} \begin{bmatrix} 1 & L \\ 0 & 1 \end{bmatrix} \begin{bmatrix} 1 & 0 \\ -\frac{i\lambda}{\pi w_p^2} & 1 \end{bmatrix},$$ (6.5)

where L is the VECSEL cavity length and ρ_M is the output coupler curvature radius (50 mm).

From the matrix in Eq. (6.5), we then solve for the beam parameter $1/q = 1/R - i\lambda/\pi w^2$ of the fundamental cavity mode (M^2=1) at the flat bottom DBR, where the wavefront is flat (R=∞). For the generalized case M$^2 \geq 1$, where M^2 is the beam quality parameter [117], we obtain the cavity mode size w and its far field angular width θ (half width at e^{-2} of maximum)

$$w = \sqrt{\frac{-M^2 \lambda}{\pi \cdot \text{Im}(1/q)}}, \quad \theta = \sqrt{\frac{-M^2 \lambda \cdot \text{Im}(1/q)}{\pi}}.$$ (6.6)

Figure 6.8 shows the fundamental mode diameter of the VECSEL cavity, plotted vs. cavity length without and with Gaussian aperture of diameter 50, 100 and 200 μm. The Gaussian aperture reduces

the cavity mode size, and its impact is especially significant for short (~25 mm) cavities and small apertures. In a 25 mm long cavity and assuming fundamental mode operation, $2w$ is 116 µm without the Gaussian aperture effect. The mode size reduces to 50 µm with a 50 µm diameter Gaussian aperture defined by the pump beam, as it is the case in the VECSEL configuration considered here.
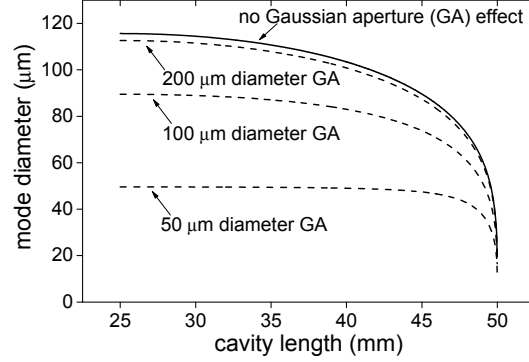
Fig. 6.8. Calculated cavity mode diameter on the VECSEL semiconductor sample vs. cavity length without (solid curve) and with the Gaussian aperture effect (dashed curves) for aperture diameter of 50, 100 and 200 µm.

In Eq. (6.3), the effective reflectivity of the top DBR stack and external mirror combination is evaluated here as

$$R_{eff} = \left[\left(\sqrt{R_2} + \chi\sqrt{R}\right)/\left(1 + \chi\sqrt{RR_2}\right)\right]^2 , \tag{6.7}$$

where R_2 and R are the top DBR and external output coupler reflectivities, respectively. Unlike the usual expression for a collimated beam and flat external retroreflector, we account for the imperfect spatial overlap between the initial mode of free-running VCSEL (defined by the pump spot) and the reflected beam off the external concave mirror. The spatial overlap coefficient χ in Eq. (6.7) is calculated by first finding the size of beam after it first propagates from the semiconductor sample (VCSEL) to the external mirror and back to the semiconductor sample again using transfer matrix analysis. With the two beam sizes, one can then find χ by calculating the area integral of the product of the two beams' normalized electric fields, assuming Gaussian beam profile, yielding $\chi=2w_p w_{ref}/(w_p^2+w_{ref}^2)$, where w_p is the VCSEL mode radius and w_{ref} is the reflected beam radius at the sample. Note that $\chi = 1$ when $w_p = w_{ref}$.

Figure 6.9 illustrates the effects of pump spot size and cavity length on R_{eff} in VECSEL samples with 7- and 4-period partial top DBRs as we used in the experiment. In the figure, R_{eff} is plotted against pump beam diameter for fixed cavity lengths of 25, 35, and 45 mm when $M^2 = 1$. We find that R_{eff} is very sensitive to the pump spot size for the 4-period top DBR sample with its less reflective top DBR. As the pump spot on the semiconductor sample is decreased, R_{eff} diverges for the different cavity lengths, highlighting the importance of the spatial overlap coefficient χ in Eq. (6.7).
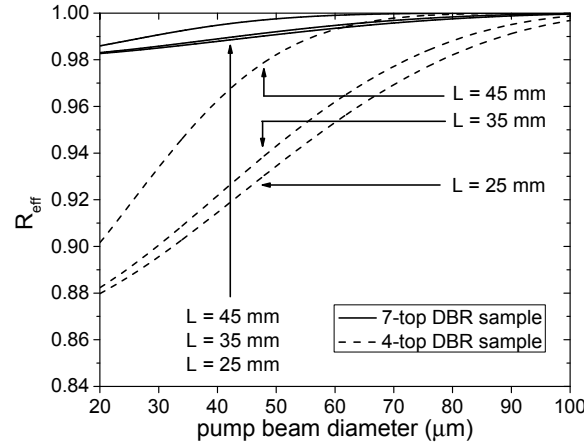
Fig. 6.9. R_{eff} vs. pump beam diameter on the semiconductor sample for VECSEL cavity lengths of 25, 35, and 45 mm and partial top DBR stack of 7 periods (solid curves) and 4 periods (dashed curves) when $M^2 = 1$.

In Fig. 6.10(a), R_{eff} is plotted against cavity length on the semiconductor sample for pump spot diameters of 30, 50, and 70 μm when $M^2 = 1$. As expected, R_{eff} increases as the cavity length is increased towards semiconfocal configuration. R_{eff} is more susceptible to the changes in cavity length for the 4-period top DBR sample, once again due to its not so highly reflective top DBR. Again, we also see that R_{eff} is greater for larger pump spots, with implication that using a highly focused beam for pumping VECSELs can be very challenging due to the increase in threshold. In Fig. 6.10(b), mismatch factors $1/2(1+w^2/w_p^2)$ and χ are plotted against cavity length for the same pump spot diameters when $M^2 = 1$.
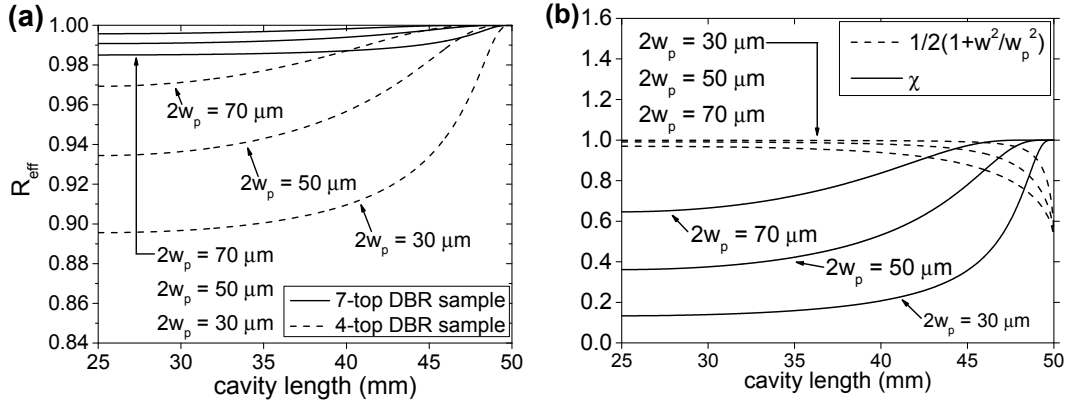
Fig. 6.10. (a) R_{eff} vs. VECSEL cavity length for pump spot diameters of 30, 50, and 70 μm in 7- (solid curves) and 4-period (dashed curves) partial top DBR stack samples. (b) Mismatch factors $1/2(1+w^2/w_p^2)$ and χ as a function of cavity length for the same pump spot diameters when $M^2 = 1$.

Figure 6.11 shows the measured ratio P_{th}/P_{th0} as a function of VECSEL cavity length (points). The fit of the threshold ratio evolution (curves) utilizes values $R_2 = 98.1\%$ (86.6%), $T_{sc} = 7\%$, $M^2 = 1.2$ (1.5), and $2w_p = 20$ μm (40 μm) for the 7-period (4-period) top DBR samples. The value for T_{sc} is taken from light scattering measurements off sample surface. The values of the top DBR reflectivity R_2 are taken from the measured values from samples. The M^2 factor and $2w_p$ were the free parameters of the fit. The M^2 values are close to the ones obtained from beam profile measurements (see

Section 6.6). The $2w_p$ values reported by the fit are smaller than the measured pump beam sizes. We attribute this discrepancy to the combination of measurement uncertainties in all other parameters, especially that of M^2.

To demonstrate the importance of the mismatch between the VECSEL cavity mode and pump beam spot as well as that of the imperfect spatial overlap between the beam reflected from the output coupling mirror with initial mode of free-running VCSEL, we also plotted the ratio P_{th}/P_{th0} assuming either $w/w_p=1$ or $\chi=1$ (two dotted curves). In the first case, we neglect the last term in the right hand side of Eq. (6.3). In the other case, we neglect the imperfect spatial overlap when calculating R_{eff}. These two curves exhibit P_{th}/P_{th0} below unity for all cavity lengths. We recover the experimentally observed ratio $P_{th}/P_{th0} > 1$ for short cavity lengths only after both effects are taken into account.
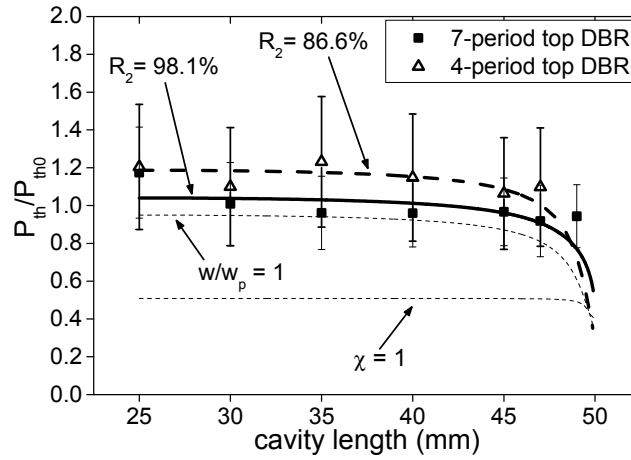
Fig. 6.11. The measured (points) and calculated (curves) threshold pump power ratio of VECSEL and VCSEL as a function of external cavity length. The pump laser duration is 400 ps. The solid/dashed curve and squares/triangles are the threshold ratios for the 7/4-period top DBR VECSEL. The two dotted curves are plotted for the 4-period top DBR VECSEL assuming $w/w_p=1$ or $\chi=1$, respectively. The error bars in the measured data points are the fitting errors in the numerical fits of L-L curves.

6.5   Lasing Spectrum

We have extensive measurements of lasing spectra at different external cavity lengths in experiments done with the 400 ps pump laser, and some of the results are presented here. Figure 6.12 shows linewidths of the lasing spectra as a function of the external cavity length at pump powers of 29.2 W and 138 W for samples with 7- and 4-period top DBR, respectively. The spectral linewidth increases when the cavity length is decreased from the edge of cavity stability (at $L = 50$ mm). This can be attributed to the fact that external cavity losses and threshold are lower for longer VECSEL cavities (see Fig. 6.11), and this results in narrower cold cavity linewidths. In addition, at constant pump power as in Fig. 6.12, the relative excess above threshold is higher for the longer cavity lengths, which further contributes to spectral narrowing. The evolution of the laser cavity output spectrum provides good evidence that the optical system operates as a VECSEL.
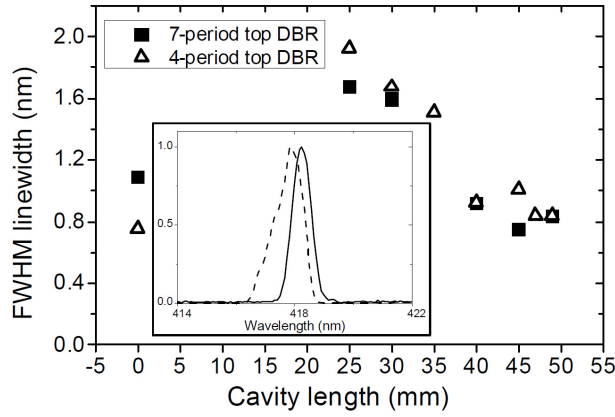
Fig. 6.12 FWHM linewidth vs. cavity length for the 7- and 4-period top DBR VECSELs, optically pumped at 29.2 and 137.5 W, respectively. The pump laser duration is 400 ps. Inset: Spectra of 7-period top DBR VECSEL at 49 (solid) and 30 mm (dotted) cavity lengths.

Figure 6.13 shows the evolution of lasing spectrum of the 45 mm long 4-period top DBR VECSEL when pumped at powers ranging from 86.7 to 147 W at the peak of the pulse. There is a slight blue shift of the spectrum with increasing pump power. The primary mechanism for spectrum blue shift is the free carrier screening effect, in which carriers generated by higher pump excitations screen the internal electric field significant in III-nitride QWs grown along the c-axis, which reduces the quantum-confined Stark effect [118]. Band-filling effect in QWs also contributes to the blue shift in spectrum. Due to the low duty cycle of the pump pulses, red shifting due to thermal effects is negligible.
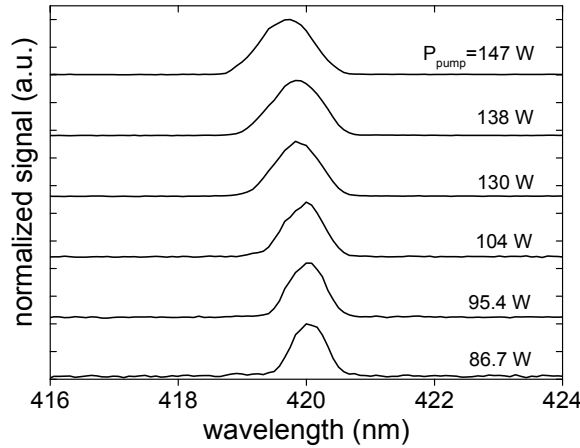
Fig. 6.13. Lasing spectra of 45 mm cavity VECSEL incorporating 4-period partial top DBR stack at different (peak) absorbed pump powers. The pump laser duration is 400 ps.

Figure 6.14 shows the full-width at half-maximum (FWHM) linewidths of the lasing spectra as a function of absorbed pump powers for the 4-period top DBR sample operating as a VCSEL or a 45 mm cavity VECSEL. Linewidth is broad below threshold and drastically shrinks once above threshold. While there are not enough data points around threshold to confirm agreement with Schawlow-Townes behavior for linewidths, this linewidth reduction is nonetheless in general

agreement. Far above threshold, linewidth broadens due to excitation of other lasing modes, and possibly also due to change in material index under high carrier population.
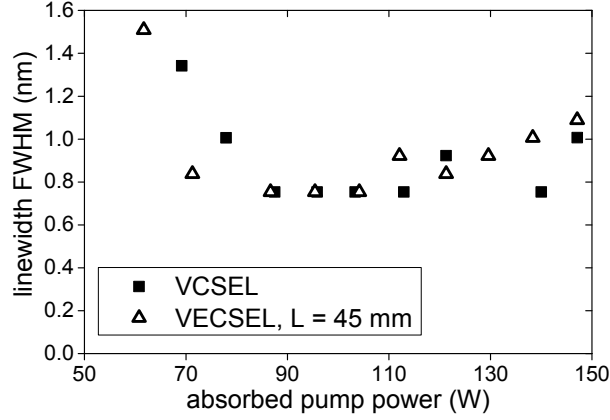
Fig. 6.14. The measured FWHM of spectrum linewidth for the 4-period top DBR sample operating as VCSEL (squares) and as 45 mm cavity VECSEL (triangles), plotted as a function of the absorbed pump power. The pump laser duration is 400 ps.

6.6 Beam Profile Measurement

To further confirm the impact of the external cavity mirror, we perform near field and far field beam profile measurements of the VECSEL cavity output, when pumped with the 400 ps laser, using a charged-couple device (CCD) camera. The far field angular spectrum of the emitted radiation is analyzed by placing the camera sensor in the focal plane of a lens. From far field and output beam profile intensity patterns, the beam quality parameter M^2 is extracted.

Measurements are made for both VECSEL samples at cavity length of 49 mm, 35 mm, and 25 mm as well as without external cavity mirror. Figure 6.15 plots the detected FWHM far field patterns. As expected, the angular width of the VECSEL lasing mode is significantly smaller than that of the semiconductor sample when operated as a VCSEL. The measured angular width exceeds that of the fundamental Gaussian mode of the cold cavity, implying beam quality factor $M^2 > 1$. The enlargement of the mode divergence angle is likely due to inhomogeneity of the VECSEL sample and/or of the pump beam profile.

For long cavity VECSEL, the beam quality parameter M^2 is evaluated from the beam parameter product $\theta \cdot w(z)$, where θ is the measured beam divergence (from the far-field angular spectrum in Fig. 6.15), and $w(z)$ is the beam size measured at distance $z \gg z_R = \pi w_0^2 / \lambda$ with w_0 being the fundamental cavity mode size at the VECSEL sample for $M^2 = 1$ (note that the measured FWHM values of 2θ and $2w(z)$ are adjusted to account for the fact that the beam parameter product is defined at e^{-2} intensity level). In our setup, we use $z = 123$ mm for Rayleigh distances z_R ranging from 0.75 mm (when $w_0 = 10$ μm) to 18.7 mm (for $w_0 = 50$ μm). We then calculate M^2 from the equation

$$M^2 = \theta \cdot w(z) / \theta_{ideal} \cdot w_{ideal}(z) \, , \tag{6.8}$$

where θ_{ideal} and $w_{ideal}(z)$ are the divergence and beam size for the ideal case of $M^2 = 1$. For $z \gg z_R$, we have $\theta_{ideal} = \lambda/\pi w_0$ and $w_{ideal}(z) = z\lambda/\pi w_0$, where w_0 is calculated using methods detailed in Section 6.4.3.

Figure 6.16 shows the extracted M^2 values. As expected, the M^2 value of the semiconductor sample when operated as a VCSEL is significantly larger than those of VECSEL. The cavity length 49 mm gives the lowest M^2 value near 1.0 for the 7-period top DBR sample. This is the expected result for a cavity approaching the semiconfocal configuration, for which the external cavity mirror provides the strongest optical feedback as shown by the relative threshold dependence in Fig. 6.11.
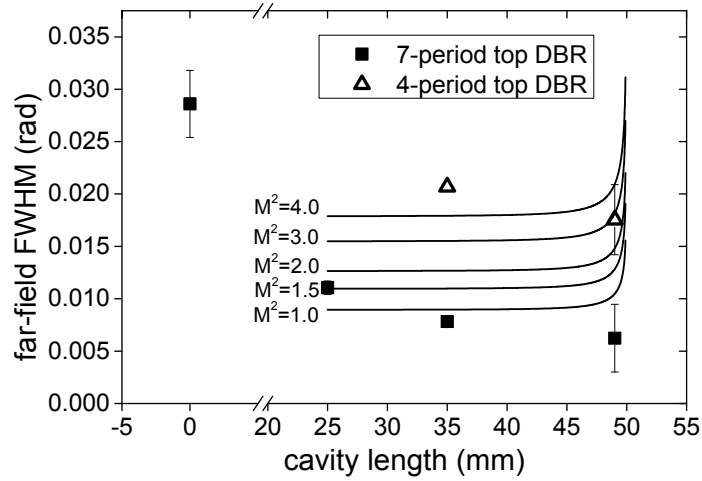
Fig. 6.15. The measured far field FWHM for VECSELs with 7 (squares) and 4 (triangles) periods of top DBR. The pump laser duration is 400 ps. The curves show calculated angular widths of a cold cavity Gaussian mode assuming Gaussian aperture of 50 μm diameter and $M^2 = 1.0$ to 4.0.
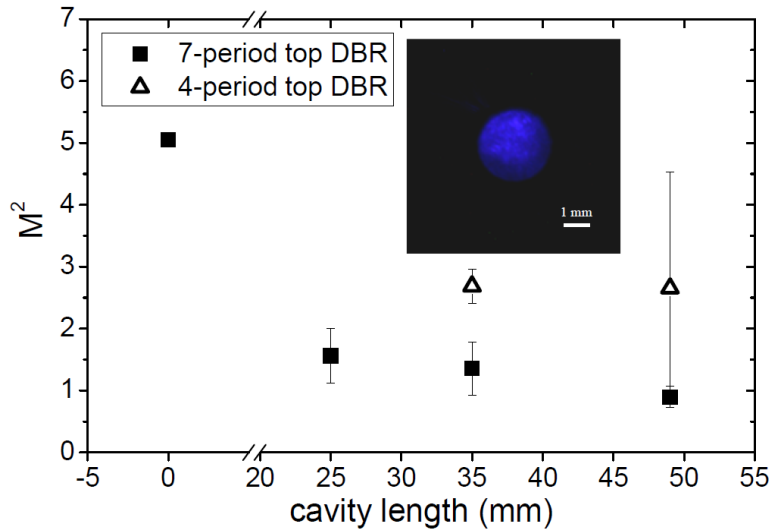
Fig. 6.16. Extracted M^2 values plotted as a function of VECSEL cavity length. The pump laser duration is 400 ps. The inset shows the beam intensity profile (true color) measured at 74 mm from the curved output coupler of 49 mm cavity VECSEL with 7-period top DBR. (This distance corresponds to $z = 123$ mm from VECSEL sample.) Note that all measured M^2 values are greater than 1.0, but some of them have large uncertainties.

Having extracted the M^2 values and the far-field angular width 2θ, one can estimate the lasing mode size at the semiconductor sample for VECSELs. Figure 6.17 shows the extracted lasing mode diameter along with the theoretical predictions for a cavity with Gaussian aperture of 50 μm diameter. The misalignments in the resonant cavity, inhomogeneity of the VECSEL sample and/or of the pump beam profile result in enhancement of the lasing mode size.
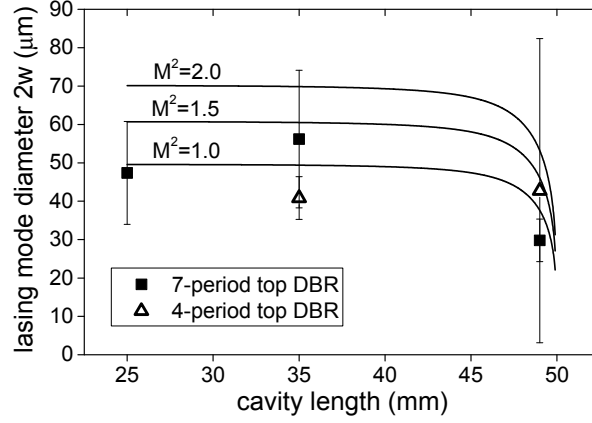
Fig. 6.17. The extracted VECSEL beam waist diameters and calculated fundamental cavity mode size at the VECSEL sample, plotted as a function of the cavity length for Gaussian aperture of diameter 50 µm and M^2 factor of 1.0, 1.5, and 2.0. The pump laser duration is 400 ps.

6.7   Spontaneous Emission

We examine variations of the spontaneous emission factor β_{sp}, which is proportional to the ratio between the spontaneous emission radiated into the solid angle occupied by the cavity mode and the total spontaneous emission radiated by the VECSEL QWs [119]. In particular, β_{sp} is expected to vary with the cavity length following the measured dependence of the mode angular FWHM in Fig. 6.15.

One can extract the spontaneous emission factor β_{sp} from measured L-L curves, using the equation for integrated output intensity [115] $I_{out} \propto r - 1 + \sqrt{(r-1)^2 + 4\beta_{sp}r}$, where $r = I_{pump}/I_{thr}$ is the normalized pump rate. In Fig. 6.18, we plot β_{sp} as a function of cavity length for VECSEL under 400 ps pumping. Using numerical fit, we estimate β_{sp} to range from 5×10^{-3} to 1.0×10^{-2} for most cavity configurations, with the outliers of 9.4×10^{-4} and 2.0×10^{-2} for the cases of 45 mm 7-period top DBR VECSEL and 47 mm 4-period top DBR VECSEL, respectively. Large variations in β_{sp} might be attributed to errors in the L-L measurements below threshold.

In the 7-period top DBR sample, β_{sp} tends to be smaller than in 4-period top DBR sample (at least at the longer cavity configuration). This is correlated with the angular widths of the lasing mode in Fig. 6.15 being smaller in the 7-DBR case. This correlation can be attributed to the fact that spontaneous emission factor is proportional to the solid angle occupied by the cavity mode [119].
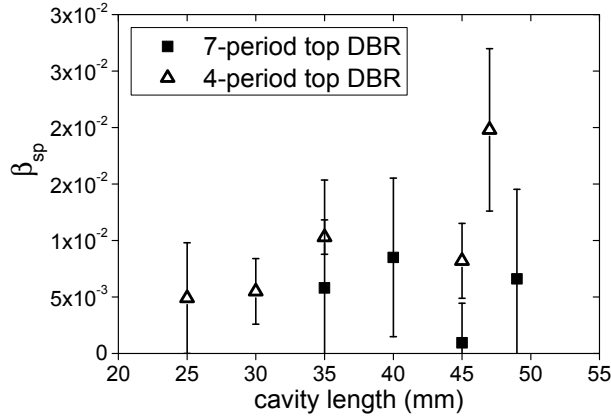
Fig. 6.18. Spontaneous emission factor β_{sp} as a function of VECSEL cavity length under 400 ps pumping for samples with 7 (squares) and 4 (triangle) top DBR periods. The pump laser duration is 400 ps.

6.8 Lasing Waveforms

For measurements made with the pump laser with 10 ns pulse duration, we examine the lasing waveforms of the VECSEL and VCSEL output pulses by using a biased photodiode (<1.0 ns rise/fall time) fed to an oscilloscope. For these measurements, a small portion of the pump pulse is deflected by a thin glass slide into a second photodiode, yielding a trigger signal to the oscilloscope.

Figure 6.19 shows two lasing waveforms: the 7-period top DBR sample operating as a semiconfocal VECSEL when pumped at peak power of 6.62 W, and the same sample operating as a VCSEL when pumped at 5.32 W (the traces are shown shifted along the vertical axis). The overshoot at the leading edge seen in the VCSEL waveform might be due to damped relaxation oscillations in the VCSEL, which cannot be resolved with our detector. The pump pulse rise time from 10% to 90% of the peak is ~5.6 ns (see the inset in the figure). The rise time of the VECSEL output lasing pulse is 4.4 ns, and the VCSEL rise time is 2.0 ns. Both are shorter than the rise time of the pump pulse, and this dynamic behavior is expected. Lasing emission builds up only when the accumulated carrier density in the QWs rise above the VCSEL lasing threshold, resulting in a delay of the lasing pulse and compression of the rising front. Contrasting to this, below threshold, the luminescence wave-form rise times are the same as those of the pump pulse.

In VECSEL, the delay time to emission is larger than for VCSEL (as measured at 50% of the rising front). This behavior is also expected as it indicates that longer time is needed for a lasing pulse to build up in 50 mm long cavity VECSEL as compared to VCSEL with ~1 μm effective cavity length (see discussion in the beginning of Section 6.3).
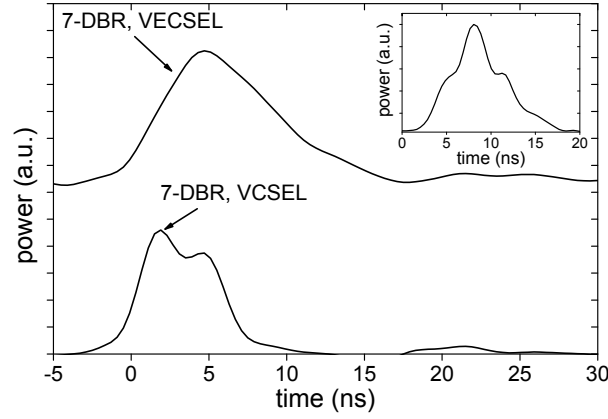
Fig. 6.19. Lasing output pulse of the 7-period top DBR sample operating as a semiconfocal VECSEL (top) and VCSEL (bottom) when pumped by 10 ns long pulses. The traces are shown shifted along the vertical axis. Inset: Envelope of pump pulse; the rise time is ~5.6 ns.

In Fig. 6.20, we plot the lasing pulse delay time (to 50% of the peak intensity) as a function of the pump power for the 7-period top DBR sample operating as a semiconfocal VECSEL and as a VCSEL. From the measured evolution of the lasing pulse delay time t_d, we evaluated the carrier lifetime τ_e in the semiconductor QWs under our optical pumping conditions, using the relationship [120]

$$t_d = \tau_e \cdot \ln[P_{pump} / (P_{pump} - P_{th})],\qquad(6.9)$$

where P_{th} is the lasing threshold pump power. The extracted carrier lifetime τ_e is 2.5 ns, typical for InGaN QWs [70], [121]. This is important parameter for the modelocked laser model in Chapter 7. Note that we cannot obtain a proper fit for the VECSEL delay times, likely because the relationship in Eq. (6.9) is not valid in the case of external cavity VECSEL.
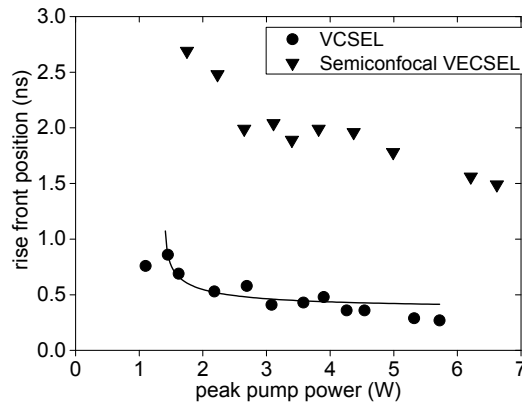
Fig. 6.20. Lasing pulse delay time vs. peak pump power for semiconfocal VECSEL with the 7-period top DBR (triangles) and for the case when it was operating as a VCSEL (circles). The pump laser duration is 10 ns.

Unfortunately, we did not have the opportunity to measure the time resolved lasing waveforms under optical pumping by 400 ps pulses. Analysis of V(E)CSEL delay times to lasing as a function of optical pump power might yield insights to additional mechanisms that would increase the lasing threshold when pumping with short pulses. For example, we expect that if the delay time is longer

than the duration of the optical pump pulse, then lasing will not occur. So under pumping by 400 ps pulses, the delay times must be less than 400 ps for lasing to occur, whereas under pumping by 10 ns pulses, lasing can still occur even if the delay times are significantly longer 400 ps (as can be seen in Fig. 6.20). This might explain some of the discrepancies between measurement and theoretical prediction in Section 6.4.3 regarding the ratio of lasing thresholds under 400 ps and 10 ns pump pulses.

6.9   Challenges and Difficulties for Atomic Clockwork

In summary, we report operation of a group III-nitride VECSEL with cavity length up to 50 mm under optical pumping by pulses of 400 ps and 10 ns. Lasing threshold is observed to be significantly lower under 10 ns pulse pumping. A model has been developed to explain the change in lasing threshold with the VECSEL cavity length. We have analyzed the lasing beam profiles and optical pulse envelopes. The achieved VECSEL cavity lengths are large enough for placement of intracavity elements (e.g., a saturable absorber), making our VECSELs suitable for various experiments in wavelengths covered by the III-nitride materials system.

We have encountered some challenges in the course of our research with optically pumped VECSELs. The first challenge is that currently, epitaxy of group III-nitride surface emitters is still not matured enough to achieve good planar uniformity. Moving the optical pump beam spot across our semiconductor samples in less than 1 mm distance, we have found large variations (a few nanometers) in the lasing spectra. Since our saturable absorber is the atomic transition of a ^{85}Rb vapor cell, which is spectrally narrow, it becomes necessary to find a spot on our VECSEL sample surface that lases at precisely the wavelength matching that of the ^{85}Rb atomic transition. This can be highly challenging given the large variations in lasing spectra obtained from different spots on a single VECSEL sample.

Another issue is specific to the measurements and characterizations performed here. Our pump lasers are pulsed 355 nm wavelength lasers (pulse duration of either 400 ps or 10 ns). We have found that the pump laser repetition frequencies drift over the course of operation. In addition, there are differences between each lasing pulse, especially in waveform shape. Furthermore, these variations are greater in the 10 ns pump laser, which was originally preferred over the 400 ps pump laser due to reasons detailed in Section 6.4.3. These issues highlight the advantages that a high power CW laser would have over pulsed lasers for optically pumping VECSELs. In any case, a CW pump laser would be needed for any VECSEL targeted for modelocked lasing work.

Chapter 7   Modeling, Analysis, and Design of Modelocked Lasers with Alkali Vapor Cell Saturable Absorber

In this chapter, we use the SVB approach to modelocked laser analysis to theoretically investigate the laser cavity configurations containing alkali vapor cell saturable absorber as described in Section 2.3.1. The modelocked laser model in Chapter 2 assumes gain and absorber sections in a multi-section laser diode, so adaptation is required for it to be applicable for our proposed laser cavity configurations. First, we will adapt the model so that it is also applicable for the surface-emitting optical gain chips as described in Section 2.3.2. Then, we adapt the model such that the description of the saturable absorber fits the theoretical and experimental characteristics of the alkali vapor cells given in Chapters 3, 4, and 5. Next, we will use this model to theoretically predict the operating parameters where modelocked operation can occur in the four cavity configurations that we can realize:

- with surface-emitting optical gain chip at 420 nm wavelength

- surface-emitting at 795 nm

- edge-emitting at 795 nm

- edge-emitting at 420 nm

Our model reveals that only some of the proposed laser cavity configurations are suitable for practical realization of modelocked operation. For the configurations that are suitable, we will finalize the design of the cavities using paraxial optics approximation and Gaussian beam analysis. These designs will serve as the starting point for experimental realization of such laser cavities.

7.1   Adaptation of Modelocking Model to Gain Chips

The four laser cavity configurations that we will investigate are Fabry-Perot cavities (two end mirrors) with the saturable absorber in the center and the gain section near a cavity end mirror as depicted in Fig. 7.1. In these cavities, the alkali vapor cell saturable absorber does not contribute to intracavity dispersion, and neither does the empty space inside the cavity. (For simplicity, we ignore dispersion effects inside intracavity optics and the quartz cell holding the alkali vapor.) In our mod-

el system, dispersion occurs only inside the semiconductor gain section. Therefore, the effective dispersion in reference to the cavity length is

$$D^* = \frac{l_L}{l_C} \omega_L{}^2 \frac{\partial^2 k}{\partial \omega^2} . \tag{7.1}$$

where l_L is the gain section length, l_C is the total cavity length, and ω_L is the half-width spectral bandwidth of the gain section. Note that cavity length l_C is the sum of gain section length, alkali cell length, and the empty space length inside cavity.
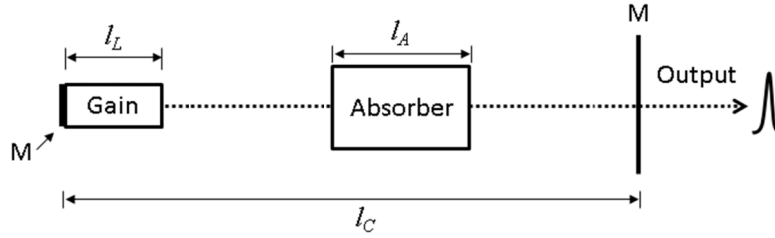
Fig. 7.1. Schematic of our proposed modelocked semiconductor diode lasers with alkali vapor cell saturable absorbers are in Fabry-Perot cavity. Dispersion occurs only in the optical gain section. Abbreviation: M – Mirror.

Our proposed cavity configurations utilize both edge-emitting and surface-emitting gain chips. Hence, for each type of emission profile, we need to develop separate expressions for cold cavity loss coefficient α_C, gain section saturation energy E_{sL}, and the unsaturated gain g_0.

7.1.1 Edge-Emitting Gain Section

In a laser cavity configuration utilizing edge-emitting gain section, intrinsic material loss exists only in the laser diode portion of the cavity. Thus, for the purpose of calculating the cold cavity loss α_C, the gain section length is simply the laser diode length, $l_L = L_{diode}$. This yields the expression

$$\alpha_C = \frac{1}{l_C} \left(\alpha_i L_{diode} + \frac{1}{2} \ln(\frac{1}{R_1 R_2}) \right). \tag{7.2}$$

The terms R_1 and R_2 are the reflectivities of each mirror that form the laser cavity. The two mirrors are (i) the output coupler, which is a high reflectivity mirror, and (ii) the back cleaved facet of the laser diode with high reflectivity (HR) coating.

For both AlGaAs (795 nm) and GaN (420 nm) edge-emitting laser diodes, L_{diode} is 750 μm according to product specification (AlGaAs diode) or measured from the mode spacing of amplified spontaneous emission (InGaN diode).

For gain section saturation energy E_{sL}, the expression is

$$E_{sL} = \hbar\omega \cdot A_L \cdot v_g / (\partial g / \partial n), \tag{7.3}$$

where $\hbar\omega$ is the photon energy, A_L is the cross-sectional optical mode area on the gain section, v_g is the group velocity in the gain medium, and $\partial g/\partial n$ is the differential material gain. The gain section active region quantum well (QW) cross-section area A_L has the expression

$$A_L = wd_{QW}N_{QW}/\Gamma, \tag{7.4}$$

where w is the ridge waveguide width, d_{QW} is the individual QW thickness, N_{QW} is the total number of QWs in the gain chip, and Γ is the optical confinement factor.

Finally, the relationship between unsaturated gain g_0 and the pump current I, as well as the expression for the current density J, are

$$J = I/wL_{diode}, \text{ and } g_0 = \frac{l_L\Gamma}{v_g\alpha_Cl_C}\left(\frac{\partial g}{\partial n}\right)\left(\frac{J \cdot T_L}{ed} - n_{tr}\right). \tag{7.5}$$

We note that the expression for g_0 is the same as that given in Eq. (2.4). The expression for J is specific for the edge-emitting gain chip.

7.1.2 Surface-Emitting Gain Section

In a laser cavity configuration utilizing surface-emitting gain chip, intrinsic material loss exists only in the semiconductor portion of the cavity, but the effective length of this region is not as well defined as in the edge-emitting structure case. Consider Fig. 7.2, which is an illustration of a laser cavity utilizing a VECSEL gain chip. The active region (specifically, the barrier region surrounding the quantum wells) is part of the overall laser cavity and should clearly be counted when considering cold cavity loss. The top capping layer is counted as well. However, the bottom side distributed Bragg reflector (DBR) stack that serves as a cavity mirror is also made of semiconductor, and the lasing pulse's electric field penetrates partially into it. Therefore, the depth of penetration should be considered for the purpose of calculating cold cavity loss α_C [122], [123].
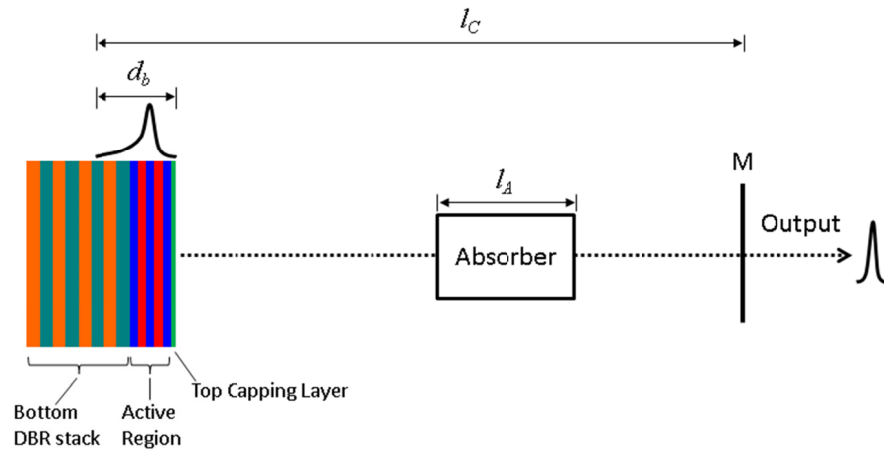
Fig. 7.2. An illustration of the optical pulse's electric field partially penetrating into the bottom side DBR stack of a VECSEL gain chip. The effective length where the optical pulse experiences intrinsic material loss needs to account for this DBR penetration depth in addition to the active region epitaxial thickness.

The expression for cold cavity loss is therefore

$$\alpha_C = \frac{1}{l_C}\left(\alpha_i d_b + \frac{1}{2}\ln(\frac{1}{R_1 R_2})\right),$$ (7.6)

where d_b is the effective active region barrier thickness (distinguished from the active region QW thickness), consisting of the sum of the actual epitaxy active region thickness as well as the penetration depth(s) into the bottom side (and top side, if applicable) DBR stacks. For commercial devices, where the actual expitaxy active region thickness is unknown, we use the approximation that it is one wavelength long.

In Eq. (7.6), the terms R_1 and R_2 are the reflectivities of each mirror that form the laser cavity. The two mirrors are (i) the output coupler mirror, and (ii) the bottom side DBR stack of the gain chip.

The expression for intracavity dispersion is also different from that of a cavity utilizing edge-emitting gain chip. In a surface-emitting gain chip, the total thickness of QWs in the chip contributes to optical gain, hence gain section length $l_L = d_{QW} N_{QW}$, where d_{QW} is the individual QW thickness and N_{QW} is the total number of QWs in the gain chip. However, contributions to dispersion comes from not just the QWs but also include the entire length in the gain chip that the electric field of the lasing pulse occupies, which is effective active region barrier thickness d_b. We modify Eq. (7.1) to read

$$D* = \frac{d_b}{l_C}\omega_L^2 \frac{\partial^2 k}{\partial \omega^2}$$ (7.7).

For gain section saturation energy E_{sL}, expression from Eq. (7.3) cannot be used because the optical confinement factor Γ is not applicable to surface-emitters. The expression here is

$$E_{sL} = \hbar\omega \cdot A_L \cdot v_g / (\partial g / \partial n),$$ (7.8)

where A_L is the optical mode area at the gain section. It is defined by oxide current confinement aperture for electrically-pumped VECSELs, or by the area of the pump beam spot for optically-pumped VECSELs.

For unsaturated gain g_0 and the pump current density J, the expressions for electrically-pumped gain chip are

$$J = I / A_L, \text{ and } g_0 = \frac{d}{v_g \alpha_C l_C}\left(\frac{\partial g}{\partial n}\right)(\frac{J \cdot T_L}{ed} - n_{tr}).$$ (7.9)

where I is the pump current. For the optically-pumped VECSEL gain chip, the concept of *pump current* does not apply. Fortunately, the rate at which carriers are generated when the VECSEL chip is under optical pumping can be easily converted to an equivalent pump current density. This carrier generation rate is found by experimentally measuring the light-light characteristics of the optically-pumped VECSEL in Chapter 6.

7.1.3 Summary of Gain Chip Parameters

In Table 7.1, we summarize the model parameters of our four optical gain chips (see Table 2.1 in Section 2.3.2), and we use them in our modelocked lasing analysis model with the SVB approach. Note that the gain chips belong to two different material systems, III-V (AlGaAs/GaAs) and III-nitride (InGaN/GaN), and each has its own material parameter such as $\partial g/\partial n$ and n_{tr}.

	InGaN VECSEL	AlGaAs VECSEL	AlGaAs Edge-Emitter	InGaN Edge-Emitter
Wavelength: λ (nm)	420	795	795	420
Differential material gain: $\partial g/\partial n$ (cm^3/s)	2.2×10^{-6}	1×10^{-6} [124]	1×10^{-6}	2.2×10^{-6}[31]
Intrinsic material loss: α_i (cm^{-1})	35	40	40	35
Transparency carrier density: n_{tr} (cm^{-3})	1.6×10^{19}	2×10^{18} [125]	2×10^{18}	1.6×10^{19}
Gain section carrier lifetime: T_L (ns)	~2 [121], also see Section 6.8	~2 [126]	~2 [126]	~2 [121]
Individual quantum well thickness: d_{QW} (nm)	2	10	10	5
Number of quantum wells: N_{QW}	24	3	1	2
Optical confinement: Γ	n/a	n/a	0.02	0.02
Surface-emitter optical mode diameter (μm)	30	4	n/a	n/a
Effective active region barrier thickness: d_b (μm)	0.420	2.4	n/a	n/a
Edge-emitter laser diode length: L_{diode} (μm)	n/a	n/a	750	750
Ridge width: w (μm)	n/a	n/a	3	2.5
Group index: $n_g=c/v_g$	3.5	3.6	3.6	3.5
Sellemeier coefficients (for calculating dispersion)	A = 3.6, B = 1.75, C = 0.256 μm	A = 3.5, B = 7.4969, C = 0.4082 μm	A = 3.5, B = 7.4969, C = 0.4082 μm	A = 3.6, B = 1.75, C = 0.256 μm

Table 7.1. Summary of optical gain chip diameters, the gain chips are in either edge-emitting or surface-emitting geometry, and in AlGaAs or InGaN material system. Note that total gain region thickness d is $d=d_{QW}N_{QW}$. Abbreviation: n/a − not applicable

One issue that a reader might take with the parameters here is that the intrinsic material loss α_i for an edge-emitting gain chip is the same as that for the surface-emitting gain chip in the same material system. In standalone laser diodes, surface-emitters usually have higher α_i than edge-emitters because of intracavity diffraction losses produced by the oxide aperture (used for current and optical confinement). In external cavity configuration, however, there is a mismatch of mode size in the edge-emitting laser diode with that of the external cavity, and this is similar to the intracavity diffraction loss effect in a standalone vertical-cavity surface-emitting laser (VCSEL). For the sake of simplicity, we take α_i to be the same for both edge-emitting and surface-emitting laser diodes. This also allows more simple comparisons between the different laser configurations in Section 7.3.

7.2 Adaptation of Modelocking Model to Alkali Vapor Absorber

The saturable absorber of our modelocked laser system, an alkali vapor cell, is very different from the semiconductor saturable absorber in the SVB approach for modelocked analysis. We need to

largely modify the absorber portion of the modelocked laser analysis model in order to correctly represent the ^{85}Rb vapor absorber.

We establish the effective absorber parameters in the small signal regime, where bleaching of the absorber by the pulse is negligible (the pulse energy is small compare to saturation energy of absorber). These parameters are the effective absorption cross-section, transparency conditions, and their "biasing" via the effects of temperature change. This will allow us to estimate the saturation energy of absorber. Finally, we elaborate the model for absorber recovery time.

7.2.1   Narrow Spectral Bandwidth of Alkali Vapor Cell Absorber

An important aspect of the alkali vapor cell saturable absorber is that its absorption spectrum can be relatively narrow compared to the spectrum of the modelocked optical pulse train, at least under low buffer gas pressure. In steady-state modelocked lasing regime, the optical spectrum consists of continuous wave (CW) cavity modes separated by a frequency equal to the hyperfine frequency splitting of the ground states of alkali atom. If the linewidth of absorption is small, it is possible that the saturable absorber interacts with only two optical modes in the pulse train spectrum. This is conceptually illustrated in Fig. 7.3 where an example optical comb constituting a modelocked pulse train is overlaid with experimentally measured absorption spectra of a ^{86}Rb cell with 6 torr of N$_2$ buffer gas.
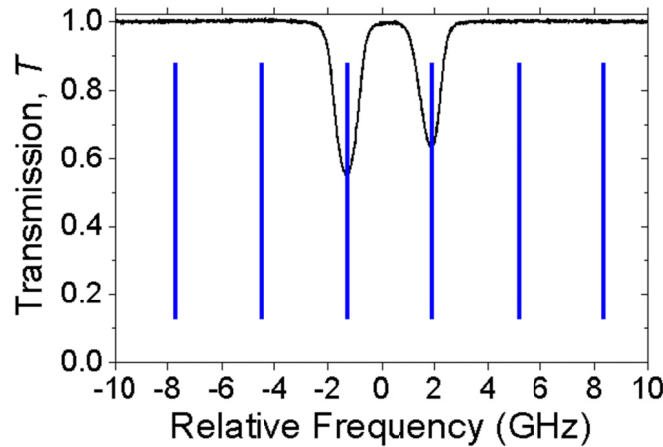
Fig. 7.3. Measured transmission vs. relative frequency for a ^{85}Rb cell with 6 torr N$_2$ buffer gas, under interrogation at 795 nm wavelength (D_1 line). Cell temperature is 60° C, and interrogating optical intensity is 0.20 mW/cm^2. An example optical frequency comb constituting a modelocked pulse is overlaid with the transmission spectrum to illustrate the limited interaction between the absorber and the lasing modes.

In contrast to the limited overlap between the absorption spectrum and the spectrum of the modelocked optical pulse train, the SVB model was made assuming that a semiconductor saturable absorber interacts with entire optical spectrum of the pulse. However in our case, even if the alkali vapor cell saturable absorber completely absorbs the two optical modes in the center of the optical pulse spectrum, the other cavity modes will be transmitted through the cell, nominally without attenuation. As a result of fixed phase relationship between these optical modes, the optical pulse train will be transmitted through the absorber cell, although the output spectrum and the pulse envelope may be distorted.

To illustrate this point, we consider transmission of an optical pulse train with pulse duration of 10 ps at full-width at half-maximum of intensity (FWHM) and with repetition rate equal to the alkali atom ground state hyperfine splitting frequency (3.036 GHz for ^{85}Rb). Recall that in modelocked lasing operation, the amplitudes of the optical modes are in steady-state. Assuming further that the *electric field* envelope of each optical pulse has hyperbolic secant shape, we then calculate the Fourier series of such optical pulse. Interaction with the absorber attenuates only two center modes, represented by scaling the amplitudes of two terms in the Fourier series. The optical pulse shape and energy after interaction with the absorber is then reconstructed and calculated from the modified Fourier series.

Figure 7.4(a) plots this example pulse *intensity* of 10 ps FWHM before and after interaction with an absorber that completely absorbs the two center modes, and Fig. 7.4(b) illustrates the frequency spectra. Because a 10 ps pulse consists of quite a few number of optical modes, the complete elimination of just the two central modes results in a relatively small change of the total pulse energy. This example also illustrates that pulse shape in time domain has not been largely distorted as opposed to the optical spectrum. In addition, the pulse envelope remains symmetric, which allows for the second-order expansion on cumulative pulse energy in the vicinity of the pulse peak, the main approximation used in the SVB method [31]. This justifies our use of the SVB approach for solving modelocked lasing dynamics in the pulse energy domain as opposed to in the frequency-domain or time-domain as in methods.
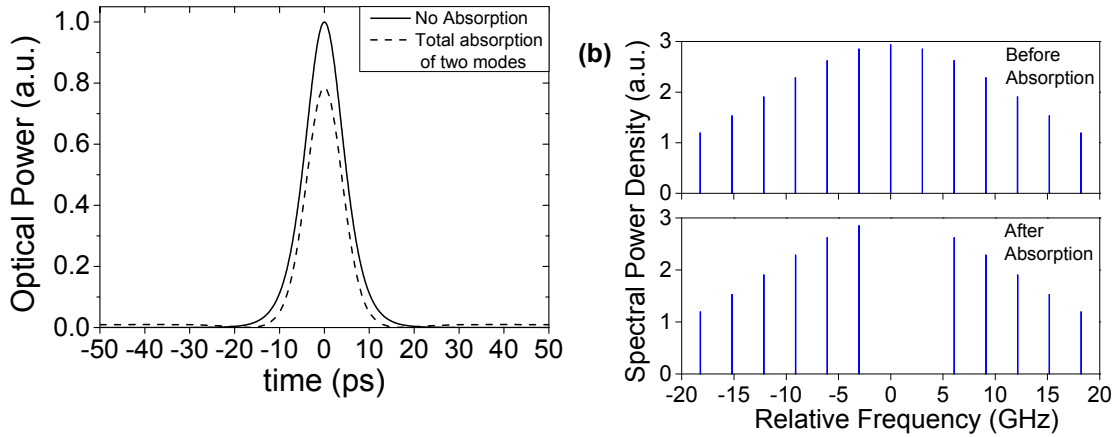
Fig. 7.4. (a) Intensity profiles and (b) center view of the optical pulse spectra of 10 ps pulse before and after interaction with an absorber that is completely absorbing on the center two modes.

This illustration brings us to an important parameter in our model, the *effective spectral overlap parameter ρ*, which allows us to account for the partial spectral overlap of the modelocked pulse train and the narrowband absorption in the cell. It is defined as the energy ratio of the transmitted and incident optical pulses with two central spectral components being totally absorbed in the cell, like in our example of Fig. 7.4(a), for which $\rho=0.832$. In cases where the modelocked pulse train has a very wide spectrum compared to the alkali vapor cell's absorption spectrum, the effect of the absorber on the transmitted pulse energy would be weak, and ρ would be close to 1. In cases where the optical pulse train has only two spectral components in perfect overlap with the absorption spec-

trum, we would have ρ being close to zero. Note that ρ does not depend on the cell length, absorption cross-section or density of Rb atoms in the cell.

To properly implement this spectral behavior in our model, we use an iterative approach for solving Eq. (2.16) in Section 2.4.2. First, we make an assumption on the modelocked optical pulse width (a seed value in our iterative approach). Then, we calculate the effective spectral overlap parameter of the optical pulse train and absorber given this two mode interaction behavior. After that, we run the modelocked laser model simulation and calculate the resulting pulse width. If this pulse width is different from our initial assumption, we change the initially assumed pulse width and rerun the simulation. This process continues until we obtain an agreement between the initial and simulation values for the pulse width.

In the general case, the two central modes are not absorbed completely. In the small signal regime, where bleaching of the absorber is negligible, their intensity transmission through the cell is defined by the CW dual frequency π-polarized interrogation scheme with transmission $T_{DF}=\exp(-\sigma n_{Rb} L_{cell}/2)$ as given by Table 3.1 (where σ is the ^{85}Rb absorption cross-section, n_{Rb} is the ^{85}Rb vapor density, and L_{cell} is the alkali vapor cell length). These should be accounted for in the Fourier series expansion of *electric field* envelope of the pulse train by scaling the amplitudes of the two corresponding spectral components of Fourier series expansion with a transmission factor $\sqrt{T_{DF}}$ (instead of their complete elimination used to define the effective spectral overlap parameter ρ). The result is illustrated in Fig. 7.5, using the same example of the pulse train with 10 ps pulse width.
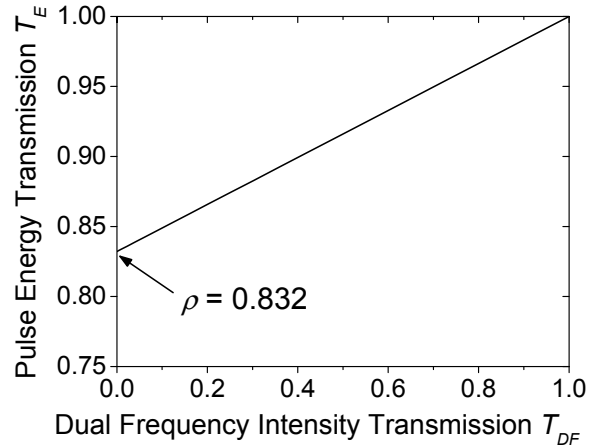
Fig. 7.5. Using the example of 10 ps optical pulse, we plot the energy transmission factor T_E of the pulse as a function of the absorber's intensity transmission factor T_{DF}. Here, the effective spectral overlap parameter $\rho=T_E(T_{DF}=0)$ is 0.832.

In Fig. 7.5, we plot the *energy* ratio T_E of the transmitted and incident pulses as a function of alkali vapor cell transmission T_{DF} under steady-state dual-frequency (DF) interrogation by the two central modes in the pulse. The energies of the transmitted and incident pulses are obtained by integrating the instantaneous optical power over time, e.g. curves in Fig. 7.4(a). We see that there is a linear relationship between transmitted pulse energy and DF intensity transmission T_{DF} of the cell. Simple analysis based on Fourier series expansion yields the relationship

$$T_E = \rho + (1 - \rho) \cdot T_{DF}. \tag{7.10}$$

In the limit of very strong resonant absorption, this expression recovers the effective spectral overlap of the pulse train and absorber: $\lim_{T_{DF} \to 0} T_E = \rho$. This expression allows us to obtain the effective small-signal (unsaturated) absorption cross-section of Rb atom in the 6-level model of alkali vapor cell absorber when interaction with entire spectrum of the pulse train is considered.

Combining Eq. (7.10) with the expression $T_{DF} = \exp(-\sigma \cdot n_{Rb} \cdot L_{cell}/2)$ for steady-state DF π interrogation, and assuming that absorption is small ($\sigma \cdot n_{Rb} \cdot L_{cell} \ll 1$), we obtain the following expression after applying linear expansion:

$$T_E \approx \rho + (1 - \rho) \cdot (1 - \sigma \cdot n_{Rb} \cdot L_{cell} / 2). \tag{7.11}$$

On the other hand, if we introduce the effective absorption cross-section σ_{eff} of Rb atom for interrogation with entire spectrum of the pulse train (like in SVB model), the cell transmission will read as $T_E = \exp(-\sigma_{eff} \cdot n_{Rb} \cdot L_{cell}/2)$, the same form for absorption under normal DF π interrogation. Applying linear Taylor expansion and equating the expression to Eq. (7.11), we obtain

$$\sigma_{eff} = \sigma \cdot (1 - \rho). \tag{7.12}$$

The effective absorption cross-section accounts for the spectral overlap between the pulse train and hyperfine line structure of absorber. It allows the six-level rate equation model of alkali vapor absorber to be used for describing interrogation of alkali atom with the entire optical pulse. For this, we replace the absorption cross-section σ in our model in Chapter 3 with $\sigma \cdot (1 - \rho)$ as per Eq. (7.12). We emphasize that the assumption about small absorption is made in order to define the effective cross-section of Rb atoms in Eq. (7.12) in such a way that it is independent of the cell length or density of Rb atoms.

Equation (7.12) is still valid when the buffer gas pressure is large enough such that the pressure broadening of the absorption linewidths Δv_L is comparable to or slightly larger than the ground state hyperfine splitting frequency v_{HF}. This is applicable for our ^{85}Rb cell with 200 torr of N_2 buffer gas, which has Δv_L of about 4 to 6 GHz compared to v_{HF} of 3.036 GHz, depending on cell temperature and atomic line (see Table 7.2). At these values of Δv_L, the two hyperfine ground states are still far from intermixed, which is an important condition for Eq. (7.12) to be valid. We experimentally confirm this with measurement data in Fig. 7.6, where we present the absorption spectra of the ^{85}Rb cell with 200 torr of N_2 buffer gas under interrogation by either one or two lasers at 795 nm wavelength (D_1 transition). In Fig. 7.6(a), we perform conventional spectroscopy by sweeping the lasing frequency of a laser across the absorption features of the ^{85}Rb D_1 line. We denote this laser as the *probe* laser, and it is operating at a single frequency (SF). The probe laser intensity is well below the saturation intensities of each absorption resonance. From the absorption spectrum, we can see that due to pressure broadening, there is significant overlap between the two absorption transitions from the ground state hyperfine levels. We denote these absorption transitions as F_g=2 and F_g=3, referring to the F quantum number of each ground state hyperfine level.

In Fig. 7.6(b), we perform the same measurement of absorption spectrum, but with a second laser, the *pump* laser, simultaneously performing SF interrogation at the F_g=2 resonance with intensity above that of optical saturation. We see that the addition of the pump laser interrogation significantly changes the spectrum acquired by the probe laser, where the transmission at F_g=2 is increased (cell is less absorbing), while the transmission at F_g=3 is reduced (cell is more absorbing). In Fig. 7.6(c), the pump laser is instead interrogating on the F_g=3 absorption resonance instead. Here, the spectrum acquired by the probe laser experiences a decrease in transmission at F_g=2, and an increase in the transmission at F_g=3.

From the two absorption spectra in Fig. 7.6(b) and (c), we clearly see that despite the significant overlap of the absorption linewidths due to pressure broadening, the two ground state hyperfine levels can still be treated as two separate levels as attested by the significant changes in absorption spectra with the addition of the pump laser. Furthermore, the overall absorption feature is still adequately narrow such that the absorber would still mainly interacts with two optical modes. Therefore, the Eq. (7.12) is still valid even for this high buffer gas pressure cell.
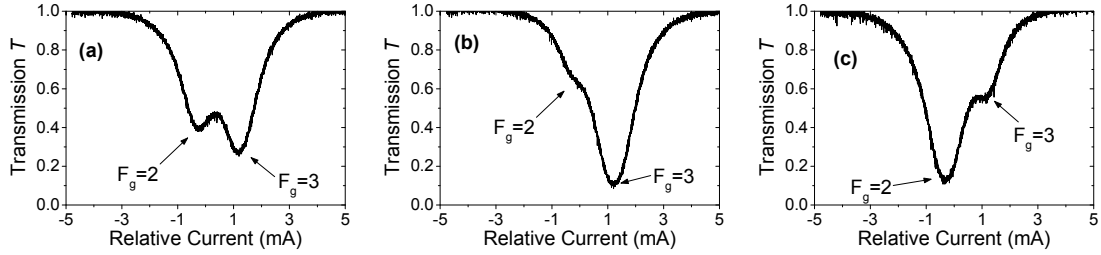
Fig. 7.6. Absorption spectra of ^{85}Rb cell with 200 torr of N$_2$ buffer gas at the D_1 line. Cell temperature is 65° C. (a) Under conventional SF interrogation with only the probe laser, we plot the optical transmission T as a function of the relative drive current of the probe laser. (b) We measure T when the pump laser is simultaneously performing SF interrogation at F_g=2. Here, transmission at F_g=2 is increased while transmission at F_g=3 is decreased. (c) Pump laser is now interrogating at F_g=3. Now, transmission at F_g=2 is decreased while transmission at F_g=3 is increased.

7.2.2 Transparency Condition and "Biasing" of Alkali Vapor Cell Absorber

The modelocked laser analysis model takes the saturable electro-absorber as a two level system with one ground state and one excited state. In the original SVB approach, the non-equilibrium carrier population density n_a in the electro-absorber is given as [99]

$$\frac{\partial n_a}{\partial t} = -\frac{n_a}{\tau_a} - (\partial g / \partial n) \cdot s \cdot [n_a - n_{tr}(1 - V_a)] \cdot |A(t)|^2 . \tag{7.13}$$

This equation for the electro-absorber is analogous to Eq. (2.12) for the gain section. Here, τ_a is the absorber recovery time, $\partial g/\partial n$ is the differential material gain of the gain section, and modelocking stability parameter s is the ratio of gain to absorber saturation energies. It is defined from both the mode area ratio in the gain and absorber sections and the ratio of differential gain to differential absorption coefficient. The term n_{tr} is the transparency population density of the absorber. The electric field amplitude of the light being absorbed is A, and it is normalized to the photon number density in the gain chip such that $|A|^2=I/\hbar\omega v_g$, where I is the light intensity, $\hbar\omega$ is the photon energy,

and v_g is the group velocity in the absorber medium. For the mode area ratio A_L/A_A in the gain and absorber sections, $|A(t)|^2 A_L/A_A$ is the photon number density in the absorber. Introducing this ratio in Eq. (7.13), one may show that $(\partial g/\partial n) \cdot s \cdot A_A/A_L$ is the differential absorption coefficient and $s \cdot A_A/A_L$ gives the ratio of differential absorption to differential gain.

We now elucidate the bleaching of absorber by arriving optical pulse. When the absorber recovery time τ_a is much longer than pulse duration, the relaxation term can be neglected. After integrating Eq. (7.13) over the pulse, this yields,

$$q_f = q_i \exp(-W_p/E_{sA}), \tag{7.14}$$

Here, $q_i = \dfrac{l_A \Gamma s}{v_g \alpha_C l_C}\left(\dfrac{\partial g}{\partial n}\right)[n_{tr}(1-V_a) - n_a(i)]$ is the normalized initial roundtrip absorption before arrival

of the pulse (see Eq. (2.3) and (2.4)), where $n_a(i)$ is the initial carrier density in absorber. The term

$q_f = \dfrac{l_A \Gamma s}{v_g \alpha_C l_C}\left(\dfrac{\partial g}{\partial n}\right)[n_{tr}(1-V_a) - n_a(f)]$ is the final normalized roundtrip absorption after the pulse, and

$n_a(f)$ is the final carrier density. Absorber section saturation energy E_{sA} is given by $E_{sA} = E_{sL}/s = \hbar\omega A_L v_g/s(\partial g/\partial n)$, and Pulse energy W_p has the expression $W_p = (wd/\Gamma)\int_{-\infty}^{\infty} \hbar\omega v_g |A(t')|^2 dt' = 2\hbar\omega v_g A_o^2 \tau_p A_L$.

We adapt the expression for the alkali vapor absorber to a form that is analytically similar to Eq. (7.13), which we do by first inspecting the rate equations in Section 3.2. Specifically, since modelocking behavior will result in multiple optical modes, and our laser system is designed for repetition frequency equal to the alkali atom ground state hyperfine splitting frequency, therefore the ^{85}Rb atoms in this laser system will be under *dual frequency* (DF) optical interrogation.

As noted in Chapter 3, short recovery time can be obtained by using linearly polarized (π) DF inter-rogation, where the alkali vapor cell absorber has recovery time equal to the excited state lifetime τ_{ex}. The use of π interrogation allows for the algebraic simplification of the six-level model into a three level model. We take Eq. (3.1) and make the substitution that $n_j = n_{j,\uparrow} + n_{j,\downarrow}$, where $j = 1$, 2, or 3. Incorporating Eq. (7.12), we obtain the rate equations

$$\frac{\partial}{\partial t}n_1 = \beta_1 \frac{n_3}{\tau_{ex}} - \frac{\sigma(1-\rho)(n_1-n_3)}{\hbar\omega}\frac{I}{2} - \frac{n_1 - n_{1,eq}}{\tau_g},$$

$$\frac{\partial}{\partial t}n_2 = \beta_2 \frac{n_3}{\tau_{ex}} - \frac{\sigma(1-\rho)(n_2-n_3)}{\hbar\omega}\frac{I}{2} - \frac{n_2 - n_{2,eq}}{\tau_g},$$

$$\frac{\partial}{\partial t}n_3 = -\frac{n_3}{\tau_{ex}} + \frac{\sigma(1-\rho)(n_1-n_3)}{\hbar\omega}\frac{I}{2} + \frac{\sigma(1-\rho)(n_2-n_3)}{\hbar\omega}\frac{I}{2} - \frac{n_3}{\tau_g}. \tag{7.15}$$

Here, I is the total intensity of the light interrogating the alkali atoms. Making the substitution that $n_g=n_1+n_2$ to denote the total ground state population density, and noting that the total Rb population density n_{Rb} is equal to the total equilibrium ground state densities, $n_{Rb}=n_{1,eq}+n_{2,eq}$, we obtain

$$\frac{\partial}{\partial t}n_g = \frac{n_3}{\tau_{ex}} - \frac{\sigma(1-\rho)(n_g-2n_3)}{\hbar\omega}\frac{I}{2} - \frac{n_g-n_{Rb}}{\tau_g},$$

$$\frac{\partial}{\partial t}n_3 = -\frac{n_3}{\tau_{ex}} + \frac{\sigma(1-\rho)(n_g-2n_3)}{\hbar\omega}\frac{I}{2} - \frac{n_3}{\tau_g}. \tag{7.16}$$

Recalling that this is a closed system, we have the relationship $n_g+n_3=n_{Rb}$, which we can use to eliminate the n_g term by replacing it with $n_g=n_{Rb}-n_3$.

We now establish the absorption coefficient. Following from Eq. (3.3), the absorption coefficient equation is given by

$$\frac{\partial I}{\partial z} = -\alpha I = -\sigma(1-\rho)\frac{n_g-2n_3}{2}I = -\sigma(1-\rho)\frac{n_{Rb}-3n_3}{2}I. \tag{7.17}$$

The absorption coefficient is $\alpha=\sigma(1-\rho)(n_{Rb}-3n_3)/2$. For condition of small signal, unsaturated absorption, which is what we are interested in, we have $n_3=0$, therefore the absorption coefficient becomes $\alpha=\sigma(1-\rho)n_{Rb}/2$. Following from normalization to the roundtrip cavity loss $\alpha_C l_C$, the expression for unsaturated absorption q_0 is

$$q_0 = \frac{\alpha L_{cell}}{\alpha_C l_C} = \frac{L_{cell}}{\alpha_C l_C}\frac{1}{2}\sigma\cdot(1-\rho)\cdot n_{Rb}. \tag{7.18}$$

The insight we gained from finding q_0 is utilized to find absorber saturation energy E_{sA}. The important term is $n_{Rb}-3n_3$, which is embedded inside the expression for absorption coefficient α and is equivalent to the carrier density n_a for an electro-absorber. To find E_{sA}, we start with the differential time expression

$$\frac{\partial}{\partial t}(n_{Rb}-3n_3) = -3\frac{\partial}{\partial t}n_3 = 3\frac{n_3}{\tau_{ex}} - 3\frac{\sigma(1-\rho)(n_{Rb}-3n_3)}{\hbar\omega}\frac{I}{2} + 3\frac{n_3}{\tau_g}. \tag{7.19}$$

Note that n_{Rb} is not time dependent, hence its time derivative is zero. The next step is to integrate Eq. (7.19) with respect to the time scale of one optical pulse. Making the assumption that the pulse duration τ_p is much shorter than all other time constants of the absorber (slow absorber), with $\tau_p \ll \tau_{ex}$ and τ_g, we use the approximation that we can ignore contribution from the $1/\tau_{ex}$ and $1/\tau_g$ terms in the integral. The integration of the pulse intensity I over time yields the pulse fluence W_p/A_{cell}, where W_p is the pulse energy and A_{cell} is the optical mode area on the alkali vapor cell. Therefore, the integration of Eq. (7.19) yields

$$n_{Rb}-3n_3(f) = [n_{Rb}-3n_3(i)]\exp\left[-\frac{3}{2}\frac{\sigma(1-\rho)}{\hbar\omega}\frac{W_p}{A_{cell}}\right]. \tag{7.20}$$

where $n_3(i)$ and $n_3(f)$ are the excited state population before and after the optical pulse, respectively. Comparing Eq. (7.20) with Eq. (7.14) gives us the expression for absorber saturation energy E_{sA},

$$E_{sA} = 2\hbar\omega A_{cell} / 3\sigma(1-\rho) \tag{7.21}$$

Equations (7.18) and (7.21) are dependent on alkali vapor cell temperature T_{cell}. This is because Rb population density n_{Rb} is dependent on T_{cell} as given by Eq. (2.1), and absorption cross-section σ is dependent on T_{cell} as well due the temperature dependence in both Doppler (Eq. (3.26)) and Pressure linewidth broadening. Thus, in lieu of the conventional voltage biasing for semiconductor saturable absorbers, the effective biasing of an alkali vapor cell absorber is the cell temperature.

Now we address the issue of the interrogating light being required to be linearly as opposed to circularly polarized. Jau and Happer's successfully operating laser system uses $\lambda/4$ waveplates [7], and thus the atoms are under interrogation by circularly polarized light. However, their laser system uses push-pull operation, whereas ours uses the modelocked lasing mechanism. According to our six-level model describing optical absorption in alkali atoms, circularly polarized DF pumping will result in absorber recovery with time characteristics equal to the spin relaxation time T_s, which is typically on the order of tens to hundreds of microseconds (see Chapter 4). This is much longer than the recovery time of the semiconductor gain media (a few nanoseconds or less), and modelocking operation should not be possible. Thus, it is definitive that the optical pulsation behavior reported by Jau and Happer [7] is not modelocked lasing. In here, we note that DF optical interrogation with linearly polarized light results in alkali atom with recovery time equal to the excited state lifetime. As measured in Section 4.4, excited state lifetimes of alkali atoms can be reduced to around 1 ns with high pressure N_2 buffer gas at 200 torr.

7.2.3   Justification of Adiabatic Treatment of Absorber Polarization

The original treatment under the SVB method is performed under the assumption that polarization relaxation time T_2 is much shorter than the optical pulse duration, thus the polarization of the absorption medium can be considered to be following the optical field adiabatically. For semiconductor saturable absorbers, T_2 is on the order of 100 fs [99], therefore the adiabatic approximation is valid for optical pulses of a few ps or more.

On the other hand, for alkali vapor absorber used in this research, T_2 is not much shorter than the optical pulse duration. Using the approximation that T_2 is the mean time between collisions for Rb atoms with buffer gas molecules, in a 200 torr N_2 cell, we have $T_2 \approx 0.3$ ns at typical operating temperatures of 60° to 100° C, which is much larger than the expected optical pulse duration of a few ps. (Adiabatic treatment of polarization in the semiconductor gain section still holds true in this research.) Nonetheless, the treatment performed in Section 7.2.2 to account for the alkali vapor cell absorber can still be considered valid even though it was based on the adiabatic treatment of polarization. In this section, we develop the justification.

Following from semiclassical Maxwell-Bloch equations, the absorber section in the original SVB method is modeled by the expressions [99]

$$\frac{\partial P_{A,\pm}}{\partial t} = -\frac{P_{A,\pm}}{T_2} + s\sqrt{\frac{\partial g/\partial n}{T_2}}(n_a - n_V)A_\pm, \quad \frac{\partial n_a}{\partial t} = -\frac{n_a}{\tau_a} - \sqrt{\frac{\partial g/\partial n}{T_2}}(A_+ P_{A,+} + A_- P_{A,-}), \qquad (7.22)$$

where the indices '+' and '−' refers to forward and backward traveling pulses associated with slowly varying amplitudes of electric field $A_\pm$ and polarization $P_{A,\pm}$. The term n_V is defined by the absorber bias, and it is related to the normalized absorber bias parameter $V_a = (n_{tr} - n_V)/n_{tr}$. For the cases considered in this research, because the absorber is placed in the center of the laser cavity, we ignore the '−' terms as there is no overlap of the optical pulse (unlike for the gain section as discussed in Section 2.4.2). Note that we are assuming that the optical pulse is hyperbolic secant with $A(t) = A_0\text{sech}(t/\tau_p)$, where A_0 refers to the amplitude of the pulse in the gain element.

The Rabi frequency in Eq. (7.22) is $\Omega_0 = A_0\sqrt{s \cdot (\partial g/\partial n)/T_2}$ and adiabatic approximation for polarization is valid if the Rabi frequency and the pulse width satisfy condition of the pulse area $\tau_p\Omega_0 \ll 1$ [127], [128].

Since Eq. (7.22) was developed for a laser system utilizing semiconductor saturable absorber, when using alkali vapor cell saturable absorber as in this research, the expression for Ω_0 need to go through some further adaptation. Recasting this to parameters of alkali vapor cell absorber established in Section 7.2.2, we find the expression for the Rabi frequency of alkali atoms to be

$$\Omega_0 = A_0\sqrt{\frac{3\sigma(1-\rho)v_g}{2T_2}\frac{A_L}{A_{cell}}} = \sqrt{\frac{W_p}{2\tau_p E_{sA} T_2}}, \qquad (7.23)$$

where v_g is the group velocity in the gain section, A_L is the gain section optical mode area, and A_{cell} is the optical mode area on the alkali vapor cell absorber.

For optical pulse energies, durations, and absorber mode sizes that are typical of simulation results (including those presented in Table 7.2 in Section 7.3.3), our $\tau_p\Omega_0$ is about 0.02 at the largest for the wavelengths and semiconductor material systems that are used in this research. Therefore, we conclude that the adiabatic approximation for absorber medium polarization is valid for this research.

7.3   Modeling and Simulation Results

In this section, we use the SVB approach for modelocked lasing analysis, with adaptations detailed in Sections 7.1 and 7.2, to investigate the viability of obtaining modelocked operation from semiconductor laser cavities with ^{85}Rb vapor cell saturable absorber. We will investigate the four different configurations detailed in Section 2.3.1: (i) configuration as in Fig. 2.2(b) with the optically pumped vertica-external-cavity surface-emitting laser (VECSEL) gain chip at 420 nm wavelength; (ii) configuration with electrically pumped surface-emitting gain chip as in Fig. 2.2(d) with the 795 nm VECSEL; (iii) configuration as in Fig. 2.2(a) using 795 nm edge-emitting gain chip; (iv) also edge-emitting but with 420 nm gain chip.

As detailed in Section 2.4.2, the modelocked lasing analysis model used here incorporates gain compression. We start by specifying the sweep ranges and step sizes of saturated gain g_i and ab-

sorption q_i. For each set of g_i and q_i, we calculate the corresponding cell temperature T_{cell}. This is an important step because T_{cell} determines the Doppler broadening linewidth and the buffer gas Pressure broadening linewidth. These two linewidth broadening terms directly affects the Rb absorption cross-section σ, calculated using Eq. (3.27) with the expression $\sigma = \pi r_e cf \cdot V(0)$, where the linewidth broadening terms are input arguments for the Voigt function V. Absorption cross-section σ determines the absorber saturation energy E_{sA} as given by Eq. (7.21). Another term that is also temperature dependent is the absorber recovery time as given by Eq. (4.12) in Section 4.4. Lastly, the Rb population density n_{Rb} is highly dependent on T_{cell}, and n_{Rb} is crucial in calculating q_0 as given in Eq. (7.18).

After finding T_{cell}, we next calculate (i) the normalized energy μ and duration τ_p of the optical pulse, (ii) the unsaturated gain g_0 and absorption q_0, (iii) check that μ is real and positive, and (iv) check for fulfillment of stable, self-starting modelocking conditions described by Eq. (2.8), (2.9), and (2.10) incorporating modifications of Eq. (2.14). Finally, g_i and q_i are transformed back into the physical operating parameter current density J.

We note that the concept of self-starting stable modelocking for laser systems that utilize alkali vapor cell saturable absorber is not as straightforward as it is for conventional modelocked laser systems (e.g., those in Section 2.2), and this is due to the alkali vapor cell absorber's limited interaction with the optical pulse train because of its relatively narrow absorption spectral bandwidth. For the laser systems considered here, the stable modelocking condition in Eq. (2.8) and (2.9) is applicable when the ^{85}Rb vapor cell absorber is already under dual frequency (DF) optical interrogation, i.e. by the modelocked lasing pulse train. Meanwhile, the self-starting condition in the analysis model as given by Eq. (2.10) is the requirement that *any* lasing can start in a cold cavity, i.e. when the small signal roundtrip optical gain is greater than the small signal roundtrip loss. However, the start of lasing is not necessarily the start of modelocked operation because this lasing might not interrogate the cell at DF absorption resonance. We address the method to start modelocked lasing in Section 7.4, when we discuss practical realization issues for these laser cavities.

For all simulations, the absorber characteristics used are adapted from the measured parameters of the ^{85}Rb cell with 200 torr of N_2 buffer gas. The choice for using this cell is due to its short excited state lifetime. For modelocked lasing operation, the saturable absorber should have recovery time shorter than that of the gain section, which is 2 ns or more. As measured in Section 4.4, the excited state lifetime of the ^{85}Rb cell with 200 torr N_2 is 1.43 ns at temperature of 65° C for the D_1 transition in ^{85}Rb. For the $5S_{1/2}$-$6P_{3/2}$ line at 420 nm wavelength, theoretical calculations made in Section 5.4.2 predicts excited state lifetime around 1 to 2 ns. For N_2 buffer gas pressure lower than 200 torr, theoretical calculations on either the D_1 or $5S_{1/2}$-$6P_{3/2}$ line predict that the excited state lifetime would not be adequately quenched to be less than 2 ns, the gain section recovery time. We therefore select the ^{85}Rb cell with 200 torr N_2 as our saturable absorber.

7.3.1 Optically Pumped III-Nitride VECSEL

In Chapter 6, we use III-nitride (InGaN) VECSEL chips with top dielectric DBR in our experiments due to the use of pulsed optical pump sources. We needed the top DBR to reduce the buildup time

of the lasing mode in the VECSEL cavity in order to obtain lasing. In this section, we assume that our III-nitride VECSEL gain chip contains no such top dielectric DBR, and that the chip is pumped by a CW source.

The cavity length of a VECSEL must be slightly shorter than 50 mm in order to match the cavity roundtrip frequency to that of the ^{85}Rb ground state hyperfine splitting frequency of 3.036 GHz. Thus, a concave external mirror with curvature of 50 mm or larger would be required to obtain a stable optical cavity. Using paraxial optics and Gaussian beam analysis, we estimate that the cavity mode size on the flat semiconductor sample range from 20 to 60 μm diameter at cavity lengths near 50 mm for a mirror with 50 mm curvature. The size of the optical pump beamspot on the VECSEL chip should match the cavity mode spot. The pump spot size on the semiconductor sample is determined by the optics focusing the pump laser. In our experiments with the III-nitride VECSEL in Chapter 6, the achievable pump spot size with a lens with focal length (FL) of 50 mm is about 30 μm diameter minimum, which falls in the range of calculated cavity mode sizes. Therefore, we use aperture size of 30 μm diameter in our simulations, as mentioned previously in Table 7.1. Note that the pump spot size on the gain chip determines the gain section saturation energy E_{sL} as given in Eq. (7.8).

We assume a realistic optical pulse duration of 5 ps FWHM in intensity as a seed value to estimate the spectral overlap parameter ρ. We find that the modelocking stability parameter s, the ratio of gain section to absorber saturation energies, is approximately 14 when the optical mode on the ^{85}Rb saturable absorber has diameter of 30 μm for cell temperatures ranging from 40 to 105° C. The value of s serves as a guide in our simulations. For a ring cavity, stable modelocked lasing can occur only when $s>1$ [31] according to the SVB approach in modelocked lasing analysis. For the Fabry-Perot laser cavities considered in this section, modifications to the SVB approach as detailed in Section 2.4.2 results in the requirement of $s>2$ for stable modelocking operation. Practical experience from using the SVB approach shows that stable modelocked lasing usually occurs when s ranges from 4 to 15 for semiconductor gain chips, and it usually favors s at around 10. Therefore, it is quite fortunate that we obtain $s≈14$ for mode diameter of 30 μm on the ^{85}Rb cell. Note that s becomes smaller as beam diameter increases, making it more difficult to obtain stable modelocking operation. We therefore select the absorber mode diameter of 30 μm in our simulations. This mode size determines the absorber section saturation energy as given in Eq. (7.21).

We present the results of our simulation and analysis in Fig. 7.7. Firstly, in panel (a), we depict the laser cavity schematic. In panel (b), we plot the regions of g_i and q_i where stable, self-starting modelocked operation is predicted to occur. The "tip" of this region corresponds to low pump power for the gain section, which is also where the modelocked optical pulse energy is lowest. At this area, the pulse energy is much smaller than the absorber saturation energy E_{sA}, and the methods to solve the Haus-New modelocking master equation in the time domain are valid. As one moves away from the tip of region in Fig. 7.7(b), the pulse energy increases, eventually until it is comparable to or higher than E_{sA}. In these high pulse energy areas, only the SVB approach to solve the modelocking master equation in the energy domain is valid because it does not require the assumption that the pulse energy is much smaller than E_{sA}. This highlights the value of the SVB approach as it is applicable to a much wider range of modelocked laser operation parameters.

We focus further analysis on the "tip" of this region in Fig. 7.7(b), at lowest pump levels where the gain chip is pumped at a level that is slightly above the lasing threshold. In panel (c), we fix q_i at 0.165 and sweep g_i across this region, and we calculate and plot the physical operating parameters of this system, which are the gain chip pump power and Rb vapor cell temperature. We note that these temperatures are achievable and reasonable for our cell holder. Lastly, the optical pulse energy and pulse duration as a function of gain chip pump power are plotted in (d) and (e), respectively. We note that the calculated pulse duration is self-consistent with the 5 ps seed value used in simulations to estimate the spectral overlap of the pulse train and absorber.
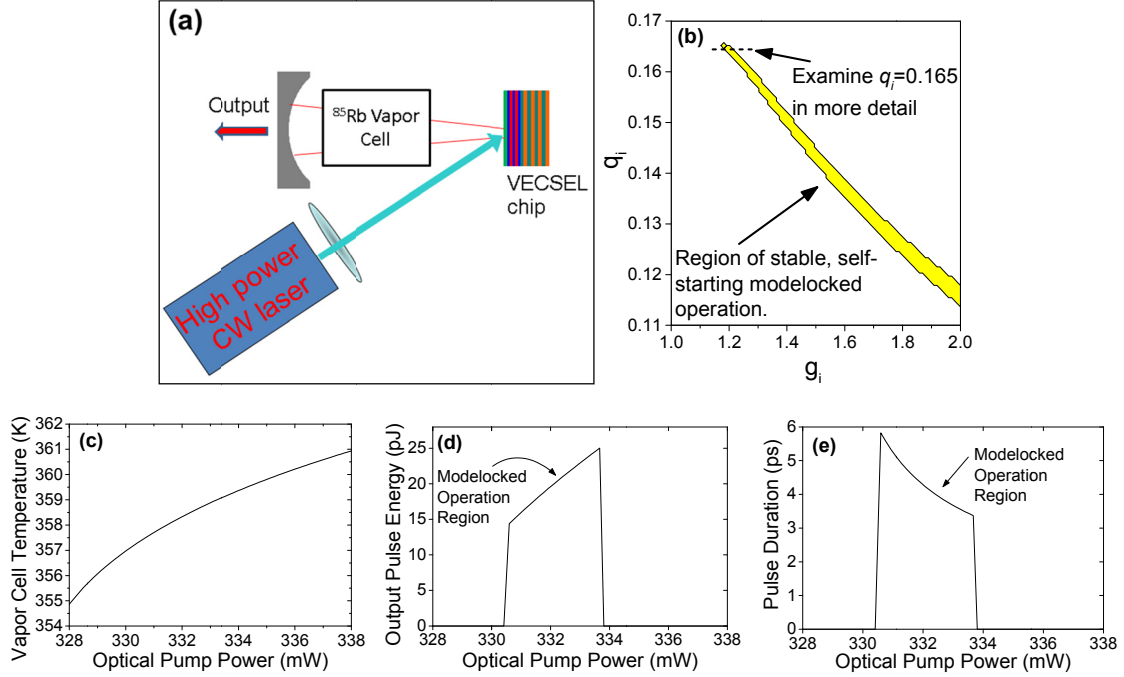
Fig. 7.7. (a) Schematic of the laser cavity configuration utilizing an optically pumped III-nitride VECSEL. Simulation results: (b) Region of q_i and g_i where stable self-starting modelocked operation is predicted. Fixing q_i at 0.165 and sweeping g_i, the optical pump power driving the gain chip and Rb vapor cell temperature are calculated (c). The output optical pulse energy (d) and pulse duration (e) are calculated and plotted vs. the optical pump power.

Unfortunately, our model predicts that stable modelocking operation is possible only with gain section spectral bandwidth $2\hbar\omega_L$ greater than 135 meV. Specifically, the largest domain of operation parameters that yields stable modelocking in Fig. 7.7(b) is when $2\hbar\omega_L$ at around 145 meV. This is an unrealistically large gain spectral bandwidth for III-nitride QWs in comparison to realistic values of around 40 meV. More careful investigation using the model reveals that over the range of realistic operation parameters (e.g., optical pump power, Rb cell temperature), the ability to obtain stable modelocked operation is highly dependent on the intracavity dispersion. From the expression for surface-emitter dispersion coefficient in Eq. (7.7), we see that D^* is directly proportional to d_b and ω_L. For the III-nitride VECSEL gain chip here, d_b is 420 nm (Table 7.1), which is relatively short. It is reasonable to assume that modelocked lasing operation is possible only for a range of D^*, therefore the small value of d_b means that modelocking can be obtained only with large ω_L. In our case, the value of ω_L that yields modelocking is unrealistically large for the III-nitride material. We there-

fore conclude from our simulation that modelocked laser operation from a cavity utilizing an optically pumped III-nitride gain chip is not feasible.

7.3.2 Electrically Pumped III-V Surface Emitter

In this section, we investigate the possibility of obtaining modelocked lasing operation from an electrically-pumped III-V surface-emitting gain chip. One potential advantage of such a gain chip is that the operating current can be much lower than that of electrically-pumped edge-emitting gain chip, on the order of a few mA for the surface-emitter rather than few tens of mA for the edge-emitter. Here, our modeling and simulation use a VECSEL chip that is similar to commercially available single mode VCSEL designed for lasing at 795 nm wavelength but does not incorporate top DBR reflector. The gain chip is therefore a VECSEL, and we justify its use by noting that it is possible to either (i) etch away the top DBR from the commercial VCSEL, or (ii) obtain such a VECSEL chip through a semiconductor epitaxy company.

Near infrared single mode electrically pumped VCSELs usually have oxide current apertures of 3 to 5 μm diameter which define the optical mode diameter. In our simulations, we assume our VECSEL chip has the same structure as the VCSEL characterized in Fig. 2.3 in Section 2.3.2, except without the top DBR stack. We assume aperture of 4 μm diameter as noted in Table 7.1, which yields free running threshold current of about 1.4 mA for a VCSEL, close to our VCSEL's measured threshold current.

Our simulations are made assuming that the optical spot size on the ^{85}Rb cell is 60 μm diameter. The main reason for this choice of mode size on the absorber is that at this beam diameter, the modelocking stability parameter s (the ratio of gain to absorber saturation energy) is around 10, which is favorable to obtaining stable modelocked operation from practical experience using the modelocked analysis model as stated previously in Section 7.3.1. Such a beam diameter cannot be achieved by collimating the VECSEL output, but it can be realized by focusing the beam onto the Rb vapor cell as indicated in Fig. 7.8(a).

Our simulations use a gain section spectral bandwidth of $2\hbar\omega_L$=56 meV, a very reasonable value for quantum wells of this material system. This also means that spectral filtering/narrowing elements like the etalon proposed in Section 2.3.1 is not needed for a III-V VECSEL gain chip. We obtained self-consistency between the resulting modelocked pulse width and the seed value of 8 ps optical pulse duration. The spectral overlap parameter ρ was calculated from this pulse duration, relating the modelocked pulse train with the absorption spectrum of the ^{85}Rb cell.

Figure 7.8(b) plots the regions of g_i and q_i where stable self-starting modelocked operation is predicted to occur. Again, we examine the "tip" portion of the region near the lasing threshold. At q_i=0.221, the corresponding ^{85}Rb cell temperature is around 44° C. This is a bit lower than the common range of operation temperatures 60-100° C used for Rb alkali vapor cell in spectroscopy or atomic clock applications. Nevertheless, it is a reasonable operating temperature, taking into account the fact that the Rb absorption spectrum can be experimentally observed at temperature >40° C in Rb cells of the same length. The simulation results for the Rb cell operating temperature are

presented in Fig. 7.8(c), the output optical pulse energy is presented in panel (d), and the pulse duration is presented in panel (e), all for q_i=0.221. Note that panel (e) confirms the self-consistency in pulse duration with the initial seed value of 8 ps. From our simulations, we conclude that the laser cavity configuration utilizing electrically-pumped III-V VECSEL at 795 nm wavelength may be viable for modelocked lasing operation.

Fig. 7.8. (a) Schematic of the III-V electrically-pumped VCSEL laser cavity configuration. Simulation results: (b) Region of q_i and g_i where stable, self-starting modelocked operation is predicted. Fixing q_i at 0.221 and sweeping g_i, the gain chip pump current and Rb vapor cell temperature are calculated (c). The output optical pulse energy (d) and pulse duration (e) are plotted as a function of the pump current.

7.3.3 Electrically Pumped III-V Edge-Emitter

The laser cavity configuration utilizing an electrically pumped III-V edge-emitter is especially interesting because a similar configuration is used by Jau and Happer to achieve their push-pull oscillator atomic clock [7]. However, we are targeting modelocked lasing operation here, a very different phenomenon from push-pull oscillation. Therefore, we tailor our simulation and modeling towards achieving stable modelocking, and some of the resulting parameters can be very different from what was used in Jau and Happer's laser cavity.

We assume optical pulse duration of 12 ps FWHM in intensity as a seed value to estimate the spectral overlap parameter ρ. We obtained self-consistency between this seed value and the modelocked pulse width from the result of simulation. The gain section spectral bandwidth used in these simulations is $2\hbar\omega_L$=50 meV, a reasonable value for III-V QWs in edge-emitters. Therefore, intracavity etalon filtering is not required to reduce the gain bandwidth.

Using Eq. (7.3) and (7.4) with parameter values summarized in Table 7.1, our edge-emitting gain chip has a very small optical mode cross-sectional area (A_L=3×10^{-10} cm^2) and hence small satura-

tion energy E_{sL}=31.2 pJ. To obtain the modelocking stability parameter s (gain to absorber saturation energy ratio) greater than 2 (see discussion in Section 7.3.1), the saturation energy of the absorber E_{sA} must be smaller than E_{sL}/2 or about 15 pJ.

The key to obtaining small E_{sA} is that the diameter of the optical beam on the Rb vapor cell absorber must also be adequately small, as given by Eq. (7.21). For edge-emitting laser diodes with elliptical output beams, we define the *effective beam diameter* as the geometric mean of the fast and slow axes beam diameters. In a typical edge-emitting laser diode using typical optics, the achievable collimated output beam has effective diameter greater than 0.5 mm. This corresponds to s of about 0.025 or less, which is completely unsuitable for modelocking lasing operation. We therefore cannot use collimated beams as Jau and Happer used for their laser cavity [7]. Instead, we must *focus* the optical emissions from the edge-emitting gain chip. This is the only way to obtain an adequately small optical mode diameter on the ^{85}Rb vapor cell absorber to fulfill the condition s>2, which occurs when the beam diameter is smaller than 55 μm. Note that it is more favorable to obtain stable modelocking when s ranges from 4 to 15 as discussed in Section 7.3.1, we therefore use a beam size of 30 μm diameter on the ^{85}Rb vapor cell, corresponding to s to be about 7.

The laser cavity schematics and simulation results are presented in Fig. 7.9. Panel (b) contains the regions of g_i and q_i that result in self-starting stable modelocking operation. Just as we have done in the previous two sections, we examine this region near the "tip," where the gain chip is pumped at currents that are too high above the absorber-free lasing threshold. At q_i=0.401, the operating current of about 58 mA is reasonable for a 750 μm long edge-emitting laser diode gain chip. We specifically tailored our simulation parameters such that the results are achievable with laser diodes of this length, which are commonly available. Panel (c), (d), and (e) presents the simulation results for the operating temperature of the Rb cell, the output optical pulse energy, and the pulse duration, respectively, when q_i=0.401. We note that panel (e) gives us the self-consistency in the pulse duration with the seeding value of 12 ps. From these simulations, we conclude that the laser cavity configuration utilizing electrically-pumped III-V edge-emitting gain chip at 795 nm wavelength may be viable for modelocked lasing operation.
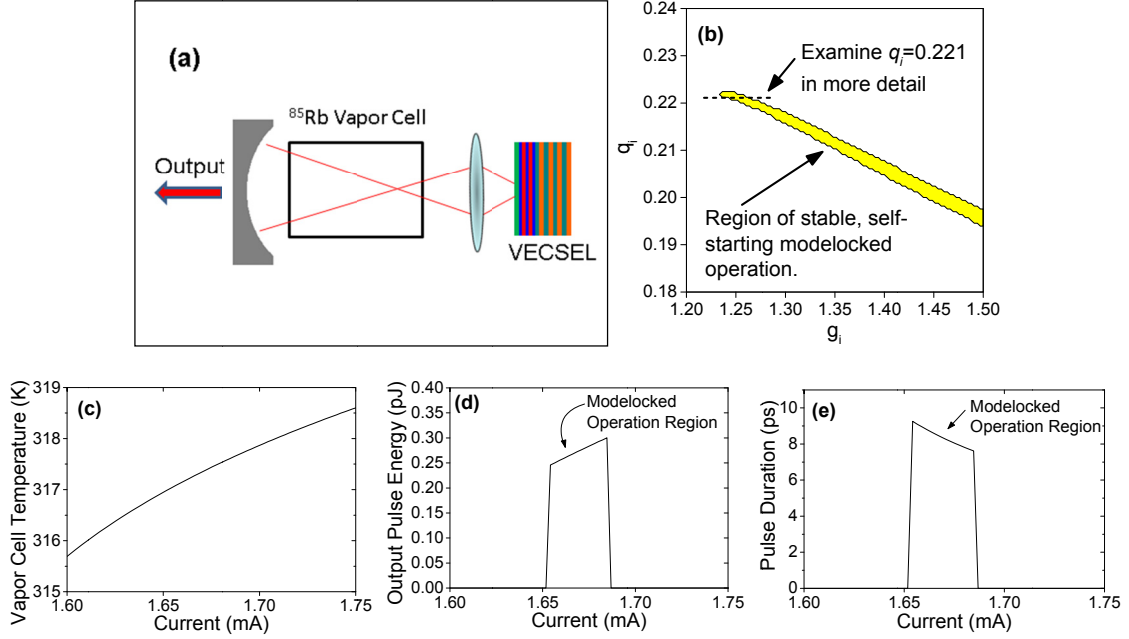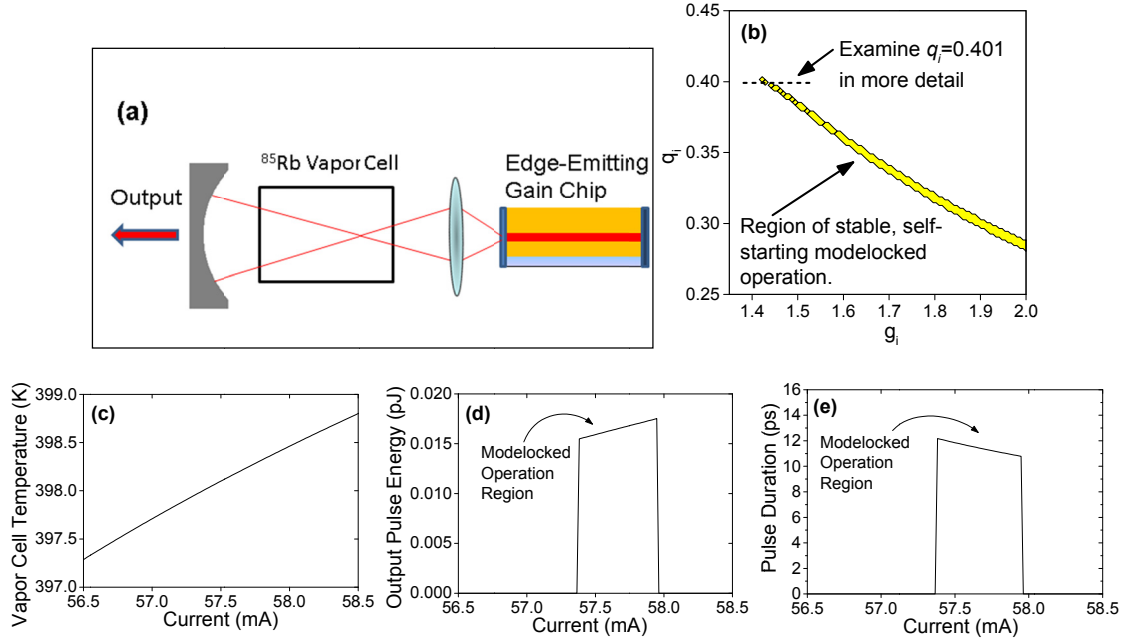
Fig. 7.9. (a) Schematic of the III-V edge-emitting gain chip laser cavity configuration. Simulation results: (b) Region of q_i and g_i where stable, self-starting modelocked operation is predicted. Fixing q_i at 0.401 and sweeping g_i, the gain chip pump current and Rb vapor cell temperature are calculated (c). The output optical pulse energy (d) and pulse duration (e) are plotted as a function of the pump current.

7.3.4 Electrically Pumped III-Nitride Edge-Emitter

For the laser cavity configuration utilizing an electrically-pumped III-nitride edge-emitting gain chip, a schematic and simulation results are given in Fig. 7.10. Our simulations have revealed that a lot of the same issue with saturation energies and optical beam size that were encountered in the case of III-V edge-emitting gain chip in Section 7.3.3 also applies here, and they are more severe. The absorption cross-section σ of ^{85}Rb is more than one order of magnitude smaller at the 420 nm wavelength $5S_{1/2}$-$6P_{3/2}$ line than the 795 nm D_1 line, and this is due to the absorber oscillator strength of the former (9.4×10^{-3}) being much smaller than that of the latter (0.342) as shown in Table 3.2. When σ is reduced, the absorber saturation energy E_{sA} increases as given by the relationship in Eq. (7.21). Therefore, achieving $s>2$ requires even smaller optical beam diameter on the ^{85}Rb vapor cell than all previous cases of gain chips considered. We obtain $s>2$ when the beam diameter on the ^{85}Rb cell is smaller than 3.7 μm. For our simulations predict, we use beam diameter of 1.7 μm in order to obtain $s \approx 9$, which should be more conducive for obtaining stable modelocking as discussed in Section 7.3.1. A beam diameter of 1.7 μm is possible to achieve using conventional optics, but it is very challenging to obtain from the point of view of practical realization.

We assume optical pulse duration of 6 ps FWHM in intensity as a seed value to estimate the spectral overlap parameter ρ, and we are able to obtained self-consistency between this seed value and the modelocked pulse width from the result of simulation. Figure 7.10(a) illustrates a schematic of the cavity configuration. Panel (b) contains the regions of g_i and q_i that result in stable modelocking

133

operation. Again, we examine this region near the "tip" which is near lasing threshold. At q_i=0.2665, the operating current for the gain chip is about 51 mA, which is reasonable for 750 μm long edge-emitting III-nitride laser diode. We note that such laser diodes are commercially available. At this value of q_i, the simulation results for the Rb cell operating temperature, the output optical pulse energy, and the pulse duration are presented in panel (c), (d), and (e), respectively. We note that panel (e) provides self-consistency in pulse duration with the initial seed value of 6 ps.

In order to obtain stable modelocking operation as shown in the operation region in Fig. 7.10(b), we use the gain section spectral bandwidth $2\hbar\omega_L$=74 meV, which is far larger than realistic value of around 40 meV for III-nitride QW in edge-emitters. From our simulations, we conclude that the laser cavity configuration utilizing III-nitride edge-emitting gain chip at 420 nm wavelength is not feasible for modelocked lasing operation.
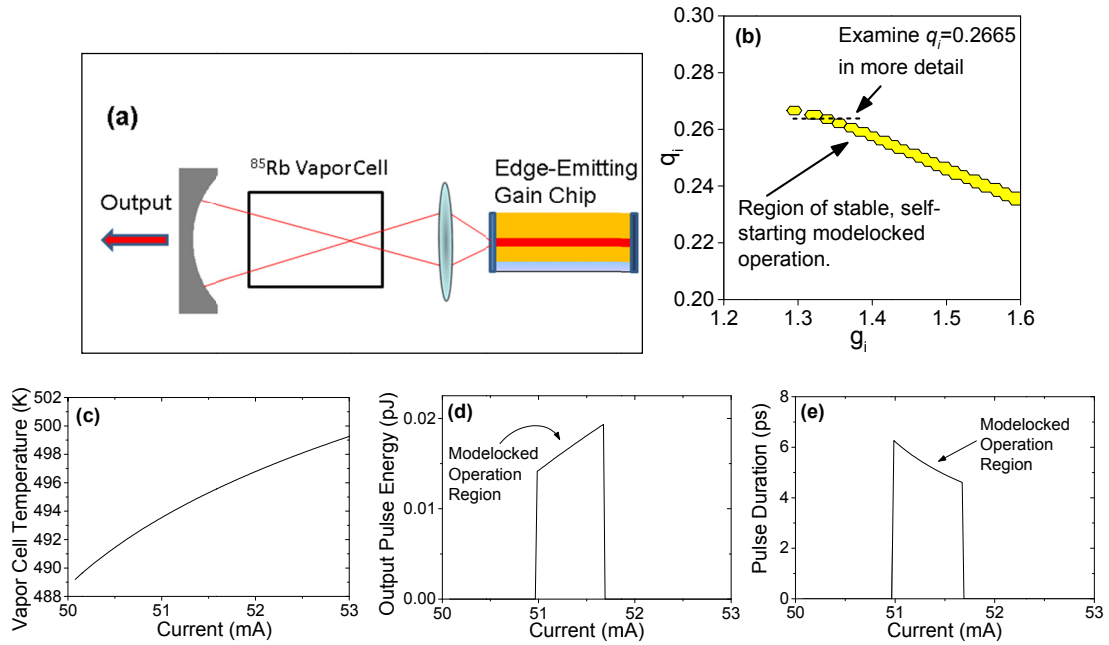
Fig. 7.10. (a) Schematic of the III-nitride edge-emitting gain chip laser cavity configuration. Simulation results: (b) Region of q_i and g_i where stable, self-starting modelocked operation is predicted. Fixing q_i at 0.2665 and sweeping g_i, the gain chip pump current and Rb vapor cell temperature are calculated (c). The output optical pulse energy (d) and pulse duration (e) are plotted as a function of the pump current.

7.3.5 Summary of Simulations and Discussion

We summarize the main parameters in our simulations that leads to stable, self-starting modelocked operation in Table 7.2. For each laser cavity configuration, we give the output coupling coefficient, gain spectral bandwidth $2\hbar\omega_L$, the gain section saturation energy E_{sL}, the beam spot diameter on the Rb vapor cell saturable absorber d_{sA}, the absorber saturation fluence F_{sat}, the vapor cell operating temperature T_{cell}, the Doppler broadened linewidth $\Delta\nu_D$, the pressure broadened linewidth $\Delta\nu_L$, the modelocking stability parameter s (the ratio of gain section to absorber saturation energy) at the operating temperature, and the optical pulse duration τ_{FWHM} (self-consistent with spectral overlap

parameter ρ). We highlight parameters that are either unrealistic or unachievable in reality, thus making that particular laser configuration unusable for our research.

Configuration	III-N VECSEL (λ=420 nm)	III-V VECSEL (795 nm)	III-V Edge-Emitter (795 nm)	III-N Edge-Emitter (420 nm)
Output Coupling Coefficient	0.772	0.343	0.168	0.168
$2\hbar\omega_L$ (meV) Gain spectral bandwidth	145*	56	50	74*
E_{sL} (pJ) Gain section saturation energy	12700	261	31.2	26.9
d_{sA} (μm) Beam spot diameter on Rb vapor cell	30	60	30	1.7
T_{cell} (K) Rb vapor cell operating temperature	359	317	398	494*
Δv_D (GHz) Doppler broadening of linewidth	1.05	0.522	0.584	1.23
Δv_L (GHz) Pressure broadening of linewidth by buffer gas	5.62	3.88	4.35	6.59
τ_{ex} (ns) Excited state lifetime of ^{85}Rb	1.03	1.06	0.95	0.88
$s = E_{sL}/E_{sA}$ Ratio of gain section to absorber saturation energy	14	11	7	9
E_{sA} (pJ) Absorber saturation energy	907	23.7	4.46	2.99
F_{sat} (μJ/cm^2) Absorber saturation fluence	128	0.84	0.63	132
τ_{FWHM} (ps) Optical pulse intensity FWHM duration	5	8	12	6
Intracavity Optical Pulse Energy (pJ)	22	0.829	0.094	0.088
Peak Output Power	3.4 W	36 mW	1.3 mW	2.5 mW
Average Output Power	52 mW	865 μW	48 μW	45 μW
Modelock Operating Current / Pump Power	331 mW	1.68 mA	57.4 mA	51.1 mA

Table 7.2. Summary of simulation parameters for each laser configuration. Parameters denoted with * are unrealistic, unachievable, or impractical for experimental realization.

The cavity configurations that are feasible for experimental realization are (i) the cavity utilizing III-V edge-emitting gain chip at 795 nm wavelength, and (ii) the laser cavity utilizing III-V VECSEL gain chip, also 795 nm wavelength. We emphasize that the VECSEL gain chip should not contain a top DBR stack.

From Table 7.2, one can see that the laser configuration utilizing III-V edge-emitting gain chip has lower output powers than that with the III-V VECSEL gain chip. The first reason for this is that the edge-emitting configuration has a smaller output coupling coefficient, given by

$$\frac{(1/2)\ln(1/R_1 R_2)}{\alpha_C l_C} \, .\tag{7.24}$$

Here, R_1 and R_2 are the reflectivities of the mirrors the form the laser cavity, α_C is the cold cavity loss, and l_C is the cavity length. The factor of 1/2 in the expression accounts for power emission from only one laser cavity mirror, which is the output coupler. Recall that α_C has different expressions depending on the gain chip profile, and the expression is given by Eq. (7.2) for edge-emitters and (7.6) for surface-emitters. Cold cavity loss α_C is larger for edge-emitter because the semiconductor portion of the laser cavity is longer (L_{diode}=750 μm) than the VCSEL case (d_b=2.4 μm or less), therefore there is larger overall material loss per cavity round trip.

The second reason that the cavity utilizing the edge-emitting gain chip has lower power than that of VECSEL gain chip is that the laser operation point chosen by our simulations in Section 7.3.3 is not far above the lasing threshold. If we were to operate the gain chip at higher drive currents, the modelocked lasing pulses would have higher output power. However, obtaining stable modelocked operation at higher drive currents is possible only with increased cell temperature. The cell temperature of 398 K for the operating point given in Table 7.2 is already relatively high.

In the next section in this chapter, we present the designs for the two cavity configurations that have the most prospect for achieving modelocked lasing operation for atomic clockwork at 795 nm wavelength.

7.4   Towards Practical Realization of Modelocked Laser Atomic Clock

Having established the two cavity configurations that have the possibility to achieve modelocked lasing operation in Section 7.3, in this section we finalize their designs.

As discussed in the beginning of Section 7.3, the narrow spectral bandwidth of the alkali vapor cell saturable absorber means that stable modelocking, defined as fulfilling Eq. (2.8) and (2.9), can only occur if the cell is already under dual frequency (DF) optical interrogation. The issue is that fulfilling the self-start condition of Eq. (2.10) only means that lasing of any kind (e.g., CW, Q-switched) can start, but that is not necessarily the same as the start of modelocked lasing. We now address the practical method of obtaining modelocked operation.

The laser cavity should be operating at above the lasing threshold, fulfilling Eq. (2.10). We next force the optical gain chip to interrogate the [85]Rb absorber in DF absorption resonance. This is done by first generating optical sidebands by modulating the drive current of the gain chip with a radio frequency (RF) synthesizer at frequency ν_{RF} equal to either the [85]Rb ground state hyperfine splitting frequency ν_{HF} or half of it, as discussed in Section 4.1.2 and 4.4. Then, we tune the optical bands onto the [85]Rb absorption resonances by careful adjustment of the DC laser drive current and temperature, and possibly using tunable optical filters such as an intracavity etalon. This modulation of the gain chip at microwave frequency also creates an oscillatory optical intensity in the time domain that, together with the DF interrogation, act as a seed to modelocked lasing operation.

Once stable modelocked operation is obtained, it should not be perturbed by the adiabatically removal of current modulation, which is done as the final step. We note that this proposed method for starting modelocked lasing operation is analogous to what Jau and Happer did to start push-pull oscillations in their laser cavity [7].

In this dissertation, we have ignored the effects of coherent population trapping (CPT) of the ^{85}Rb atoms on the operation of our modelocked laser system. CPT slightly reduces absorption when the DF interrogation is perfectly on absorption resonance. In our modelocked analysis, we ignore the effects of CPT because the reduction in absorption is small compare to absorption variations due to cavity roundtrip dynamics of modelocked pulses. However, CPT should have an impact after modelocked lasing operation starts. This is because when two of the optical modes of the modelocked pulse train are near DF absorption resonance, CPT effects should pull the modes to be on perfect resonance. Therefore we may speculate that CPT effects will define the stability of the modelocking repetition frequency in the atomic clock.

We now turn to the design of the laser cavities. Using ray transfer matrix with Gaussian beam analysis, we calculate and select realistically achievable positions and characteristics of all laser cavity components. This includes the focal length of the focusing lens, the distance between semiconductor gain chip and focusing lens, the distance between the focusing lens and the alkali vapor cell, and the output coupler cavity mirror curvature radius (and whether it should be flat or concave). The goal is to obtain optical cavity designs that are both stable and consistent with the modelock simulations.

7.4.1 III-V Edge-Emitter Cavity Design

Since the alkali atom species chosen for this modelocked laser research is ^{85}Rb, its ground state hyperfine splitting frequency of 3.036 GHz dictates that the laser cavity *optical length* to be 49.3 mm. However, the laser cavity consist not just free space but also semiconductor, lens, and alkali cell walls, thus the *physical length* of the cavity is slightly shorter. For the purpose of experimental realization of the laser cavity, we need to calculate the physical separation between the semiconductor chip and the external cavity mirror.

For the edge-emitting III-V laser diode gain chip (795 nm wavelength), the length of the diode is 750 μm as given by the manufacturer. Scaling this penetration depth by the group index of refraction, which we take as n=3.6, we obtain the optical length of the gain chip. To find the physical separation between the gain chip and the output coupler cavity mirror, this chip optical path length is one of the numbers to be subtracted from 49.3 mm.

The vapor cell has two walls in the path of the beam. Each wall is 2 mm thick. The wall material is quartz, and it has index n=1.453 at 795 nm. The difference between the cell wall optical path length and the physical path length, or $(n-1)$*4mm, is a length enhancement, and this is another number that must be subtracted out from 49.3 mm.

Similar treatment applies for the focusing lens. Given a lens with physical thickness of d_{lens} and index n_{lens}, the length enhancement is $(n_{lens}-1)d_{lens}$. After subtracting this and the above two values (gain chip length, cell wall length enhancement) from 49.3 mm, we obtain the physical distance between gain chip output facet and the output coupler mirror. For the design, we choose lens focal length (FL) and d_{lens} that are realistic when compared to commercially available products. The lens characteristics are summarized in Table 7.3.

Summary of Lens Characteristics	
FL (mm) Lens focal length	2.00
d_{lens} **(mm)** Lens thickness	1.90
Lens Material	D-ZLaF52LA
n_{lens} Index at λ=795 nm	1.793

Table 7.3. Summary of the characteristics of the lens used in cavity designs.

Our design places the Rb vapor cell in the middle of the cavity as oppose to near the output coupler cavity mirror. The reasons are (i) placing the cell very near the cavity mirror is impossible due to mechanical constraints, and (ii) the modelocked analysis model used in Section 7.3 were made with account for such mechanical constraints, such that the Rb cell is not placed near the cavity mirror. As previously discussed in Section 2.4.2, there are significant differences in how a gain or absorber section should be treated in the SVB approach to modelocked analysis depending on whether or not it is near a cavity mirror. Intracavity elements near a cavity mirror experiences overlap of the optical pulses incident to and reflected from the mirror, effectively doubling the pulse energy on that element while the interaction is once per cavity roundtrip. Meanwhile, elements far away from the cavity mirrors interact with the modelocked optical pulse twice per cavity roundtrip. These effects drastically modify the modelocked stability conditions. The simulations in Section 7.3 are only valid if the Rb cell is in the middle of the cavity, therefore our design must place the cell in such a way.

We design the cavity so that the beam waist of the focusing lens is located in the middle of the cavity, where alkali cell will be placed. The beam waist at the center of alkali cell should be close to what was used in our simulations, which was 30 μm diameter for the case of III-V edge-emitting gain chip as given in Section 7.3.3 and Table 7.2. However, modelocked analysis simulations were made assuming circular beams while the output beam from an edge-emitting laser diode is elliptical. We account for this difference by defining the effective beam waist diameter d_{beam} as the geometric mean of the beam diameter in the slow and fast optical axes, d_{slow} and d_{fast} respectively. The expression is $d_{beam} = \sqrt{d_{slow}d_{fast}}$. Note that when d_{beam} is 30 μm, the elliptical beam has the same optical mode area as a circular beam with 30 μm diameter and hence the same absorber saturation energy E_{sA}.

Using ray transfer matrix with Gaussian beam analysis, we theoretically investigate the placement positions and characteristics of optical elements. For these calculations, we utilize the Gaussian aperture formalism presented in Section 6.4.4 and Eq. (6.4) to model the output aperture of the gain chip, which defines the optical output mode size. The free running laser mode size was defined from quoted divergence angles of about 30° and 10° for fast and slow axes (FWHM values), respectively. In the fast axis, the FWHM mode size is 670 nm. Therefore the Gaussian aperture parameter

Δ is defined by the mode diameter, defined at the e^{-2} intensity level of maximum, of $2\Delta=(670\text{nm}\times2)/(2\ln2)^{1/2}=1.1\,\mu\text{m}$. In the slow axis, the FWHM mode size is 2.0 μm, and the Gaussian aperture parameter Δ is such that mode diameter is $2\Delta=3.4\,\mu\text{m}$ (at e^{-2} intensity level).

We present the cavity design in Fig. 7.11, where we illustrate the design schematics and give the placement positions of the elements. This design utilizes a single lens to focus the output beam from the optical gain chip and an external cavity mirror (the output coupler) with curvature radius ρ_M of 25 mm. In addition, we plot the calculated optical mode sizes (at half maximum intensity level) as a function of position inside the cavity. We have good agreement between the calculated d_{beam} of 32.9 μm with the target of 30 μm. The used lens is commercially available, and the working distance of ~0.5 mm between the edge-emitting gain chip and the lens is not unreasonably small, especially if the cap is removed from the TO can of the gain chip. The alkali vapor cell position is nearly in the center between the lens and the output coupler cavity mirror, where there is adequate space for our cell holder.

Fig. 7.11. III-V edge-emitter (795 nm wavelength) cavity design. The gain chip output aperture is placed at position x=0. The calculated optical mode sizes (at half maximum level) for fast and slow axes are plotted as a function of position. The element sizes are not drawn to scale for illustration purposes. Abbreviations: FL – focal length; ρ_M – radius of curvature.

7.4.2 III-V Surface-Emitter Cavity Design

We perform the same procedure in designing the laser cavity utilizing III-V surface-emitting gain chip. We first calculate the physical distance separating the gain chip with the external cavity mirror. For the III-V *VECSEL* (no top DBR stack) chip at 795 nm wavelength, we do not know the exact epitaxial structure, so we must make approximation. The bottom side DBR stack is one of the cavity mirrors. Optical field partially penetrates into the bottom side DBR, and we make the assumption about DBR penetration as we made in Section 7.1.2, which was one wavelength long penetration (~800 nm). The full chip length is the effective active region barrier thickness d_b or 2.4 μm as given in Table 7.1.

Next, we decide on the placement of the laser cavity optical elements and their characteristics. The beam waist should be located in the middle of the cavity, and this is where alkali cell will be placed. To obtain the same absorber saturation energy E_{sA} as our simulation in Section 7.3.2, the beam waist diameter should be 60 μm, the same as what was used in simulation as shown in Table 7.2. We use ray transfer matrix with Gaussian beam analysis to analyze our cavity design. As the modelocking simulations were made assuming cavity mode size at VECSEL chip of 4 μm diameter (at FWHM), the Gaussian aperture Δ that mimics the effect of oxide confinement aperture leading to such mode size has the parameter $2\Delta=(4\mu m\times2)/(2\ln2)^{1/2}=3.40\mu m$.

We present the design with VECSEL gain chip in Fig. 7.12, where we illustrate the design schematics and give the placement positions of the elements. We use the same procedure that was used in Section 7.4.1 to obtain this design. Our cavity here utilizes a single lens with focal length of 2.00 mm (same as in Table 7.3) to focus the output beam from the optical gain chip, along with an external cavity mirror with curvature radius ρ_M of 25 mm. In Fig. 7.12, we also plot the calculated optical mode sizes (at half maximum intensity level) inside the cavity as a function of position. The divergence angle of the cavity mode emanating from VECSEL chip is 12.6°, very close to that of a standalone device (no external cavity mirror). The calculated beam waist diameter of 53.7 μm is close to the target of 60 μm.

The design we present in Fig. 7.12 should be feasible to build. The lens is commercially available, and the working distance of ~0.5 mm between VECSEL chip and the lens is not unreasonably small, especially if the packaging on the gain chip is minimized for size (e.g., no TO can). The alkali vapor cell position is nearly in the center between the lens and the output coupler cavity mirror, where there is adequate space for our cell holder.
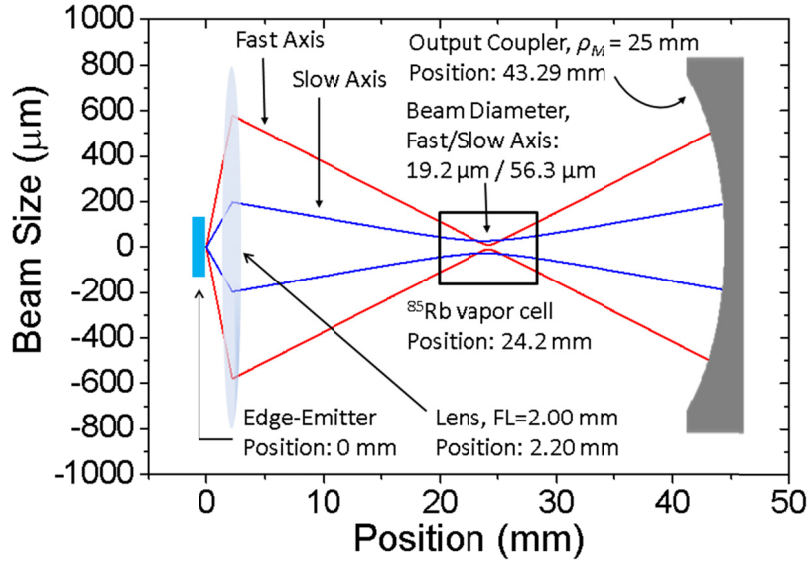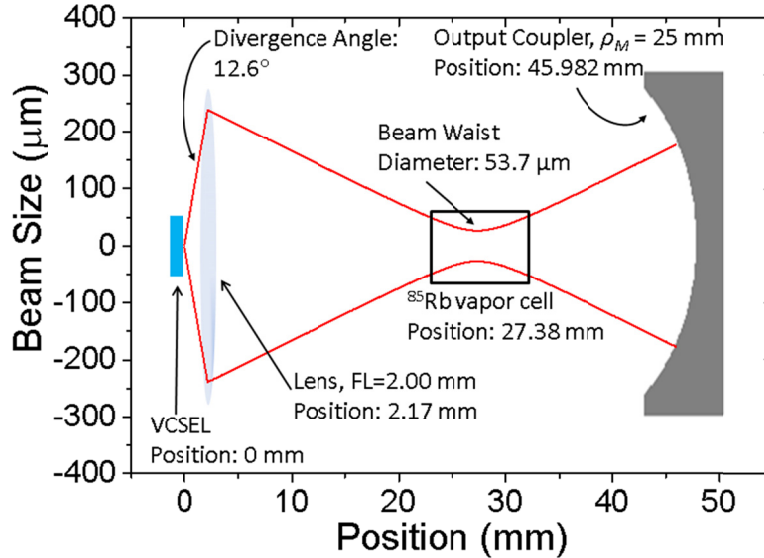

Fig. 7.12. III-V VECSEL (795 nm wavelength) cavity design. The VECSEL emission aperture is placed at position x=0. The calculated optical mode size (at half maximum level) is plotted as a function of position. The element sizes are not drawn to scale for illustration. Abbreviations: FL – focal length; ρ_M – radius of curvature of mirror.

7.5   Summary and Implications

In this chapter, we adapt the SVB approach to modelocked laser analysis model, first presented in Section 2.4, for an alkali vapor cell saturable absorber as well as the possibility of using either surface-emitting or edge-emitting optical gain chips. Then, we used this modified model to investigate the four laser cavity configurations: (i) optically-pumped surface-emitting configuration with a 420 nm VECSEL chip; (ii) electrically-pumped surface-emitting configuration with the 795 nm VECSEL gain chip; (iii) edge-emitting configuration using a 795 nm edge-emitting gain chip; (iv) also edge-emitting configuration but with 420 nm gain chip.

Simulations using the modelocked laser analysis model revealed that two laser configurations utilizing 795 nm wavelength gain chips (III-V material system), in both edge-emitting and in surface-emitting configuration, are more feasible from practical realization point of view in achieving stable, self-starting modelocked operation at reasonable driving parameters. We note that the edge-emitting configuration at 795 nm wavelength is more practical than the surface-emitting configuration due to the wide commercial availability of edge-emitting gain chips.

We then use ray transfer matrix with Gaussian beam analysis to design optical cavities that will allow one to reach the modelocked operation regime in experiment. These stable optical cavity designs are consistent with outcomes of the simulations used to analyze modelocked operation regime. The design here will serve as the starting point for experimentally building active atomic clocks based on semiconductor modelocked laser and ^{85}Rb vapor saturable absorber.

Chapter 8   Conclusion and Future Outlook

This dissertation addresses the various aspects of a potential active atomic clock based on modelocked external cavity semiconductor laser with ^{85}Rb vapor cell saturable absorber. Toward the goal of realizing such atomic clock, theoretical and experimental work has been performed, yielding novel results in the field of semiconductor lasers and atomic physics.

The most important component in any modelocked laser is the saturable absorber. In this research, we investigate the feasibility of utilizing not only the traditional D_1 line of ^{85}Rb atoms (795 nm wavelength) for saturable absorber work, but also the less used $5S_{1/2}$-$6P_{3/2}$ line (420 nm). To properly treat an alkali vapor cell as a saturable absorber, we have developed a model for its optical absorption characteristics along with experimental measurements of ^{85}Rb parameters that are vital for modelocked lasing analysis.

We have developed a six-level atomic model for the absorption characteristics of alkali atoms. This model is applicable when the atoms are under optical interrogation by a narrow linewidth laser, as it would be inside a modelocked laser cavity. From this model, we theoretically develop the effects of optical beam size and buffer gas pressure on ground state relaxation time τ_g and spin relaxation time T_s, building on realistic atomic population distribution profile arising from diffusion. We developed steady-state optical interrogation methods to measure τ_g and T_s. Lastly, we developed a novel pump-probe technique to measure the excited state lifetime τ_{ex}, a vital parameter for saturable absorber operation.

In the D_1 atomic line, we experimentally measured the τ_g and T_s of alkali atoms with optical beams of different diameters, and we have found good agreement with our theoretical predictions. We also measured the dependence of τ_g and T_s on buffer gas pressure. Lastly, we use our novel pump-probe technique to measure excited state lifetime τ_{ex} of ^{85}Rb cells in the D_1 line.

To perform spectroscopy measurements of ^{85}Rb in the $5S_{1/2}$-$6P_{3/2}$ line at 420 nm wavelength, one needs a single wavelength, narrow linewidth laser in the blue-violet spectral range with relatively low noise characteristics. Because such an optical source with precisely quoted linewidth and noise performances is not readily available, we have built and characterize a blue wavelength external cavity diode laser (ECDL) for spectroscopy applications. Our characterization and analysis of this ECDL lead us to conclude that micro-crack formation and propagation is a major contributor to the mode clustering effect in III-nitride laser diodes, contributing to the ongoing discussion on the exact origin of the mode clustering effect.

On the $5S_{1/2}$-$6P_{3/2}$ line, we measured the pressure linewidth broadening and frequency shift coefficients of N_2 buffer gas, which are not found in literature. For the purpose of measuring the excited state lifetime τ_{ex}, we started with the objective of obtaining a short optical pulse with precise wave-

length, which we intended to use as the optical pump in a pump-probe technique for τ_{ex} measurement. We were able to obtain solitary optical pulse generation with precise wavelength by using our ECDL, as the master laser, to optically injection lock a passively Q-switched InGaN multi-section laser diode (MSLD). To the best of our knowledge, the optical injection locking of a Q-switched III-nitride MSLD has never been done before.

Due to inadequate pulse energy from the MSLD, we then attempted to measure the lifetime τ_{ex} in the excited state $6P_{3/2}$ by using a continuous wave pump laser on the $5S_{1/2}$-$5P_{1/2}$ line (instead of a pulsed one at $5S_{1/2}$-$6P_{3/2}$ line) and a probe laser on the $5S_{1/2}$-$6P_{3/2}$ line. We performed pump-probe measurements by using a distributed feedback laser at 795 nm wavelength as the pump laser and our 420 nm wavelength ECDL as the probe laser. We note that the value of $6P_{3/2}$ lifetime found in literature [102], [103] is provided without supporting evidence, and this value is very different from what one would obtain by taking the reciprocal of the $5S_{1/2}$-$6P_{3/2}$ line transition strength [104]. Thus, it is of great interest to us to obtain a definitive lifetime value. In our experiments, the measured τ_{ex} of a ^{85}Rb cell with no buffer gas is close to the literature value in [102], [103]. Our pump-probe measurements also showed that τ_{ex} in the $6P_{3/2}$ state is reduced when in the presence of N_2 buffer gas.

One of the possible realizations of our atomic clock based on modelocked laser with alkali vapor cell absorber, as initially envisioned, incorporate III-nitride based vertical-external-cavity surface-emitting laser (VECSEL) at 420 nm wavelength for operation on the $5S_{1/2}$-$6P_{3/2}$ line of Rb. Prior to this dissertation work, there were no reports of centimetric length external cavity III-nitride VECSEL suitable for incorporation of intracavity elements. Therefore, we experimentally realized an optically pumped III-nitride VECSEL with injection seeding from a microcavity, and we were able to obtain lasing for a cavity as long as 50 mm, making such VECSEL suitable for incorporation of intracavity elements such as a saturable absorber. This is the longest III-nitride VECSEL cavity that we know of at the time of its realization. We have extensively characterized parameters such as the lasing threshold, spectra, and beam quality factor as a function of the external cavity length, and developed models detailing these dependence.

Finally, from the six-level model for alkali atoms and measurements from spectroscopy experiments, we have adapted a state of the art modelock lasing analysis technique to incorporate a ^{85}Rb vapor cell saturable absorber, for both the D_1 and the $5S_{1/2}$-$6P_{3/2}$ lines. From this, we investigated different laser cavity configurations and the operation conditions that will yield modelocked lasing operation. Possible realizations of our atomic clock based on modelocked laser with alkali vapor cell absorber include III-V alloy based ECDL and VECSEL as well as III-nitride based ECDL and VECSEL. We conclude that two configurations are mostly suitable for being attempted in experiment, with the first configuration having the most prospects from a practical point of view: (i) the cavity utilizing III-V edge-emitting gain chip at 795 nm wavelength, and (ii) the laser cavity utilizing III-V VECSEL gain chip, also 795 nm wavelength. We then use optical transfer matrix and Gaussian beam analysis methods to design these laser cavities. These designs will serve as the starting point for future experimental realization of such laser systems.

For the continuation of this research, the immediate plan would be the physical implementations of the laser cavities. Through careful tuning of the gain chip drive current and the ^{85}Rb vapor cell tem-

perature, the goal is to reach the modelocked lasing regime. Finding the correct operation parameters will be aided by modelocked lasing analysis simulations in Chapter 7, and these will be vital as the operation parameter range has been predicted to be narrow. Once modelocked lasing is achieved, the stability of the optical oscillation frequency would be characterized using standard techniques for atomic clocks.

There are additional physics phenomena to be explored when modelocked lasing is achieved. For one, the ^{85}Rb atoms would be subjected to resonant coherent population trapping (CPT) effect. Although this slightly affects the absorption characteristics by creating a shallow absorption dip of ~1% or less, CPT resonance is expected to be the key mechanism which will determine the stability of modelocked pulse repetition frequency. A better understanding of this mechanism would likely aid in designing and building better active atomic clocks based on modelocked lasers.

As mentioned in Chapter 1, the choice of ^{85}Rb as the atomic species in this research is due to the challenges of building short length optical cavities and small cell holders with conventional glass-blown alkali vapor cells. Nevertheless, atoms with higher hyperfine splitting frequency such as ^{87}Rb and Cs are very attractive because atomic clocks that utilize them should, in theory, have better frequency stability than clocks utilizing ^{85}Rb. To utilize these atoms as saturable absorbers in modelocked lasers, one should turn to short length alkali vapor cells fabricated using micro electro-mechanical systems (MEMS) technology. This is an active field of engineering research that is currently pursued for micro atomic clocks based on CPT, and the research and development to fabricate suitable MEMS-cells for modelocked laser saturable absorber should benefit from such synergy. Potentially, very compact active atomic clocks shorter than 2 cm long can be achieved through the use of MEMS-cells filled with Cs vapor. The theoretical and experimental methods developed in this dissertation should lay a foundation in the development of such clocks.

Bibliography

[1] J. Vanier and C. Audoin, *The Quantum Physics of Atomic Frequency Standards*, 1st ed. A. Hilger, 1989.

[2] J. C. Camparo, "The rubidium atomic clock and basic research," *Phys. Today*, vol. 60, no. 11, pp. 33–39, 2007.

[3] H. R. Gray, R. M. Whitley, and C. R. Stroud, "Coherent trapping of atomic populations," *Opt. Lett.*, vol. 3, no. 6, pp. 218–220, Dec. 1978.

[4] J. Vanier, "Atomic clocks based on coherent population trapping: a review," *Appl. Phys. B*, vol. 81, no. 4, pp. 421–442, Aug. 2005.

[5] D. Schneuwly, "Fundamentals: Frequency & Time Generation." [Online]. Available: http://www.chronos.co.uk/files/pdfs/itsf/2012/Day1/0900_Frequency_and_Time_Generation_Dominik_Schneuwly_Oscilloquartz.pdf. [Accessed: 11-Oct-2014].

[6] B. J. Bloom, T. L. Nicholson, J. R. Williams, S. L. Campbell, M. Bishof, X. Zhang, W. Zhang, S. L. Bromley, and J. Ye, "An optical lattice clock with accuracy and stability at the 10-18 level," *Nature*, vol. 506, no. 7486, pp. 71–75, Feb. 2014.

[7] Y.-Y. Jau and W. Happer, "Push-Pull Laser-Atomic Oscillator," *Phys. Rev. Lett.*, vol. 99, no. 22, pp. 223001–1 – 223001–4, Nov. 2007.

[8] Y.-Y. Jau, E. Miron, A. Post, N. Kuzma, and W. Happer, "Push-Pull Optical Pumping of Pure Superposition States," *Phys. Rev. Lett.*, vol. 93, no. 16, pp. 160802–1 – 160802–4, Oct. 2004.

[9] Y.-Y. Jau, "New Studies of Optical Pumping, Spin Resonances, and Spin Exchange in Mixtures of Inert Gases and Alkali-Metal Vapors," Ph.D. dissertation, Princeton University, Princeton, NJ, 2005.

[10] E. Breschi, Z. D. Grujić, P. Knowles, and A. Weis, "A high-sensitivity push-pull magnetometer," *Appl. Phys. Lett.*, vol. 104, no. 2, p. 023501, Jan. 2014.

[11] K. Masuda, M. Pellaton, G. Mileti, L. Arissian, and J. C. Diels, "Push-pull optical pumping with mode-locked laser," in *European Frequency and Time Forum*, Neuchatel, Switzerland, 2014, p. 280.

[12] X. Liu, J.-M. Mérolla, S. Guérandel, C. Gorecki, E. de Clercq, and R. Boudot, "Coherent-population-trapping resonances in buffer-gas-filled Cs-vapor cells with push-pull optical pumping," *Phys. Rev. A*, vol. 87, no. 1, p. 013416, Jan. 2013.

[13] D. L. Boiko, M. Krakowski, and S. Kundermann, "Review of requirements and identification of applicable technologies," in "Use of the Novel Modelocked Semiconductor Lasers Technique in the Sub-Picosecond Regime for Space Missions," European Space Agency, Contract 4000107051/12/NL/SFe, Ref. CSEM-261-ES.1326-TN-1, 2013.

[14] D. J. Derickson, J. G. Wasserbauer, R. J. Helkey, A. Mar, J. E. Bowers, D. R. Coblentz, R. Logan, and T. Tanbun-Ek, "Comparison of colliding pulse and self-colliding pulse monolithic cavity mode-locked semiconductor lasers," in *Digest of Conference on Optical Fiber Communication*, 1992, vol. 5, p. ThB3.

[15] Y. K. Chen, M. C. Wu, T. Tanbun-Ek, R. A. Logan, and M. A. Chin, "Subpicosecond monolithic colliding-pulse mode-locked multiple quantum well lasers," *Appl. Phys. Lett.*, vol. 58, no. 12, pp. 1253–1255, Mar. 1991.

[16] D. I. Nikitichev, Y. Ding, M. Ruiz, M. Calligaro, N. Michel, M. Krakowski, I. Krestnikov, D. Livshits, M. A. Cataluna, and E. U. Rafailov, "High-power passively mode-locked tapered InAs/GaAs quantum-dot lasers," *Appl. Phys. B*, vol. 103, no. 3, pp. 609–613, Jun. 2011.

[17] Y. Ding, R. Aviles-Espinosa, M. A. Cataluna, D. Nikitichev, M. Ruiz, M. Tran, Y. Robert, A. Kapsalis, H. Simos, C. Mesaritakis, T. Xu, P. Bardella, M. Rossetti, I. Krestnikov, D. Livshits, I. Montrosset, D. Syvridis, M. Krakowski, P. Loza-Alvarez, and E. Rafailov, "High peak-power picosecond pulse generation at 1.26 μm using a quantum-dot-based external-cavity mode-locked laser and tapered optical amplifier," *Opt. Express*, vol. 20, no. 13, pp. 14308–14320, Jun. 2012.

[18] U. Keller, D. A. B. Miller, G. D. Boyd, T. H. Chiu, J. F. Ferguson, and M. T. Asom, "Solid-state low-loss intracavity saturable absorber for Nd:YLF lasers: an antiresonant semiconductor Fabry-Perot saturable absorber," *Opt. Lett.*, vol. 17, no. 7, pp. 505–507, Apr. 1992.

[19] U. Keller, K. J. Weingarten, F. X. Kartner, D. Kopf, B. Braun, I. D. Jung, R. Fluck, C. Honninger, N. Matuschek, and J. Aus der Au, "Semiconductor saturable absorber mirrors (SESAM's) for femtosecond to nanosecond pulse generation in solid-state lasers," *IEEE J. Sel. Top. Quantum Electron.*, vol. 2, no. 3, pp. 435–453, Sep. 1996.

[20] A.-R. Bellancourt, D. J. H. C. Maas, B. Rudin, M. Golling, T. Südmeyer, and U. Keller, "Modelocked integrated external-cavity surface emitting laser," *IET Optoelectron.*, vol. 3, no. 2, pp. 61–72, Apr. 2009.

[21] Y. Barbarin, M. Hoffmann, W. P. Pallmann, I. Dahhan, P. Kreuter, M. Miller, J. Baier, H. Moench, M. Golling, T. Südmeyer, B. Witzigmann, and U. Keller, "Electrically Pumped Vertical External Cavity Surface Emitting Lasers Suitable for Passive Modelocking," *IEEE J. Sel. Top. Quantum Electron.*, vol. 17, no. 6, pp. 1779–1786, Nov. 2011.

[22] D. Lorenser, D. J. H. C. Maas, H. J. Unold, A.-R. Bellancourt, B. Rudin, E. Gini, D. Ebling, and U. Keller, "50-GHz Passively Mode-Locked Surface-Emitting Semiconductor Laser With 100-mW Average Output Power," *IEEE J. Quantum Electron.*, vol. 42, no. 8, pp. 838–847, Aug. 2006.

[23] M. Mangold, C. A. Zaugg, S. M. Link, M. Golling, B. W. Tilma, and U. Keller, "Pulse repetition rate scaling from 5 to 100 GHz with a high-power semiconductor disk laser," *Opt. Express*, vol. 22, no. 5, p. 6099, Mar. 2014.

[24] "Novalux." [Online]. Available: http://web.archive.org/web/20060616055303/http:/www.novalux.com/. [Accessed: 10-Oct-2014].

[25] S. Jiang, Z. Pan, M. Dagenais, R. . Morgan, and K. Kojima, "Influence of external optical feedback on threshold and spectral characteristics of vertical-cavity surface-emitting lasers," *IEEE Photonics Technol. Lett.*, vol. 6, no. 1, pp. 34–36, Jan. 1994.

[26] M. Wong, "Pressure Accumulation in PMT due to Helium Permeation," Apr-2002. [Online]. Available: http://home.fnal.gov/~mlwong/quartz.pdf.

[27] W. Happer, "Optical Pumping," *Rev. Mod. Phys.*, vol. 44, no. 2, pp. 169–249, Apr. 1972.

[28] D. A. Steck, "Rubidium 85 D Line Data," 2008. [Online]. Available: http://steck.us/alkalidata/rubidium85numbers.pdf. [Accessed: 07-Jan-2014].

[29] H. Haus, "Theory of mode locking with a slow saturable absorber," *IEEE J. Quantum Electron.*, vol. 11, no. 9, pp. 736–746, Sep. 1975.

[30] G. H. C. New, "Pulse evolution in mode-locked quasi-continuous lasers," *IEEE J. Quantum Electron.*, vol. 10, no. 2, pp. 115–124, Feb. 1974.

[31] I. V. Smetanin, P. P. Vasil'ev, and D. L. Boiko, "Theory of the ultrafast mode-locked GaN lasers in a large-signal regime," *Opt. Express*, vol. 19, no. 18, pp. 17114–17120, 2011.

[32] "Blue Femtosecond Laser Implemented with Group-III Nitrides." [Online]. Available: http://femtoblue.epfl.ch/. [Accessed: 17-Sep-2014].

[33] J. L. A. Dubbeldam, J. A. Leegwater, and D. Lenstra, "Theory of mode-locked semiconductor lasers with finite absorber relaxation times," *Appl. Phys. Lett.*, vol. 70, no. 15, pp. 1938–1940, Apr. 1997.

[34] R. G. Koumans and R. van Roijen, "Theory for Passive Mode-Locking in Semiconductor Laser Structures Including the Effects of Self-Phase Modulation, Dispersion, and Pulse Collisions," *IEEE J. Quantum Electron.*, vol. 32, no. 3, pp. 478–492, 1996.

[35] J. A. Leegwater, "Theory of Mode-Locked Semiconductor Lasers," *IEEE J. Quantum Electron.*, vol. 32, no. 10, pp. 1782–1790, 1996.

[36] C. H. Henry, "Theory of the linewidth of semiconductor lasers," *IEEE J. Quantum Electron.*, vol. 18, no. 2, pp. 259–264, 1982.

[37] M. Osinski and J. Buus, "Linewidth broadening factor in semiconductor lasers–An overview," *IEEE J. Quantum Electron.*, vol. 23, no. 1, pp. 9–29, 1987.

[38] D. L. Boiko and M. Krakowski, "Preliminary MLSCL designs, performance predictions and definition of experimental validation approach," in "Use of the Novel Modelocked Semiconductor Lasers Technique in the Sub-Picosecond Regime for Space Missions," European Space Agency, Contract 4000107051/12/NL/SFe, Ref. CSEM-261-ES.1326-TN-2, 2013.

[39] T. G. Walker and W. Happer, "Spin-exchange optical pumping of noble-gas nuclei," *Rev. Mod. Phys.*, vol. 69, no. 2, p. 629, 1997.

[40] D. A. Steck, "Rubidium 87 D Line Data," 2008. [Online]. Available: http://steck.us/alkalidata/rubidium87numbers.pdf. [Accessed: 09-Jan-2014].

[41] E. Arimondo, M. Inguscio, and P. Violino, "Experimental determinations of the hyperfine structure in the alkali atoms," *Rev. Mod. Phys.*, vol. 49, no. 1, pp. 31–75, Jan. 1977.

[42] J. Vanier, J.-F. Simard, and J.-S. Boulanger, "Relaxation and frequency shifts in the ground state of Rb^{85}," *Phys. Rev. A*, vol. 9, no. 3, pp. 1031–1040, Mar. 1974.

[43] M. E. Wagshul and T. E. Chupp, "Laser optical pumping of high-density Rb in polarized ^{3}He targets," *Phys. Rev. A*, vol. 49, no. 5, p. 3854, 1994.

[44] M. D. Rotondaro and G. P. Perram, "Collisional broadening and shift of the rubidium D_1 and D_2 lines ($5^2S_{1/2} \rightarrow 5^2P_{1/2}, 5^2P_{3/2}$) by rare gases, H$_2$, D$_2$, N$_2$, CH$_4$, and CF$_4$," *J. Quant. Spectrosc. Radiat. Transfer*, vol. 57, no. 4, pp. 497–507, 1997.

[45] D. Aumiler, T. Ban, and G. Pichler, "High-resolution measurements of the pressure broadening and shift of the rubidium $5^2S_{1/2}$–$6^2P_{3/2}$ line by argon and helium," *Phys. Rev. A*, vol. 70, no. 3, pp. 032723–1 – 032723–5, 2004.

[46] E. Caliebe and K. Niemax, "Oscillator strengths of the principal series lines of Rb," *J. Phys. B At. Mol. Phys.*, vol. 12, no. 2, pp. L45–L51, 1979.

[47] R. K. Ghosh, "Spin Exchange Optical Pumping of Neon," Ph.D. dissertation, Princeton University, Princeton, NJ, 2009.

[48] K. Yiorgos, "Spin Noise, Decoherence and Magnetic effects in Alkali Atoms and Biomolecules," Ph.D. dissertation, University of Crete, Heraklion, Greece, 2010.

[49] L. P. Pitaevskii and E. M. Lifshitz, *Physical Kinetics: Volume 10*, 1st edition. Oxford England: Butterworth-Heinemann, 1976.

[50] S. Chapman, T. G. Cowling, and C. Cercignani, *The Mathematical Theory of Non-uniform Gases: An Account of the Kinetic Theory of Viscosity, Thermal Conduction and Diffusion in Gases*, 3rd edition. Cambridge ; New York: Cambridge University Press, 1991.

[51] I. Novikova, A. B. Matsko, and G. R. Welch, "Influence of a buffer gas on nonlinear magneto-optical polarization rotation," *J. Opt. Soc. Am. B*, vol. 22, no. 1, pp. 44–56, 2005.

[52] G. Baum, C. D. Caldwell, and W. Schröder, "Dual-frequency optical pumping for spin-polarizing a lithium atomic beam," *Appl. Phys.*, vol. 21, no. 2, pp. 121–126, Feb. 1980.

[53] U. Volz and H. Schmoranzer, "Precision lifetime measurements on alkali atoms and on helium by beam–gas–laser spectroscopy," *Phys. Scr.*, vol. 1996, no. T65, p. 48, Jan. 1996.

[54] J. E. Simsarian, L. A. Orozco, G. D. Sprouse, and W. Z. Zhao, "Lifetime measurements of the 7p levels of atomic francium," *Phys. Rev. A*, vol. 57, no. 4, pp. 2448–2458, Apr. 1998.

[55] D. V. Giri, "Effective Rise Time Resulting from a Convolution of Waveforms with Exponential and Gaussian Rise Characteristics," 1987. [Online]. Available: http://www.ece.unm.edu/summa/notes/Measure/0033.pdf. [Accessed: 22-May-2014].

[56] E. S. Hrycyshyn and L. Krause, "Inelastic collisions between excited alkali atoms and molecules. VII. Sensitized fluorescence and quenching in mixtures of rubidium with H_2, HD, D_2, N_2, CH_4, CD_4, C_2H_4, and $C_2H_6^1$," *Can. J. Phys.*, vol. 48, no. 22, pp. 2761–2768, Nov. 1970.

[57] R. Hofmann, V. Wagner, H.-P. Gauggel, F. Adler, P. Ernst, H. Bolay, A. Sohmer, F. Scholz, and H. C. Schweizer, "Realization and characterization of optically pumped GaInN-GaN DFB lasers," *IEEE J. Sel. Top. Quantum Electron.*, vol. 3, no. 2, pp. 456–460, 1997.

[58] H. Schweizer, H. Gräbeldinger, V. Dumitru, M. Jetter, S. Bader, G. Brüderl, A. Weimar, A. Lell, and V. Härle, "Laterally Coupled InGaN/GaN DFB Laser Diodes," *Phys. Status Solidi A*, vol. 192, no. 2, pp. 301–307, 2002.

[59] T. Onishi, O. Imafuji, K. Nagamatsu, M. Kawaguchi, K. Yamanaka, and S. Takigawa, "Continuous Wave Operation of GaN Vertical Cavity Surface Emitting Lasers at Room Temperature," *IEEE J. Quantum Electron.*, vol. 48, no. 9, pp. 1107–1112, Sep. 2012.

[60] G. Cosendey, A. Castiglia, G. Rossbach, J.-F. Carlin, and N. Grandjean, "Blue monolithic AlInN-based vertical cavity surface emitting laser diode on free-standing GaN substrate," *Appl. Phys. Lett.*, vol. 101, no. 15, p. 151113, 2012.

[61] H. Leinen, D. Gläßner, H. Metcalf, R. Wynands, D. Haubrich, and D. Meschede, "GaN blue diode lasers: a spectroscopist's view," *Appl. Phys. B*, vol. 70, no. 4, pp. 567–571, 2000.

[62] D. J. Lonsdale, A. P. Willis, and T. A. King, "Extended tuning and single-mode operation of an anti-reflection-coated InGaN violet laser diode in a Littrow cavity," *Meas. Sci. Technol.*, vol. 13, no. 4, pp. 488–493, 2002.

[63] L. Hildebrandt, R. Knispel, S. Stry, J. R. Sacher, and F. Schael, "Antireflection-coated blue GaN laser diodes in an external cavity and Doppler-free indium absorption spectroscopy," *Appl. Opt.*, vol. 42, no. 12, pp. 2110–2118, 2003.

[64] O. M. Maragò, B. Fazio, P. G. Gucciardi, and E. Arimondo, "Atomic gallium laser spectroscopy with violet/blue diode lasers," *Appl. Phys. B Lasers Opt.*, vol. 77, no. 8, pp. 809–815, Dec. 2003.

[65] J. Hult, I. S. Burns, and C. F. Kaminski, "Wide-bandwidth mode-hop-free tuning of extended-cavity GaN diode lasers," *Appl. Opt.*, vol. 44, no. 18, pp. 3675–3685, 2005.

[66] M. Horstjann, V. Nenakhov, and J. P. Burrows, "Frequency stabilization of blue extended cavity diode lasers by external cavity optical feedback," *Appl. Phys. B*, vol. 106, no. 2, pp. 261–266, Sep. 2011.

[67] S. Pralgauskaite, V. Palenskis, and J. Matukas, "Low Frequency Noise Characteristics of Multimode and Singlemode Laser Diodes," in *Semiconductor Laser Diode Technology and Applications*, D. S. Patil, Ed. InTech, 2012, pp. 133–160.

[68] K. Motoki, "Development of gallium nitride substrates," *SEI Tech Rev*, vol. 70, pp. 28–35, 2010.

[69] "GaAs wafer specifications from AXT Inc.," *GaAs wafer specifications from AXT Inc.* [Online]. Available: http://www.axt.com/site/index.php?q=node/37. [Accessed: 07-Jan-2014].

[70] S. Nakamura, M. Senoh, S. Nagahama, N. Iwasa, T. Yamada, T. Matsushita, Y. Sugimoto, and H. Kiyoku, "Optical gain and carrier lifetime of InGaN multi-quantum well structure laser diodes," *Appl. Phys. Lett.*, vol. 69, no. 11, pp. 1568–1570, 1996.

[71] I. V. Smetanin and P. P. Vasil'ev, "Enhanced longitudinal mode spacing in blue-violet InGaN semiconductor lasers," *Appl. Phys. Lett.*, vol. 100, no. 4, p. 041113, 2012.

[72] P. P. Vasil'ev, A. B. Sergeev, I. V. Smetanin, T. Weig, U. T. Schwarz, L. Sulmoni, J. Dorsaz, J.-M. Lamy, J.-F. Carlin, N. Grandjean, X. Zeng, T. Stadelmann, S. Grossmann, A. C. Hoogerwerf, and D. L. Boiko, "Mode locking in monolithic two-section InGaN blue-violet semiconductor lasers," *Appl. Phys. Lett.*, vol. 102, no. 12, p. 121115, 2013.

[73] A. S. Zubrilov, V. I. Nikolaev, D. V. Tsvetkov, V. A. Dmitriev, K. G. Irvine, J. A. Edmond, and C. H. Carter, "Spontaneous and stimulated emission from photopumped GaN grown on SiC," *Appl. Phys. Lett.*, vol. 67, no. 4, pp. 533–535, 1995.

[74] R. G. Waters, "Diode laser degradation mechanisms: a review," *Prog. Quantum Electron.*, vol. 15, no. 3, pp. 153–174, 1991.

[75] I. Ratschinski, H. S. Leipner, F. Heyroth, W. Fränzel, O. Moutanabbir, R. Hammer, and M. Jurisch, "Indentation-induced dislocations and cracks in (0001) freestanding and epitaxial GaN," *J. Phys. Conf. Ser.*, vol. 281, p. 012007, Feb. 2011.

[76] R. K. Sink, "Cleaved-Facet Group-III Nitride Lasers," PhD Dissertation, University of California at Santa Barbara, Santa Barbara, USA, 2000.

[77] L. D. Turner, K. P. Weber, C. J. Hawthorn, and R. E. Scholten, "Frequency noise characterisation of narrow linewidth diode lasers," *Opt. Commun.*, vol. 201, no. 4, pp. 391–397, 2002.

[78] G. Di Domenico, S. Schilt, and P. Thomann, "Simple approach to the relation between laser frequency noise and laser line shape," *Appl. Opt.*, vol. 49, no. 25, pp. 4801–4807, 2010.

[79] M. Yamada, "Variation of intensity noise and frequency noise with the spontaneous emission factor in semiconductor lasers," *IEEE J. Quantum Electron.*, vol. 30, no. 7, pp. 1511–1519, 1994.

[80] J. J. McFerran and A. N. Luiten, "Fractional frequency instability in the 10^{-14} range with a thermal beam optical frequency reference," *J. Opt. Soc. Am. B*, vol. 27, no. 2, pp. 277–285, 2010.

[81] C. Affolderbach and G. Mileti, "A compact laser head with high-frequency stability for Rb atomic clocks and optical instrumentation," *Rev. Sci. Instrum.*, vol. 76, no. 7, p. 073108, 2005.

[82] K. Matsuoka, K. Saeki, E. Teraoka, M. Yamada, and Y. Kuwamura, "Characteristics of intensity noise in blue-violet InGaN semiconductor lasers," presented at the Proceedings of SPIE, 2006, p. 61330P–61330P–9.

[83] R. J. Fronen and L. K. Vandamme, "Low-frequency intensity noise in semiconductor lasers," *IEEE J. Quantum Electron.*, vol. 24, no. 5, pp. 724–736, 1988.

[84] R. Koda, T. Oki, T. Miyajima, H. Watanabe, M. Kuramoto, M. Ikeda, and H. Yokoyama, "100 W peak-power 1 GHz repetition picoseconds optical pulse generation using blue-violet GaInN diode laser mode-locked oscillator and optical amplifier," *Appl. Phys. Lett.*, vol. 97, no. 2, p. 021101, 2010.

[85] W. G. Scheibenzuber, C. Hornuss, U. T. Schwarz, L. Sulmoni, J. Dorsaz, J.-F. Carlin, and N. Grandjean, "Self-Pulsation at Zero Absorber Bias in GaN-Based Multisection Laser Diodes," *Appl. Phys. Express*, vol. 4, no. 6, p. 062702, 2011.

[86] K. Holc, G. Lükens, T. Weig, K. Köhler, J. Wagner, and U. T. Schwarz, "Gallium nitride laser diodes with integrated absorber: on the dynamics of self-pulsation," *Phys. Status Solidi C*, 2014.

[87] S. Kobayashi and T. Kimura, "Injection locking in AlGaAs semiconductor laser," *IEEE J. Quantum Electron.*, vol. 17, no. 5, pp. 681–689, May 1981.

[88] J. R. Tredicce, F. T. Arecchi, G. L. Lippi, and G. P. Puccioni, "Instabilities in lasers with an injected signal," *J. Opt. Soc. Am. B*, vol. 2, no. 1, pp. 173–183, Jan. 1985.

[89] K. Komori, Y. Takasu, M. Kumakura, Y. Takahashi, and T. Yabuzaki, "Injection-Locking of Blue Laser Diodes and Its Application to the Laser Cooling of Neutral Ytterbium Atoms," *Jpn. J. Appl. Phys.*, vol. 42, no. Part 1, No. 8, pp. 5059–5062, 2003.

[90] B. C. Keitch, N. R. Thomas, and D. M. Lucas, "Injection locking of violet laser diodes with a 3.2 GHz offset frequency for driving Raman transitions in $^{43}Ca^{+}$," *Opt. Lett.*, vol. 38, no. 6, pp. 830–832, Mar. 2013.

[91] N. Stelmakh, J.-M. Lourtioz, and A. Barthelemy, "Ultrashort pulse generation from a Q-switched AlGaAs laser with cw injection," *Appl. Phys. Lett.*, vol. 59, no. 6, pp. 624–626, Aug. 1991.

[92] J. Dorsaz, A. Castiglia, G. Cosendey, E. Feltin, M. Rossetti, M. Duelk, C. Velez, J.-F. Carlin, and N. Grandjean, "AlGaN-Free Blue III–Nitride Laser Diodes Grown on c-Plane GaN Substrates," *Appl. Phys. Express*, vol. 3, no. 9, p. 092102, Sep. 2010.

[93] L. Sulmoni, J.-M. Lamy, J. Dorsaz, A. Castiglia, J.-F. Carlin, W. G. Scheibenzuber, U. T. Schwarz, X. Zeng, D. L. Boïko, and N. Grandjean, "Static and dynamic properties of multi-section InGaN-based laser diodes," *J. Appl. Phys.*, vol. 112, no. 10, p. 103112, Nov. 2012.

[94] D. L. Boiko, G. M. Stéphan, and P. Besnard, "Fast polarization switching with memory effect in a vertical cavity surface emitting laser subject to modulated optical injection," *J. Appl. Phys.*, vol. 86, no. 8, pp. 4096–4099, Oct. 1999.

[95] P. P. Vasil'ev, V. Olle, R. V. Penty, and I. H. White, "Experimental study of delay-time statistics of superradiant pulses generated from semiconductor structures," *Appl. Phys. Lett.*, vol. 103, no. 24, p. 241108, Dec. 2013.

[96] L. A. Coldren and S. W. Corzine, *Diode lasers and photonic integrated circuits*. New York: Wiley, 1995.

[97] T. Fleischmann, J. M. Ulloa, M. Moran, G. J. Rees, J. Woodhead, and M. Hopkinson, "Characterisation of strained (111)B InGaAs/GaAs quantum well lasers with intracavity optical modulator," *Microelectron. J.*, vol. 33, no. 7, pp. 547–552, Jul. 2002.

[98] J. Sacher, D. Baums, P. Panknin, W. Elsässer, and E. O. Göbel, "Intensity instabilities of semiconductor lasers under current modulation, external light injection, and delayed feedback," *Phys. Rev. A*, vol. 45, no. 3, pp. 1893–1905, Feb. 1992.

[99] D. L. Boiko and P. P. Vasil'ev, "Superradiance dynamics in semiconductor laser diode structures," *Opt. Express*, vol. 20, no. 9, pp. 9501–9515, Apr. 2012.

[100] J. Dorsaz, D. L. Boïko, L. Sulmoni, J.-F. Carlin, W. G. Scheibenzuber, U. T. Schwarz, and N. Grandjean, "Optical bistability in InGaN-based multisection laser diodes," *Appl. Phys. Lett.*, vol. 98, no. 19, p. 191115, May 2011.

[101] M. Ibrahim and M. A. Alhaider, "Injection-locked passively Q-switched lasers," *IEEE J. Quantum Electron.*, vol. 18, no. 1, pp. 109–112, Jan. 1982.

[102] A. S. Zibrov, M. D. Lukin, L. Hollberg, and M. O. Scully, "Efficient frequency up-conversion in resonant coherent media," *Phys. Rev. A*, vol. 65, no. 5, pp. 051801–1 – 051801–4, Apr. 2002.

[103] T. Meijer, J. D. White, B. Smeets, M. Jeppesen, and R. E. Scholten, "Blue five-level frequency-upconversion system in rubidium," *Opt. Lett.*, vol. 31, no. 7, pp. 1002–1004, 2006.

[104] J. E. Sansonetti, "Wavelengths, Transition Probabilities, and Energy Levels for the Spectra of Rubidium (Rb I through Rb XXXVII)," *J. Phys. Chem. Ref. Data*, vol. 35, no. 1, pp. 301–421, 2006.

[105] H. P. Hooymayers and G. Nienhuis, "Quenching of excited rubidium (5^2P) atoms in flames," *J. Quant. Spectrosc. Radiat. Transf.*, vol. 8, no. 3, pp. 955–960, 1968.

[106] B. Rudin, A. Rutz, M. Hoffmann, D. Maas, A.-R. Bellancourt, E. Gini, T. Südmeyer, and U. Keller, "Highly efficient optically pumped vertical-emitting semiconductor laser with more than 20 W average output power in a fundamental transverse mode," *Opt. Lett.*, vol. 33, no. 22, pp. 2719–2721, 2008.

[107] A. Laurain, M. Myara, G. Beaudoin, I. Sagnes, and A. Garnache, "Multiwatt–power highly–coherent compact single–frequency tunable vertical–external–cavity–surface–emitting–semiconductor–laser," *Opt. Express*, vol. 18, no. 14, pp. 14627–14636, 2010.

[108] R. Debusmann, N. Dhidah, V. Hoffmann, L. Weixelbaum, U. Brauch, T. Graf, M. Weyers, and M. Kneissl, "InGaN-GaN Disk Laser for Blue-Violet Emission Wavelengths," *IEEE Photonics Technol. Lett.*, vol. 22, no. 9, pp. 652–654, May 2010.

[109] T. Wunderer, J. E. Northrup, Z. Yang, M. Teepe, A. Strittmatter, N. M. Johnson, P. Rotella, and M. Wraback, "In-well pumping of InGaN/GaN vertical-external-cavity surface-emitting lasers," *Appl. Phys. Lett.*, vol. 99, no. 20, p. 201109, 2011.

[110] S.-H. Park, J. Kim, H. Jeon, T. Sakong, S.-N. Lee, S. Chae, Y. Park, C.-H. Jeong, G.-Y. Yeom, and Y.-H. Cho, "Room-temperature GaN vertical-cavity surface-emitting laser operation in an extended cavity scheme," *Appl. Phys. Lett.*, vol. 83, no. 11, p. 2121, 2003.

[111] G. Cosendey, J.-F. Carlin, N. A. K. Kaufmann, R. Butté, and N. Grandjean, "Strain compensation in AlInN/GaN multilayers on GaN substrates: Application to the realization of defect-free Bragg reflectors," *Appl. Phys. Lett.*, vol. 98, no. 18, p. 181111, 2011.

[112] G. Christmann, R. Butté, E. Feltin, A. Mouti, P. Stadelmann, A. Castiglia, J.-F. Carlin, and N. Grandjean, "Large vacuum Rabi splitting in a multiple quantum well GaN-based microcavity in the strong-coupling regime," *Phys. Rev. B*, vol. 77, no. 8, Feb. 2008.

[113] G. Christmann, R. Butté, E. Feltin, J.-F. Carlin, and N. Grandjean, "Room temperature polariton lasing in a GaN∕AlGaN multiple quantum well microcavity," *Appl. Phys. Lett.*, vol. 93, no. 5, p. 051102, Aug. 2008.

[114] J. H. Rakels, "Influence of the surface height distribution on the total integrated scatter (TIS) formula," *Nanotechnology*, vol. 7, no. 1, p. 43, Mar. 1996.

[115] A. E. Siegman, *Lasers*. Sausalito, CA: University Science Books, 1986.

[116] P. Laporta and M. Brussard, "Design criteria for mode size optimization in diode-pumped solid-state lasers," *IEEE J. Quantum Electron.*, vol. 27, no. 10, pp. 2319–2326, Oct. 1991.

[117] A. E. Siegman, "Defining, measuring, and optimizing laser beam quality," presented at the Proc. SPIE, 1993, vol. 1868, pp. 2–12.

[118] T. Kuroda and A. Tackeuchi, "Influence of free carrier screening on the luminescence energy shift and carrier lifetime of InGaN quantum wells," *J. Appl. Phys.*, vol. 92, no. 6, pp. 3071–3074, Sep. 2002.

[119] G. Björk, H. Heitmann, and Y. Yamamoto, "Spontaneous-emission coupling factor and mode characteristics of planar dielectric microcavity lasers," *Phys. Rev. A*, vol. 47, no. 5, pp. 4451–4463, May 1993.

[120] K. Konnerth and C. Lanza, "DELAY BETWEEN CURRENT PULSE AND LIGHT EMISSION OF A GALLIUM ARSENIDE INJECTION LASER," *Appl. Phys. Lett.*, vol. 4, no. 7, pp. 120–121, Apr. 1964.

[121] T. Kuroda, A. Tackeuchi, and T. Sota, "Luminescence energy shift and carrier lifetime change dependence on carrier density in $In_{0.12}Ga_{0.88}N/In_{0.03}Ga_{0.97}N$ quantum wells," *Appl. Phys. Lett.*, vol. 76, no. 25, pp. 3753–3755, Jun. 2000.

[122] D. I. Babic and S. W. Corzine, "Analytic expressions for the reflection delay, penetration depth, and absorptance of quarter-wave dielectric mirrors," *IEEE J. Quantum Electron.*, vol. 28, no. 2, pp. 514–524, Feb. 1992.

[123] J. Piprek, *Semiconductor Optoelectronic Devices: Introduction to Physics and Simulation*, 1st edition. Amsterdam ; Boston: Academic Press, 2003.

[124] Y. Arakawa and A. Yariv, "Theory of gain, modulation response, and spectral linewidth in AlGaAs quantum well lasers," *IEEE J. Quantum Electron.*, vol. 21, no. 10, pp. 1666–1674, Oct. 1985.

[125] P. L. Derry, A. Yariv, K. Y. Lau, N. Bar-Chaim, K. Lee, and J. Rosenberg, "Ultralow-threshold graded-index separate-confinement single quantum well buried heterostructure (Al, Ga) As lasers with high reflectivity coatings," *Appl. Phys. Lett.*, vol. 50, no. 25, pp. 1773–1775, 1987.

[126] J. D. Ralston, S. Weisser, I. Esquivias, E. Larkins, J. Rosenzweig, P. J. Tasker, and J. Fleissner, "Control of differential gain, nonlinear gain and damping factor for high-speed application of GaAs-based MQW lasers," *IEEE J. Quantum Electron.*, vol. 29, no. 6, pp. 1648–1659, Jun. 1993.

[127] S. L. McCall and E. L. Hahn, "Self-Induced Transparency," *Phys. Rev.*, vol. 183, no. 2, pp. 457–485, 1969.

[128] M. D. Crisp, "Adiabatic-following approximation," *Phys. Rev. A*, vol. 8, no. 4, pp. 2128–2135, 1973.

Curriculum Vitae

Xi Zeng
Citizenship: United States of America
Email: xi.zeng1@gmail.com
Mobile Phone: +41 76 528 94 65 (Switzerland), +1 217 721 3717 (USA)
Birthday: November 6, 1983

Education

École Polytechnique Fédérale Lausanne (EPFL) (Oct. 2010 – Jan. 2015)
Ph.D. in Photonics
Thesis Directors: Professor Nicolas Grandjean (EPFL), Dr. Dmitri L. Boïko (CSEM SA)
Dissertation: *Perspectives of Active Atomic Clock Based on Modelocked Semiconductor Laser with Rubidium Vapor Cell Saturable Absorber*

University of Illinois at Urbana-Champaign (UIUC) (Aug. 2002 – Aug. 2009)
Master of Science in Electrical Engineering: Oct. 2008
    Thesis: *Toward a Photomixing-Based Monolithically Integrated Terahertz Generator*
Bachelor of Science with High Honors in Electrical Engineering: May 2006
Minor in Math

Work Experiences

Centre Suisse d'Electronique et de Microtechnique SA (CSEM SA)
Neuchâtel, Switzerland
Ph.D. Student (Jun. 2010 – Dec. 2015), joint with EPFL
Research Supervisor: Dr. Dmitri L. Boïko

University of Illinois at Urbana-Champaign
Urbana, IL, USA
Graduate Research Assistant (May 2007 – Sept. 2008)
Adviser – Assistant Professor Xiuling Li

Peer Reviewed Publications

X. Zeng and D. L. Boïko, "1/f noise in external-cavity InGaN diode laser at 420 nm wavelength for atomic spectroscopy," Optics Letters, **39** (6), 1685 (2014).

P. P. Vasil'ev, A. B. Sergeev, I. V. Smetanin, T. Weig, U. T. Schwarz, L. Sulmoni, J. Dorsaz, J.-M. Lamy, J.-F. Carlin, N. Grandjean, **X. Zeng**, T. Stadelmann, S. Grossmann, A. C. Hoogerwerf, and D. L. Boiko, "Mode locking in monolithic two-section InGaN blue-violet semiconductor lasers," Applied Physics Letters, **102** (12), 121115 (2013).

X. Zeng, D. L. Boïko, G. Cosendey, M. Glauser, J.-F. Carlin, and N. Grandjean, "In-depth analysis of injection-seeded long external cavity InGaN/GaN surface-emitting laser", Journal of Applied Physics **113** (4), 043108 (2013).

L. Sulmoni, J.-M. Lamy, J. Dorsaz, A. Castiglia, J.-F. Carlin, W. G. Scheibenzuber, U. T. Schwarz, **X. Zeng**, D. L. Boïko, and N. Grandjean, "Static and dynamic properties of multi-section InGaN-based laser diodes", Journal of Applied Physics **112** (10), 103112 (2012).

X. Zeng, D. L. Boïko, G. Cosendey, M. Glauser, J.-F. Carlin, and N. Grandjean, "Optically pumped long external cavity InGaN/GaN surface-emitting laser with injection seeding from a planar microcavity", Applied Physics Letters **101** (14), 141120 (2012).

Conference Presentations

X. Zeng, Christine Y. Wang, and D. L. Boïko, "Optical Beam Size Effects in Spin Polarized Pumping", postdeadline oral presentation in *2014 European Frequency and Time Forum*, Neuchâtel, Switzerland, 2014.

X. Zeng and D. L. Boïko, "Mode Clustering and Frequency Noise in an External Cavity GaN Diode Laser at 420 nm Wavelength for Atomic Spectroscopy", in *European Semiconductor Laser Workshop 2013*, Bristol, U. K., 2013.

X. Zeng, D. L. Boïko, G. Cosendey, M. Glauser, J.-F. Carlin, and N. Grandjean, "Optically pumped long external cavity InGaN/GaN surface-emitting laser with injection seeding from a planar microcavity", in *European Semiconductor Laser Workshop 2012*, Brussels, Belgium, 2012.

Conference Posters

X. Zeng, L. Sulmoni, J-M. Lamy, T. Stadelmann, S. Grossmann, A. C. Hoogerwerf, N. Grandjean and D. L. Boïko, "Solitary Pulse-on-Demand Production by Optical Injection Locking of Passively Q-Switched InGaN Diode Lasers Near Lasing Threshold", poster presentation in *IEEE International Semiconductor Laser Conference,* Palma de Mallorca, Spain, 2014.

X. Zeng, L. Sulmoni, J-M. Lamy, T. Stadelmann, S. Grossmann, A. C. Hoogerwerf, N. Grandjean and D. L. Boïko, "Solitary Pulse-on-Demand Production by Optical Injection Locking of Passively Q-Switched InGaN Diode Lasers Near Lasing Threshold", in *EPS-QEOD Europhoton Conference*, Neuchâtel, Switzerland, 2014.

X. Zeng and D. L. Boïko, "Absorption Spectroscopy of ^{85}Rb Atoms at 420 nm: Pressure Broadening with N_2 Buffer Gas and Saturation Intensity", in *2014 European Frequency and Time Forum*, Neuchâtel, Switzerland, 2014.

X. Zeng and D. L. Boïko, "External Cavity Diode Laser at 420 nm Wavelength for Atomic Spectroscopy", in *2013 European Frequency and Time Forum*, Prague, Czech Republic, 2013.

X. Zeng and D. L. Boïko, "Towards First Active Clock Based on Mode-Locked InGaN VECSEL with Rubidium Vapor Cell Saturable Absorber", in *2012 European Frequency and Time Forum*, Gothenburg, Sweden, 2012. *winner of the student award in the Microwave Frequency Standards category*

X. Zeng and D. L. Boïko, "Towards First Active Rubidium Clock Based on Mode-Locked InGaN/GaN VECSEL with Rb Vapor Cell Saturable Absorber", in *European Semiconductor Laser Workshop 2011*, Lausanne, Switzerland, 2011.